STUDIA

UNIVERSITATIS BABEŞ-BOLYAI

Chemia

CLUJ-NAPOCA 2004

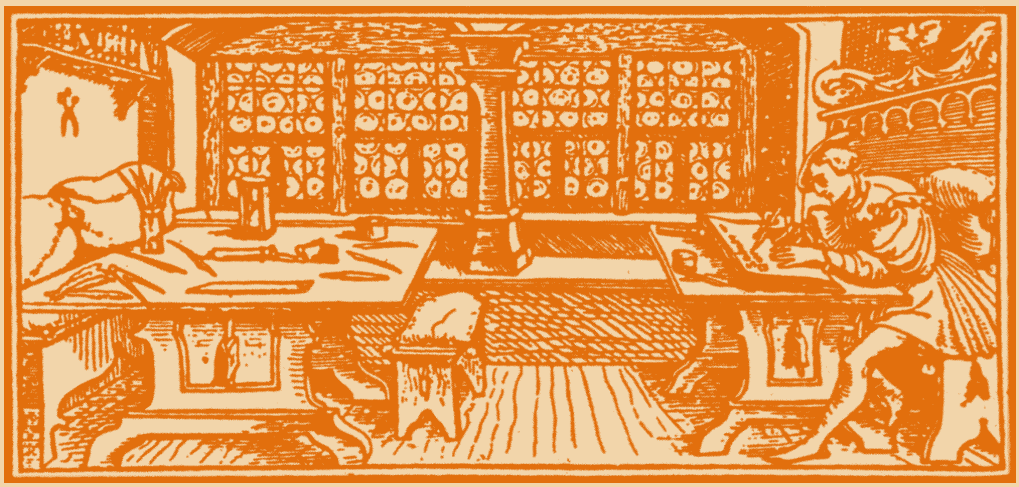

2

ANUL XLIX **2004**

S T U D I A
UNIVERSITATIS BABEŞ-BOLYAI
CHEMIA
2

EDITORIAL OFFICE: Republicii no. 24, 400015 Cluj-Napoca ♦ Phone 0264-40.53.52

SUMAR - CONTENTS - SOMMAIRE - INHALT

Professor Valer Fărcăşan at his 85th anniversary

Professor Valer Fărcăşan was born 85 years ago, on October the 3rd, 1919, in Zlatna, one of the three points of the fabulous well known auriferous triangle of the country. After finishing the high school (1939) at the Universitary Pedagogical Seminary ("Seminarul Pedagogic Universitar") in Cluj, he distinguished himself as an excellent student of the Faculty of Sciences, section Physics/Chemistry belonging to the University of Cluj, temporary moved to Timisoara in 1940 as a result of the "Vienna Dictate". He graduated in 1943 obtaining the licence diploma and in the same year, as a result of his remarcable theoretical and practical competence, was hired as a teaching assistant at the same faculty, returned after the war to Cluj. Under the guidance of Professor Ioan Tănăsescu he obtained in 1948 his PhD degree in the field of the chemistry of acridones.

All his teaching and scientific activity was developed more than 40 years at the Faculty of Chemistry and Chemical Engeneering of the "Babeş-Bolyai" University. He competently and merituously succeded to ascent step by step all the university degrees as a lecturer (1949), associate professor (1950) and finally full professor (1967) of organic chemistry, correlated also to biochemistry.

Retireing in 1985 he is now consulting professor at the Organic Chemistry Department of the faculty. As a professor he taught general chemistry, organic chemistry, biochemistry and chemistry of natural products, being also author or coauthor of organic textbooks and of an important treatise of vegetal chemistry (Phytochemistry) edited in three volumes. He is also one of the coworkers in three volumes of the "Enciclopedia de Chimie". As a PhD supervisor, 25 candidates obtained their PhD degrees under his guidance.

The main important domain in professor Fărcăşan's scientific activity implies the competent and detalied study in the field of aromatic heterocycles.

Concerning **compounds with acridinic structure,** pertinent studies were carried out in order to elucidate the structure of monochloro- and monobromoacridones, including also researches connected with an improved synthesis of Atebrine. New syntheses of thiazoloacridines, of amides and hydrazines with acridine nucleus as well as of sulphonamides starting from aminoacridone were established.

In the field of the **chemistry of phenothiazines**, new compounds were obtained, namely nitro-, formil-, N-methylphenothiazines as well as phenothiazineazlactones.

Another main research field was dedicated to compounds containing the **furane-, benzo-** and **dibenzofurane structure.** Anilides and sulphonamides of the furoic acid were synthesized as well as amides, thioamides and Schiff bases of dibenzofurane.

An important contribution to the **Jacobson reaction** in the synthesis of benzothiazols is also to be mentioned along with the extension of the method for the obtaining of polycyclic systems such as benzofuro-benzothiazols, indeno-benzothiazols, benzofuro-acridines.

For many of the newly synthesized compounds, a systematic study concerning the reaction mechanism or the influence of the substituents on their chemical and biological activity was undertaken.

One can't speak about the whole professor Fărcăsan activity without mentioning his wonderful, charming, kindness, sense of humor, honesty, qualities which made him so loved by the whole community knowing him. We all want to express him our gratitude, to wish him a long life with good health, serenity and deserved satisfactions.

THE EDITORIAL BOARD

Prof. Dr. Valer Fărcăşan
Faculty of Chemistry and Chemical Engineering
„Babeş-Bolyai" University, Cluj-Napoca, Romania

LIST OF PUBLICATIONS

BOOKS

1. E. Pora, D. Roşca, V. Fărcăşan
Tehnica pentru lucrări de fiziologie animală
Litografia Ministerului Invățământului, Braşov, 1955

2. C. Macarovici, E. Tarangul, V. Fărcăşan, E. Goina
Chimie generală (manual pentru şcolile tehnice)
Ed. Tehnică, Bucureşti, 1957

3. C. Bodea, V. Fărcăşan, E. Nicoară, H. Sluşanschi
Tratat de biochimie vegetală, Partea I, Fitochimie, vol. I – III
Ed. Acad. RSR, Bucureşti, 1964-1966

4. M. Ionescu, V. Fărcăşan, C. Anghel, A. Benkö
Chimie organică, partea I, fasc. 1
Litografia UBB, Cluj-Napoca, 1976

5. V. Fărcăşan, A. Benkö, C. Anghel
Chimie organică, partea I, fasc. 2
Litografia UBB, Cluj-Napoca, 1983

6. **Enciclopedia de chimie** (colaborare la vol. 2-4)
Ed. St. Şi Enciclopedică, Bucureşti, 1986-1987

ARTICLES

1. I. Tănăsescu, V. Fărcăşan
Despre acridone (XIII). Constituția monocloracridonelor
Analele Acad. RPR, **1949**, Ser. A., T. II, 445
Revue de chimie, **1956**, *T. I*, 27 (în limba franceză)

2. I. Tănăsescu, V. Fărcăşan
Despre acridone (XIV). Studii sintetice pentru obținerea atebrinei
Acad. RPR. Lucrările sesiunii ştiințifice, 2-12 iunie, **1950**

3. I. Tănăsescu, M. Ionescu, V. Fărcăşan
Contribuții la sintezele atebrinei şi plasmochinei
Studii şi cercet. chim., **1955**, *T. III*, 183

4. I. Tănăsescu, Al. Silberg, V. Fărcăşan, M. Ionescu, M. Terdie
Despre sterine (VI). Acțiunea acidului iodhidric asupra colesterinei şi acizilor biliari
Studii şi cercet. chim., **1954**, T. II, 223
Revue de chimie, **1957**, *T. II*, 172 (în limba germană)

5. I. Tănăsescu, V. Fărcăşan
Sesizarea unei erori esențiale în sinteza 2,4-dinitrobenzaldehidei după metoda propusă de G. M. Bennet şi F. V. Bell
Studii şi cercet. chim. (Cluj), **1957**, 169

6. V. Fărcăşan, C. Makkay
Derivați ai furanului (I). Anilide p-substituite ale acidului 5-nitrofuroic
Studii şi cercet. chim. (Cluj), **1957**, 151

7. V. Fărcăşan, C. Makkay
Derivați ai furanului (II). Produşi clorurați şi nitrați ai 2-furanilidei
Studii şi cercet. chim. (Cluj), **1957**, 363

8. V. Fărcăşan, C. Makkay
Derivați ai furanului (III). 2-Tiofuranilide şi 2-(furil)-benztiazoli
Studii şi cercet. chim. (Cluj), **1959**, 145

9. I. Tănăsescu, V. Fărcăşan, C. Toma
Sur les acridones (XVII). Sulfonamides dans la serie des acridones et acridines
Bull. Soc. Chim. Fr., **1960**, 691

10. V. Fărcăşan, C. Makkay
Über einige 5-nitro-2-brenzschleinsaureaanilide
Revue de chimie, **1960**, *T. V*, 129

11. C. Bodea, V. Fărcăşan
Despre fenotiazine (V). Acțiunea bicromatului de potasiu asupra 5-aciloxi- şi 5-metoxi-clorfenotiazinelor
Studii şi cercet. chim. (Cluj), **1960**, 121

12. C. Gh. Macarovici, V. Fărcăşan, G. Schmidt, V. Bota, M. Macarovici, A. Doruțiu, I. Pîrvu, E. Tesler
Asupra determinării elementelor metalice grele şi a arsenului în uleiurile comestibile, grăsimi, stearină şi oleină tehnică
Studia Univ. „Babeş-Bolyai" Chem., **1961**, 103

13. I. Tănăsescu, V. Fărcăşan, O. Piringer
Despre acridone (XXVI). Constituția monobromacridonelor
Studii şi cercet. chim. (Cluj), **1961**, 285

14. V. Fărcăşan
Derivați ai furanului (IV). Asupra unor produşi de substituție ai 2-furil-(2')-benztiazolului
Studii şi cercet. chim. (Cluj), **1963**, 103

15. C. Bodea, V. Fărcăşan, I. Oprean
Noi contribuții la cunoaşterea halogen-nitro-fenotiazinelor
Studii şi cercet. chim. (Cluj), **1963**, 173

16. C. Bodea, V. Fărcăşan, I. Oprean
Deistvie azotnoi kislotî na polibromfenotiazinî
Jurnal Obsscei Himii, **1964**, *XXXIV*, 2369

17. C. Bodea, V. Fărcăşan, I. Oprean
Azlactones of the phenothiazine series (I). The azlactone of 3-formyl-10-methyl-phenothiazine and 3-formyl-10-methyl-phenothizine-5,5-dioxide
Rev. Roum. Chim., **1965**, *10*, 1103
Studii şi cercet. chim., **1965**, *13*, 1157 (în limba română)

18. C. Bodea, V. Fărcăşan, T. Panea
The action of 60% nitric acid on some phenothiazines
Rev. Roum. Chim., **1966**, *11*, 239

19. C. Bodea, V. Fărcăşan, I. Oprean
Sulfonamides of 3-amino-phenothiazines
Rev. Roum. Chim., **1966**, *11*, 1117

20. V. Fărcăşan, F. Paiu
Derivați ai furanului (V). Unele observații privind preparea 2-(5'-nitrofuril(2')-benztiazolului
Studia Univ. „Babeş-Bolyai" Chem., **1966**, *2*, 107

21. V. Fărcăşan, I. Meşter
Derivați ai furanului (VI). Derivați monobromurați ai 2-furil-(2')-benztiazolului
Studia Univ. „Babeş-Bolyai" Chem., **1967**, *2*, 69

22. V. Fărcăşan, I. Balázs, F. Paiu
Cromatografia în strat subțire a unor benztiazoli
Studia Univ. „Babeş-Bolyai" Chem., **1967**, *2*, 75

23. C. Bodea, V. Fărcăşan, T. Panea
Synthetical phenothiazine glycosides (I). O-glucosides of 3-hydroxy-1,7,9-trichloro-phenothiazine and N-glucozides of phenothiazine
Rev. Roum. Chim., **1967**, *12*, 697

24. C. Bodea, V. Fărcăşan, T. Panea
Synthetical Phenothiazine Glycosides
Agressologie, **1968**, *IX*, 1

25. V. Fărcăşan, I. Balázs
Derivați ai furanului (VII). 2,2'-(α, α-furilen)-bis-benztiazolul
Studia Univ. „Babeş-Bolyai" Chem., **1968**, *1*, 123

26. V. Fărcăşan, I. Oprean, C. Bodea
Azlactones of the phenothiazine series (II). Ethanolysis of some azlactones of the phenothiazine series
Rev. Roum. Chim., **1968**, *13*, 647

27. C. Bodea, V. Fărcăşan, T. Panea
Reductive dehalogenation of polyhalogeno-phenothiazines
Rev. Roum. Chim., **1968**, *13*, 971

28. V. Fărcăşan, F. Paiu
Derivați ai furanului (VIII). Sulfonamide cu nucleu furanic
Studia Univ. „Babeş-Bolyai" Chem., **1968**, *2*, 103

29. V. Fărcăşan, I. Balázs
Tiazoloacridine (I). Studii privind prepararea tiazoloacridonelor
Studia Univ. „Babeş-Bolyai" Chem., **1969**, *1*, 43

30. C. Bodea, V. Fărcăşan, T. Panea
Synthetical phenothiazine glycosides (II). O-glucosides of 3-hydroxi-1,9-dibromo-7-chloro phenothiazine
Rev. Roum. Chim., **1969**, *14*, 523

31. C. Bodea, I. Oprean, V. Fărcăşan
Azlactones of the phenothiazine serie (III). Aminolysis of a some phenothiazine azlactones
Rev. Roum. Chim., **1969**, *14*, 673

32. V. Fărcăşan, S. Florea, R. Boju
Benzofuro-benzothiazoles (I). Application de la reaction Jacobson pour l'obtention des benzofuro-benzothiazoles
Studia Univ. „Babeş-Bolyai" Chem., **1970**, *1*, 63

33. I. Oprean, C. Bodea, V. Fărcăşan
On the synthesis of 3-nitro-10-methyl-phenothiazine
Rev. Roum. Chim., **1970**, *15*, 135

34. V. Fărcăşan, I. Oprean, C. Bodea
Sur la formylation des methyl-10-phenothiazines
Rev. Roum. Chim., **1970**, *15*, 1435

35. V. Fărcăşan, F. Paiu, I. Balázs
Derivatives of furan (XX). The anilide of 5-(2-benzothiazolyl)-furan-2-carboxylic acid
Studia Univ. „Babeş-Bolyai" Chem., **1970**, *2*, 97

36. V. Fărcăşan, F. Paiu
O nouă metodă de preparare a 2-[5'-nitrofuril]-(2')-benztiazolului (notă de laborator)
Studia Univ. „Babeş-Bolyai" Chem., **1970**, *2*, 145

37. C. Bodea, T. Panea, V. Fărcăşan
Synthetical phenothiazine glycosides (III). Oxidation reaction
Rev. Roum. Chim., **1970**, *15*, 1923

38. V. Fărcăşan, F. Paiu
Derivatives of furan (X). 5-(2-Benzothazolyl)-2-formylfuran
Studia Univ. „Babeş-Bolyai" Chem., **1971**, *1*, 111

39. T. Panea, C. Bodea, V. Fărcăşan
Phenothiazones (XVIII). Phenothiazones from 2-nitro- and 2-acetyl-phenothiazines
Rev. Roum. Chim., **1971**, *16*, 759

40. V. Fărcăşan, S. Florea
Über benzofuro-benzthiazoles (II). Die Struktur der bei der Oxidation von 3-Thiobenzolamino-dibenzofurane isolierten Benzofurobenzthiazoles
J. pr. Chem., **1970**, *312*, 1007

41. V. Fărcăşan, S. Florea
Benzofuro-benzthiazoles (III). 2-Furyl-benzofuro-benzothiazoles
Studia Univ. „Babeş-Bolyai" Chem., **1972**, *1*, 57

42. V. Fărcăşan, I. Balázs
Benzofuro-benzimidazoles (I). 2-Aminomethyl-benzfuro-[2,3-f]-benzimidazo les
Studia Univ. „Babeş-Bolyai" Chem., **1972**, *1*, 121

43. I. Oprean, V. Fărcăşan, F. Paiu
Derivatives of furan (XI). Electron impact fragmentation of some 5-benzothiazolyl-(2)-furans
Rev. Roum. Chim., **1972**, *17*, 1901

44. V. Fărcăşan, S. Florea
Benzofuro-benztiazoli (IV). Derivați substituiți ai 2-furil-benzofuro-benztiazolului
Studia Univ. „Babeş-Bolyai" Chem., **1973**, *1*, 143

45. Al. Silberg, V. Fărcăşan, A. Donea, M. Tomoaia
On the nitration of 2.4-diphenylthiazole
Studia Univ. „Babeş-Bolyai" Chem., **1973**, *1*, 59

46. V. Fărcăşan, I. Cristea
Dibenzofurans (I). The formylation of 3-dimethylamino-dibenzo-furan by the Vilsmeier-Haack method
Rev. Roum. Chim., **1973**, *18*, 469

47. T. Panea, V. Fărcăşan, C. Bodea
Hydroxy-phenothiazine-5,5-dioxides (I). 1,7,9-Trichloro-3-hydroxy-5,5-dioxi-phenothiazine
Rev. Roum. Chim., **1973**, *18*, 1259

48. I. Oprean, C. Bodea, V. Fărcăşan
IR CO Stretching frequencies in phenothiazine derivatives
Studia Univ. „Babeş-Bolyai" Chem., **1974**, *19(1)*, 25

49. V. Fărcăşan, F. Paiu, I. Meşter
Derivatives of furan (XII). On the bromination of 2-furyl-(2')-benzothiazole
Studia Univ. „Babeş-Bolyai" Chem., **1974**, *19(2)*, 51

50. W. Rieppe, S. Florea, V. Fărcăşan, I. Cristea
Massenspektrometrische Untersuchungen von izomeren Stikstoff-verbindungen des Dibenzofurans
Org. Mass Spectrometry, **1974**, *2*, 1046

51. V. Fărcăşan, S. Florea
Benzofuro-benzothiazoles (V). 2-Amino- and 2-mercapto-benzofurobenzothiazoles
Rev. Roum. Chim., **1976**, 2*1*, 621

52. I. Silberg, V. Fărcăşan, M. Diudea
Free radicals of phenothiazine and related compounds (III). Selective chlorination of phenothiazine with copper (II) chloride
J. pr. Chem., **1976**, *318*, 353

53. V. Fărcăşan, F. Paiu, C. Iuşan
Derivatives of furan (XIII). 2-[5'-Formyl(2')]-benzothiazoles
Studia Univ. „Babeş-Bolyai" Chem., **1977**, *22(1)*, 15

54. V. Fărcăşan, I. Balázs
Benzofuro-benzimidazoles (II). 2-Substituted benzofuro[2,3-f]-benzimidazoles
Studia Univ. „Babeş-Bolyai" Chem., **1977**, *22(1)*, 30

55. S. Florea, W. Kimpenhaus, V. Fărcăşan
Benzofurobenzthiazole (VI). ^{1}H und ^{13}C-NMR-Spektren von 2-aminobenzofuro [2,3-f]benzthiazol in Vergleich mit Dibenzofuran und 2-Aminobenzthiazol
Org. Magn. Resonance, **1977**, *9(3)*, 133

56. V. Fărcăşan, I. Cristea, S. Florea
Dibenzofurans (II). Schiff's bases from 3-aminodibenzofuran
Studia Univ. „Babeş-Bolyai" Chem., **1977**, *22(2)*, 72

57. I. Balázs, V. Fărcăşan, I. Haiduc
Synthesis of di- and triphenyllead polychloroacetates
Rev. Roum. Chim., **1977**, *22*, 379

58. V. Fărcăşan, A. Donea
Schiff's bases from 2-phenyl-4-(4'-amino-phenyl)-thiazole and 4-amino-biphenyl
Studia Univ. „Babeş-Bolyai" Chem., **1979**, *24(1)*, 42

59. V. Fărcăşan, A. Donea
Schiff's bases from 2-phenyl-4-(4'-amino-phenyl)-thiazole and 4-amino-biphenyl. Some UV data
Studia Univ. „Babeş-Bolyai" Chem., **1980**, *25(1)*, 76

60. V. Chiorean, S. Mager, V. Fărcăşan, A. Silberg
Die Darzens-Reaktion mit Thizoloaldehyden
J. pr. Chem., **1980**, *322*, 207

61. I. Oprean, I. Cristea, V. Fărcăşan
Electron impact mass spectra of some biphenyl und dibenzofuran derivatives
Studia Univ. „Babeş-Bolyai" Chem., **1980**, *25(2)*, 37

62. I. Balázs, V. Fărcăşan, C. Sârbu
Dibenzofurans (III). On the nitration of 3-acetylamino-2-bromo-dibenzofuran
Studia Univ. „Babeş-Bolyai" Chem., **1981**, *26(1)*, 24

63. I. Cristea, V. Fărcăşan
Dibenzofurans (IV). 3-Dipyrimidinylamino-(2')-dibenzofurans
Studia Univ. „Babeş-Bolyai" Chem., **1981**, *26(1)*, 28

64. I. Bâldea, A. Donea, M. Tomoaia-Cotişel, V. Fărcăşan
Kinetics of the hydrolysis of N-benzoyl-derivatives of 2-phenyl-4(4'-amino-phenyl)thiazole, 4-aminobiphenyl and related compounds
Studia Univ. „Babeş-Bolyai" Chem., **1981**, *26(2)*, 62

65. V. Fărcăşan, F. Paiu, A. Donea, C. Sârbu, G. Coman
Derivatives of furan (XIV). 5-Bromo- and 5-nitro-2-furanilides
Studia Univ. „Babeş-Bolyai" Chem., **1982**, *27(2)*, 22

66. S. Florea, V. Fărcăşan
Benzofurobenztiazoli (VI). 2-Furil-benzofuro[2,3-e]-benztiazolul
Revista de chimie, **1982**, *33*, 429

67. M. Ionescu, V. Fărcăşan
Contribuții ale cercetătorilor din Cluj-Napoca la prepararea acridonelor
Memoriile secțiilor ştiințifice (Acad. RSR), **1981**, *ser. IV, T. IV, nr. 1*, 175

68. V. Fărcăşan, Byambaa Tserejantsiin, V. Chiorean
Derivatives of amines and hydrazines with acridinic nucleus
Studia Univ. „Babeş-Bolyai" Chem., **1983**, *XXVIII*, 67

69. I. Bâldea, V. Fărcăşan, I. Olteanu
Kinetics of the Jacobson reaction
Rev. Roum. Chim., **1985**, *30*, 385

70. V. Fărcăşan, F. Paiu, I. Olteanu, H. Demian
Indeno-benzothiazoles (I). 2-Substituted indeno-benzo-thiazoles
Studia Univ. „Babeş-Bolyai" Chem., **1985**, *XXX*, 5
71. V. Fărcăşan, Byambaa Tserejantsiin
Benzofuroacridines (I). Compounds with benzofuro [3,2-b] acridinic and benzofuro [2,3-a] acridinic skeleton
Studia Univ. „Babeş-Bolyai" Chem., **1985**, *XXX*, 47

72. V. Fărcăşan, I. Olteanu, I. Meşter, V. Chiorean
Some new amines and sulfonamides and their biological activity
Studia Univ. „Babeş-Bolyai" Chem., **1985**, *XXX*, 41

73. M. Diudea, V. Fărcăşan
Condensation products of 3-formyl-10-methyl-phenohiazine with nitrogen compounds
Studia Univ. „Babeş-Bolyai" Chem., **1986**, *XXXI (2)*, 49

74. I. Cristea, V. Fărcăşan
Sinteza unor derivați de 1-(2-primidinil)-5-pirazolone
Revista de chimie, **1987**, *38(8)*, 674

75. I. Olteanu, F. Paiu, V. Fărcăşan
TCL of some derivatives of fluorene
Studia Univ. „Babeş-Bolyai" Chem., **1987**, *XXXII (2)*, 74

76. R. D. Pop, A. Donea, V. Chiorean, V. Fărcăşan
The biological activity of some Schiff's bases of 4-amino-biphenyl and 2-phenyl-4-(p-aminophenyl)-thiazole
Studia Univ. „Babeş-Bolyai" Chem., **1987**, *XXXII (2)*, 85

77. I. Cristea, V. Fărcăşan
The reaction of some 1-(2-pyrimidinul)-pyrazolin-5-ones with hydrazine hydrate
Studia Univ. „Babeş-Bolyai" Chem., **1989**, *XXXIV*, 60

78. I. Bâtiu, I. Cristea, V. Fărcăşan
Some new hydrazones and hydrazido-hydrazones of terpenoids and related compounds
Studia Univ. „Babeş-Bolyai" Chem., **1993**, *XXXVIII*, 125

79. S. Florea, E. Glodeanu, V. Fărcăşan
Studii RMN cu privire la ciclizarea unor N-tioacilamino-dibenzofurani la oxidare cu fericianură de potasiu în mediu bazic
Revista de chimie, **1999**, *50(7)*, 518

80. L. Ferencz, V. Fărcăşan, I. A. Silberg
Synthesis in mixture of some new sulfonamides with acridinic nucleus
Anal. St. ale Univ. „Al. I. Cuza" Iaşi Chim., **2003**, *XI*, 139

81. L. Ferencz, V. Fărcăşan, I. A. Silberg
New sulfonamides with acridinic nucleus
Rev. Roum. Chim., **2003**, *38*, 801

PATENTS

1. Procedeu de obținere a clorhidratului de o-metil izouree
(în colaborare cu I. Cristea, S. Mager, F. Paiu, I. Hopârtean, I. Panea)
Brevet de invenție nr. 75975 / 22.11.1980

2. Procedeu de obținere a 5-butil-6-metil-2-metoxi-4-pirimidinolului
(în colaborare cu S. Mager, I. Cristea, I. Hopârtean, I. Panea, F. Paiu)
Brevet de invenție nr. 76712 / 1981

3. Procedeu de obținere a 2-metoxi- şi 2-metiltio-5-butil-6-metil-4-pirimidinolului
(în colaborare cu S. Mager, I. Cristea, I. Hopârtean, F. Paiu, I. Panea, V. Popa)
Brevet de invenție nr. 77114 / 31.03.1981

4. Coloranți polimetinici şi procedeu pentru prepararea acestora
(în colaborare cu, I. Cristea, I. Panea)
Brevet de invenție nr. 77770 / 17.06.1981

5. Procedeu de obținere a 5-butil-2-etilamino-6-metil-4-pirimidinolului
(în colaborare S. Mager, F. Paiu, I. Hopârtean, I. Cristea)
Brevet de invenție nr. 79028 / 17.12.1981
6. Derivați de 1-(2-pirimidinil)-5-pirazolone şi procedeu de preparare a acestora
(în colaborare cu I. Cristea, I. Panea)
Brevet de invenție nr. 84355/ 31.01.1984

7. Procedeu de obținere a tioglicolatului de amoniu
(în colaborare cu M. V. Diudea, A. S. Todor, D. Breazu, S. Mager,)
Brevet de invenție nr. 88237/ 25.05.1985

8. Procedeu pentru obținerea 1-(4-hidroxi-6-metil-2-pirimidinil)-3-metil-5-pirazolonei
(în colaborare cu I. Cristea, I. Panea)
Brevet de invenție nr. 89139/ 30.10.1985

STUDIA UNIVERSITATIS BABEŞ-BOLYAI, CHEMIA, XLIX, 2, 2004

Dedicated to Professor Valer Fărcăşan at his 85th anniversary

MODELING AND SIMULATION OF PANTOLACTONE SYNTHESIS

CĂLIN CORMOS, ŞERBAN AGACHI

"Babeş-Bolyai" University, Faculty of Chemistry and Chemical Engineering, Arany Janos 11, 400028 Cluj-Napoca, Romania, cormos@chem.ubbcluj.ro, sagachi@chem.ubbcluj.ro

ABSTRACT. In this paper the mathematical model and the simulation for the discontinuous synthesis of racemic pantolactone (an intermediary product in the synthesis of calcium pantothenate) have been described. The chemical steps of the synthesis take place in two continuous stirred tank reactors, operated batchwise. The synthesis process consists of four reactions, which were studied. The first two reactions are highly exothermic. For a good quality of the product, the reactor temperature must be maintained between 12 – 14^{o}C. A control of reactor solution temperature was studied using PID controllers. The α,γ-dihydroxy-β,β-dimethyl-butyronitrile, obtained in the first two steps of the synthesis, is then hydrolyzed in acidic conditions in order to obtain racemic pantolactone. The mathematical model of the synthesis process was simulated using ChemCAD 5.0 software package. From the simulation results very valuable information can be obtained regarding real plant operation.

1. INTRODUCTION

Calcium pantothenate is one of the most used pro-vitamins in the therapy for the human beings and for the veterinary use. Pantothenic acid is a vitamin from the complex of vitamins B, it plays an important role in the metabolism [1, 8] (its biological active form is Coenzyme A). The chemical formula of calcium pantothenate is presented below:

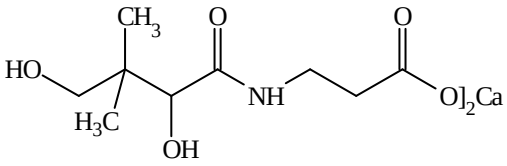

The synthesis of racemic calcium pantothenate is a complex process including chemical steps and physical separations of the intermediaries and the final product. The synthesis involves three major steps, the first step is the manufacture of pantolactone (α-hydroxy-β,β-dimethyl-γ-butyrolactone), the second step consists of the manufacture of sodium β-alaninate and in the final step of the synthesis these intermediaries are coupled resulting the final product [2].

Because the technology is very complex including a large category of operations, the mathematical models have been developed for the different steps of the synthesis. These mathematical models have been used to simulate

the process, in which purpose ChemCAD software package has been employed. The goals of modeling and simulation of these processes were to find the best operating points for the equipment, to try different control algorithms, to improve the energy consumption of the plant [5, 6, 7, 8].

In this paper the mathematical model for the discontinuous synthesis of racemic pantolactone has been described.

The chemical reactions for pantolactone synthesis are presented below [2]:

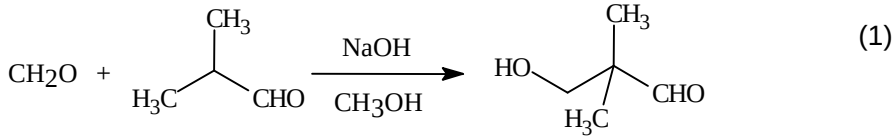

(1)

Formic aldehyde — Isobutyric aldehyde — α,α-Dimetil-β-hydroxy-propionic aldehyde

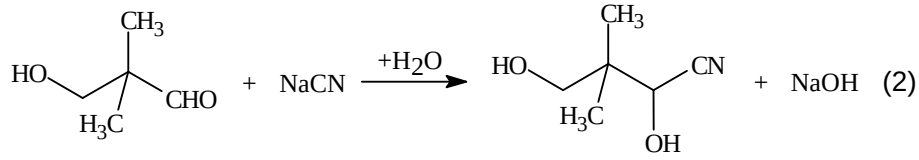

(2)

α,α-Dimetil-β-hydroxy-propionic aldehyde — Sodium cyanide — α,γ-Dihydroxy-β,β-dimethyl-butyronitrile — Sodium hydroxide

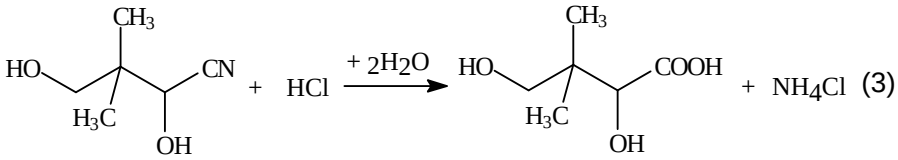

(3)

α,γ-Dihydroxy-β,β-dimethyl-butyronitrile — Hydrochloric acid — α,γ-Dihydroxy-β,β-dimethyl-butyric acid — Ammonium chloride

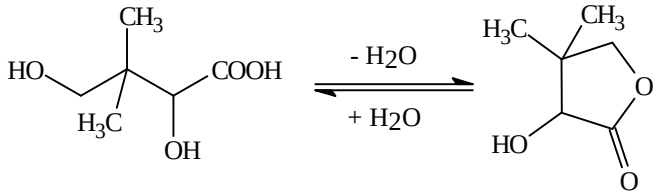

(4)

α,γ-Dihydroxy-β,β-dimethyl-butyric acid — Racemic pantolactone

The process takes place in two CSTR (continuous stirred tank reactors), operated batchwise. First step of the synthesis consists in the preparation of a mixture containing formaldehyde and isobutyraldehyde using methanol as a

solvent. For a good control of the temperature, the reactor is equipped with an external jacket and an internal coil. As cooling agent a mixture of methanol and ethylene glycol, with a low temperature (-12^{o}C), is used. After the reactor mass temperature decreases below 12^{o}C a sodium hydroxide solution is added in the reactor. The sodium hydroxide catalyzes the first reaction between formaldehyde and isobutyraldehyde. The reaction 1 is highly exothermic (ΔH_1= - 36.45 kJ/mole). The reactor temperature must be maintained at less than 14^{o}C, for which purpose, PID controllers are used. The control of reactor temperature is achieved using the sodium hydroxide flow added into the reactor and the cooling agent flows (from the jacket and the coil of the reactor). The first reaction product is α,α-dimethyl-β-hydroxy-propionic aldehyde (oxymethyle).

After the reactor solution temperature goes below 12^{o}C, a sodium cyanide solution is added in the reactor. The reaction between α,α-dimethyl-β-hydroxy-propionic aldehyde and sodium cyanide is highly exothermic (ΔH_2= - 84.4 kJ/mole). The control of the reactor solution temperature (12 – 14^{o}C) is achieved using PID controllers, controlling sodium cyanide solution flow and cooling agent flows (from the jacket and the coil) as manipulated variables. The second reaction product is α,γ-dihydroxy-β,β-dimethyl-butyronitrile (nitrile).

The α,γ-dihydroxy-β,β-dimethyl-butyronitrile solution is then transferred in a different continuous stirred tank reactor (operated batchwise) and hydrolyzed in acidic condition in order to obtain an aqueous racemic pantolactone solution.

2. MODELING AND SIMULATION OF THE SYNTHESIS

The discontinuous synthesis of racemic pantolactone was modeled and simulated using ChemCAD 5.0 software package.

The parameters of the mathematical model for pantolactone synthesis are presented in tables 1, 2, 3 and 4 [8].

Table 1.

Synthesis reactors parameters

Characteristics	Reactor 1	Reactor 2
Reactor volume	4 m^3	6 m^3
Jacket volume	0.6 m^3	0.6 m^3
Coil volume	0.1 m^3	-
Heat transfer area (jacket)	12 m^2	15 m^2
Heat transfer area (coil)	1.5 m^2	-
Reactor diameter	1.4 m	1.8 m
Impeller diameter	0.6 m	0.8 m
Impeller speed	120 rpm	120 rpm
Motor power	6 kW	11 kW

Table 2.

Heat transfer coefficients [3]

Heat transfer coefficients	Reactor 1	Reactor 2
Cooling agent (jacket)	831 W/m^{2}K	800 W/m^{2}K
Cooling agent (coil)	1932 W/m^{2}K	-
Heating agent (jacket)	-	6148.8 W/m^{2}K

Table 3.

Kinetic and thermodynamic parameters [4, 5]

Parameters	Reaction 1	Reaction 2	Reaction 3	Reaction 4
Heat of reaction	-36.45 kJ/mole	-84.4 kJ/mole	-190.8 kJ/mole	+23 kJ/mole
Kinetic data	$k_1 C_{NaOH} C_{Isobutyraldehyde}$	$k_2 C_{NaCN} C_{Oxymethyle}$	$k_3 C_{Nitrile} C_{HCl}$	$k_4 C_{Pantoic\ acid}$
Frequency factor	10^{11} m^3/kmole · s	$2 \cdot 10^{11}$ m^3/kmole · s	10^9 m^3/kmole · s	10^{10} m^3/kmole · s
Activation energy	73.2 kJ/mole	75 kJ/mole	83.7 kJ/mole	75.3 kJ/mole

Table 4.

Control systems parameters

Parameters	Proportional band	Integral time	Derivative time
PID 1 (NaOH solution)	150	5 min.	10 min.
PID 2 (jacket cooling agent)	200	2 min.	10 min.
PID 3 (coil cooling agent)	200	2 min.	10 min.
PID 4 (NaCN solution)	150	2 min.	1 min.

The synthesis processes were modeled and simulated with ChemCAD 5.0 software package.

The main window of the application for α,α-dimethyl-β-hydroxy-propionic aldehyde (oxymethyle) synthesis is presented in the figure 1.

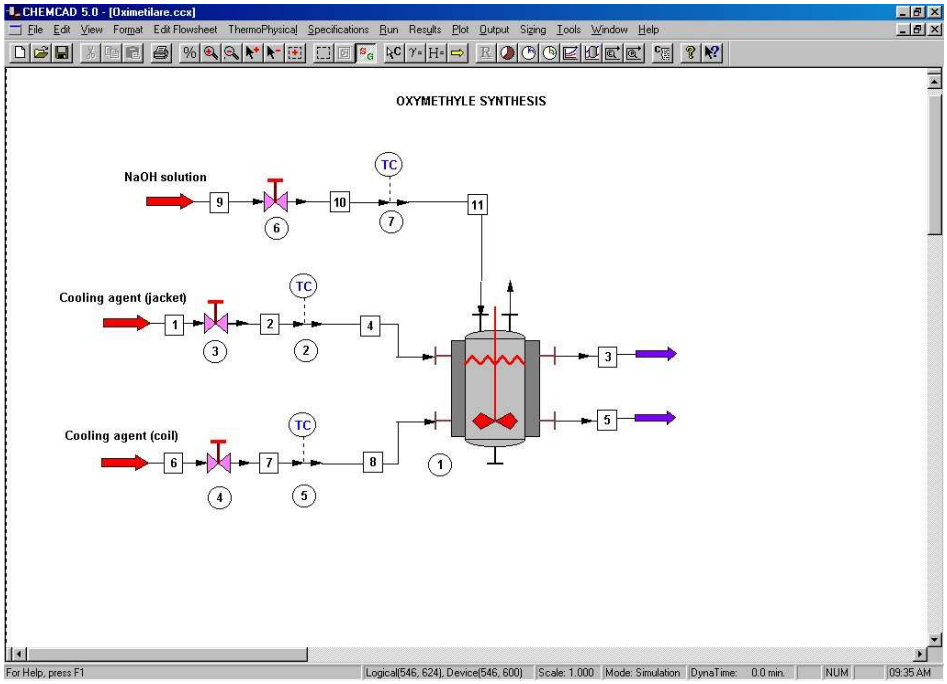

Figure 1. Simulation of α,α-dimethyl-β-hydroxy-propionic aldehyde synthesis

The main window of the application for α,γ-dihydroxy-β,β-dimethyl-butyronitrile (nitrile) synthesis is presented in the figure 2.

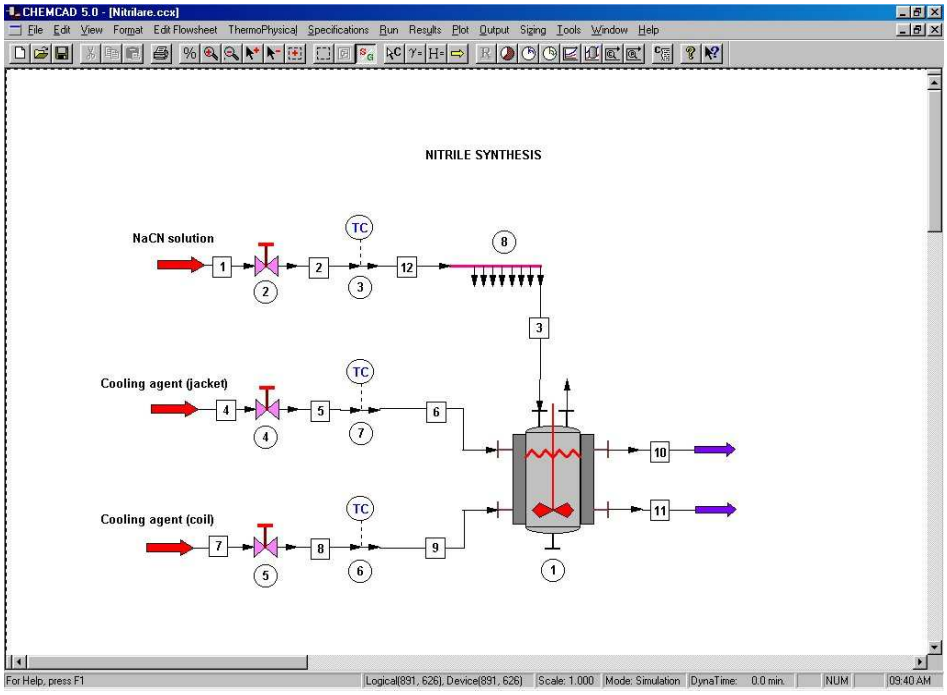

Figure 2. Simulation of α,γ-dihydroxy-β,β-dimethyl-butyronitrile synthesis

For both above applications, four PID control systems of reactor solution temperature were simulated. First temperature control system uses sodium hydroxide flow as manipulated variable. The second and third temperature control systems use jacket and coil cooling agent flows as manipulated variable. The fourth temperature control system uses sodium cyanide flow as manipulated variable.

The main window of the application for pantolactone synthesis (α,γ-dihydroxy-β,β-dimethyl-butyronitrile hydrolysis) is presented in the figure 3.

3. RESULTS AND DISCUSSIONS

The mathematical model of racemic pantolactone synthesis process was simulated using ChemCAD 5.0 software package.

The variation of the chemical species concentrations during the α,α-dimethyl-β-hydroxy-propionic aldehyde synthesis are presented in figure 4.

The variation of the temperatures (reactor mass, jacket cooling agent and coil cooling agent) during the α,α-dimethyl-β-hydroxy-propionic aldehyde (oxymethyle) synthesis are presented in figure 5.

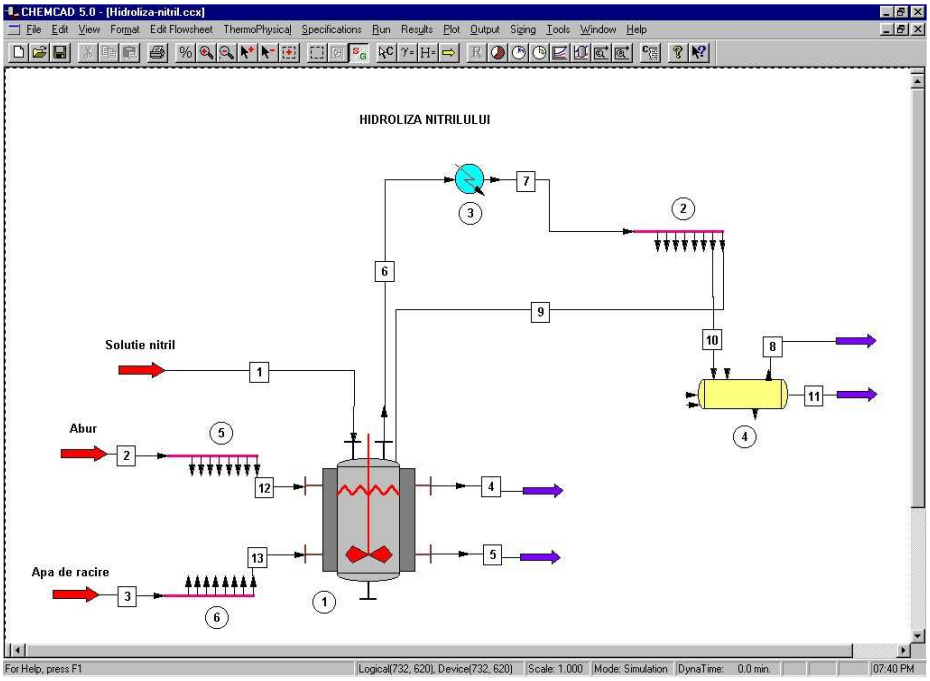

Figure 3. Simulation of racemic pantolactone synthesis

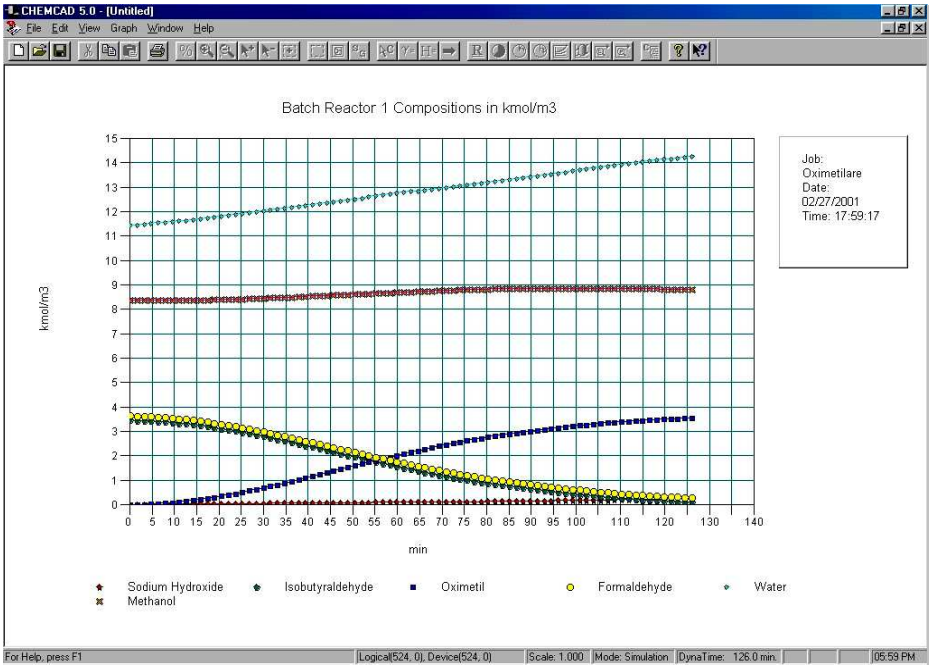

Figure 4. Variation of chemical species concentrations during the oxymethyle synthesis

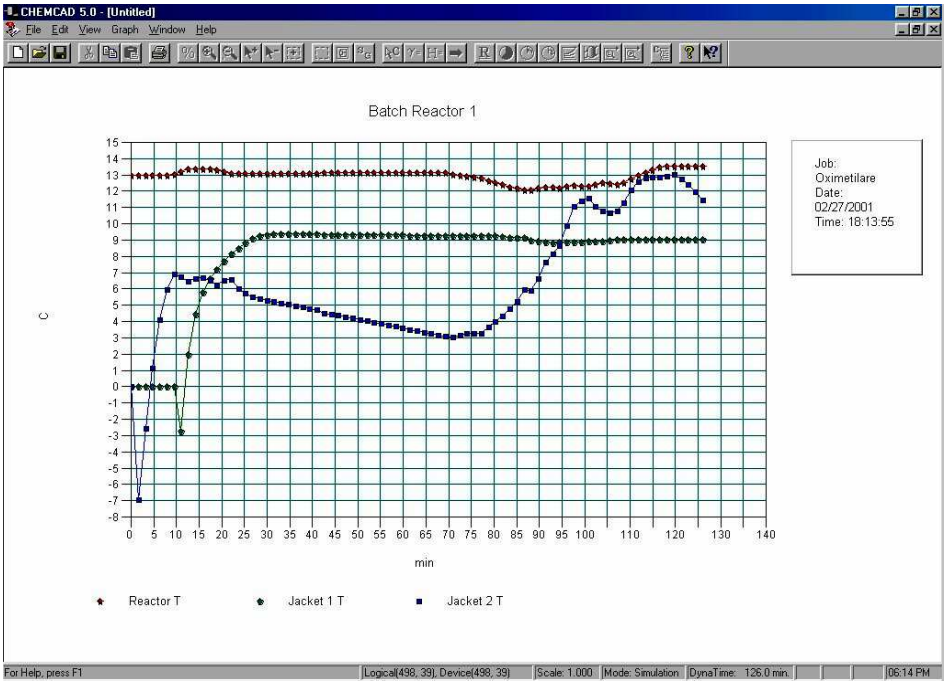

Figure 5. Variation of temperatures during the oxymethyle synthesis

The reactor mass temperature must be maintained between 12 and 14^{o}C (set point temperature 13^{o}C). If the reactor temperature exceeds 14^{o}C secondary reactions take place [2, 7]. During the α,α-dimethyl-β-hydroxy-propionic aldehyde synthesis the reactor temperature is good controlled between 12 and 14^{o}C.

The variation of the chemical species concentrations during the α,γ-dihydroxy-β,β-dimethyl-butyronitrile (nitrile) synthesis are presented in figure 6.

The variation of the temperatures (reactor mass, jacket cooling agent and coil cooling agent) during the α,γ-dihydroxy-β,β-dimethyl-butyronitrile synthesis are presented in figure 7.

From the figure 7 one can observe that the reactor solution temperature during α,γ-dihydroxy-β,β-dimethyl-butyronitrile synthesis is good controlled between 12 and 14^{o}C (set point temperature 13^{o}C).

The variation of the chemical species quantities from reactor the solution during racemic pantolactone synthesis (α,γ-dihydroxy-β,β-dimethyl-butyronitrile hydrolysis process) are presented in figures 8 and 9.

The real plant has only two PID control systems for the reactor temperature using sodium hydroxide and sodium cyanide flows as manipulated variables [2].

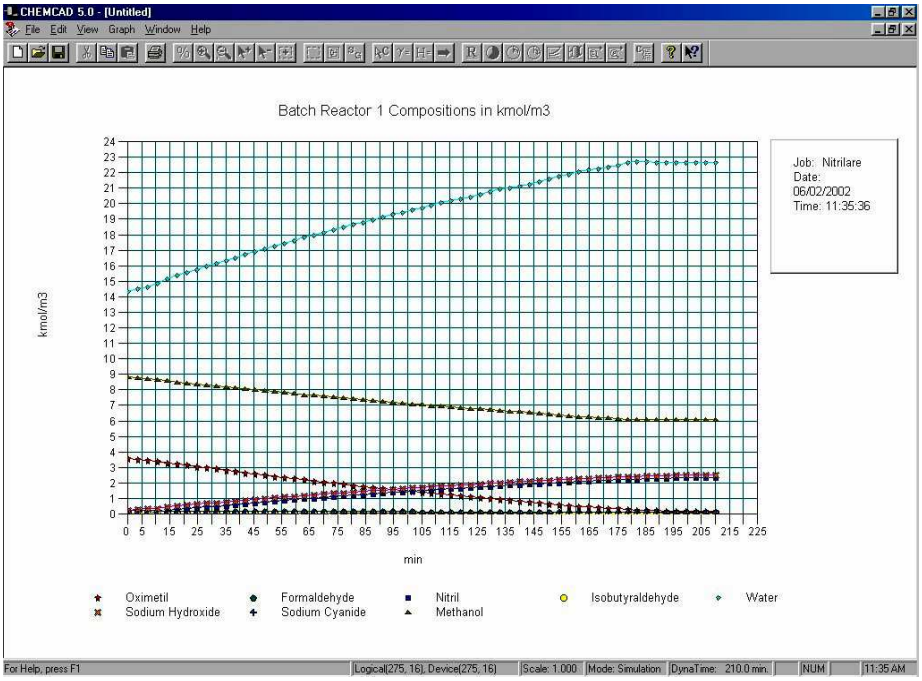

Figure 6. Variation of chemical species concentrations during the nitrile synthesis

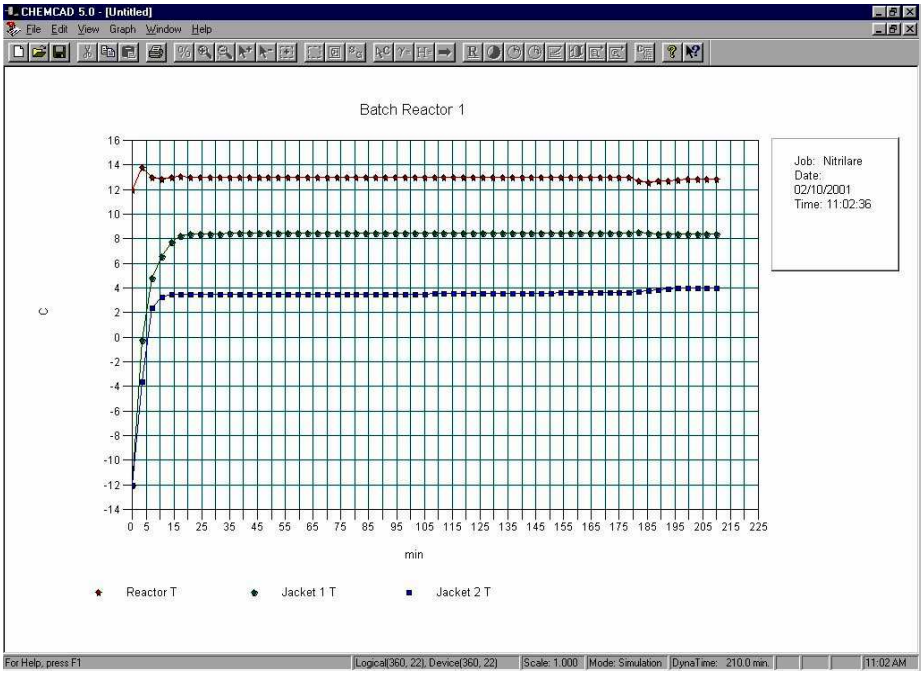

Figure 7. Variation of temperatures during the nitrile synthesis

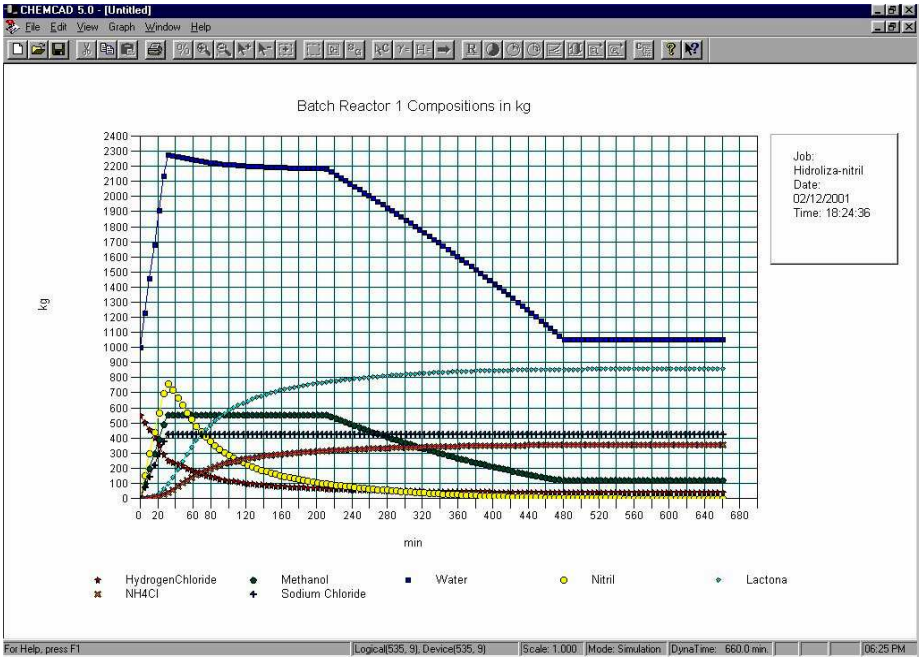

Figure 8. Variation of chemical species quantities from the synthesis reactor (1)

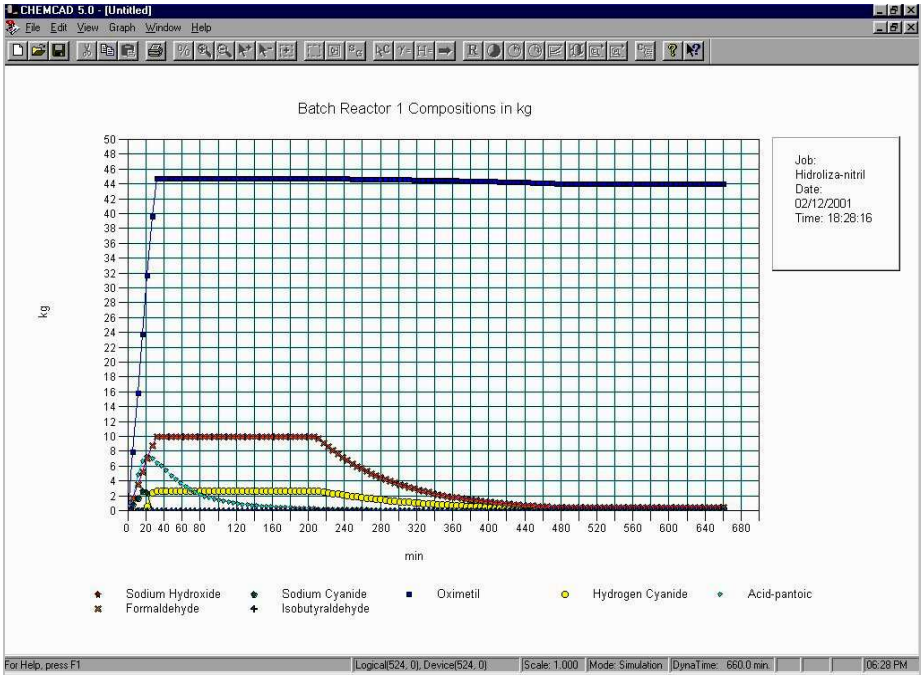

Figure 9. Variation of chemical species quantities from the synthesis reactor (2)

Comparing the simulation results obtained with two temperature control systems and the simulation results obtained using the others two control systems for reactor temperature (using the cooling agent flows), one can observe that the introduction of the supplementary temperature control systems leads to cooling agent economy (10 – 15 %). The annual cooling agent economy is $2,500.

In addition, the introduction of supplementary temperature control systems leads to a better reactor temperature control in comparison with the present situation used in practice, with benefic consequences on the quality of the product.

4. CONCLUSIONS

In this paper the discontinuous synthesis of racemic pantolactone was presented. The mathematical model of the synthesis process was simulated using ChemCAD 5.0 software package. The variations of different parameters (concentration of chemical species, reactor solution temperature, cooling and heating agent temperature) during the synthesis were presented.

The model proved to be a reliable tool for analyzing pantolactone synthesis process. Using the model of the synthesis process and the simulation results (for different operational conditions) very valuable information can be obtained for the real plant operation (temperature control improvement, reduction of cooling agent consumption, investigation of different control strategies etc.).

REFERENCES

1. G. Neamțu, *Substanțe naturale biologic active*, Editura Ceres, Bucureşti, 1996, vol. 1, pag. 329-346
2. ***, *Regulament de fabricație „Pantotenat de calciu”*, S.C. Terapia S.A., Cluj-Napoca, 2001
3. C. F. Pavlov, P. G. Romankov, A. A. Noskov, *Procese şi aparate în industria chimică*, Editura Tehnică, Bucureşti, 1981, pag. 155-178
4. A. A. Frost, R. G. Pearson, *Kinetic and Mechanism - A Study of Homogenous Chemical Reactions*, Wiley International, Second Edition, 1961, pag. 335-351
5. C. Cormoş, Ş. Agachi, *Modeling and simulation the process of synthesis of D,L calcium pantothenate*, Conferință Internațională de Control, Automatică şi Robotică Q&A-R 2000, Cluj-Napoca, 2000, vol. 2, pag. 7-12
6. C. Cormoş, Ş. Agachi, *Modeling and simulation the synthesis process of sodium pantothenate*, Simpozion Internațional de Inginerie Chimică - SICHEM 2000, Bucureşti, România, 2000, pag. 305-312
7. C. Cormoş, Ş. Agachi, *Modeling and simulation of pantolactone synthesis using ChemCAD*, 30-th International Conference of Slovak Society of Chemical Engineering, Tatranske Matliare, Slovakia, 2003
8. C. Cormoş, *Modelarea matematică şi simularea sintezei pantotenatului de calciu racemic*, Teză de doctorat, Cluj-Napoca, 2004, pag. 119-150

STUDIA UNIVERSITATIS BABES-BOLYAI, CHEMIA, XLIX, 2, 2004

Dedicated to Professor Valer Fărcăşan at his 85th anniversary

MODELING AND SIMULATION OF RESIDUAL PANTOLACTONE EXTRACTION FROM CALCIUM PANTOTHENATE SOLUTION

CĂLIN CORMOS, ŞERBAN AGACHI

"Babes-Bolyai" University, Faculty of Chemistry and Chemical Engineering, Arany Janos 11, 400028 Cluj-Napoca, Romania, cormos@chem.ubbcluj.ro, sagachi@chem.ubbcluj.ro

ABSTRACT. In this paper the mathematical model and the simulation for the extraction process of residual pantolactone from racemic calcium pantothenate solution have been described. The aqueous solution of calcium pantothenate resulted from synthesis process contains residual racemic pantolactone that is extracted using dichloromethane. The pantolactone extraction process can be done in two technological ways. The first possibility is to use an extraction system consisting of a reactor and a packed extraction column, operated batchwise. The second possibility is to use a continuous counter-current centrifugal extractor. In this second way, economy of time, extraction solvent and energy savings are achieved. The mathematical models of the extraction process were simulated using ChemCAD 5.0 software package. From the simulation results very valuable information can be obtained regarding real plant operation.

1. INTRODUCTION

Calcium pantothenate is one of the most used pro-vitamins in the therapy for the human beings and for the veterinary use. Pantothenic acid is a vitamin from the complex of vitamins B, it plays an important role in the metabolism [1, 6] (its biological active form is Coenzyme A). The chemical formula of calcium pantothenate is presented below:

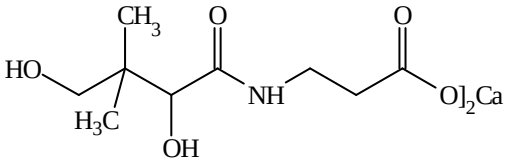

The synthesis of racemic calcium pantothenate is a complex process including chemical steps and physical separations of the intermediaries and the final product. The synthesis involves three major steps, the first step is the manufacture of pantolactone (α-hydroxy-β,β-dimethyl-γ-butyrolactone), the second step consists of the manufacture of sodium β-alaninate and in the final step of the synthesis these intermediaries are coupled resulting the final product [2].

Because the technology is very complex including a large category of operations, the mathematical models have been developed for the different steps of the synthesis. These mathematical models have been used to simulate the process, in which purpose ChemCAD software package has been employed.

The goals of modeling and simulation of these processes were to find the best operating points for the equipment, to try different control algorithms, to improve the energy consumption of the plant [4, 5, 6].

In this paper the mathematical model for the extraction process of residual pantolactone from racemic calcium pantothenate solution using dichloromethane has been described. The extraction of residual pantolactone from racemic calcium pantothenate solution is done in order to purify the finite product [2].

The pantolactone extraction process from the calcium pantothenate aqueous solution is achieved using dichloromethane as extraction solvent [3].

Practically, pantolactone extraction process can be performed using two technological ways. The first possibility is to use an extraction system consisting of a reactor and a packed extraction column, operated batchwise. This technological way for pantolactone extraction is used in the real plant [2]. Dichloromethane is loaded in the reactor and racemic calcium pantothenate aqueous solution is loaded in the extraction column. Dichloromethane from the reactor is vaporized and, after condensation and cooling in two heat exchangers, enters in the extraction column. Pantolactone from the aqueous solution is extracted by dichloromethane and, because of the density difference, the organic phase (pantolactone in dichloromethane) leaves the extraction column and returns in the reactor.

The second possibility is to use a continuous counter-current centrifugal extractor. In this second way, economy of time, extraction solvent and energy savings (it is not necessary to make the vaporization – condensation cycle for pantolactone extraction) are achieved.

2. MODELING AND SIMULATION OF THE EXTRACTION

The extraction process of residual pantolactone from calcium pantothenate solution was modeled and simulated using ChemCAD 5.0 software package.

The parameters of the mathematical models for racemic pantolactone extraction are presented in tables 1, 2 and 3 [2, 6].

Table 1.

Extraction reactor characteristics

Reactor volume	4 m^3
Jacket volume	0.4 m^3
Heat transfer area	10 m^2
Reactor diameter	1.6 m
Impeller diameter	1 m
Impeller speed	180 rpm
Motor power	5 kW

Table 2.

Packed column characteristics

Column volume	6 m^3
Number of stages	6
Packing characteristics	Raschig ring D x H x d = 25 x 30 x 15 mm

Table 3.

Centrifugal extractor characteristics

Number of stages	6
Phases circulation mode	Counter-current

Pantolactone extraction coefficient in dichloromethane – water system [3]:

$$K = \frac{X_{Pantolactone\ in\ dichloromethane\ phase}}{X_{Pantolactone\ in\ water\ phase}} = 2$$

The two technological ways for residual pantolactone extraction process were modeled and simulated with ChemCAD 5.0 software package.

Figure 1 presents the main window of pantolactone extraction application developed using ChemCAD 5.0 software packages for the mathematical modeling and the simulation of extraction process using a continuous counter-current centrifugal extractor.

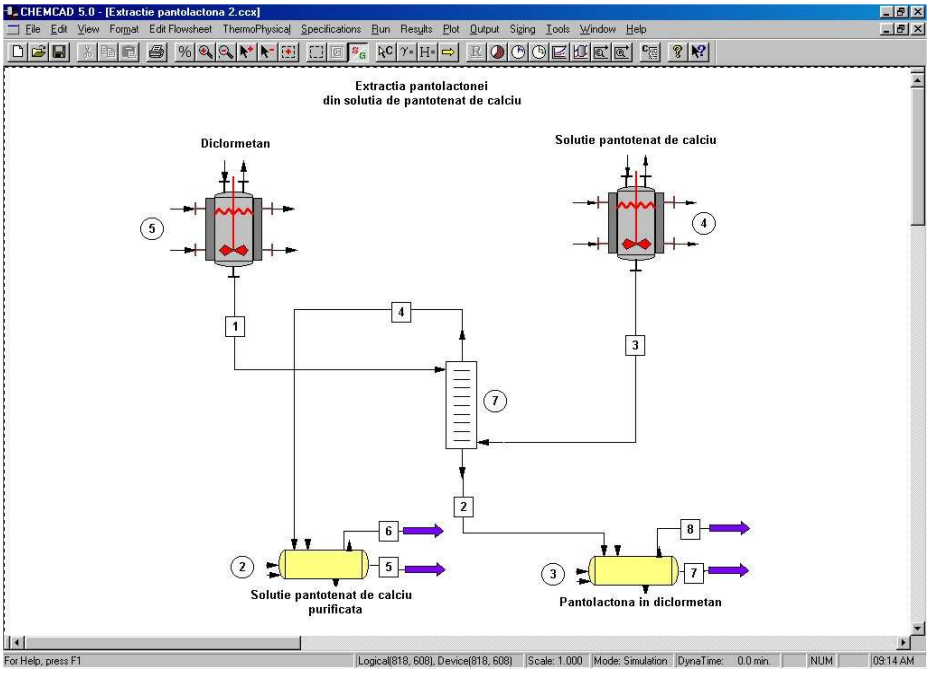

Figure 1. Simulation of pantolactone extraction using a centrifugal extractor

Figure 2 shows the main window for pantolactone extraction application (developed in ChemCAD 5.0) using a reactor and a packed column.

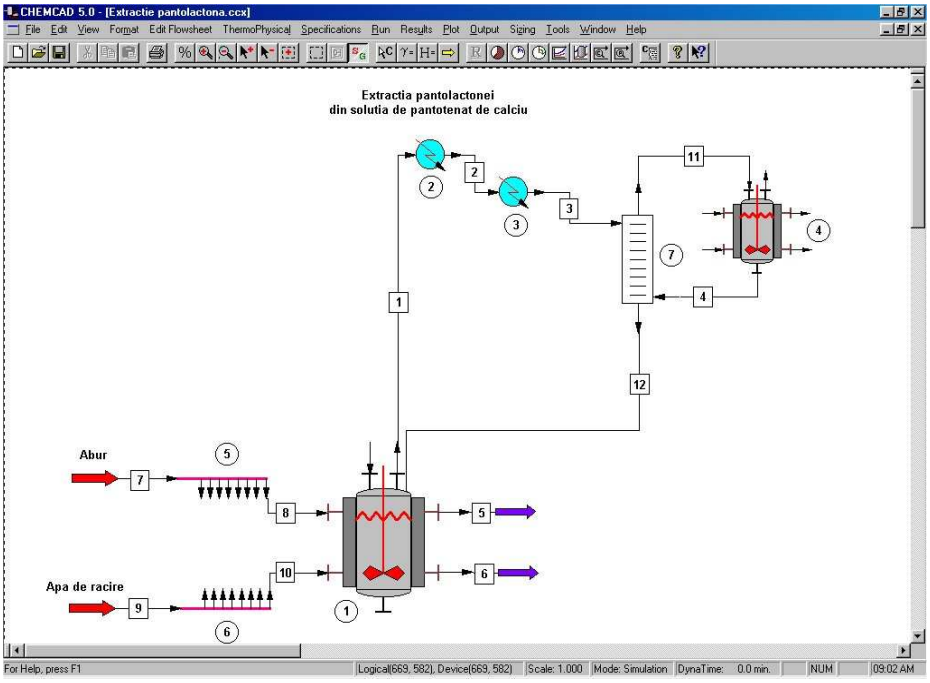

Figure 2. Simulation of pantolactone extraction using a packed column

3. RESULTS AND DISCUSSIONS

The mathematical model of residual pantolactone extraction process from calcium pantothenate solution was simulated using ChemCAD software package.

For extraction process using a counter-current centrifugal extractor, the variation of components quantities for the aqueous phase (calcium pantothenate solution) leaving the centrifugal extractor are presented in figure 3.

The variation of composition (mass fractions) for the aqueous phase (racemic calcium pantothenate solution) that leaves the centrifugal extractor is presented in figure 4.

The variation of the composition (mass fractions) for the organic phase (pantolactone in dichloromethane) that leaves the centrifugal extractor is presented in figure 5.

For the extraction process using a reactor and a packed column, the variation of chemical species composition (mass fractions) for the solution collected in reactor during the extraction process are presented in figure 6.

The variation of the composition (mass fractions) for the aqueous solution from the extraction column during the process is presented in figure 7.

The variation of the composition (mass fractions) for the flow that leaves the extraction column and goes to reactor is presented in figure 8.

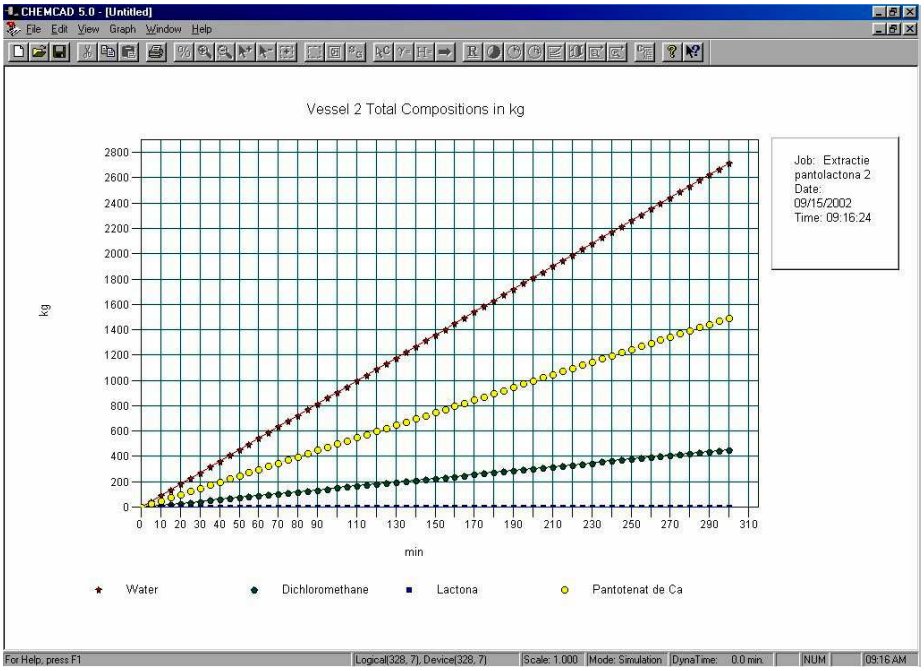

Figure 3. Variation of chemical species quantities for the aqueous phase

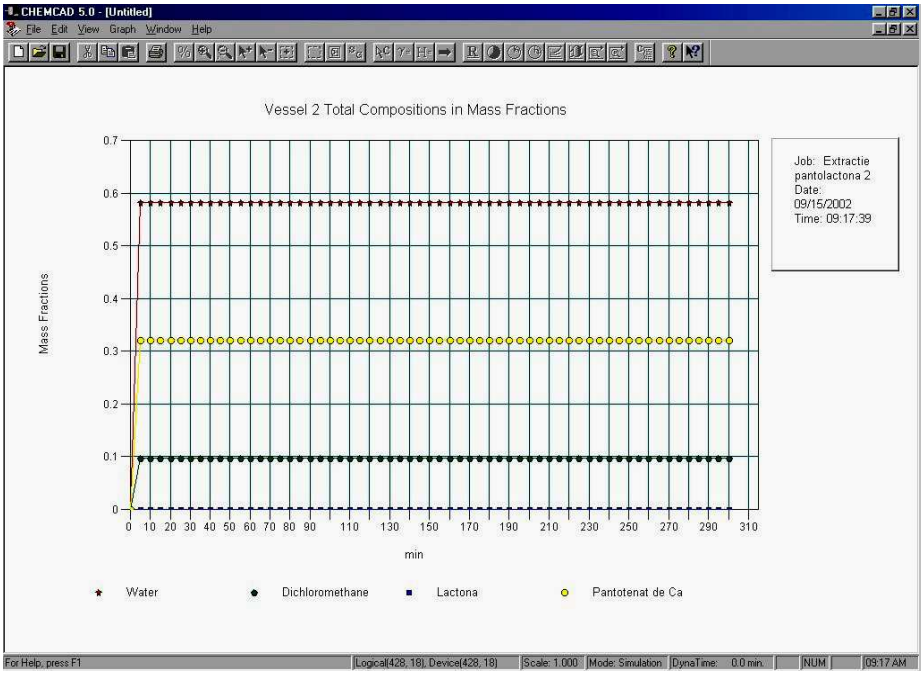

Figure 4. Variation of composition for the aqueous phase (mass fractions)

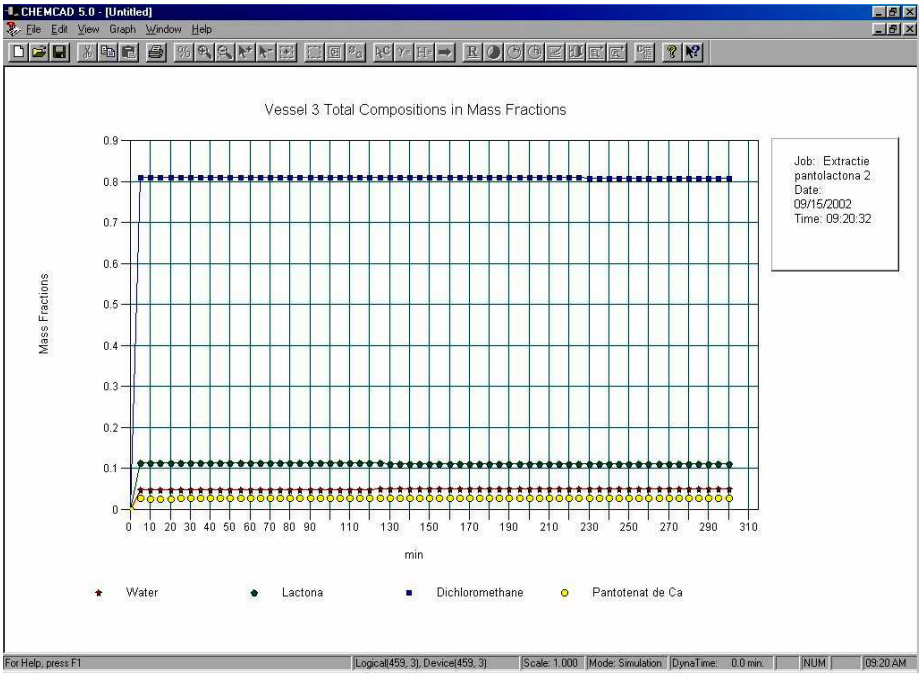

Figure 5. Variation of composition for the organic phase (mass fractions)

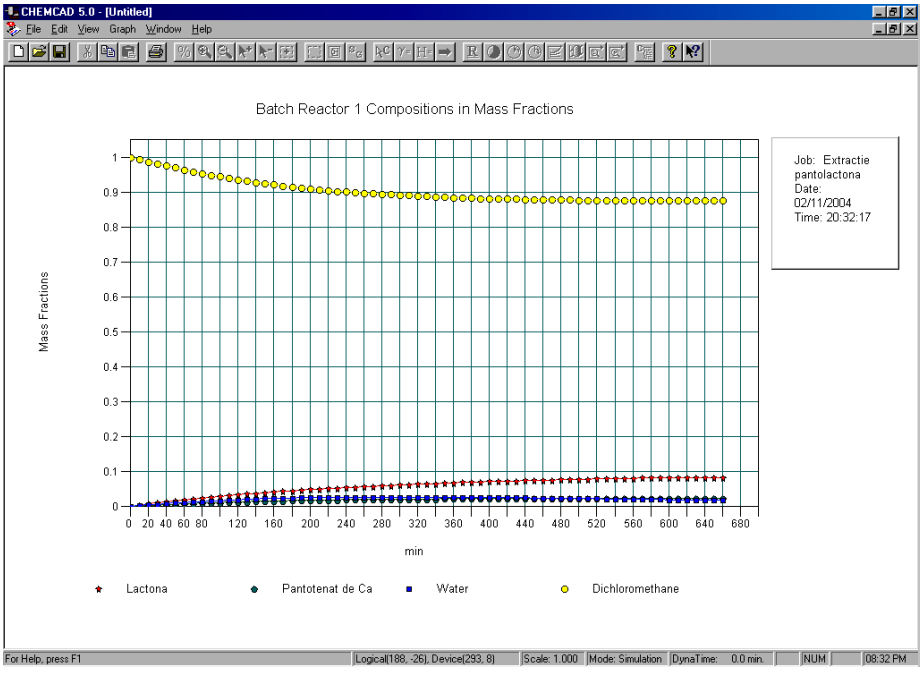

Figure 6. Variation of composition for the organic phase from the reactor

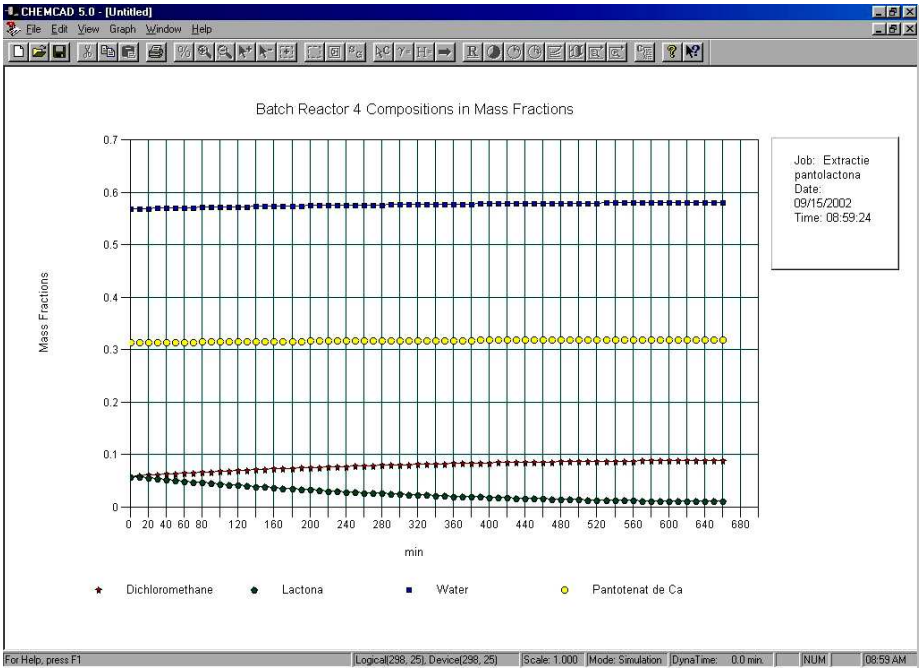

Figure 7. Variation of composition for the aqueous phase from the extraction column

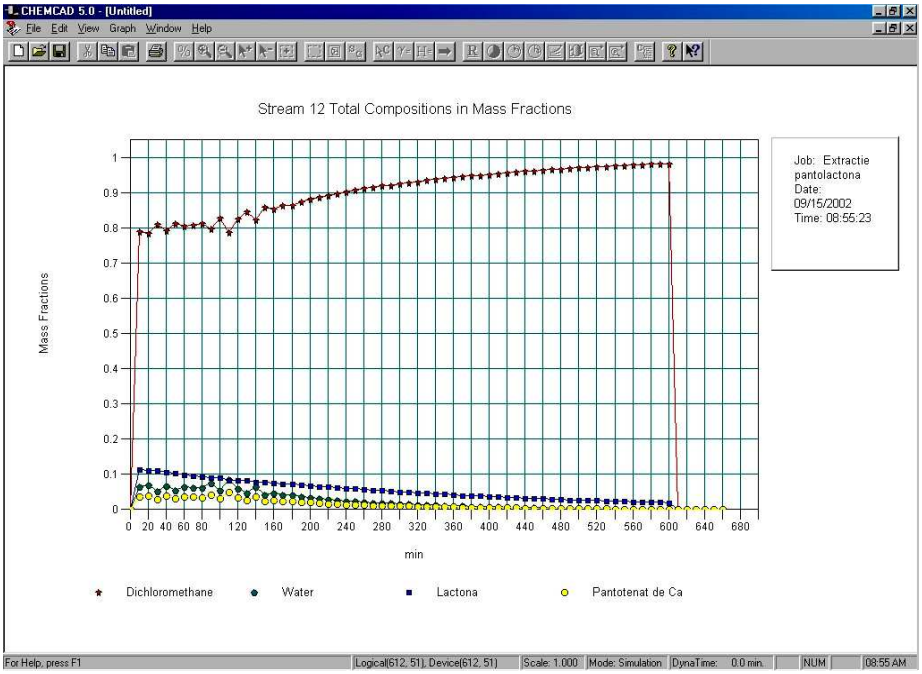

Figure 8. Variation of the composition for the flow that leaves the extraction column

The main difference between the first and the second way of pantolactone extraction is the utility consumption. Utility consumption is greater when we use an extraction system composed of a reactor and a packed column [6].

In the table 4, the utility consumptions and extraction time for one racemic calcium pantothenate batch are presented.

Table 4.

Utility consumption and extraction time for pantolactone extraction process

Comparison criterion	Reactor and packed column	Centrifugal extractor
Utility consumption (for one calcium pantothenate batch)	Steam (R 1): 0.5333 Gcal Cooling water (R 1): 0.0634 Gcal Cooling water (SC 2): 0.3283 Gcal Refrig. agent (SC 3): 0.0157 Gcal Electric power (R 1): 50 kWh	Electric power: 20 kWh
Extraction time	10 h	5 h

Considering the value of technologic utilities for the extraction system with reactor and packed column ($18,700/year) and adding the dichloromethane losses ($18,300/year) results as evident the attractiveness of the extraction system that uses a counter-current centrifugal extractor [2, 6].

When we use a counter-current centrifugal extractor, the annual economy is $37,000 (counting only the utilities consumption and the dichloromethane losses).

In addition to the above-mentioned aspects, operating a counter-current centrifugal extractor is much easier and the environmental impact is lower than using an extraction system with reactor and packed column operated batchwise [6].

4. CONCLUSIONS

In this paper the extraction process of residual pantolactone from racemic calcium pantothenate solution was presented. Two technological ways for residual pantolactone extraction were considered for analysis. The first possibility is to use an extraction system consisting of a reactor and a packed extraction column, operated batchwise. The second possibility is to use a continuous counter-current centrifugal extractor.

The mathematical models of the pantolactone extraction process were simulated using ChemCAD 5.0 software package. The variations of different parameters during the extraction process were presented.

The mathematical models proved to be a reliable tool for analyzing pantolactone extraction process. Using the mathematical models of the extraction process and the simulation results, the two technological ways of residual pantolactone extraction process were analyzed.

It was demonstrated, by simulation results, that using a centrifugal extractor the annual economy is $37,000 (counting only the utilities consumption and dichloromethane losses). Also, operating a centrifugal extractor is much easier and the environmental impact is lower compared to the situation of using an extraction system with reactor and packed column.

In conclusion, using a counter-current centrifugal extractor, economy of time, extraction solvent and energy savings (it is not necessary to make the vaporization – condensation cycle for pantolactone extraction) are achieved.

REFERENCES

1. G. Neamțu, *Substanțe naturale biologic active*, Editura Ceres, Bucureşti, 1996, vol. 1, pag. 329-346
2. ***, *Regulament de fabricație „Pantotenat de calciu”*, S.C. Terapia S.A., Cluj-Napoca, 2001
3. Paust J., Schmidt W.*, Extraction of pantolactone from its aqueous solution*, BASF AG, US patent 4359582, 1982
4. C. Cormoş, S. Agachi, *Modeling and simulation the process of synthesis of D,L calcium pantothenate*, Conferință Internațională de Control, Automatică şi Robotică Q&A-R 2000, Cluj-Napoca, 2000, vol. 2, pag. 7-12
5. C. Cormoş, Ş. Agachi, *Modeling and simulation of pantolactone synthesis using ChemCAD*, 30-th International Conference of Slovak Society of Chemical Engineering, Tatranske Matliare, Slovakia, 2003
6. C. Cormoş, *Modelarea matematică şi simularea sintezei pantotenatului de calciu racemic*, Teză de doctorat, Cluj-Napoca, 2004, pag. 151-170; 234-245

STUDIA UNIVERSITATIS BABEŞ-BOLYAI, CHEMIA, XLIX, 2, 2004

Dedicated to Professor Valer Fărcăşan at his 85th anniversary

MODELING AND SIMULATION OF CALCIUM CARBONATE THERMAL DECOMPOSITION IN THE VERTICAL LIME KILN BASED ON THE SHRINKING UNREACTED CORE MODEL

CRISTEA VASILE-MIRCEA[*], CORMOŞ ANA-MARIA[*], TRIF DAMIAN[**]

[*] *"Babeş-Bolyai" University, Faculty of Chemistry and Chemical Engineering, 11 Arany Janos, 400028 Cluj-Napoca, e-mail: mcristea@chem.ubbcluj.ro*
[**] *"Babeş-Bolyai" University, Faculty of Mathematics and Computer Science, 1 M. Kogălniceanu, 400084 Cluj-Napoca*

ABSTRACT. The paper presents the dynamic simulation results obtained by modelling the vertical lime kiln for thermal decomposition of limestone. The simulator relies on the rate controlling heat balance equations describing the advance of the reaction front in the spherical limestone boulder, according to the shrinking unreacted core model. The vertical lime kiln is considered to be divided in three distinct zones along the moving flux of the solids: heating, reaction and cooling zone. Each of the zones are described by the limestone boulder travelling down along the kiln height. Results reveal the time and space distribution of temperature in the lime kiln for both solids and gases, based on the time and space distribution of the temperature in the limestone boulder and the gases surrounding it. The dynamic simulator serves as a useful tool for investigating the way that lime kiln may be operated and controlled for improved performance.

1. INTRODUCTION

Thermal decomposition of limestone has been of large interest over the past, as both calcium oxide and carbon dioxide are basic raw materials for a large range of products in chemical or construction material industries. Despite the important advances performed in process equipment design, the vertical lime kiln remains one of the main units for performing the industrial scale calcium carbonate decomposition.

Developments of information technology and computer sciences, during the last decades, make possible the study and investigation of the limestone decomposition by simulation. The continuous growing complexity of the dynamic models is supported by specific software tools allowing a thorough analysis of the process with direct effects on the improvement of the product yields.

Results of the presented dynamic simulator emerge from a different approach for solving the mathematical model of the lime kiln simulator presented in earlier studies [1], [2].

The vertical lime kiln under study is presented in figure 1. It is considered to have three distinct zones along the direction of transport of the solids moving in counter-current with the gaseous flux.

The heating zone is the place where the solid phase temperature is increased up to the decomposition conditions (temperature around 900 ^{o}C) by the help of the gases coming from the reaction zone. In the reaction zone hot gases emerged from the fuel combustion provide the necessary heat for the endothermic decomposition process (temperature exceeding 900 ^{o}C) and for the previous limestone preheating step. The third zone is the cooling one where solids temperature is reduced and the inlet combustion air flux is preheated from the ambient temperature. The products of the vertical kiln are the lime flux evacuated at the bottom of the kiln and the gaseous flux exhausted at the top of it, having rich 35-40 vol. %, carbon dioxide concentration.

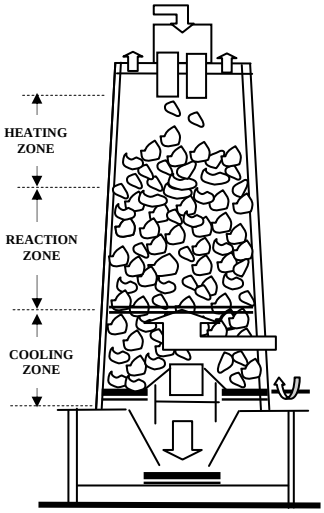

Figure 1. Vertical kiln scheme.

Due to the large dimensions, the lime kiln dynamic behaviour exhibits important time constants and considerable dead time resulting in negative impact on the controllability of the decomposition process. As a consequence, it is important to investigate the dynamic behaviour and the influence of different operating parameters or disturbance factors for the benefit of improved operation of the industrial unit.

2. MATHEMATICAL MODEL DESCRIPTION

The mathematical model is developed based on the large accepted considerations that heat transfer is the rate-controlling step of the process [1], [2].

In order to describe the macroscopic behaviour of the kiln in its three aforementioned zones, phenomena taking place in a limestone spherical boulder is investigated. The shrinking unreacted core model has been chosen to reflect the complex heat and mass transfer processes taking place during limestone decomposition [1]. Nevertheless, the mathematical model takes into account several simplifying assumptions. They are: the limestone is uniformly distributed across the kiln section and the circulation regime is ideal for both the solid and the gaseous phase; the limestone boulders are spherical shaped and have homogenous initial properties, such as: constant and identical diameters, uniform external surface temperature, reaction surface propagation within the limestone boulder has a spherical symmetry; heat capacity, density and thermal conductivity of both calcium carbonate and calcium oxide are temperature independent; properties of the gaseous phase may be considered constant for each of the three kiln zones.

These assumptions lead to the following equations.

1. For the heating and the cooling zone:

- within the solid boulder the heat transmitted by conduction is described by the one-dimensional model with spherical symmetry:

$$\frac{\partial T_S}{\partial t} = a\left(\frac{\partial^2 T_S}{\partial r^2} + \frac{2}{r}\frac{\partial T_S}{\partial r}\right), \tag{1}$$

- in the gaseous phase the heat transferred between the solid surface and the gases is described by the equation:

$$\frac{dT_G}{dt} = k_T\ S_V\ (v_S / w_G)(T_G - T_{Sp}). \tag{2}$$

These equations have associated the following initial and boundary conditions:

$$\begin{aligned} &t = 0, \quad 0 \le r \le R; \quad T = T_0, \quad T_G = T_{G_0} \\ &t > 0; \quad r = R, \quad T = T_{Sp}, \quad \lambda \frac{\partial T}{\partial r} = k_T (T_G - T_{Sp}) \\ &r = 0; \quad \frac{\partial T}{\partial r} = 0 \end{aligned} \tag{3}$$

2. For the reaction zone the main phenomena taking place are: heat transfer by convection and radiation from the gaseous phase to the solid phase surface, heat transfer by conduction through the already formed calcium oxide layer, chemical reaction in the dissociation layer, carbon dioxide diffusion from the reaction layer to the gaseous phase associated with its heating up to the gaseous phase temperature and heating the unreacted limestone core up to the decomposition temperature. The equations for this zone describe:

- the heating of the unreacted limestone core:

$$\frac{\partial T_2}{\partial t} = a_2\left(\frac{\partial^2 T_2}{\partial r^2} + \frac{2}{r}\frac{\partial T_2}{\partial r}\right) \tag{4}$$

- the heating by conduction of the already formed calcium oxide layer together with the heating of the carbon dioxide contained in it:

$$\frac{\partial T_1}{\partial t} = a_1\left(\frac{\partial^2 T_1}{\partial r^2} + \frac{2}{r}\frac{\partial T_1}{\partial r}\right) + \frac{M_{CO_2}\, c_{p(CO_2)}\rho_2}{M_{CaCO_3}\, c_{p(CaCO_3)}\rho_1}\frac{r_m^2}{r^2}\frac{dr_m}{dt}\frac{dT_1}{dr} \tag{5}$$

- the heat transfer between the solid surface and the gases, described by the equation (2).

The initial and boundary conditions associated with this zone are:

$$\begin{aligned} &t = 0, \quad 0 \le r \le R; \quad T_1 = T_2 = T_0, \quad T_G = T_{G0} \\ &t \ge 0; \quad r = R, \quad T_1 = T_S, \quad \lambda_1 \frac{\partial T_1}{\partial r} = k_T (T_G - T_S) \\ &r = r_m; \quad T_1 = T_2 = T_d \quad \lambda_1 \frac{\partial T_1}{\partial r} + (\Delta H_R)\rho_2 \frac{dr_m}{dt} = \lambda_2 \frac{\partial T_2}{\partial r} \end{aligned} \tag{6}$$

Solving the set of time and space dependent system of partial differential equations has to face the challenge of the moving boundary feature. First the equations are scaled introducing dimensionless variables. For solving the scaled system of PDE equations the partial differential terms are replaced by finite difference terms using simultaneous discretization of both time and space independent variables. The moving boundary problem is managed by reconsidering the time discretization step (as the reaction layer advances) such as to preserve the space discretization network [1]. The emerged algebraic system of linear equations is solved using specific MATLAB software tools.

3. SIMULATION RESULTS

The investigation has been carried out for the case of a limestone boulder of spherical shape with a radius of 45 mm, considered as a typical case for the industrial practice [3].

The simulation results obtained for the solid surface temperature and for the gaseous phase temperature variations, in the heating zone, are shown in figure 2 and figure 3. They reflect the heating process taking place outside the limestone boulder as it passes over the heating zone.

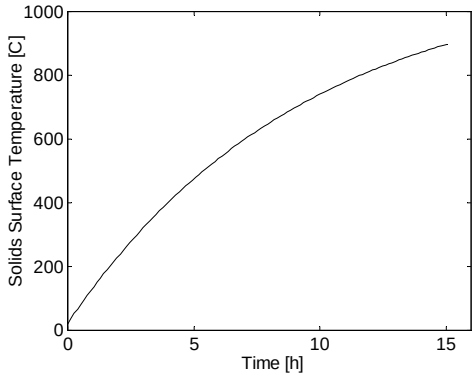

Figure 2. Solids surface temperature during the heating step.

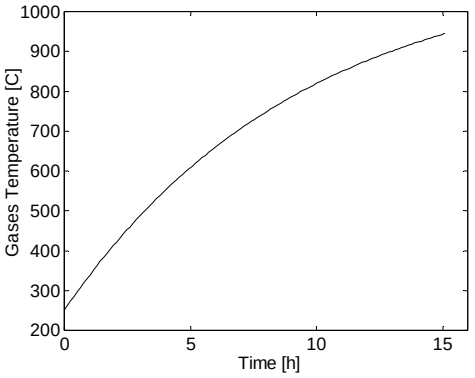

Figure 3. Gases temperature during the heating step.

The way temperature changes within the limestone boulder during the heating period, finished as soon as the surface temperature reaches the decomposition threshold, is presented in figure 4.

As it may be concluded from the presented figures, the time necessary for the limestone boulder to pass the heating zone and to reach the decomposition temperature is of t=15 hours.

Further investigations have been carried out to determine the temperature variations of the limestone boulder passing the reaction zone.

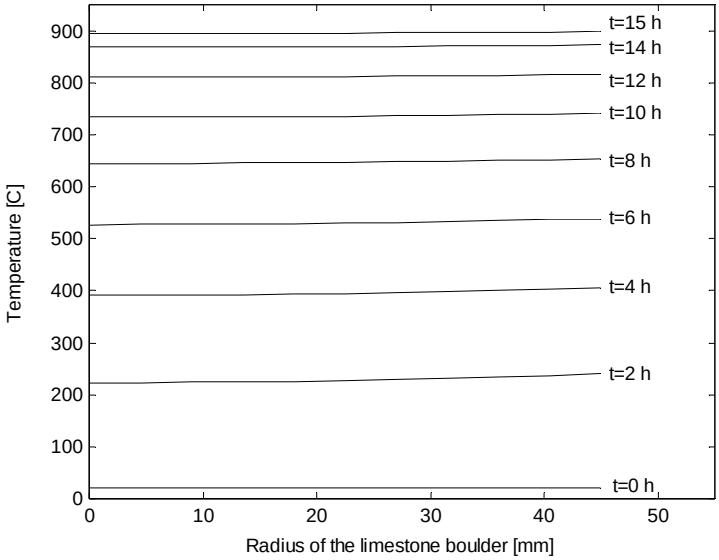

Figure 4. Temperature change within the limestone boulder during the heating step.

The simulation results obtained for the solid temperature (at different distances from the limestone boulder centre) and for the gaseous phase temperature, in the reaction zone, are shown in figure 5 and figure 6.

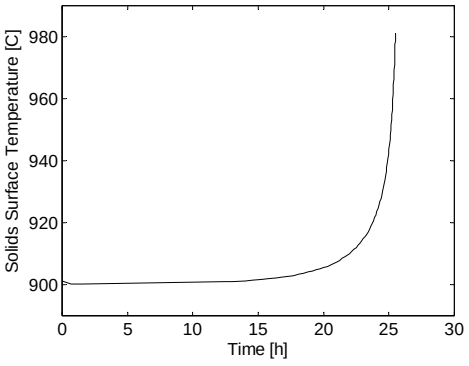

Figure 5. Solids surface temperature during the reaction step.

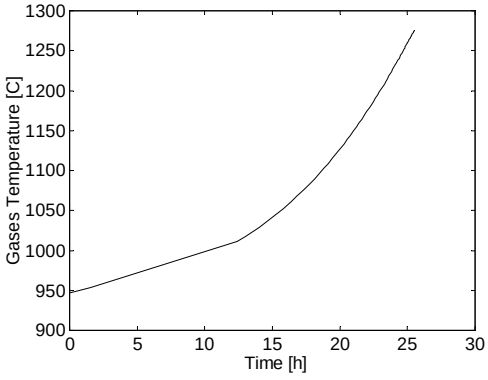

Figure 6. Gases temperature during the reaction step.

Figure 7 presents the temperature evolution along the distance from the centre of the limestone boulder during the reaction stage.

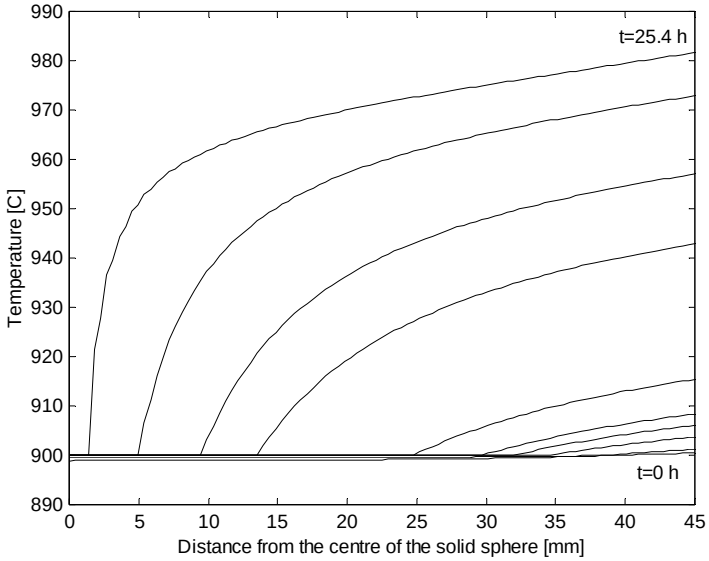

Figure 7. Temperature changes within the limestone boulder during reaction step.

The reaction stage extends over a period of t=25.5 h. At temperatures exceeding 900 ^{o}C, the lime porous structure presents a large specific surface leading to a fast decomposition of the limestone. For higher temperatures the occurrence of calcium oxide re-crystallisation determines a reduction of the specific surface hence leading to a diminished reactivity.

Finally, results for the cooling stage are presented in figure 8 and figure 9 for the solids surface (calcium oxide boulder) and for the surrounding gases temperature.

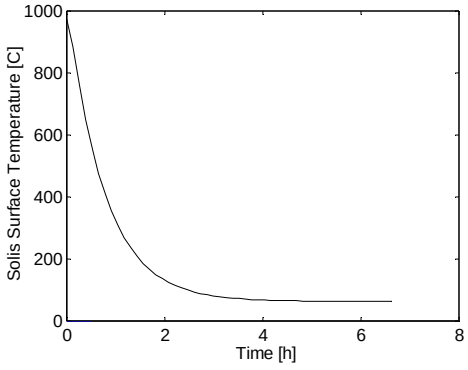

Figure 8. Solids surface temperature during the cooling step.

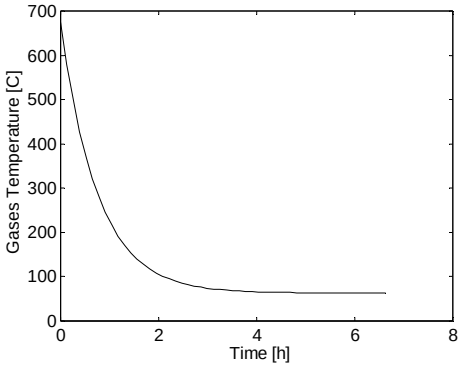

Figure 9. Gases temperature during the cooling step.

Temperature changes within the lime boulder during the cooling period of t=6.6 h are shown in figure 10.

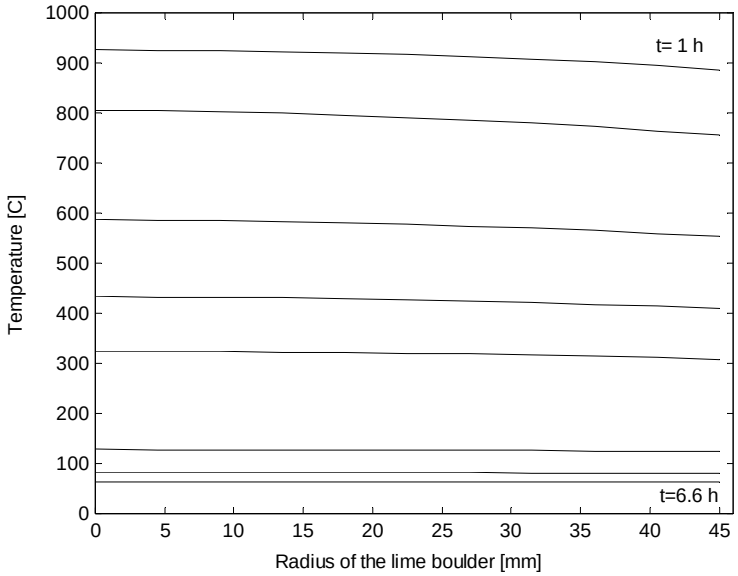

Figure 10. Temperature changes within the lime boulder during the cooling step.

As it may be noticed, the reaction stage is the most time consuming period of the limestone decomposition cycle while the cooling stage is smaller than the heating one.

Simulations reveal that due to the fact that properties of the limestone mineral have varying values, corresponding to various sources, the constants of the model equations have to be fitted to the particular source [4].

4. CONCLUSIONS

The developed simulator gives the opportunity to investigate the dynamic behaviour of a chemical process taking place according to the shrinking unreacted core model, applied to the limestone decomposition.

Dynamic evolution of the reaction surface within the limestone-lime boulder allows the disclosure of gases and solids temperature profile along the limestone kiln using natural gas fuel introduced at the limit between the reaction and cooling zones. The moving boundary problem is solved using a special mathematical approach based on space and time discretization network, implementing an effective algorithm for solving the system of partial differential equations.

The simulation results for the 90 mm diameter limestone boulder show residence times of 15 h, 25.4 h and 6.5 h, for the three zones of the kiln, presenting a good fit with the industrial unit values of 15 h, 25 h and 9 h. Further development of

the simulator is possible and necessary in order to reveal changing operating conditions and variable distribution of limestone boulders dimensions.

The simulator serves as a useful tool for looking into the details of the limestone decomposition process for revealing ways for obtaining optimal operating regimes of the vertical kiln and also offering an application example for other processes evolving in accordance to the same mechanism.

NOMENCLATURE

a – thermal diffusivity [m^2/h]
c_p – heat capacity [kcal/kg·grd]
k_T – heat transfer coefficient [kcal/m^2·h·^{0}C]
r – distance from the centre of the sphere [m]
t – time [h]
v_S – velocity of the limestone boulder [m/s]
v_G – velocity of the gases [m/s]
M – molecular mass [kg/kmole]
R – radius of the boulder sphere [m]
S_V - specific surface [m^2/m^3 of the kiln]
T – temperature [^{o}C]
w_G – heat capacity of the gaseous flux [kcal/m^2·h·^{0}C]
ΔH_R – heat of reaction [kcal/kg $CaCO_3$]
λ – thermal conductibility [kcal/m·^{0}C·h]
ρ – density [kg/m^3]

Indices

1 – calcium oxide (lime)
2 – calcium carbonate (limestone)
m – core
0 – initial
G – gaseous phase
S – solid phase
p – surface

REFERENCES

1. R. Mihail – *Modelarea Reactoarelor Chimice*, Editura Tehnica, Bucuresti, 1976.
2. A. M. Cormos, M. V. Cristea, S. P. Agachi, G. Zaha – *Dynamic Simulation of the Calcium Carbonate Thermal Decomposition in Vertical Lime Kiln*, CHISA Symposium, 2000.
3. M. S. Murthy, B. R. Harish, K. S. Rajanandam, K. Y. Ajoy Pavan Kumar, *Investigation on the kinetics of thermal decomposition of calcium carbonate*, Chemical Engineering Science, Vol. 49, no.13, 2198-2204, 1994.
4. R. H. Perry, D. W. Green – *Perry's Chemical Engineers' Handbook*, McGraw-Hill, 1999.

STUDIA UNIVERSITATIS BABEŞ-BOLYAI, CHEMIA, XLIX, 2, 2004

Dedicated to Professor Valer Fărcăşan at his 85th anniversary

HYDROAMINATION OF 1,3-CYCLOHEXADIENE IN WATER – HEPTANE LIQUID-LIQUID TWO-PHASE CATALYTIC SYSTEM

J. BÓDIS[1,2], T. E. MÜLLER[2] and J. A. LERCHER[2]

[1] *Babes-Bolyai University, Department of Organic Chemistry, str. Arany Janos nr. 11, 400028 Cluj, Romania. E-mail: jbodis@chem.ubbcluj.ro*

[2] *Institut für Technische Chemie, Technische Universität München, Lichtenbergstr. 4, D-85747, Garching bei München, Germany*

ABSTRACT. The direct addition of substituted aromatic amines to 1,3-cyclohexadiene was efficiently catalyzed in a liquid - liquid two phase system comprised of a polar catalyst of $Zn(CF_3SO_3)_2$ in water and the substrate and reactant mixture in n-heptane. The successful replacement of 1-ethyl-3-methyl-imidazolium trifluoromethanesulfonate with water, a greener and cheaper polar solvent than any ionic liquid (IL), for hydroamination reactions of cyclohexadiene with aromatic amines, was demonstrated.

Keywords: Hydroamination, 1,3-Cyclohexadiene, Amines, Catalysis, Lewis and Brönsted acids, Water

INTRODUCTION

The direct reaction of unsaturated compounds (alkenes or alkynes) with ammonia or primary/secondary amines (hydroamination) is an atom-economical route for the synthesis of nitrogen containing organic compounds [1]. The resulting amines or imines are of great importance for the chemical and pharmaceutical industry. While the new amines are potential drug candidates, the pharmaceutical companies have a serious deficit concerning their amine libraries [2]. Intensive explorative research has been made worldwide in the last years in order to develop efficient hydroamination processes [3]. Unfortunately, a real breakthrough did not occur in this area and only one process, the synthesis of *t*-butylamine from ammonia and isobutene in the presence of a zeolite catalyst has been commercialized [4]. None of other catalysts (homogeneous or heterogeneous) developed and tested until now reached sufficient activity for commercial applications [5].

Since the rate of the hydroamination reactions is directly dependent on the amount of catalyst employed, one of the most efficient strategies to achieve higher reaction rates is the use of a high concentration of catalysts, coupled with an efficient separation. This can be realized in solid-gas, solid-liquid or liquid-liquid heterogeneous systems. The possibility of catalyzing hydroamination reactions with Zn^{2+} ion exchanged zeolites has been demonstrated for the addition of methylamine to propyne (solid-gas system) [6] and for the cyclization of 6-aminohex-1-yne (solid-liquid system) [7,8].

The first hydroamination reaction in a liquid-liquid two-phase system has been realized for the cyclization of *o*-ethynylanilines to indoles with palladium(II)-salts in CH_2Cl_2 and aqueous HCl [9].

The challenge of the recent studies was to develop a new liquid-liquid two-phase system using green solvents, which would allow to perform hydroamination reactions in a more general manner. The selection of the solvent pair faces several boundary conditions: (i) most transitional metal catalysts for hydroamination reactions are cationic (*e.g.*, Rh^+, Pd^{2+}, Cu^+, Zn^{2+}) [10-12], and therefore, to dissolve the corresponding salts, a polar solvent is required, (ii) to achieve high reaction rates, the metal ion should be only weakly coordinated to the solvent, and (iii) the catalyst bearing liquid phase has to be immiscible with an appropriate apolar organic solvent in which the reactants and product should have high solubility. For the intramolecular hydroamination of 6-aminohex-1-yne, an ionic liquid (IL), 1-ethyl-3-methylimidazolium trifluoromethanesulfonate was chosen as polar phase (solvent for the catalyst precursor, $Zn(CF_3SO_3)_2$) and *n*-heptane as apolar phase (solvent for the starting materials and products) [5]. Based on the promising results (good conversions and yields, fast reaction, no leaching of the catalyst, possibility of continuous operation), the liquid-liquid two-phase catalytic procedure was extended to intermolecular hydroamination reactions [13-15], as well (see Fig.1).

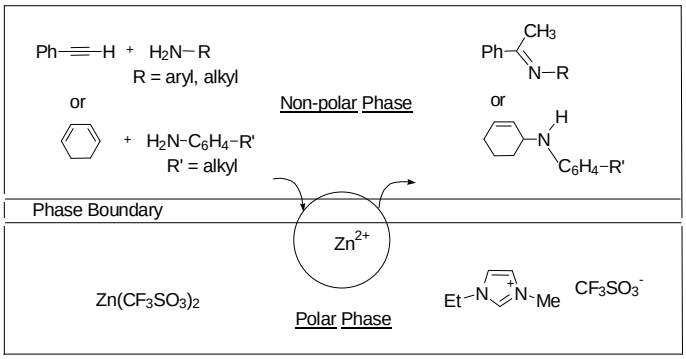

Fig. 1. Schematic model of liquid-liquid two-phase catalytic intermolecular hydroamination reactions.

The present contribution is focused on liquid-liquid, water-heptane two-phase catalytic intermolecular hydroamination reactions of an alkene-type substrate (hydroamination of 1,3-cyclohexadiene, see Eq. 1).

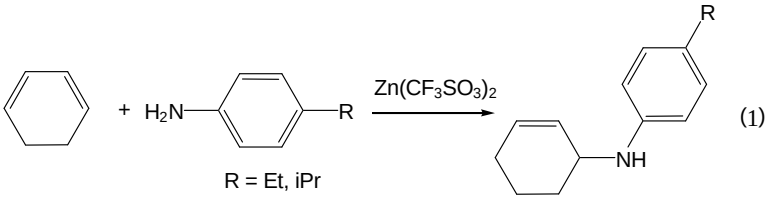

(1)

RESULTS AND DISCUSSION

To test the scope and suitability of two-phase catalysis by using water as polar solvent, the hydroamination reaction of 1,3-cyclohexadiene with phenylamine, 4-ethyl-phenylamine, 4-isopropyl-phenylamine and 4-fluoro-phenylamine were explored. The reactions were performed in the batch mode stirring the reaction mixture sufficiently fast (1000 rpm) to obtain a fine emulsion of the polar water phase in heptane. In this case, a large surface area was achieved, enabling a relatively fast mass transfer across the phase boundary.

The reaction between 1,3-cyclohexadiene and 4-isopropyl-phenylamine provided cyclohex-2-enyl-(4-isopropyl-phenyl)-amine as the major product (Eq. 2).

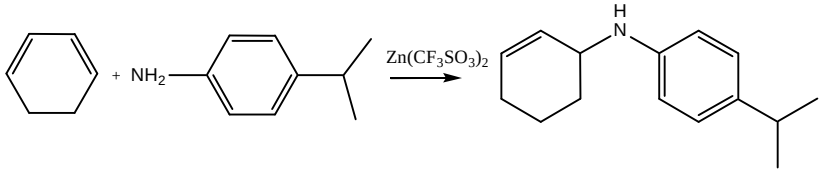

(2)

4-ethyl-phenylamine is giving cyclohex-2-enyl-(4-ethyl-phenyl)-amine (Eq. 3), but phenylamine and 4-fluoro-phenylamine did not react with cyclohexadiene.

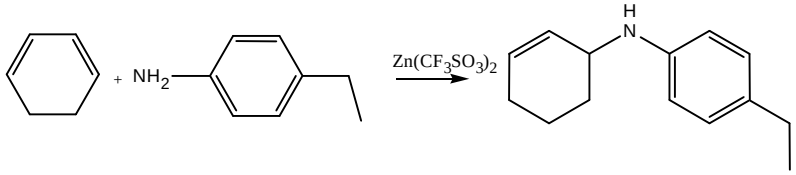

(3)

For both reactions, the concentration of the starting materials in the apolar phase decreased rapidly within the first minutes of the reaction (see the concentration-time diagrams for the hydroamination reaction of 1,3-cyclohexadiene with 4-isopropyl-phenylamine on Fig. 2). The formation of the major product follows first order kinetics, k_{init} = 0.000652 min^{-1}, TOF = 3.9 h^{-1}, (TOF = turnover frequency). 42% yield is reached after 25 hrs reaction time. At longer reaction times, the reactants were consumed at a lower rate. Only a few amount of the dimer of 1,3-cyclohexadiene is formed as a secondary product, no other products were identified in the reaction mixture.

We estimated the partitioning of each component between the heptane phase and a solution of $Zn(CF_3SO_3)_2$ in water. The starting materials, 1,3-cyclohexadiene and both 4-isopropyl-phenylamine and 4-ethyl-phenylamine were considerably more soluble in heptane than in water (solubility close to 0) at a temperature range of 25 - 98ºC (Eq. 4, *React* stands for 1,3 cyclohexadiene and for the amines used).

$$K_{eq}^{React} = \frac{c^{React}(H_2O)}{c^{React}(Heptane)} = 0 \qquad (4)$$

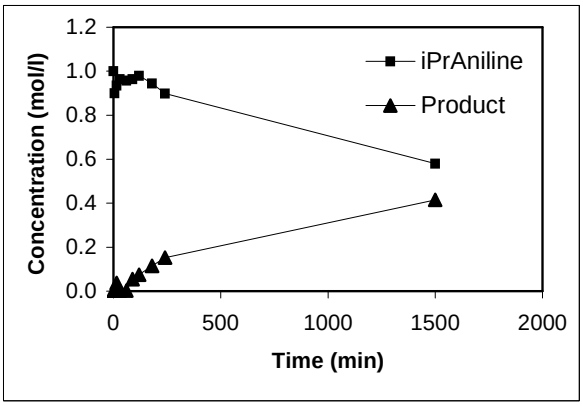

Fig. 2. Concentration *versus* time diagram for the hydroamination reaction between cyclohexadiene and 4-isopropyl-phenylamine (stoichiometic ratio) catalysed by $Zn(CF_3SO_3)_2$ in water-heptane liquid-liquid two-phase system.

The same behavior was found for the main products of the reactions, they were found also to be present only in the heptane phase (Eq. 5).

$$K_{eq}^{Product} = \frac{c^{Product}(H_2O)}{c^{Product}(Heptane)} = 0 \qquad (5)$$

Based on the observation that homogeneous hydroamination reactions could be accelerated by addition of a Brønsted acid, trifluoromethanesulfonic acid was added to the reaction mixture of 1,3-cyclohexadiene and 4-isopropyl-phenylamine. The same product, cyclohex-2-enyl-(4-isopropyl-phenyl)-amine was formed with almost the same reaction rate. Similarly, the rate of reaction was very close, when trifluoromethanesulfonic acid was employed as the only catalyst. This indicates that the two-phase reaction of 1,3-cyclohexadiene proceeds almost the same when the catalyst $Zn(CF_3SO_3)_2$ is employed under neutral or acidic conditions or CF_3SO_3H alone is used as catalyst. Thus, the reaction seems to be most likely Brønsted acid catalyzed, being different from the reaction of phenylacetylene with aromatic amines in ionic liquid-heptane two-phase system, where the results revealed a Lewis acid catalysis [13-16].

The new reaction system employed in this study is very close to the ideal synthesis [17] (environmentally acceptable, resource efficient, available materials, one step, safe, simple, high yield).

CONCLUSIONS

It has been demonstrated that the addition of aromatic amines (with alkyl groups on the benzene ring) to 1,3-cyclohexadiene can be efficiently catalyzed with $Zn(CF_3SO_3)_2$ or with CF_3SO_3H in a liquid-liquid water-heptane two-phase system. The major advantage is that after the reaction the catalyst remains quantitatively in water, which can be easily separated from the organic phase. The product is obtained after removal of heptane in a high quality.

Water as a green (ecological) and cheap solvent is able to substitute the highly expensive and less greener 1-ethyl-3-ethylimidazolium trifluoromethanesulfonate ($EtMeIm^+TfO^-$) ionic liquid found recently a good catalyst bearing solvent for two-phase catalytic intermolecular hydroamination [13-15]. The new reaction system employed in this study is very close to the ideal synthesis.

EXPERIMENTAL

Materials and Methods

n-heptane (99%) was obtained dry from Aldrich. 1,3-cyclohexadiene (97%, Aldrich) and the amines (phenylamine, 4-ethyl-phenylamine, 4-isopropyl-phenylamine and 4-fluoro-phenylamine) were obtained in high purity (98-99%) from Aldrich and used as received. Zinc trifluoro-methanesulfonate ($Zn(CF_3SO_3)_2$, 98%, Aldrich) and trifluoro-methanesulfonic acid (CF_3SO_3H, 99%, Aldrich) were employed as catalysts without further purification.

Physical and Analytical Methods

^1H- and $^{13}C\{^1H\}$- NMR spectra were recorded on a Bruker GX 360 NMR instrument and referenced in ppm relative to the solvent shift [18] or tetramethyl-silane. GC-analyses were performed on a HP 5890A gas chromatograph with FID detector and a HP 5890 series II gas chromatograph with HP 5971 mass selective detector HP 5730A. Both gas chromatographs were equipped with a crosslinked 5% diphenyl- 95 % dimethyl-polysiloxane column (30 m, Restek GmbH, Rtx-5 Amine). Infrared spectra were obtained on a Perkin Elmer 2000 FT-IR spectrometer as thin film of the neat compound. Elemental analyses were performed by the Microanalytical Laboratory of the TU München.

Preparation and kinetic measurements

The kinetic experiments were performed in the batch mode in magnetically stirred custom built 60 cm^3 autoclaves at 180-200 ºC and 6-10 bar. In a typical experiment, the reactor was charged with $Zn(CF_3SO_3)_2$ (0.07 g, 0.2 mmol) and distilled water (0.5 cm^3, home made) under nitrogen. After the catalyst had dissolved in water (several minutes) n-heptane (15 cm^3) and amine (20 mmol) were introduced. The mixture was stirred at 1000 rpm and the reactor heated to the reaction temperature. 1,3-cyclohexadiene was then introduced with a HPLC pump. Samples were taken for GC and MS analyses. The final reaction mixture was separated, the water phase was washed with n-heptane and the unified organic phase concentrated in a rotating evaporator. The liquid product was purified by distillation in a partial vacuum.

Cyclohex-2-enyl-(4-isopropyl-phenyl)-amine.
Yield: 1.72 g, 40%.
B.p. 105-107℃ (0.3 mbar).
Found: C, 84.2; H, 9.9; N, 6.4%.
Calc. for $C_{15}H_{21}N$: C, 83.7; H, 9.8; N, 6.5%.
$^{13}C\{^1H\}$-NMR (CD_3COCD_3): 166.2 (s, *C*N), 151.3 (s, *C*^{i}Pr), 145.0 (s, Ph), 141.2 (s, Ph), 131.9 (s, Ph), 129.8 (s, Ph), 128.7 (s, Ph), 128.3 (s, Ph), 120.9 (d, Ph), 35.0 (s, CH), 25.2 (s, 2 CH_3), 18.0 (s, *C*H_3CN) ppm.

^{1}H-NMR (CD_3COCD_3): 6.93 (dtd, 2H, Ph), 6.54 (dd, 2H, Ph), 5.89 (mt, 1H, C=C*H*), 5.64 (mq, 1H, *H*C=C), 4.26 (b, 1H, N*H*), 3.47 (m, 1H, NC*H*), 2.75 (sept, 1H, CH), 2.0 - 1.3 (m, not resolved, 6H, 3 CH_2), 1.19 (d, 6H, 2 CH_3) ppm.
IR (neat): 3448 (m), 3365 (m), 3017 (s), 2956 (vs), 2929 (vs), 2864 (s), 1622 (vs), 1502 (vs), 1458 (m), 1429 (w), 1381 (w), 1361 (w), 1279 (s), 1156 (w), 1046 (w), 994 (w), 886 (m) cm^{-1}.
m/z (FAB) 215 (M^+), 200 (M^+-CH_3).

ACKNOWLEDGEMENT

The Deutsche Forschungsgemeinschaft (DFG) is acknowledged for financial support.

REFERENCES

1. T.E. Müller and M. Beller, Chem. Rev., 1998, **98**, 675.
2. W. Bender, From Synthons to Bioactive Molecules: Efficient Strategies in Modern Lead structure Research, lecture at ICS-UNIDO Workshop on Trends and Applications of Combinatorial Chemistry and Combinatorial Technologies, Budapest, Hungary, October 15-18, 2001, pp. 20-46.
3. a) J.S. Johnson and R. G. Bergman, J. Am. Chem. Soc., 2001,**123**, 2923; b) O. Löber, M. Kawatsura and J.F. Hartwig, J. Am. Chem. Soc., 2001, **123**, 4366; c) C. Cao, J.T. Ciszewski and A.L. Odom, Organometallics, 2001, **20**, 5011; d) C.G. Hartung, A. Tillack, H. Trauthwein and M. Beller, J. Org. Chem., 2001, **66**, 6339; e) M. Nobis and B. Drießen-Hölscher, Angew. Chem., Int. Ed., 2001, **40**, 3983.
4. W.F. Hoelderich and G. Heitman, Catal. Today, 1997, **38**, 227.
5. V. Neff, T.E. Müller and J.A. Lercher, J. Chem. Soc., Chem. Comm., 2002, **6**, 906.
6. R.S. Neale, L. Elek and R.E. Malz, J. Catal., 1972, **27**, 432.
7. J. Penzien, T.E. Müller and J.A. Lercher, Chem. Commun., 2000, **18**, 1753.
8. J. Penzien, T.E. Müller and J.A. Lercher, Micropor. Mesopor. Mater., 2001, **48**, 285.
9. S. Cacchi, V. Carnicelli and F. Marinelli, J. Organomet. Chem., 1994, **475**, 289.
10. T.E. Müller, M. Grosche, E. Herdtweck, A.-K. Pleier, E. Walter, and Y.-K. Yan, Organometallics, 2000, **19**, 170.
11. T.E. Müller, M. Berger, M. Grosche, E. Herdtweck and F.P. Schmidtchen, Organometallics, 2001, **20**, 4384.
12. R.Q. Su and T.E. Müller, Tetrahedron, 2001, **57**, 6027.
13. J. Bódis, Ch. Hauser, T.E. Müller and J.A. Lercher, DECHEMA Conference on “Green Solvents for Catalysis”, Bruchsal, Germany, October 13-16, 2002, B.A., pp. 110.
14. J. Bódis, T.E. Müller and J.A. Lercher, 36th Annual Meeting of the German Catalytic Society, Weimar, Germany, March 19-21, 2003, B.A., pp.321-322.
15. J. Bódis, T.E. Müller and J.A. Lercher, Green Chemistry, 2003, **5**, 227.
16. H.M. Senn, P.E. Blöchl and A. Togni, J. Am. Chem. Soc., 2000, **122**, 4098.
17. P.A. Wender, S.T. Handy and D.L. Wright, Chem. Ind., 1997, 765.
18. H.E. Gottlieb, V. Kotlyar and A. Nudelman, J. Org. Chem., 1997, **62**, 7512.

STUDIA UNIVERSITATIS BABEŞ-BOLYAI, CHEMIA, XLIX, 2, 2004

Dedicated to Professor Valer Fărcăşan at his 85th anniversary

INTERACTIONS OF METHANOL WITH $AlPO_4$-5 AND SAPO-5 SINGLE CRYSTALS

J. BÓDIS[1], J. KORNATOWSKI[2] and J. A. LERCHER[2]

[1] Babes-Bolyai University, Department of Organic Chemistry, str. Arany Janos nr. 11, 400681 Cluj, Romania. e-mail: jbodis@chem.ubbcluj.ro
[2] Institut für Technishe Chemie, Technische Universität München, Lichtenbergstrasse 4, D-85747, Garching bei München, Germany

ABSTRACT. The interactions of methanol as polar probe molecule with the framework of $AlPO_4$-5 and SAPO-5 molecular sieves in the form of single large crystals were investigated with FT-IR micro-spectroscopy. Methanol exhibited weak interactions with $AlPO_4$-5. The polar molecules of methanol on SAPO-5 interacted primarily with the bridging OH groups. Polar molecules of methanol revealed a bimodal distribution of acid strength of the bridging OH groups. Two adsorbate species have been found to occur, both bound via hydrogen bonds of different strength dependent on the adsorption site. The interactions between the probe molecules and the framework are stronger in the confined environment of the narrow channels than in the wide channels. However, all these interactions are weak and do not lead to irreversible structure changes of $AlPO_4$-5 and SAPO-5 materials.

Keywords*:* $AlPO_4$-5 and SAPO-5; Single crystals; Adsorption of methanol, FT-IR spectroscopy

INTRODUCTION

Extensive IR spectroscopy studies of methanol [1,2] allowed the assignment of the bands at 3682 and 1080 cm^{-1} to the stretching and bending vibrations of OH groups in free methanol molecules, respectively. Associated methanol gave rise to new bands at around 3300 and 1340 cm^{-1}. They were assigned to the same hydroxyl group vibrations which underwent a red and blue shift, respectively, due to mutual interactions *via* hydrogen bonding. An increasing strength of the hydrogen bonding, *i.e*., liquid and solid state of methanol, led to a further red shift of the OH stretching vibration to 3200 cm^{-1} and a blue shift of the OH bending vibration to around 1500 cm^{-1}.

Interpretation of the IR spectra of methanol adsorbed on acidic molecular sieves is especially complex and related to the question whether methanol is protonated by strong Brønsted acid sites or not. While Ison and Gorte [3] proposed that methanol occurs as strongly hydrogen bound species, Mirth *et al.* [4] and Jentys *et al.* [5] assigned certain patterns of bands to protonated methanol. The spectra of methanol adsorbed on zeolites were also assigned to the so called A-B-C patterns [6], caused by a Fermi resonance between the out-of-plane deformation vibrations of the bridging OH groups and the perturbed hydrogen bound OH groups. *Ab initio* studies by Haase and Sauer [7] supported the latter interpretation: strongly hydrogen bound methanol is the most favourable adsorption complex. As the energy difference between this neutral complex and an ion pair

complex with protonated methanol is small, the authors proposed that the latter is a transition structure between the transfer of a proton from one oxygen atom to a neighbouring one *via* an adsorbed methanol molecule (Fig. 1). These calculations relate to a rather perfect environment and only one adsorbed methanol molecule per acid site. Calculations fail to explain fully the IR absorption band found normally between 3500 and 3630 cm^{-1}. Mirth *et al.* [4], assigned it to protonated methanol molecules which interact *via* methyl groups with $(SiOAl)^-$ groups of the framework. However, the calculations by Blaszkowski and van Santen [8] revealed the ratio between the number of methanol molecules interacting with the SiOHAl group *via* the hydroxyl group to those interacting *via* the methyl group to be equal to $4.5 \cdot 10^4$. Thus, in the light of the hydrogen-bonding model, the most convincing explanation seems to be that the OH group of alcohol is only weakly perturbed and shows such a small downward shift.

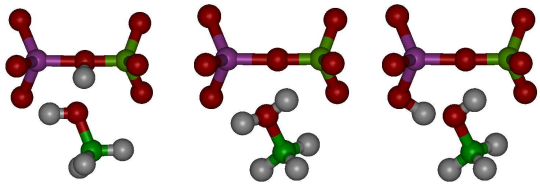

protonated methanol

Fig.1. Possible surface species of methanol interacting with the bridging hydroxyl group.

We aimed at a better understanding of acidic sites in $AlPO_4$-5 and SAPO-5 *via* determination of interactions between the metal substituted materials and methanol by means of highly sensitive IR studies. The probe compound has been chosen as relatively small dimension and high polarity able of penetration into the whole adsorption space of the molecular sieves. Moreover, methanol is an interesting compound used in numerous industrial processes such as *methanol-to-gasoline* (MTG) [9] or alkylation of aromatics [10]. The IR measurements were performed using *in situ* IR micro-spectroscopy on single large crystals of $AlPO_4$-5 and SAPO-5 that allowed us to avoid any intercrystalline effects.

EXPERIMENTAL

Synthesis of the $AlPO_4$-5 and SAPO-5 single crystals, the applied procedures, as well as the IR measurements methodology have been described in details elsewhere [11-15]. Absolute methanol (>99.8%, Merck) was used as probe molecule. The experiments were carried out in a vacuum cell, equipped with IR transparent windows, which was attached to the stage of a BRUKER IR microscope coupled to a BRUKER IFS 88 spectrometer. The calcined crystals were placed in the IR cell and heated at 10 K/min to 770 K under vacuum of 10^{-6} mbar for 30 min. After cooling down at 10 K/min to 310 K under vacuum, spectra of the selected crystals were recorded. The sorbates were introduced into the IR cell via a differentially pumped gas inlet system. The partial pressures (10^{-3} to 1 mbar) were hold constant until sorption/desorption equilibrium was achieved. The sorption was followed in situ by time resolved FT-IR micro-spectroscopy (1000 scans/spectrum, 4 cm^{-1} resolution). Subsequently, the cell was evacuated (10^{-6} mbar, 310 K) and temperature was increased to 775 K at 10 K/min.

RESULTS AND DISCUSSION

$AlPO_4$ –5. In contact with 10^{-1} mbar methanol, $AlPO_4$-5 showed the ν_{OH} bands at 3675 (negative), 3597 and 3178 cm^{-1}, and the band of the in-plane bending vibrations of the OH groups [4] at 1489 cm^{-1}. The ν_{CH} bands of methanol [4] were found at 2995(sh), 2960, 2925(sh) and at 2850 cm^{-1} (Fig. 2). Increase in pressure to 1 mbar led to a blue shift of the band at 3597 cm^{-1} to 3630 cm^{-1} and a shoulder at 3610 cm^{-1}. The broad absorption band at 3178 cm^{-1} shifted to 3228 cm^{-1} and had a shoulder at 3375 cm^{-1}. The CH stretching vibration bands grew in intensity. The last pressure step did not cause negative bands in the region of the OH stretching vibrations, which means that all accessible terminal P-OH groups were covered at 10^{-1} mbar.

The 3597 cm^{-1} band of methanol adsorbed on $AlPO_4$ –5 is assigned to a weakly perturbed stretching vibration of methanol OH hydrogen bound to the terminal P-OH groups (negative band at 3675 cm^{-1}). The corresponding deformation OH vibration of methanol was found at 1489 cm^{-1}. The ν_{OH} band at 3178 cm^{-1} is attributed to the perturbed terminal P-OH groups. The positions of these bands indicate a weak interaction of methanol with the P-OH groups. The presence of the relatively free vibrating methanol OH groups shows that the interaction of methanol with the framework is weaker than that of water [15]. The high frequency bands at 3630 and 3610 cm^{-1} stem from the free vibrating methanol OH groups. The broad bands at 3375 and 3228 cm^{-1} are assigned to methanol hydroxyl groups of the mutually interacting methanol molecules. The fact that the absorption bands occur in pairs can be explained by the different adsorption of methanol in the wide and narrow channels, in the latter with a higher strength of interaction due to a confined environment [12].

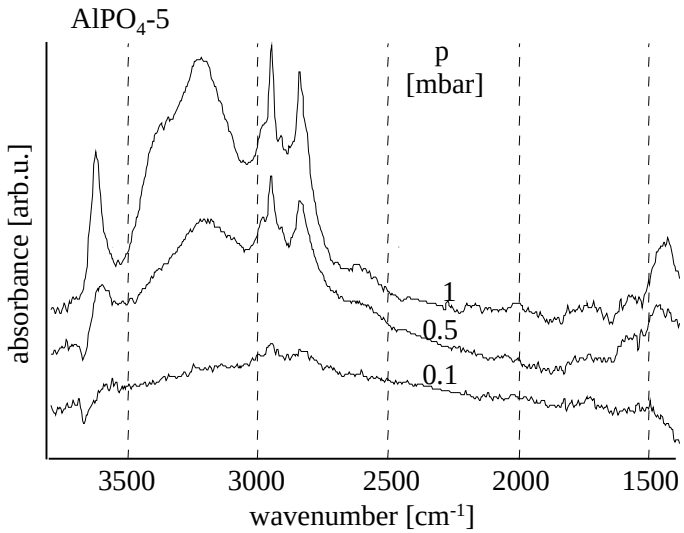

Fig. 2. Difference spectra between individual steps of the uptake of methanol in the pores of $AlPO_4$-5 single crystals.

SAPO-5. The spectrum of SAPO-5 in contact with methanol at a low pressure (10^{-1} mbar) showed negative bands of the stretching OH vibrations at 3632 and 3496 cm^{-1}, which were masked by a new positive ν_{OH} band at 3568 cm^{-1}. The broad bands at ~3100, 2807 and 2473 cm^{-1} were assigned to the stretching vibrations of hydroxyl groups as well. The bands of the bending OH vibrations were found at 1735 and 1525 cm^{-1} (Fig. 3). Increase in pressure to 0.25 and 0.5 mbar led to an increase in intensities of all the bands and to a shift of the band at 3568 cm^{-1} to 3587 cm^{-1}. After the pressure raise to 1 mbar, new negative bands of stretching OH vibrations were found at 3733 and 3675 cm^{-1}, assigned to the terminal Si-OH and P-OH groups, respectively. The broad band from 3100 cm^{-1} appeared shifted to 3205 cm^{-1}. The negative absorption bands of the strong Brønsted acid sites at 3632 and 3496 cm^{-1} increased the intensity in parallel with those at 3598 (shifted from 3587 cm^{-1}), 2790, 1750, 1690 and 1525 cm^{-1} (Fig. 3). Also the stretching CH vibrations increased in intensity. Extension of the equilibration time led to a coverage of all acid sites. The bands increased in intensity and shifted to 3615, 3209, 2785 and 1712, 1580 and 1482 cm^{-1}, respectively.

The spectra of methanol adsorbed on SAPO-5 at low pressure show a typical pattern of three doublets: a high frequency one above 3500 cm^{-1}, the second one consisting of broad bands at 2807 and 2473 cm^{-1}, and the third one below 1750 cm^{-1}. The two broad bands at 2807 and 2473 cm^{-1} have a similar height and half width. In accordance with the recent calculations [6,7], this is the so-called A-B-C pattern caused by a strong hydrogen bonding between methanol and Brønsted acid sites. However, no explanation can be given for the doublet at the highest frequency and for one low frequency deformation band. Another idea that protonated molecules may interact with the acid sites in two ways, *i.e.*, *via* OH or methyl group, is not probable considering both the ratio of intensities and the high intensity of the high frequency bands. From the IR data alone, it can not be decided which of the models is valid.

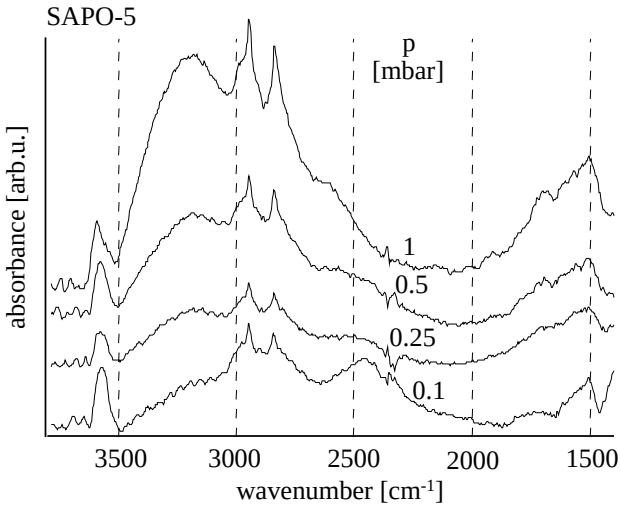

Fig. 3. Difference spectra between individual steps of the uptake of methanol in the pores of SAPO-5 single crystals.

At a higher pressure of methanol on SAPO-5, new bands arise at 3568, 2900, 2785, 1690 and 1525 cm^{-1}, attributed to methanol molecules strongly hydrogen bound to the acid sites located in two various channel systems. It is assumed that the band of ν_{OH} vibration at around 3600 cm^{-1} contains at least two bands as can be concluded from both the shape and the fact that the band is cut on both sides by the negative absorption bands of the strong Brønsted acid sites. Methanol adsorbed in the large channels is reflected in the bands at 3568 (weakly perturbed ν_{OH} of methanol), around 2900 (perturbed high frequency OH band) and 1525 cm^{-1} (bending OH band of methanol). Methanol molecules adsorbed on the strong acid sites in the narrow channels interact more strongly due to the space constraint [12]. This is reflected in the bands at 3568 (ν_{OH} of methanol), 2785 (ν_{OH} of perturbed low frequency OH), and 1690 cm^{-1} (OH bending of methanol). The reason for the different assignment of these bands as compared to those observed at the lowest pressure is a different intensity and half-width of the bands at 2900 and 2785 cm^{-1}. This is in agreement with the findings from experiments with methanol in the gas, liquid and solid phases [3,4] as well as with the common observation that stretching vibrations undergo a red shift with increasing interaction strength. In contrast, the deformation vibrations show the opposite trend. The broad band around 3100 cm^{-1} is assigned to the perturbed ν_{OH} vibrations of methanol engaged into mutual hydrogen bonding. At a higher pressure, an over-proportional intensity increase occurs for the bands attributed to methanol interacting with the bridging OH groups and to hydrogen bound methanol. This intensity increase, occurring mainly for more weakly adsorbed methanol molecules, is followed by a blue shift of the bands originally located at 3568 and 3100 cm^{-1}.

The experiments leave open the question why two adsorption states of different interaction strength are observed for methanol (similarly to water [15]) on SAPO-5. At present, we may speculate that this is related to the formation of siliceous islands in the structure as described by Barthomeuf [16]. Such islands would create a zeolite-like environment and, since aluminium is less electronegative than silicon, the protonic strength should increase with the increasing number of silicon neighbours. Consequently, the strong Brønsted acid sites should be the preferred adsorption sites. This agrees well with the fact that these sites are covered before the regular bridging hydroxyl groups, which have only one silicon as neighbour. Note that previous results on single crystal samples with apolar compounds [12] did not indicate a distribution of acid strength of the bridging OH groups. Thus, we speculate that the bimodal distribution of strength is only seen for strongly polar molecules.

The temperature programmed desorption of methanol led to removal of all the adsorbed methanol molecules from $AlPO_4$-5 and SAPO-5 at around 550 and 730 K, respectively.

The adsorption/desorption cycles for all the single crystal samples measured did not lead to any changes of the spectra in relation to the unloaded molecular sieves. Therefore, it has been accepted that adsorption of methanol does not lead to changes in the structure of the $AlPO_4$-5 and SAPO-5 materials studied.

CONCLUSIONS

Adsorption of methanol on $AlPO_4$-5 reveals a weak coordinative interaction of methanol molecules with framework aluminium and a weak hydrogen bonding interaction with the terminal P-OH groups of the channels.

Small polar molecules of methanol adsorbed on the SAPO-5 single crystals reveal that two various surface species of the adsorbates occur. Both of them are bound *via* hydrogen bonds of different strength dependent on the adsorption sites. Interactions with the bridging hydroxyl groups are of the primary role. It is not clear why SAPO-5 exhibits bridging hydroxyl groups of different acid strength in relation to methanol, especially that the measurements with basic molecules [12] did not give evidence for a distribution of acid strength. The investigations also suggest that a single polar molecule adsorbed on a Brønsted site is hydrogen bound. A higher number of polar molecules enhances the interaction with the acid site by polarization of the primarily interacting molecule. SAPO-5 has shown IR bands of the adsorbed species at the lowest values of the adsorbate pressure. This indicates a higher adsorption affinity of SAPO-5, which is also supported by the higher desorption temperature as compared to $AlPO_4$-5 sample.

Interactions between the framework and the probe molecules in the narrow channels of both the $AlPO_4$-5 and SAPO-5 materials are stronger than in the large channels most likely due to the confined environment. Adsorption/desorption cycles of methanol does not lead to changes of framework structure of the single crystals.

REFERENCES

1. A.V. Stuart, G.B.B.M. Sutherland, J. Chem. Phys., 1956, **24**, 559.
2. M. Falk, E. Whalley, J. Chem. Phys., 1961, **34**, 1554.
3. A. Ison, R.J. Gorte, J. Catal., 1984, **89**, 150.
4. G. Mirth, J.A. Lercher, M.W. Anderson, J. Klinowski, J. Chem. Soc., Faraday Trans. 1, 1990, **86**, 3039.
5. A. Jentys, G. Warecka, M. Derewinski, J.A. Lercher, J. Phys. Chem., 1989, **93**, 4837.
6. A.G. Pelmenschikov, R.A. van Santen, J. Jänchen, E. Meijer, J. Phys. Chem., 1993, **97**, 11071.
7. F. Haase, J. Sauer, J. Am. Chem. Soc., 1995, **117**, 3780.
8. S.R. Blaszkowski, R.A. van Santen, in: H. Chon, S.K. Ihm, Y.S. Uh (Eds.), Progress in Zeolite and Microporous Materials, Stud. Surf. Sci. Catal., Vol. 105, Elsevier, Amsterdam, 1997, p. 1707.
9. S.L. Meisel, J.P. McCullogh, C.H. Lechthaler, P.B. Weisz, Chem. Tech., 1976, **6**, 86.
10. F.G. Dwyer, P.J. Lewis, F.M. Schneider, Chem. Eng., 1976, **83**, 90.
11. G. Müller, J. Bódis, G. Eder-Mirth, J. Kornatowski, J. A. Lercher, J. Mol. Structure, 1997, **410-411**, 173.
12. G. Müller, E. Bódis, J. Kornatowski, J.A. Lercher, Phys. Chem. Chem. Phys., 1999, **1**, 571.
13. J. Bódis, G. Müller, J. Kornatowski, J.A. Lercher, Acta Universitatis Cibiniensis-Seria F Chemia, 2001, **4**, (2), 3.
14. J. Bódis, G. Müller, J. Kornatowski, J.A. Lercher, Studia-Chem., 2002, **47**, (1-2), 177.
15. G. Müller, J. Bódis, J. Kornatowski, Micropor. Mesopor. Mat., 2004, **69**, 1.
16. D. Barthomeuf, Zeolites, 1994, **14**, 394.

STUDIA UNIVERSITATIS BABEŞ-BOLYAI, CHEMIA, XLIX, 2, 2004

Dedicated to Professor Valer Fărcăşan at his 85th anniversary

CATALYTIC REDUCTIVE AMINATION OF BUTANAL OVER CARBON SUPPORTED NOBLE METALS

J. BÓDIS[1] and J. A. LERCHER[2]

[1] *Babes-Bolyai University, Department of Organic Chemistry, str. Arany Janos nr. 11, 400028 Cluj, Romania. E-mail: jbodis@chem.ubbcluj.ro*
2 Institut für Technische Chemie, Technische Universität München, Lichtenbergstr. 4, D-85747, Garching bei München, Germany

ABSTRACT. The reductive amination of butanal with ammonia (at ammonia/butanal molar ratios of ~ 14.5) and hydrogen has been performed at 50 bar and 323-353 K over graphite and charcoal supported noble metal catalysts. Rhodium and platinum based catalysts showed the highest activity. The BET area and metal dispersion markedly influenced the activity without changing the selectivity. The products (butylamine, dibutylamine and tributylamine) were detected in the reaction mixture only after an apparent induction period. Butylamine and dibutylamine seem to be primary products, which are hardly interconverted. Good hydrogenolysis catalysts (Ru, Rh) produced mostly primary amines, while active hydrogenation catalysts (Pt, Pd) directed the reductive amination of butanal towards secondary and tertiary amines.

Keywords: Reductive amination, Butanal, Amines, Noble metal catalysts, Carbon supports

INTRODUCTION

The reductive amination of aldehydes and ketones with ammonia and hydrogen is an important synthetic route to amines and proceeds through an intermediately formed aminoalcohol [1]. This may be dehydrated to imine, which is subsequently hydrogenated or can be directly hydrogenolized to primary amine in presence of a catalyst. The primary amine formed can also behave as an aminating agent for the carbonyl compound forming a Schiff base, which is reduced to secondary amine [1]. The addition of a primary amine to the imine with subsequent reduction of the adduct also leads to secondary amine. The secondary amine can react similarly with the carbonyl compound or with the imine, forming tertiary amine. The principal side reaction is the hydrogenolysis reaction of the carbonyl compound involving the formation of the corresponding alcohol. Apparently, the formation of the primary amine should proceed only through aminoalcohol-imine intermediates, but there is evidence that secondary and tertiary amine precursors could be present at concentrations much higher than the amount of secondary and tertiary amine obtained at the end [2]. Thus, the reaction paths leading to the final product and, so, determining the selectivity of a particular catalyst under a set of reaction conditions are not clearly known.

There are numerous reports on the use of supported and unsupported Ni, Co and noble metal catalysts [1,3-11]. Metal sulfides (Re, Fe, Co, Ni, W, Pt, Rh) were also used [12-14] as catalysts in the reductive amination of ketones. The relative inactivity of these catalysts for the hydrogenation of the aromatic ring, ketones, nitriles, esters and other unsaturated functional groups, often permits useful selectivity in case of multifunctional compounds.

Butanal [15] was chosen as test molecule in this study because of lack of literature information concerning the reductive amination of this substrate with ammonia and hydrogen over supported noble metal catalysts.

EXPERIMENTAL

CATALYSTS: The catalysts tested in the reductive amination of butanal are presented in Table 1 together with some physicochemical characterization data as well. The charcoal supported catalysts contained 55-60% moisture. The quantitative values used for these samples refer to dry material.

Table 1

Catalysts characterization data (metal dispersions were calculated by using n_S values estimated according to literature [16])

Type of catalyst	S_{sp} (m^2/g)	S_M (m^2/g)	Metal location	Dispersion (%)	BET area (m^2/g)
5%Rh/charcoal	950	11.1	Intermediate	50.4	817.8
5%Rh/HSAgraphite	130	9.5	Surface	43.2	94.6
5%Ru/HSAgraphite.	130	8.0	Surface	43.8	41.6
5%Pd/charcoal	995	18.5	Intermediate	83.0	n.a.
5%Pd/HSAgraphite	130	11.4	Surface	51.1	87.6
5%Pt/HSAgraphite	130	5.0	Surface	40.5	80.1
5%Pt/LSAgraphite	n.a.	3.5	Surface	28.0	56.7

Ssp specific surface area of the support
S_M metal surface area determined by hydrogen chemisorption
HSA high surface area
LSA low surface area

CATALYSTS TESTING: The reactions were carried out in batch reactors with a volume of about 65 ml. Magnetic stirring at a speed of 1100 rpm was used. The temperature inside the autoclave was measured by a thermocouple mounted on the lid of the autoclave. Weighed amount of catalysts were introduced into the autoclave. In order to assure a well-defined starting time for every reaction, the following experimental procedure was applied: after addition of butanal (>99%, Merck) and of the solvent (ethanol), the autoclave was flushed with nitrogen to remove the atmospheric oxygen. Ammonia was then added from the liquid ammonia cylinder at room temperature. Then the autoclave was placed in a thermostat bath preset to the reaction temperature. Adding hydrogen and completing fast to the working pressure occurred only after the preformed imine solution reached the desired reaction temperature (t = 0 is set for the time when the final pressure was established).

The progress of reaction in time was evaluated from the hydrogen consumption by measuring the hydrogen flow with a flow meter (BROOKS) having the pressure inside the autoclave controlled by a pressure regulator (BROOKS). Liquid sampling was used for monitoring the evolution of products in time.

The reactions were conducted mostly at 50 bar and at 50 and 80 ºC. The products were analyzed by using a Hewlett Packard 5890A gas chromatograph equipped with a DB Wax 1701 column and FID detector. Pure butylamine dibutylamine and tributylamine were used for the identification of the main products in the reaction mixtures. GC/MS analyses were performed in order to identify reaction intermediates. The metal leaching was followed by XRF analysis of the filtered reaction mixtures. Rhodium was found not to dissolve during one catalytic cycle at a detection limit of 0.002%.

Experiments were done in order to find whether mass transfer rate limitations occurred or not for the highly active catalysts. According to results obtained, mass transfer limitations of hydrogen diffusion from liquid to solid did not influence the measured reaction rates.

RESULTS AND DISCUSSION

Graphite and charcoal were chosen as catalyst support as it was expected that these materials will have little effect on the reacting carbonyl compound or intermediates in contrast to oxide supports (basic or acidic) that could induce unwanted and very different transformations of the substrate.

In the product mixture resulted during the reductive amination of butanal with ammonia and hydrogen over supported noble metal catalysts butylamine, dibutylamine and tributylamine were identified. According to the obtained analysis results, the reactions occurring in the reactor under the working conditions used (V_{EtOH} = 8 cm^3, $n_{Butanal}$ = 0.0222 mol (2 cm^3), n_{NH3} = 0.3235 mol, $n_{NH3}/n_{Butanal}$ = 14.57, $V_{EtOH}/V_{Butanal}$ = 4, p = 50 bar, T = 323-353 K) are given in Scheme 1.

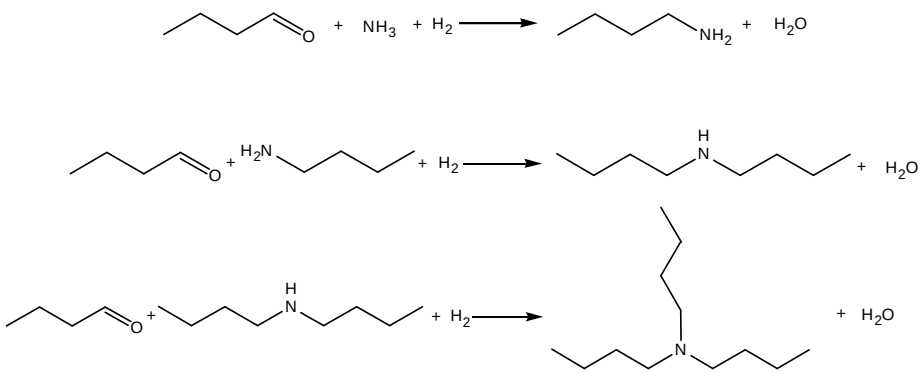

Scheme 1. Main chemical reactions during the reductive amination of Butanal.

The hydrogen consumption (normalized to moles of metal in the catalysts) indicates that Pt and Rh are the most active metals (Fig.1).

The very high activity of 5%Rh/charcoal relative to 5%Rh/HSA graphite (HSA = high surface area) can be attributed to the high surface area of the charcoal support, which resulted in a higher metal dispersion. The increased activity of 5%Pt/HSA graphite versus 5%Pt/LSA graphite can be attributed to the higher metal dispersion of the 5%Pt/HSA graphite catalyst.

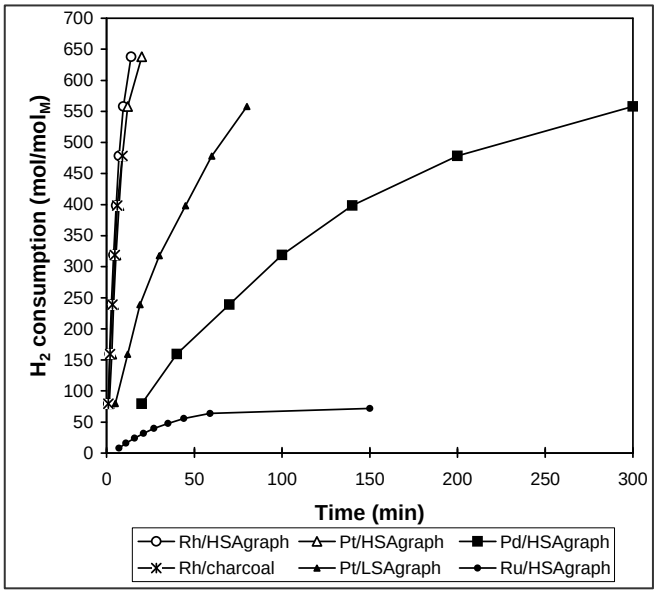

Fig. 1. Hydrogen consumption normalized to moles of metal as a function of reaction time for the reductive amination of butanal over carbon supported noble metal catalysts (n_M: moles of metal, $n_M = 2.22 \cdot 10^{-5}$ mol, $n_{Ru} = 2.22 \cdot 10^{-4}$ mol, $n_{Butanal} = 0.0222$ mol, $n_{NH3} = 0.3235$ mol, $n_{NH3}/n_{Butanal} = 14.57$, p = 50 bar, T = 353 K).

Fig. 2 illustrates the final yields of the corresponding amines over the catalysts tested.

The less active 5%Ru/HSA graphite showed the highest selectivity towards butylamine followed by 5%Rh/charcoal and 5%Rh/HSA graphite. 5%Pt/LSA graphite (LSA = low surface area) and 5%Pt/HSA graphite directed the reductive amination of butanal mostly to dibutylamine. 5%Pd/HAS graphite and 5% Pd/charcoal were the least selective catalysts, yielding primary, secondary, and tertiary amines at almost the same level (see Fig 2). As for platinum and palladium catalysts, the selectivity observed for the two Rh based catalysts was also almost the same, allowing us to conclude that the selectivity during reductive amination of butanal is mostly metal dependent, and is little influenced by the support.

Fig. 3 indicates the rates of formation (TOFs, global rates normalized to moles of metal) of butylamine, dibutylamine, and tributylamine over the tested catalysts. The rate over 5%Rh/charcoal was ~3-4 times higher than over 5%Rh/HSA graphite and 5%Pt/HSA graphite, ~5-6 times higher than over 5%Pt/LSA graphite and Pd/charcoal, ~40 times higher than over 5%Pd/HSA graphite, and about 75 times higher than over 5%Ru/HSA graphite. The highly selective ruthenium based

catalyst had the lowest activity. As observed in case of hydrogen consumption with reaction time, the rates of the product formation were also strongly correlated to the BET area and the metal dispersion of the catalysts.

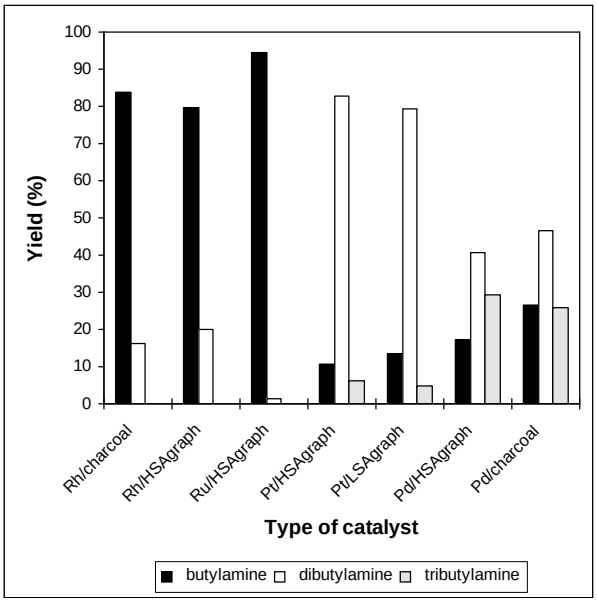

Fig. 2. Final yields of the corresponding amines for the reductive amination of butanal over carbon supported noble metal catalysts (n_M: moles of metal, $n_M = 2.22 \cdot 10^{-5}$ mol, $n_{Ru} = 2.22 \cdot 10^{-4}$ mol, V_{EtOH} = 8 cm^3, $n_{Butanal} = 0.0222$ mol, $n_{NH3} = 0.3235$ mol, $n_{NH3}/n_{Butanal} = 14.57$, p = 50 bar, T = 353 K).

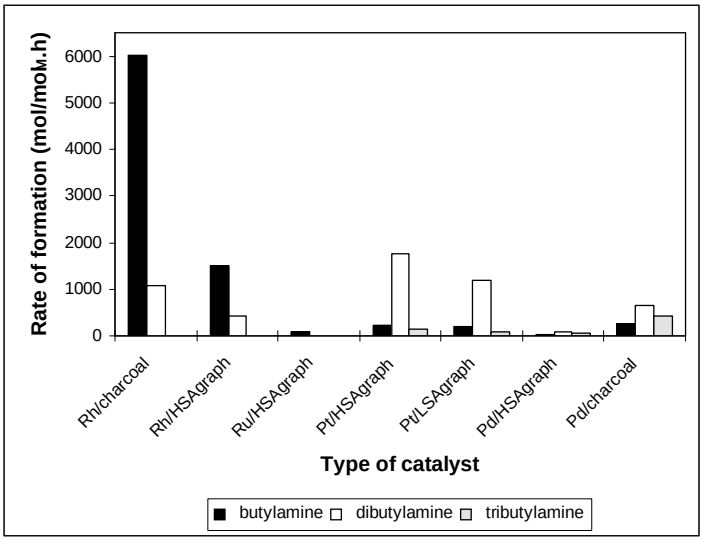

Fig. 3. Rates of formation of the butylamine, dibutylamine and tributylamine during reductive amination of butanal on carbon supported noble metal catalysts (n_M: moles of metal, $n_M = 2.22 \cdot 10^{-5}$ mol, n_{Ru} = $2.22 \cdot 10^{-4}$ mol, $n_{Butanal} = 0.0222$ mol, $n_{NH3} = 0.3235$ mol, $n_{NH3}/n_{Butanal} = 14.57$, p = 50 bar, T = 353 K).

The reductive amination of butanal strongly depends upon the noble metal used in the catalyst (see Figs. 1-3). Among the catalysts investigated, Rh and Pt based showed the highest activity. The Ru based catalyst had the lowest activity, but the highest selectivity for butylamine. Tributylamine was detected only during reductive amination of butanal over supported Pt and Pd catalysts underlining that selectivity is metal dependent.

Charcoal appears to be a good support providing high activity and selectivity for the supported Rh catalyst and leads to significantly more active catalysts than graphite (see Figs. 1 and 3). In case of Pd, the charcoal supported catalyst was also more active than the graphite supported one (see Fig. 3). This shows that the nature of the carbon support influences the catalytic properties. It is noteworthy that the metal dispersion of the charcoal supported Pd catalyst is almost twice as high (see Table 1) than of Pd/HSA graphite. The reaction rate measured for the same type of metal seems to strongly depend on the metal dispersion of the catalysts (see Table 1 and Fig. 3 for Rh, Pd and Pt catalysts). In contrast, the selectivities for the two rhodium (two palladium or two platinum) catalysts on charcoal and graphite, respectively, are very close (see Fig. 2). The support, thus, influences only the activity and not the selectivity, having an important role in the stabilization of the metal dispersion.

More detailed studies were focused on 5%Rh/HSA graphite catalyst. Fig. 4 shows the yields for the reductive amination of butanal at 353 K and 50 bar total pressure (~ 28 bar hydrogen pressure) over 5%Rh/HSA graphite catalyst as a function of reaction time.

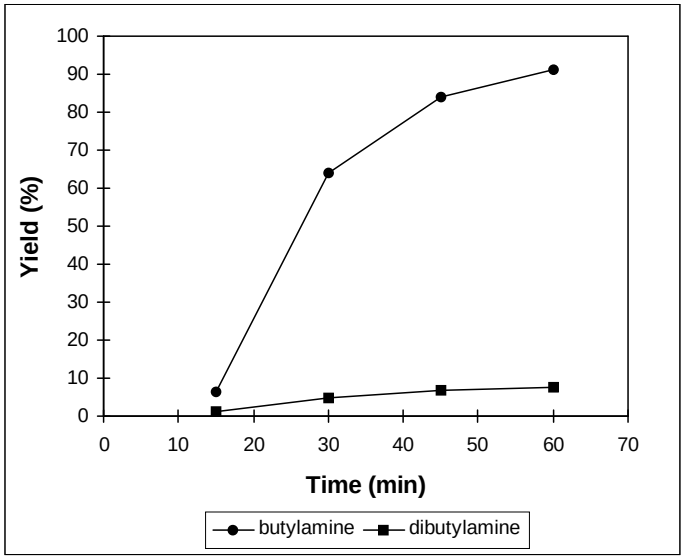

Fig. 4. Yields of butyl- and dibutylamine versus reaction time on 5%Rh/HSA graphite catalyst ($n_{Rh} = 1.11 \cdot 10^{-5}$ mol, $n_{Butanal} = 0.0222$ mol, $n_{NH3} = 0.3235$ mol, $n_{NH3}/n_{Butanal} = 14.57$, p = 50 bar, T = 353 K).

Concerning the products, the reaction seems to have an induction period (see Fig.4), which is not reflected in the hydrogen consumption (being quite fast at the beginning of the reaction). The yield of dibutylamine followed a slow (almost linear) increase with time, while the yield of butylamine after a fast increase became almost parallel with the yield of secondary amine.

When the experiment was repeated at 323 K and 50 bar (~ 37 bar hydrogen pressure), the apparent induction period was longer and the selectivity to primary and secondary amine was different. The yields for the butylamine were lower, and for the dibutylamine higher, compared to those obtained at 353 K. For comparison, Fig. 5 illustrates the dependence of the selectivity in butylamine versus reaction time obtained on 5%Rh/HSA graphite at 323 K and 353 K.

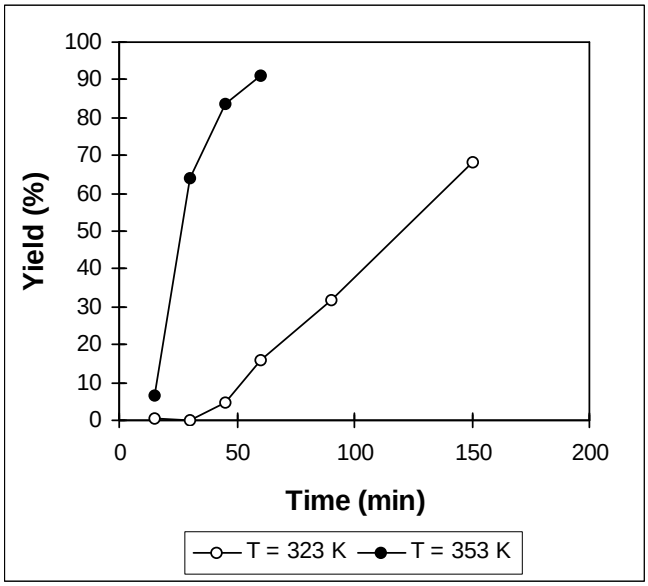

Fig. 5. Selectivity towards butylamine versus reaction time at 323 K and 353 K during the reductive amination of butanal over 5%Rh/HSA graphite catalyst ($n_{Rh} = 1.11 \cdot 10^{-5}$ mol, $n_{Butanal} = 0.0222$ mol, $n_{NH3} = 0.3235$ mol, $n_{NH3}/n_{Butanal} = 14.57$, p = 50 bar).

The evolution of the amines during the reaction over 5%Rh/HSA graphite catalyst (Fig. 4) indicates that butylamine and dibutylamine apparently are primary products. The secondary amine is formed in parallel with the primary amine and the primary amine is not consumed at higher conversions or reaction times. This suggests that butylamine and dibutylamine are formed from the same intermediate.

From the data obtained in this study it is striking to note that metals that are good hydrogenolysis catalysts, such as Rh and Ru [17,18], are selective for producing butylamine, while catalysts that are good hydrogenation catalysts, such as Pt and Pd [17,18], catalyze the preferential formation of dibutyl- and tributylamine.

CONCLUSIONS

Among the studied carbon supported catalysts the Rh and Pt based ones show the highest activity in the reductive amination of butanal. The Ru based catalysts had the lowest activity, but the highest selectivity for the primary amine. Tertiary amine was detected only in the product mixtures obtained over Pt and Pd catalysts. This observation underlines the major role of metal in determining the activity and selectivity of the supported catalysts.

Charcoal appears to be a good catalyst support providing high activity and selectivity for the supported Rh catalyst being significantly more active compared to Rh/graphite. This emphasizes the important role of the support materials. The support seems to influence the activity, but not the selectivity of the catalyst. The BET area and especially the metal dispersion have a strong influence on the catalyst activity for the reductive amination of butanal

Rhodium was found not to dissolve from 5% Rh/charcoal and 5%Rh/HSA graphite catalysts during one catalytic cycle.

Good hydrogenolysis catalysts such Ru and Rh tend to produce mostly primary amine, while metals that have high hydrogenation capacity (Pt and Pd) tend to yield mostly secondary and tertiary amines.

ACKNOWLEDGEMENT

Financial support from the DSM company is greatly appreciated.

REFERENCES

1. J. Bódis, and J.A. Lercher, Studia-Chemia, Studia-Chem., 2002, **47**, 169.
2. S. Yada, Y. Takagi and M. Hiyamizu, Nippon Kagaku Kaishi, 1995, (2), 107.
3. M. Freifelder, W.D. Smart and G.R. Stone, J. Org. Chem., 1962, **27**, (6), 2209.
4. K.A. Pollart and R.E. Miller, J. Org Chem., 1962, **27**, (7), 2392.
5. A.L. Bris, G. Lefebre and F. Coussemant, Bull. Soc. Chim. France, 1964, **6**, 1374.
6. A.L. Bris, G. Lefebre and F. Coussemant, Bull. Soc. Chim. France, 1964, **7**, 1584.
7. A.L. Bris, G. Lefebre and F. Coussemant, Bull. Soc. Chim. France, 1964, **7**, 1594.
8. R.W. White, S.W. King and J.L. O'Brien, Tetrahedron Lett., 1971, **39**, 3591.
9. M.V. Klyuev and M.L. Khidekel, Russ. Chem. Rev., 1980, **49**, (1), 542.
10. P.L. Mills, D.E. Willis and R.L. Fenton, Ind. Eng. Chem. Res., 1988, **27**, (7), 1121.
11. S. Yada and Y. Takagi, Nippon Kagaku Kaishi, 1991, (1), 20.
12. F.S. Dovell and H. Greenfield, J. Org. Chem., 1964, **29**, (5), 1265.
13. F.S. Dovell and H. Greenfield, J. Am. Chem. Soc., 1965, **87**, (12), 2767.
14. H. Greenfield and F.S.Dovell, J. Org. Chem., 1966, **31**, (9), 3053.
15. J. Bódis and J.A. Lercher, Confidential Reports to DSM Company, (1997-1998).
16. J.J.F. Scholten, A.P. Pijpers and A.M.L. Hustings, Catal. Rev.-Sci. Eng., 1985, **27**, (1) 151.
17. G.C. Bond, Catalysis by Metals, Academic Press, London and New York, 1962.
18. P.N. Rylander, Catalytic Hydrogenation over Platinum Metals, Academic Press, New York and London, 1967.

STUDIA UNIVERSITATIS BABEŞ-BOLYAI, CHEMIA, XLIX, 2, 2004

Dedicated to Professor Valer Fărcăşan
at his 85th anniversary

HYDANTOIN DERIVATIVES HPLC-RT LIPOPHILICITIES: A QSPR STUDY

OLEG URSU[a], MIRCEA V. DIUDEA[b]

[a,b] *Faculty of Chemistry and Chemical Engineering*
Babes-Bolyai University, 400028 Cluj, Romania

ABSTRACT. A quantitative structure-property relationship QSPR investigation was performed on the lipophilicities of a number of hydantoin derivates as measured RT-HPLC retention times provided by Scholl et al[1]. The lipophilicities (S) were correlated with a series of graph theoretical, geometrical, and electronic descriptors provided by TOPOCLUJ 3.0 software package from PM3-optimized geometry. In second step these descriptors were incorporated into the descriptor matrix to build several QSPRs in view of obtaining prediction models for lipophilicity.

INTRODUCTION

Hydantoins find important applications as medicines (e.g., as anticonvulsant drugs in treatment of epilepsy) and as agrochemicals. Lipophilicity represents the affinity of a molecule or a moiety for a lipophilic environment. It is commonly measured by its distribution behavior in a biphasic system, either liquid-liquid (e.g., partition coefficient in 1-octanol/water) or solid-liquid (retention on reversed-phase high-performance liquid chromatography (RT-HPLC) or thin-layer chromatography (TLC) system). Lipophilicity plays a vital role in physicochemical, environmental, and biological, processes as it determines the transport phenomena in vivo such as through cell membrane barrier. With the advent of inexpensive and rapid computation, there has a remarkable growth interest in the field of quantitative structure-property relationships QSPR and use of multivariate linear regression and latent variables methods to model relevant properties as a function of molecular structural parameters (*i. e*., molecular descriptors).

DATA ACQUISITION

Data set. The series of hydantoin HPLC-RT (Table 1) reported by Scholl et al[1] was used in this QSPR study; lipophilicities could be expressed as partition coefficient in 1-octanol/water *logP* biphasic system, but lipophilicities derived from HPLC-RT are preferred due to the following advantages: analytical procedure, easy use of mixtures, and absence of incertitude in determination of concentration.

Derivation of descriptors. The structures of all the hydantoins (Figure 1) were drawn with HYPERCHEM molecular modeling software package.[2] After preoptimization using Molecular Mechanics (MM+, HYPERCHEM), the geometries of these compounds were further optimized using the semiempirical PM3 parameterization of the HYPERCHEM. The resulting output files containing the refined geometry represent the input for the TOPOCLUJ to calculate the molecular

descriptors. This provided a number of electronic, topological, and geometrical descriptors, used in building the descriptors matrix with dimensions 635 x 73. It was subsequently employed for correlating the lipophilicity values of the hydantoins.

TABLE 1.

HPLC-RT Lipophilicity (S) Data of Substituted Hydantoins

No.	S	No.	S	No.	S
1		26	-0.197	51	-0.147
2	-0.157	27	-0.183	52	-0.170
3	-0.157	28	-0.222	53	-0.191
4	-0.174	29	-0.224	54	-0.165
5	-0.180	30	-0.233	55	-0.174
6	-0.144	31	-0.202	56	-0.184
7	-0.142	32	-0.190	57	-0.174
8	-0.145	33	-0.173	58	-0.182
9	-0.141	34	-0.210	59	-0.193
10	-0.186	35	-0.164	60	-0.191
11	-0.157	36	-0.200	61	-0.190
12	-0.168	37	-0.210	62	-0.225
13	-0.211	38	-0.191	63	-0.233
14	-0.209	39	-0.197	64	-0.211
15	-0.227	40	-0.222	65	-0.208
16	-0.193	41	-0.209	66	-0.197
17	-0.178	42	-0.260	67	-0.236
18	-0.190	43		68	-0.216
19	-0.231	44	-0.221	69	-0.219
20	-0.193	45	-0.208	70	-0.210
21	-0.210	46	-0.229	71	-0.240
22	-0.192	47	-0.176	72	-0.196
23	-0.213	48	-0.157	73	-0.248
24	-0.187	49	-0.157	74	-0.207
25	-0.209	50	-0.199	75	-0.206

Molecular structure of the compounds is presented in Figure 1.

A large variety of descriptors have been used: electronic (VEA, VRA, VED, VRD indices[2]) geometrical (3D-Wiener index[3]), and topological Wiener[4]

$$W = (1/2) \sum_i \sum_j [\mathbf{D}]_{ij} \quad (1)$$

where $[D]_{ij}$ denote the entries in the distance matrix D which are just the just the topological distances d_{ij} between *i* and *j*.

The Cluj indices are calculated[5.] as half-sum of the entries in a Cluj symmetric matrix, **M**, (**M = CJD, CJΔ, CFD, CFΔ**), defined as follows:

$$[\mathbf{UM}]_{ij} = \max_{k=1,2,\ldots} \left| V_{i,j,p_k} \right| \quad (2)$$

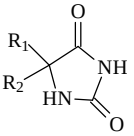

No.	R_1	R_2	No.	R_1	R_2	No.	R_1	R_2
1	H	Me	18	Ph	EtOOC	35	Et	3-ClC_6H_4
2	H	Ph	19	Ph	Ph	36	Me	4-ClC_6H_4
3	H	$PhCH_2$	20	Ph	$PhCH_2$	37	Et	4-ClC_6H_4
4	H	$PhCH_2CH_2$	21	Et	4-MeC_6H_4	38	^{n}Pr	4-ClC_6H_4
5	H	$^{c}C_6H_{11}CH_2CH_2$	22	^{n}Pr	4-MeC_6H_4	39	^{i}Pr	4-ClC_6H_4
6	Me	^{c}Pr	23	^{n}Bu	4-MeC_6H_4	40	^{n}Bu	4-ClC_6H_4
7	Me	^{i}Pr	24	^{i}Pr	4-MeC_6H_4	41	$(CH_3)CHCH_2$	4-ClC_6H_4
8	Me	$(CH_3)CHCH_2$	25	$(CH_3)CHCH_2$	4-MeC_6H_4	42	$^{n}C_7H_{15}$	4-ClC_6H_4
9	Me	^{t}Bu	26	Me	4-$^{t}BuC_6H_4$	43	$HOOCCH_2$	4-ClC_6H_4
10	Me	$(CH_3)CH(CH_2)_2$	27	Et	4-$MeOC_6H_4$	44	$MeOOCCH_2$	4-ClC_6H_4
11	Ph	Me	28	^{i}Pr	4-$MeOC_6H_4$	45	Me	4-BrC_6H_4
12	Ph	Et	29	$(CH_3)CHCH_2$	4-$MeOC_6H_4$	46	^{n}Bu	4-BrC_6H_4
13	Ph	^{n}Pr	30	^{n}Bu	4-$MeOC_6H_4$	47	Et	4-O_2NC6H4
14	Ph	^{i}Pr	31	^{n}Pr	4-$MeOC_6H_4$	48	Me	2-thienyl
15	Ph	^{n}Bu	32	Et	4-FC_6H_4	49	Me	2-furanyl
16	Ph	$^{c}C_6H_{11}$	33	Et	2-FC_6H_4	50	Me	2-benzofuranyl
17	Ph	MeOOC	34	Et	3-ClC_6H_4			

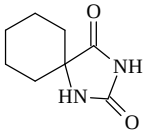

51

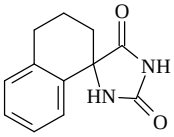

52

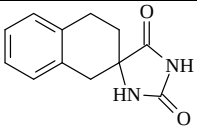

53

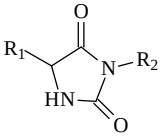

No.	R_1	R_2
54	$PhCH_2$	Me
55	Me	$PhCH_2$
56	$PhCH_2$	$PhCH_2$

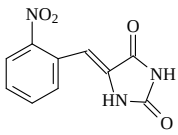

57

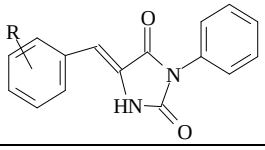

No.	R	No.	R	No.	R
58	H	64	2-Cl	70	4-Br
59	2-Me	65	3-Cl	71	4-F_3C
60	3-Me	66	2,6-Cl	72	2-MeO
61	4-Me	67	2,4-Cl	73	4-$PhCH_2O$
62	2,4,6-Me	68	2-Br	74	4-MeS
63	4-^{i}Pr	69	3-Br	75	4-NC

Figure 1. Structures of Hydantoins

$$V_{i,j,p_k} = \{v \mid v \in V(G); d_{iv} < d_{jv};\ \ (i,v)_h \cap p_k = \{i\};\ p_k \in D(G) \text{ or } \Delta(G)\};\ h,k = 1,2,... \quad (3)$$

$$IE(M) = (1/2)\sum_i \sum_j [\mathbf{M}]_{ij}[\mathbf{A}]_{ij} \quad (4)$$

$$IP(M) = (1/2)\sum_i \sum_j [\mathbf{M}]_{ij} \quad (5)$$

or from an asymmetric Cluj matrix, by

$$IE2(UM) = (1/2)\sum_i \sum_j [\mathbf{UM}]_{ij}[\mathbf{UM}]_{ji}[\mathbf{A}]_{ij} \quad (6)$$

$$IP2(UM) = (1/2)\sum_i \sum_j [\mathbf{UM}]_{ij}[\mathbf{UM}]_{ji} \quad (7)$$

In the above, *D*(*G*) and Δ(*G*) represents the distance and detour sets in *G*.

The number defined on edge, *IE*, is an *index* while the number defined on path, *IP* is a *hyper-index*. Note that the operators IE and IP, as well as $IE2$ and $IP2$ may be applied to both symmetric and asymmetric matrices. When the last two operators are calculated on a symmetric matrix, the terms of sum represent squared entries in that matrix.

Randic[7] and DSI[6] index use the relation (8) to describe features of molecules.

$$\chi = \sum_{(i,j)\in E(G)} (\delta_i \delta_j)^{-1/2} \quad (8)$$

where δ_i and δ_j represent the corresponding vertex degrees. In analogy to Randic index was defined the DSI index by using group electronegativity valences EVG_i:

$$DS_{\boldsymbol{i}} = \sum_{j:(i,j)\in E(G)} (EVG_i EGV_j)^{-1/2} \quad (9)$$

$$DS = \sum_i DS_{\boldsymbol{i}} \quad (10)$$

For the definition of other indices see.[5,8]

REGRESSION ANALYSIS

The quantitative relationship between calculated descriptors and property is a difficult task due to large number of descriptors, and there is no guarantee that the best subset is found. There is the possibility to eliminate descriptors irrelevant to property of interest by stepwise regression eventually followed by more sophisticated statistical methods analysis like PLS, CoMFA.

PLS is a projection method in which the data matrix represented as a set of n points in an m-dimensional space is projected on to a k-dimensional hyperplane, in such way that the coordinates of the projection are good predictors of some *y* property. PLS allows the simultaneous use of strongly intercorrelated x-descriptors by focusing the systematic covariances in the X block in a few latent variables.

In this work we use the following methodology: (a) divide the initial set by property values in 4 subsets and one external prediction set; (b) autoscaling descriptors matrix; (c) PLS with Leave one out (LOO) (MATLAB[8] and PLS toolbox[9]) modeling of 4 subsets of data; the number of factors is determined by improvement of percent variance captured by model (PRESS), and additional factor is taken at each 2% improvement of PRESS; (d) model validation with external prediction set.

The regression analysis summary and best PLS models are presented in Table 2 and Figure 2.

TABLE 2

Correlations of Lipophilicities of Hydantoins by PLS method

Subset	R^2	RMSECV	Percent cumulative variance	No. of LVs	Lipophilicity interval	Compounds in the model
A	0,984	0,0010843	98,42	4	-(0,14-0,17)	7,8,51,49,3,2,11,35, 54,52
B	0,985	0,001969	98,54	9	-(0,17-0,20)	33,57,55,4,47,17,5,27, 10,32,18,60,53,22,59 16,72,66,39,26,50,36
C	0,982	0,00094949	98,22	10	-(0,20-0,23)	31,75,65,45,25,14,70,3 7,64,13,23,44,40,28,46
D	0,998	0,00048575	99,79	4	-(0,23-0,26)	19,63,30,67,73,42

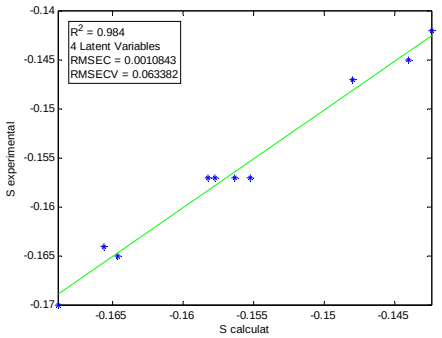

Subset A

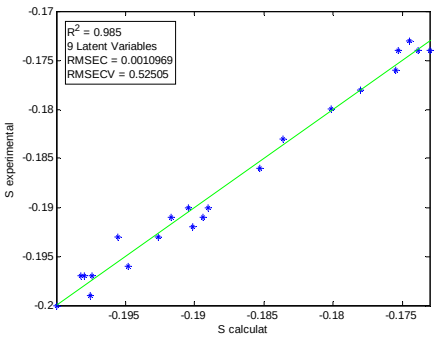

Subset B

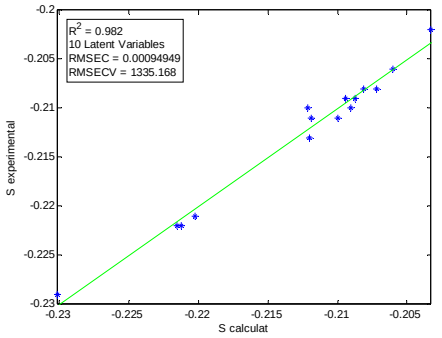

Subset C

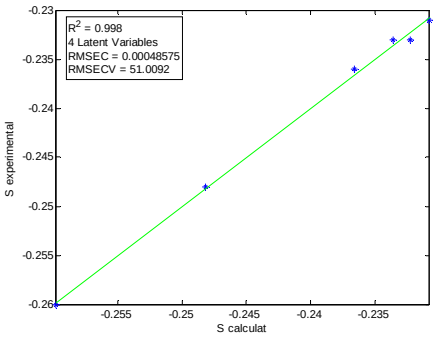

Subset D

Figure 2. Best PLS models for chosen Hydantoins subsets

Validation of the PLS models. For each compound from external prediction subset, the PLS model for lipophilicity was chosen according to property value. The prediction summary and graph is presented in Table 3 and Figure 3.

TABLE 3.

Experimental and predicted lipophilicities for testing model robustness.

No.	*S* Experimental	*S* Calculated	RES	R^2	F
71	-0.240	-0.230	0.0021	0.9059	163.6176
15	-0.227	-0.212	0.0091		
62*	**-0.225**	**-1.358**	-		
29	-0.224	-0.203	0.0163		
69	-0.219	-0.213	0.0012		
68	-0.216	-0.222	-0.0103		
21	-0.210	-0.207	0.0000		
34	-0.210	-0.210	-0.0029		
41	-0.209	-0.217	-0.0105		
74	-0.207	-0.203	0.0016		
20	-0.193	-0.199	-0.0064		
38	-0.191	-0.186	0.0049		
61	-0.190	-0.192	-0.0023		
24	-0.187	-0.194	-0.0066		
56	-0.184	-0.188	-0.0034		
58	-0.182	-0.197	-0.0140		
12	-0.168	-0.161	0.0097		
48	-0.157	-0.157	0.0050		
6	-0.144	-0.146	0.0048		
9	-0.141	-0.146	0.0015		

*Excluded from validation subset

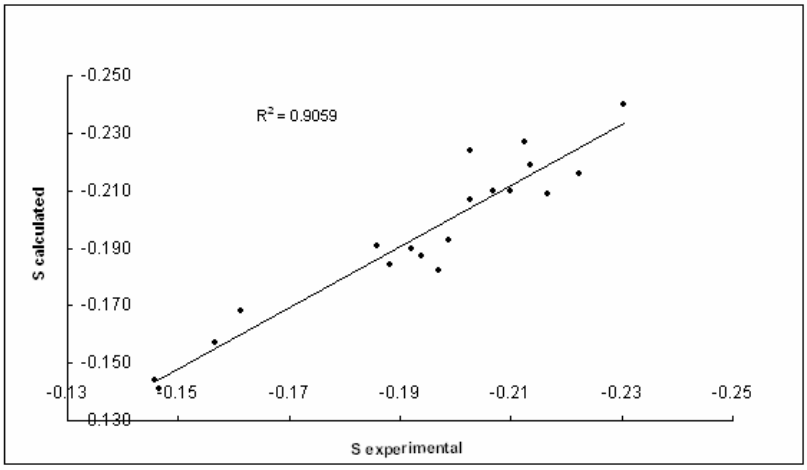

Figure 3. Plot of calculated vs experimental lipophilicities

CONCLUSIONS

This study provided improved correlations (R^2=0.9059) of the lipophilicity data of hydantoins by using TOPOCLUJ descriptors. Recall that the best literature result was R^2=0.829[10]. This study is useful in clustering and diagnosis of hydantoin compounds. For predicting new structures with desired lipophilicity, similarity studies are in progress in our laboratory.

REFERENCES

[1] Scholl, S.; Koch, A.; Henning, D.; Kempter, G.; Kleinpeter, The influence of structure and lipophilicity of hydantoin derivatives on anticonvulsant activity**,** E. Struct. Chem. 1999, **10**, 355-366

[2] Alexandru T. Balaban, Dan Ciubotariu, and Mihai Medeleanu, Topological indices and real number vertex invariants based on graph eigenvalues or eigenvectors, J. Chem. Inf. and Comput. Sci. 1992, **31**, 4, 517-523

[3] Bogdanov, B.; Nikolić, S.; Trinajstić, N. On the Three-Dimensional Wiener Number, *J. Math. Chem*. 1989, **3**, 299-309.

[4] Wiener, H., Structural determination of paraffin boiling points. J. Am. Chem. Soc. 1947, **69**, 17-20

[5] Lorentz Jantschi, Gabriel Katona and Mircea V. Diudea, Modeling Molecular Properties by Cluj Indices, MACH **41**, 2000, 151-188

[6] Mircea V. Diudea, Ivan Gutman, Jantschi Lorentz, Molecular topology, Nova Science Publishers, New-York, 2002.

[7] Randić, M. Characterization of molecular branching, J. Am. Chem. Soc. 1975, **97**, 6609-6615.

[8] Matlab 6.5.1, Mathworks Inc., www.mathworks.com

[9] PLS Toolbox 3.0 Eigenvector Research Inc., www.eigenvector.com

[10] Alan R. Katritzky, Subbu Perumal, Ruslan Petrukhin, and Erich Kleinpeter, CODESSA-Based Theoretical QSPR Model for Hydantoin HPLC-RT Lipophilicities, J. Chem. Inf. and Comput. Sci. 2001, **41**, 3, 569-574

STUDIA UNIVERSITATIS BABEŞ-BOLYAI, CHEMIA, XLIX, 2, 2004

Dedicated to Professor Valer Fărcăşan at his 85th anniversary

TOPOLOGICAL DESCRIPTORS IN WEIGHTED MOLECULAR GRAPHS, APPLICATIONS IN QSPR MODELING

OLEG URSU[a], MIRCEA V. DIUDEA[b]

[a,b] *Faculty of Chemistry and Chemical Engineering*
Babes-Bolyai University, 400028 Cluj, Romania

ABSTRACT. Organic compounds containing heteroatoms or multiple bonds can be represented as vertex weighted and edge weighted molecular graphs. Different types of weighting schemes can be applied by computing parameter set containing each type of heteroatom. Topological descriptors derived from such weighting schemes are used to develop quantitative structure – property relationship (QSPR) models (property being the molar refraction) for a mixed set of alcohols, amines, and organic halides.

INTRODUCTION

Among a large variety of topological descriptors used today, many of them are defined only for simple graphs, representing eventually alkanes and cycloalkanes, ideal classes of compounds for investigating the molecular connectivity, size, branching, cyclicity, and shape on the variation of molecular properties. However, most of the organic compounds of interest are functional derivatives containing heteroatoms and/or multiple bonds. Usually, such a compound can be represented as a weighted molecular graph. Early applications of weighted molecular graphs are connected with computation of polynomials and spectra of heteroconjugated compounds. Several particular methods of computing topological descriptors from molecular graphs containing heteroatoms and/or multiple bonds were proposed: *Kier* and *Hall*[1] electrotopological state descriptors, *EATI* super-indices[2], Sanderson electronegativity valences (*SEV*)[3], walk matrix and walk operator derived descriptors[4,5]. In this study we discuss the use of following weighting schemes: formal charge, Sanderson electronegativity and covalent radius, within walk matrix and walk operator to provide weighted molecular descriptors for a QSPR study.

WEIGHTING SCHEMES, MOLECULAR MATRICES AND STRUCTURAL DESCRIPTORS

Sanderson electronegativity valences. *Diudea* and *Silaghi*[3] have proposed group electronegativity valences denoted *SEV* and defined by:

$$SEG_i = \left(SEA_i \cdot SEH^{\,hi}\right)^{1/(1+hi)} \quad (1)$$

$$SEV_i = \left(SEG_i\right)^{1/(1+v_i)} \quad (2)$$

SEA and *SEH* denote the Sanderson electronegativity for the atom *i* and hydrogen respectively, the number of hydrogen atoms attached to the group *i* is denoted by h_i while v_i stands for the degree of *i*. In the case of multiple bonds $v_i = \sum_j b_{ij}$ where b_{ij} is the conventional bond order for the bonds around *i*. Note that group electronegativities obey the electronegativity equalizing principle within the group and per molecule. The *SEV* values are used further in the construction of the *DS* index which showed good correlation with several physicochemical properties.

^{e}W$_M$ matrix. In its general form, the walk degree can be defined as:

$$^{e}w_{i} = \sum_{j} [\mathbf{M}^{e}]_{ij} \tag{3}$$

The raising at a power *e*, of a square matrix **M**, can be eluded by applying the algorithm of Diudea, Topan and Graovac.[4] It evaluates a (topological) property of a vertex *i*, by iterative summation of the first neighbors contributions. The algorithm, called **^{e}W$_M$** , is defined as:

$$\mathbf{M} + \mathbf{P} = {}^{0}\mathbf{W}_{M} \tag{4}$$

$$[{}^{e+1}\mathbf{W}_{M}]_{ii} = \sum_{j} ([\mathbf{M}]_{ij} [{}^{e}\mathbf{W}_{M}]_{jj}) \tag{5}$$

$$[{}^{e+1}\mathbf{W}_{M}]_{ij} = [{}^{e}\mathbf{W}_{M}]_{ij} = [\mathbf{M}]_{ij} \tag{6}$$

where **^{e}W$_M$** is the matrix of walk degrees. The diagonal elements, $[{}^{e}\mathbf{W}_{M}]_{ii}$ equal the row sum RS_i of $\mathbf{M}^e$, or in other words, they are *walk degrees,* **^{e}w$_{M,i}$** (weighted with the property collected by the vertex property **P** diagonal matrix):[5]

$$[{}^{e}\mathbf{W}_{M}]_{ii} = \sum_{j} [\mathbf{M}^{e}]_{ij} = {}^{e}w_{M,i} \tag{7}$$

The half sum of the local invariants **^{e}w$_{M,i}$**, in a graph, defines a global invariant, called the *walk number*, **^{e}W$_M$**:

$$^{e}W_{M} = {}^{e}W_{M}(G) = \frac{1}{2}\sum_{i} {}^{e}W_{M,i} \tag{8}$$

When **M = A; C**, the quantity **^{e}W$_M$** (or simply **^{e}W**) represents the so called *molecular walk count*; when **M = D**, (*i.e*., the distance matrix) then **^{e}W$_M$** is the Wiener number of rank *e*.

Within *TOPOCLUJ* program[6] the formal charges are calculated as:

$$ch_{i,j} = \log\left[(SEG_j / SEG_i)^{1/(d_{i,j})^2} \right] \tag{9}$$

$$ch_i = \sum_j ch_{i,j}$$

In the above relations, the log function provides the sign for the formal charge ch_{ij}, viewed as a distance decreasing perturbation of SEG_i produced by the atom *j* (see the exponent, d_{ij} being the Euclidean distance separating atoms *i* and *j*).

An *N*×*N* array collecting the entries ch_{ij} is called the charge matrix **CH**, whose row sums ch_i represent the total partial charge on hydride group/atom *i* in the molecule. This matrix can be processed by our program in various weighting schemes.

METHOD

Data input. All structures were sketched and optimized using *PM3* semiempirical parameterization with *HYPERCHEM* molecular modeling software package.[7] Molar refraction data reported by Diudea and Silaghi[3], and optimized geometries for the three sets of organic derivatives (see Tables 1, 2, 3) represent the input for molecular descriptors generation by *TOPOCLUJ* software package. The molecular descriptors thus generated are used as input for statistical analysis.

Statistical analysis. All three data sets were analyzed using simple linear regression, in STATISTICAL TOOLBOX, MATLAB.[8] The best models, showing excellent correlation with the chosen property (see eqs. 10-12) were validated by *LOO* (*Leave one Out*) method. Data are presented as follows: Tables 1 to 3 list the sets of compounds, the values for the experimental property, calculated property by the best estimation model (given in the QSPR eqs. Below each table) and the predicted property by *LOO*.

TABLE 1

Molar refractions of halogen derivatives

No.	Compound	Molar refraction		Predicted values
		Exp	Calc	by LOO
1	1-chloropropane	20.847	22.248	22.570
2	1-choloro-2-methypropane	33.940	31.628	31.462
3	3-cholorpentane	38.354	37.383	37.274
4	2-brompropane	38.314	37.485	37.390
5	1-brompropane	38.264	37.281	37.171
6	2-brombutane	42.891	43.024	43.062
7	1-bromo-2-methylpropane	47.610	48.794	49.611
8	1-brombutane	25.360	26.119	26.215
9	3-brompentane	30.161	30.809	30.858
10	2-iodobutane	23.935	22.599	22.308
11	3-iodopentane	23.679	24.129	24.206
12	2-iodopentane	28.651	28.405	28.383
13	1-iodopentane	28.537	27.897	27.834
14	1-iodohexane	28.347	29.975	30.103
15	1-iodoheptane	33.068	34.186	34.270

$$MR = 5.588 - 36.584 \cdot {}^{1}W_{[AD]}[CH] \quad (10)$$

R^2=0.977; n = 15; *s* = 1.199; *F* = 564.062; R^2_{pred} = 9.969

TABLE 2

Molar refractions of amines

No.	Compound	Molar refraction		Predicted values
		Exp	Calc	after LOO
1	Trimethylamine	19.595	20.192	20.336
2	1-aminopropane	33.641	33.582	33.578
3	2-amino-2-methylpropane	33.816	34.025	34.037
4	1-aminobutane	33.794	34.025	34.038
5	1-amino-2,2-dimethylpropane	33.452	33.582	33.589
6	1-amino-3-methylbutane	33.290	33.139	33.131
7	3-aminopentane	38.281	38.636	38.672
8	Dipropylamine	38.038	37.750	37.724
9	1-aminopentane	38.003	37.750	37.727
10	Diisopropylamine	42.920	42.804	42.781
11	Butyldimethilamine	33.852	34.025	34.035
12	Triethylamine	19.401	19.305	19.279
13	Butylethylamine	47.783	47.858	47.891
14	1-aminohexane	24.257	23.917	23.871
15	Dimethylpentylamine	24.079	23.917	23.895
16	2-aminoheptane	28.471	28.528	28.531
17	1-aminoheptane	28.672	28.528	28.518
18	Diisobutylamine	28.617	28.528	28.522
19	Dimethylisobutylamine	33.515	33.582	33.585
20	Tripropylamine	28.728	28.528	28.514

$$MR = 5.030 + 1.803 \cdot {}^{1}W_{[AD]}[SEG] \quad (11)$$

R^2=0.999; n = 20; s = 0,241; F = 16842; R^2_{pred} = 0.998

TABLE 3

Molar refractions of alcohols

No.	Compound	Molar refraction		Predicted values
		Exp	Calc	after LOO
1	Isopropanol	17.705	17.488	17.447
2	^{n}Propanol	26.618	26.719	26.725
3	2-methyl-1-propanol	31.211	31.335	31.339
4	^{n}Butanol	31.183	31.335	31.340
5	2-methyl-2-butanol	31.351	31.335	31.334
6	2-pentanol	31.138	31.335	31.342
7	3-methyl-1-butanol	31.489	31.335	31.330
8	2-methyl-1-butanol	31.164	31.335	31.341
9	^{n}Pentanol	31.180	31.335	31.340
10	3-pentanol	31.429	31.335	31.332
11	2-methyl-3-pentanol	35.675	35.951	35.962
12	3-methyl-3-pentanol	17.529	17.488	17.480
13	4-methyl-2-pentanol	35.822	35.951	35.956
14	4-methyl-3-pentanol	35.931	35.951	35.951
15	4-methyl-1-pentanol	36.094	35.951	35.945
16	2-methyl-1-pentanol	40.899	40.566	40.542

No.	Compound	Molar refraction		Predicted values
		Exp	Calc	after LOO
17	2-ethyl-1-butanol	40.447	40.566	40.575
18	^{n}Hexanol	40.439	40.566	40.575
19	2,4-dimethyl-3-pentanol	40.737	40.566	40.554
20	3-ehtyl-3-pentanol	40.625	40.566	40.562
21	2-methyl-1-haxanol	40.638	40.566	40.561
22	^{n}Heptanol	45.521	45.182	45.136
23	2-methyl-2-heptanol	22.103	22.104	22.104
24	3-methyl-3-heptanol	45.207	45.182	45.178
25	4-methyl-4-heptanol	44.920	45.182	45.217
26	6-methyl-1-heptanol	22.067	22.104	22.108
27	2-ehtyl-1-hexanol	26.722	26.719	26.719
28	^{n}Octanol	26.680	26.719	26.722
29	2,6-dimethyl-4-heptanol	26.904	26.719	26.709
30	2-methyl-2-octanol	26.697	26.719	26.721
31	4-ethyl-4-heptanol	26.801	26.719	26.715

$$MR = 3.971 + 5.994 \cdot {}^{1}W_{[AD]}[CR] \tag{12}$$

R^2=0.999; n = 31; *s* = 0,16; *F* = 70162; R^2_{pred} = 0.999

Excellent results in simple linear regression, gave opportunity to test correlation ability of these descriptors in mixed sets of compounds. Thus we tried a global correlation model for all three above sets. The obtained model, with all three descriptors used before, has also shown a good correlation (see eq. 13), thus proving the weighting schemas and molecular descriptors are suitable and useful in QSPR studies. The calculated molar refractions by (13) were plotted against the experimental values (Fig. 1).

$$MR = 11.809 - 10.167 \cdot {}^{1}W_{[AD]}[CH] + 22.914 \cdot {}^{1}W_{[AD]}[CR] - 12.975\,{}^{1}W_{[AD]}[SEV]$$

R^2=0.987; *n*=66; *F*=1583.48 (13)

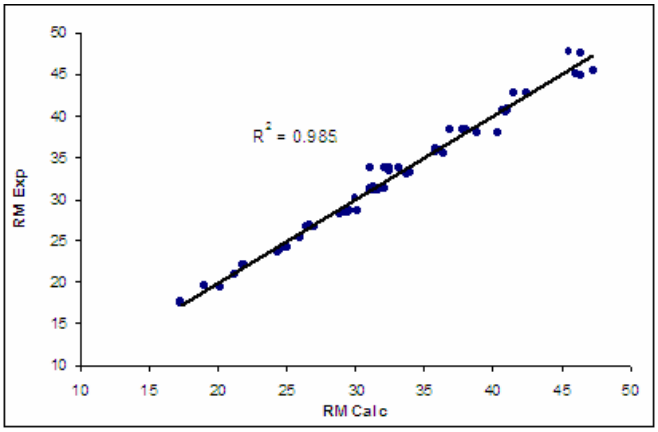

Figure 1. Plot of experimental vs calculated molar refractions for all three data sets.

CONCLUSIONS

Using weighting schemes and molecular descriptors derived from them showed that good models can be obtained even for mixed sets of organic compounds. The statistics of the obtained models appear excellent, both in estimation and prediction. The ability of TOPOCLUJ software program in providing various weighting schemes is a real promise.

REFERENCES

[1] Kier, L. B.; Hall, L. H. *Molecular Structure Description. The Electrotopological State*; Academic Press: New York, **1999**.

[2] Guo, M.; Xu, l.; Hu, C.Y.; Yu, S.M. Study on Structure-Activity Relationship of Organic Compounds - Applications of a New Highly Discriminating Topological Index, *Commun. Math. Comput. Chem. (MATCH),* **1997**, *35*, 185-197.

[3] Diudea, M.V.; Silaghi-Dumitrescu, I. Valence Group Electronegativity as a Vertex Discriminator, *Rev. Roum. Chim.* **1989**, *34*, 1175-1182.

[4] Diudea, M. V.; Topan, M.; Graovac, A. Layer Matrices of Walk Degrees, *J. Chem. Inf. Comput. Sci.* **1994**, *34*, 1071 -1078.

[5] Diudea, M. V. Wiener and Hyper-Wiener Numbers in a Single Matrix, *J. Chem. Inf. Comput. Sci*. **1996**, *36*, 833-836.

[6] Diudea, M. V.; Ursu O., Layer matrices and distance property descriptors. *Indian J. Chem.*, 42*A*, **2003**, 1283-1294.

[7] Hyperchem 7.03, Hypercube Inc. http://www.hyper.com

[8] STATISTICS TOOLBOX, MATLAB 6.5.1, Mathworks Inc., http://www.mathworks.com

STUDIA UNIVERSITATIS BABEŞ-BOLYAI, CHEMIA, XLIX, 2, 2004

Dedicated to Professor Valer Fărcăşan
at his 85th anniversary

STRUCTURAL SAFETY, RELIABILITY AND SENSITIVITY

CĂLIN I. ANGHEL

Department of Chemical Engineering, Faculty of Chemistry and Chemical Engineering, Babes-Bolyai University, 400028 Cluj-Napoca, Romania

ABSTRACT. The purpose of this paper is to present some methods available for performing reliability analysis. There are three main objectives. The first focuses on the fundamental link between safety and risk managing or evaluation. The second present the importance of sensitivity and probabilistic uncertainty analysis on complex technological or structural systems. The last introduces one's own procedure, hybrid cyclic recursive method, suitable for engineers in the stage of a preliminary risk analyze. It focuses on the reliability assessment concept.

Finally the study reveals a comparative assessment for the probability of failure implicit for reliability of a tank under technological loads and design parameters. The study estimates the risk of damage as a measure for the safety. Highly values for *most probable point* (*MPP*) lead to low values for the risk of failure. This threshold value is a key factor for engineers to decide when the structures become unsafe. The method is established to predict the probability of failure such as the limit-state in risk and reliability analysis. This type of study is suitable for structural or chemical engineers to work out optimal inspection and maintenance schedules, to avoid major technological incidents.

1. INTRODUCTION

Probabilistic methods and risk assessment also, started to be applied in the process industry in the late 1970s. It is now a well established tool for assessing most types of planned and existing chemical and hazardous materials installations, i.e. major accident hazard installations. Methodologies for both reliability and risk analysis advanced significantly in the 1980s. Since the early 1990s, probabilistic and quantified risk assessment is routinely applied to designs in many areas – structural failure represents one failure event, often the most important, in such risk assessments. The basic key features of the approach of risk assessment are hazard identification and risk analysis. Generally in engineering and particularly in structural engineering safety is perceived as a state or a quality - something to be achieved or assured it is a question of threats. Often safety, can be roughly defined as the state in which:

- a structure will not fail under some foreseeable conditions and it is unlikely to fail under some extreme circumstances;
- the probability of failure of structures during its serviceable life, are less than specified values.

Because the safety is a state or a quality, it can be achieved in different ways, but safety generally is not quantifiable. However there is a variety of ways in which safety can be assessed quantitatively when necessary. Despite the fact that "safety"

and “risk” are very different in nature, “safety and risk” are closely related concepts; generally “risk” is quantifiable. A general principle is that whenever is possible the focus must change from measures of safety to managing risk. An important distinction between risk and safety is that risk is a quantity that can become very small indeed, but can never be zero. Because the ”risk” relates to a future event, it is an estimate, and is therefore uncertain. A number of definitions of risk may be found in the literature. The most usually definitions for “risk” are:

- a combination of the likelihood and the consequences of a future event;
- the failure probabilities for a number of different scenarios;
- the product between the probability of occurrence and the quantified consequence of a future event [2,3];

$$Risk = function(p_f \times Consequences) \approx p_f \times Consequences; \quad (1)$$

For technological or offshore structures, the probability of partial or complete failure of the structural integrity during the service life is one input, often the key input, into a risk assessment. When considering risk, structural engineers generally focus on probability of failure rather than on the consequence of a future event. Despite the fact that probability of failure by itself is limited as a measure of safety, this assumption is generally agreed as the right measure of safety. The last definition tends to be more useful in the process industry, in environmental contexts risk management, rather than in structural engineering. In Probabilistic Risk Assessment (*PRA*) the strategies of achieving safety are related closely to risk management ideas.

The assessment can be both direct, using various analytic procedures or it could be indirect using for example an indicator method. In any case, a two-tier approach is preferable: ensure the structure does not fail, but if it does, then minimize the consequences. In any possible strategies, both direct and indirect, dealing with risk management the problems of complexity and uncertainty must be in the center.

The behavior of any technological equipment for process industries under operating conditions are always affected by variations and uncertainties: fluctuations and variations in service loading, scatters in material properties, uncertainties regarding the analytical models, chemical degradation and so on. The level of safety of these structures diminishes with time and the risk of a major technological accident increases. Many studies [1-7] were developed in order to maintain an acceptable level of safety and avoid technological incidents, in operating conditions affected by variations and uncertainties.

Sensitivity analysis, as it is applied to risk assessment, is a common technique used to understand how risk estimates and in particular, risk-based decisions are dependent on variability and uncertainty in the factors contributing to risk. In short, sensitivity analysis identifies what is “driving” the risk estimates. It is used in both point estimate and probabilistic approaches to identify and rank important sources of variability as well as important sources of uncertainty. The quantitative information provided by sensitivity analysis is important for guiding the complexity of the analysis; such sensitivity analysis plays a central role in the tiered process for risk assessment.

There are some alternative methods of dealing with uncertainty (fuzzy theory, possibility theory), but the present discussion will be limited to those methods based on probability theory. Generally, uncertainties typically fall into one of two categories: probabilistic or possibilistic. Probabilistic techniques are characterized by the use of random variables to describe the various sources of uncertainty and are often referred to as reliability methods by structural engineers. These techniques are typically applied when the systems are of small to moderate: complexity from 100 to150 random variables. Possibilistic techniques involve the use of fuzzy set theory or possibility theory to model uncertainty and variability and are particularly useful when dealing with large, complex systems.

In the light of the previous discussion, the aims of this paper are:

♦ to present some methods available for performing reliability analysis;

♦ to present the importance of sensitivity and probabilistic uncertainty analysis on complex systems;

♦ to present one's own developed procedure, suitable for engineers in the stage of a preliminary risk analyze;

2. THEORETICAL CONSIDERATIONS

Briefly, the reliability of an engineering system can be defined as its ability to fulfill its design purpose for a time period. So the reliability of a structure can be viewed as the probability of its satisfactory performance under specific service conditions within a stated time period. There are two major categories of analysis methods used to estimate the probability of failure:

- analytical techniques
- random sampling methods

The first category is characterized by the use of analytical techniques to find a particular point in design space that can be related (at least approximately) to the probability of system failure. This point is often referred to as the most probable point (*MPP*) or the design point [5, 6, 8, 9,11].

The *First-Order Reliability* method (*FORM*) is widely used in reliability analysis due to its simplicity and speed. However, for problems with nonlinear limit states, the accuracy or convergence of *FORM* cannot be assured satisfactory. The *Second-Order Reliability* method (*SORM*) can improve the reliability estimation for nonlinear problems. However, it is found that reliability estimates from *SORM* may be far from the accurate solution as well. Moreover, for problems with a large number of random variables and implicit limit state, each *FORM* or *SORM* procedures will need many function evaluations and advanced second moment method (*ASM*) and computer-based simulation methods were developed.

The second category includes a broad class of random sampling methods characterized by the random selection of observations of each system parameter [6, 8, 11]. This category is dominated by traditional Monte Carlo methods (*MCS*) as well as numerous variations such as stratified sampling, *Latin Hypercube Sampling - LHS*, *Importance Sampling* (*IS*) and *Adaptive Importance Sampling* (*AIS*).

Monte Carlo methods have a long history in reliability and uncertainty analysis as function integrators. The basic concept of *Monte Carlo Simulation* is to replace a continuous average by a discrete approximation for that average. *Iterative Monte Carlo Simulation* (*IMCS*) procedure, utilizes results from simulation to adapt the importance sampling density. This method is especially suitable for system reliability analysis to estimate failure probability since multiple failure modes need not be treated separately. However, *Monte Carlo Simulation* or *Latin Hypercube Sampling* often requires prohibitively large computational effort, especially for low probability of failure, although the number of simulations is independent of the number of basic variables. Thus, in reliability and risk assessment, several more efficient and accurate calculation algorithms for analyzing complicated models have been proposed.

The *Adaptive Importance Sampling* (*AIS*) method can be used to compute component and system reliability and reliability sensitivities. The *AIS* approach uses a sampling density that is proportional to the joint probability density function of the random variables. Starting from an initial approximate failure domain, sampling proceeds adaptively and incrementally to reach a sampling domain that is slightly greater than the failure domain to minimize oversampling in the safe region. The *Robust Importance Sampling* method (*RISM*) calculates the reliability or its converse, the probability of failure. *RISM* first uses a tracking scheme to locate the failure domain. Further, an efficient adaptive sampling scheme is used to calculate the reliability with minimum computational effort. Fundamental to the approach, for both two previous categories of analysis methods used to estimate the probability of failure are the following goals:

- the concept of a limit state function;
- the characterization of uncertainty in system response due to uncertainty in either internal system parameters;
- the sensitivity analysis of system response to uncertainties in the system variables;

2.1 Limit State Concept

The starting point for all these methods is a performance function, which gives the relation between the chosen performance and the inputs of the model. This function represents the total performance of the structure and includes the main operating and dimensional parameters. Usually it is named as the *performance function,* the *limit state function* (*LSF=G*), or *system response function;* this function may be explicit or implicit.

For simplicity of discussion, in this section we use ***z*** to represent any element of the system output vector $\vec{z}_i$, x_i to represent all the input of random variables generally referred as *design* variables and *G* to represent the analysis corresponding to $\vec{z}_i$. Therefore, outputs of interest have formal functional relationship *z = G(x).* In the reliability field, *z = LSF(x) = G(x)* characterizes the function of a specific performance criterion *z* named a *limit state function*. The failure surface or the limit state (a set defined by the locus of points *G(x))* is defined as $G(x) = g_0$ or simply *G(x) =0* [5, 6, 9, 10, 11].

This is the boundary between the safe and failure regions in the random variables space: a region Ω̣ where combinations of system parameters lead to an unacceptable or unsafe system response and a safe region Ω where system response is acceptable. When *G(x) > 0*, the system is considered safe and when *G(x) < 0*, the system can no longer fulfill the function for which it was designed. Only for simplicity Fig. 1 shows the limit state for a particular state, a two dimensional problem. The use of the terms “failure” is also customary, since only the likelihood of a particular system state may be of interest rather than system failure.

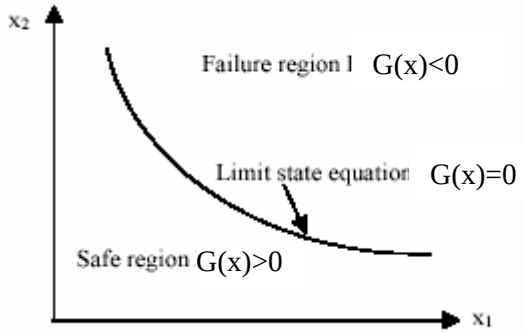

Fig. 1. Limit State Concept

The probability of system failure p_f is defined as the probability of the event that the system can no longer fulfill its function and is given by the expression:

$$p_f = P\{G(x) < 0\} \tag{2}$$

generally calculated by the integral

$$p_f = \underset{G(x)<0}{\int\int ... \int} f(x)dx \tag{3}$$

where *f(x)* is the joint probability density function (*PDF*) of *x* and the probability is evaluated by the multidimensional integrals over the failure region *G(x) < 0*.

Because the reliability *R* is the probability that the system works properly, it is given by the expression:

$$R = P\{G(x) > 0\} = 1 - p_f \tag{4}$$

In many situations it is very difficult or even impossible to analytically compute the multidimensional integrals (2). Alternative methods to evaluate the integration are random sampling methods. However, when the probability of failure p_f is very small the computational efforts of random sampling methods are extremely expensive.

To overcome this difficulty, Hasofer and Lind had proposed the concept of the *Most Probable Point* (*MPP*) to approximate the integration [6]. This *MPP* is the point on the limit state that lies closest to the origin, $u^* = (u^*_1 \ldots u^*_n)$. There is a direct relationship between the safety index and the probability of failure:

$$p_f = \Phi(-\beta) \tag{5}$$

where β is the safety index defined (Hasofer and Lind) as the shortest distance, in normal space u, from the origin to a point on the limit state surface (Fig. 2). When it is used in the context of $p_f = \Phi(-\beta)$ it is assumed that $\beta > 0$. In general, the relationship (5) is only approximate, but in the unique case of a linear combination of Gaussian distributed random variables where $\Phi(\ldots)$ is the cumulative normal density function, the relationship is exact.

Using the *MPP* concept, the input random variables $x = \{x_1 \ldots x_n\}$ - in the original design space x_n - must be transformed into an independent standardized normal space $u = \{u_1 \ldots u_n\}$. Rackwitz -Fiessler - Rosenblatt in addressing statistical dependency between the random variables [6, 11,14] gives the most commonly used transformation. The methods imply that the transformation forces the two cumulative densities function and joint probability density function to have equivalent similar statistical properties or to be identical both in x_n-space and u_n-space. The limit state function may be now rewritten as:

$$G(x) = G(u) = 0 \tag{6}$$

Searching for β can be formulated as a minimization problem with an equality constraint:

$$\left\{\beta = \min(u^T u)^{0.5} \ldots subjected..to..G(u) = 0\right\} \tag{7}$$

The joint probability density function on the limit state surface has its highest value at the *MPP* (Fig. 2) and therefore the *MPP* has the property that in the standard normal space it has the highest probability of producing the value of limit state function $G(u)$.

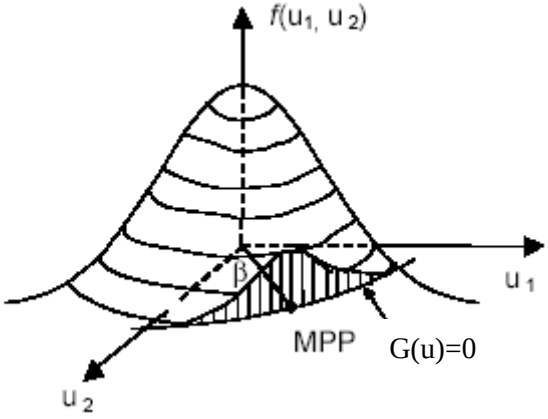

Fig. 2. The MPP Concept

If, in the u_n space, the limit state function $G(u)$ is linear or the principal curvatures of the limit state surface is not so large, *FORM* give an accurate estimate for probability of system failure p_f by the expression (5). Contrary, other optimization algorithms or searching methods well known in structural reliability [6, 9, 10, 14] must be used to solve (7). Assume *"n"* the number of the system inputs – random variables *" x_i "* in the ***LSF*** and a formal expression for this limit state function in real Euclidean R^n space as:

$$LSF = g_j(x_i) : R^n \rightarrow R \quad (i = 1,2,\ldots n \; ; \; j = 1,2,\ldots m, \text{ and } m<n) \qquad (8)$$

Because the input random variables $x_i = \{x_1..x_n\}$, in the original design space x_n, must be transformed into a standardized normal space $u_i = \{u_1 \ldots u_n\}$ the new limit function in terms of reduced variables, is given by the expression:

$$LSF = g_j(u_i) : R^n \rightarrow R \quad (i = 1,2,\ldots n \; ; \; j = 1,2,\ldots m, \text{ and } m<n) \qquad (9)$$

The point on the limit state that lies closes to the origin, $u^* = (u^*_1, u^*_2, \ldots, u^*_n)$ referred as *MPP*, must be evaluated. In general [6, 11] the distance from the point u^* to the limit state $g_j(u_i) = 0$ is given by the expression:

$$d = \left[\sum_1^n u_i^* \right]^{0.5} \qquad (10)$$

The difficulty then lies in determining the minimum distance for a general nonlinear function. The reduced variables corresponding to the *MPP* can be found in a various number of ways [9, 10, 12, 14], following approaches involving iterative, vectorial or gradient solutions. It is obviously a straightforward nonlinear constrained optimization problem:

$$\text{Minimize: } d = \left[\sum_1^n u_i^* \right]^{0.5} = \left(u^{*T} u^* \right)^{0.5}$$
$$\text{Subject to : } g_j(u_i) = 0 \qquad (11)$$

2.2 Characterization of uncertainty and sensitivity analysis

In the risk and structural analysis there are many variabilities and uncertainties in loading, material properties, geometry, and environmental conditions. These uncertainties should be taken into consideration carefully in order to ensure that the design performs its function within the desired confidence limit without failure. In robust design, it is important not only to achieve design objectives but also to maintain the robustness of design feasibility under the effects of variations caused by uncertainties. In the light of these the main demands of these previous mentioned methods are:

- ♦ characterization of variability and uncertainty in system;
- ♦ sensitivity analysis of system response to uncertainties in the system variables;

In response to the problem, methods have been developed to deal with the random nature of loads material properties and environmental conditions. ***Variability and Uncertainties*** are typically modeled in terms of the mean, the variance and the distribution. Various reliability estimation techniques use part or all of this information in different ways [4, 5, 6, 8].

Sensitivity Analysis can involve more complex mathematical and statistical techniques such as correlation and regression analysis to determine which factors in a risk or structural model contribute most to the variance in the final estimate. These techniques have their specific advantages and limitations. Because optimization algorithms or searching methods in structural reliability, based on *MPP* method, are developed in independent standardized normal space $\boldsymbol{u} = \{u_1 \ldots u_n\}$, this paper provides additional information only on the underlying principles of *Sensitivities of Limit State Function* and *Probabilistic Sensitivities of the Safety Index.* Nevertheless, it is not a comprehensive summary and is not intended to substitute for the numerous statistical books and journal articles on sensitivity analysis [1, 2]. The basic concept of this sensitivity analysis is to understand how variability and uncertainty in the reliability problems influence the estimates. So, sensitivity analysis can provide information to support additional testing in an efficient manner. Sensitivity measures when used in the context of the previous analytical methods are often referred to as *importance factors*. The magnitudes of these factors characterize the impact of each of the random variables on the safety index and thereby, their impact on the probability of failure. The importance factors represent the direction cosines of the individual random variables in reduced space and are defined as:

$$\gamma_i = \left(\frac{\partial G(u)}{\partial u_i} \right)_{u=u^*} \Bigg/ \left(\left(\sum_1^n \left(\frac{\partial G(u)}{\partial u_i} \right)^2 \right)^{0.5} \right)_{u=u^*} \tag{12}$$

where u is the current variable in reduce space and u^* is the variable corresponding to the possible *MPP* on limit state surface. As a computation check it is noted that:

$$\Sigma \gamma^2_i = 1 \text{ and } 1 \le \gamma_i \le 1 \tag{13}$$

The partial derivative of G (Fig. 3) with respect to each random variable u gives a measure of its sensitivity to that variable. If the probabilistic characteristics of the response of a system are not significantly impacted by statistical variation in certain variables, those variables can be omitted from the probabilistic analysis.

The sensitivity of Y ($Y=G(u_i, X_i)$) denotes a model output with respect to u or X calculated as the slope at a specific point, or the partial derivative.

Thus the generality of the analyze diminishes, dominant and secondary variables may be establish and the searching for safety index β are simplified. Information from sensitivity analysis can be important when trying to determine where to focus additional resources. If the input variables are all discrete and take a small number of values, it is possible to evaluate the influence of the various input variables at each of the defined points by considering all possible combinations

of the inputs by computing normalized partial derivatives at each point. This detailed approach is limited to situations where the number of inputs and the number of possible values for each input are relatively small or moderate.

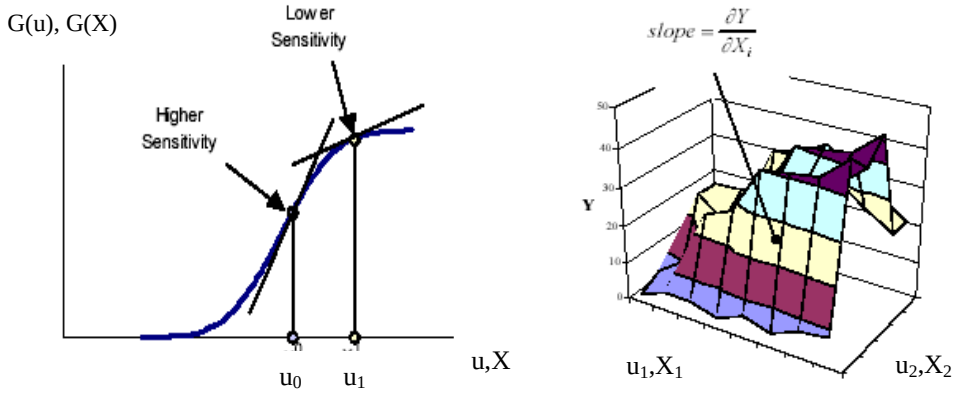

Fig. 3. Exemplary sensitivity state.

A similar approach may be used to analyze inputs that are continuous variables. Generally, in a *PRA*, many of the inputs will be random variables described by probability distributions and it will be necessary to quantify the influence of each input, u_i over the entire range of $\boldsymbol{u}$. As previously noted, if the relationship between the model output and all of the inputs is nonlinear, the influence of a particular input may vary depending on the value of that input. One approach to this problem is to consider a range of values for the input and to examine the influence over that range. If the input is considered to be a random variable following some specified probability distribution, then it may be desirable to look at the influence that the random input has on the model output across the distribution of input values.

To improve the efficiency of sensitivity analysis, when evaluating the influence at different points on the input-output simultaneously, it is important to take into account the probability associated with each of those points. The fact that a particular input has a large influence on the model output at a particular point would be discounted if the probability associated with that particular point is very low. Changes to the distribution of a variable with a high sensitivity could have a profound impact on the risk estimate, whereas even large changes to the distribution of a low sensitivity variable may have a minimal impact on the final result. To overcome this difficulty we propose one hybrid cyclic recursive method "*sensitivity analysis - safety index - sensitivity analysis"* conducted by random sampling points across the distribution of input values.

2.3. Cyclic recursive method and reliability analysis

By principle, this cyclic recursive algorithm belongs to the *Most Probable Point* (*MPP*) methods. Roughly it is a hybrid sampling-analytical procedure, conducted by random sampling points across the distribution of input values.

The proposed method will be presented in this section and demonstrative examples will be given in the next section. This particular method has its own specific advantages and limitations. As was shown in previous section the starting point of the method is to establish a performance function- named as the *limit state function* (*LSF=g*). This function may be of explicit or implicit form. For simplicity we chose one explicit form, to be presented. This function, giving the relation between the chosen performance-or critical state and the inputs of the model, must represent the total performance of the structure and includes the main operating and dimensional parameters.

To avoid some cumbersome approaches, unnecessary for the purpose of this paper the main assumptions are mentioned:

• we consider a series type structural system;

• basic variables: material properties, design parameters, operating parameters, environmental conditions, etc. are assumed to be random variables;

• at any stage the active loads are assumed to be stationary and ergodic;

• any estimator is statistic, hence any estimated parameter is a random variable;

• the random variables may be statistically independent or dependent-correlated;

• in the u_n space the limit state function g*(u)* may be nonlinear or the magnitude of the curvatures of the limit state may be large;

• we consider the functions that define the curvatures of the limit-state surface as a convex one and belonging at least to category C^1;

• the technique considers information regarding the underlying density function by random sampling points across the distribution of input values;

Based on these assumptions and the previous approach outlined in this section the main stages of this approach are presented.

2.3.1. Establishing the LSF

The first step is a random sampling procedure in agreement to the original distribution of all the input variables. An ample number of random sampling points [2,12,13] are necessary to establish a values domain, enough to reflect the variability and uncertainty of each variable. Thus the original inputs that are continuous variables described by probability distributions are transformed in some equivalent discrete, thus the number of combinations to be evaluated will be reasonable managed. The ranges of values for these inputs are considered intervals between sampling points. These statements are necessary both on sensitivity analysis to establish the model output across the distribution of input values and for searching or solving the *MPP*.

2.3.2. Searching for β or the MPP

At this stage we propose a dual mathematical approach involving *MPP* searching. The proposed approach consists in the following intermediate steps:

♦ Perform a sensitivity analysis to establish dominant *"k"* variables, thus new reduced Gaussian space becomes $u_k = \{u_1 \ldots u_k\}$, where $k < n$;

♦ All the other variables are expressed in terms of the mean of their distributions;

♦ Focus on these new variables a new limit function in terms of only these variables is given:

$$LSF = g_j(u_k) : R^k \rightarrow R \quad (i = 1,2,\ldots k\ ;\ j = 1,2,\ldots m,\ and\ \ m < k) \tag{14}$$

♦ Transform the problem of *MPP* searching into one dual problem:

• Consider the limit state function as one closed domain –surface in u_k space:

$$S : g_j(u_k) = 0 \tag{15}$$

• Consider the objective function *f(u)* a distance function from one point $O(u_{01},u_{02},\ldots,u_{0n})$ in u_k -space (particularly identical with the origin of standardized normal space u_i) to the previous mentioned closed domain – surface, $S(u_1,u_2,\ldots,u_k)$ as one strict convex function:

$$f(u) = d^2(P,S) \ = \ d^2(u_0,u\ ) = \sum_1^n (u-u_0)^2 \tag{16}$$

♦ Searching for *MPP* is then formulated as an extreme searching problem, with a nonlinear equality constraint:

$$\min\left(f \mid g_i = 0;...i = 1,2...m;..m < n\right) \tag{17}$$

These statements suggest that the extreme point - associated *MPP* - are placed at the base of a normal straight line through the point *"P"* belonging to the surface *"S"*. The range of values of the input variables – in multiple random combinations – are considered as searching points. Multiple cyclic searching approaches are done to solve the system of equations (17). Thus the location of a lot of possible *MPP*, has been found. These points may represent a vector of the safety index $\boldsymbol{u_{jk}}$, associated with their importance factors at each step. Based on direct relationship like (5), the probability of failure for all possible *MPP* may be established.

♦ Checking the concordance between the probability of failure and the importance factors, associated with each of these points, we accept only those points that have not been discounted for low associated probability.

Obviously these points must to belong to the domain of random sampling points and satisfy the system of equations (17). This cyclic algorithm will be stopped when no significant changes in concordance between the probability of failure and the importance factors, will be accomplished.

2.3.3. Establishment of β or the MPP

There are some possibilities to establish the *MPP* or the probability of failure.

♦ One direct possibility is the value expressed as *min (vector of the safety index* $\boldsymbol{u_{jk}}$*)*. This gives a unique assessment for safety and risk. It is well suited for analyses with unique limit state function.

♦ Another possibility to establish the *MPP* and the probability of failure is based on interval probability theory [15, 16].

3. NUMERICAL APPLICATIONS AND DISCUSSIONS

To avoid cumbersome approaches, we present only a demonstrative example based on several already published papers [6, 16]. Accordingly some scenarios the admissible value of a pre-existing flaw (a void on welding joints) in both area of interest [16] *"Area I - II"* is considered as a threshold value for possible fracture propagation. For a specific length of time in storage, the crack size, *"$A_i = 2a$"*, as a function of initial stress, S_0 and grain size Δ is approximated by [6]:

$$A = S_0 \cdot \left[0.01694 - 0.01353 \cdot \exp\left(-\frac{0.4158}{\Delta} \right) \right] \tag{18}$$

Failure of the welding seams may occur when *"$A_i = 2a$"* the initial or current size of the flaws, exceeds some critical level, named *Ac*. Thus:

$$p_f = P\{A_C < A\} \quad or \quad p_f = P\{A_C - A < 0\} = P\{g(\mathbf{x}) < 0\} \tag{19}$$

Based on the previous statements the form of the *LSF = g(x)* in this stage is:

$$g = A_C - S_0 \cdot \left[0.01694 - 0.01353 \cdot \exp\left(-\frac{0.4158}{\Delta} \right) \right] \tag{20}$$

Note that here $\boldsymbol{x} = \{ x_1 , x_2 \} = \{S_0 , \Delta \}$. It will suffice to assume that, critical level named *Ac* , random variables - initial stress S_0 and grain size Δ - are independent statistically with known first and second moments and exact form of the probability density function (Table 1).

Table 1.

The main values of design and simulation parameters

Parameters	Nominal Value	Statistical distribution
Critical width *Ac[mm]*	2.7	Constant
Initial stress S_0 [N/mm^2] (variable x_1)	300	Weibull μ = 300 α = 5.687 η = 324.34
Grain size Δ [mm] (variable x_2)	1.25	LogNormal μ = 300 σ = 60

Since the random variables are independent, the first step is to transform the random variables into reduced Gaussian space $x = x (x_1, x_2) \rightarrow u (u_1, u_2)$, using the moments of the equivalent normal distribution and transformation given by Rackwitz and Fiessler. That is:

$$\mu' = x - S' \cdot \Phi^{-1}[F(x)] \quad and \quad \sigma' = \frac{\phi\{\Phi^{-1}[F(x)]\}}{f(x)} \tag{21}$$

where $\Phi(\ldots)$ and $\phi(\ldots)$ are the standard normal *cdf* and *pdf*, respectively *F(x)* and *f(x)* are the proper cumulative density function and density function of original variables. The new variables in reduced Gaussian space become:

$$u_{1,2} = x_{1,2} - \mu'_{1,2} \big/ \sigma'_{1,2} \tag{22}$$

An ample number of random sampling points, in accordance with the original distribution for each variable, are sampled to establish domain values. In every points of this domain the previous equations set (22-23) are applied. The new expression for *LSF* in normal reduced space is determined:

$$g(u_{1,2}) = A_C - (\mu_1 + x_1 \cdot \sigma_1) \cdot \left[0.01694 - 0.01353 \cdot \exp\left(- \frac{0.4158}{\mu_2 + x_2 \cdot \sigma_2} \right) \right] \tag{23}$$

To establish the location of *MPP,* the proposed cyclic recursive algorithm is applied for the simultaneous system of equations (17), reduced to a particular form. Since the case of a linear combination of Gaussian distributed random variables is established we can evaluate the probability of failure by the previous expression (5).

Based on the approach outlined in previous section, a suitable computer program in *MATLAB* package was implemented on a *PC - AT* microcomputer *IBM* compatible. It allows a complete analysis to estimate the probability of failure. Comparative numerical results are presented in the form of graphs and tables.

The first step, establishing the new limit state function (in reduced space) is depicted in the following figures, Fig. 4. The quantitative information provided by sensitivity analysis (Fig. 5), characterize the impact of each of the random variables on the probability of failure. Thus the *"u1"* variable may be named the principal variable in reduced space and it has the main impact on the safety index β. For a two dimensional problem such this one, the minimum distance to the failure surface - the associated *MPP* and the safety index β is found on the base of the previous mentioned cyclic recursive algorithm.

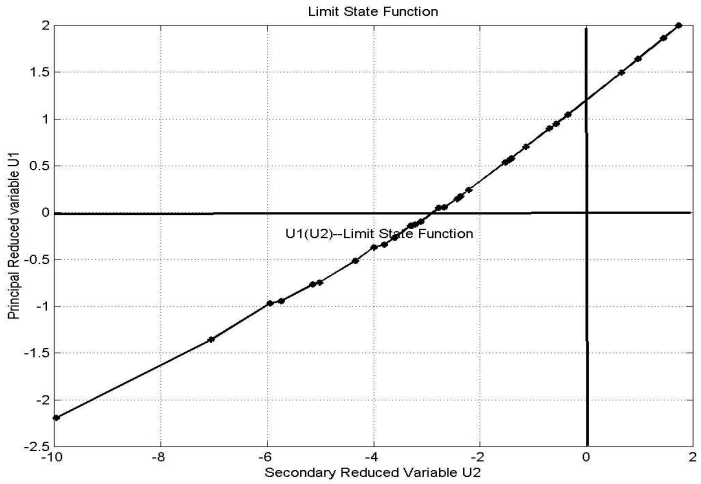

Fig. 4. Limit state function in reduced space

Table 2 and Figures 6-7 outlines the results from the intermediate steps. The best probability associated with each of the safety index β (see Table 2 and Fig. 5-6) arise on the following model outputs:

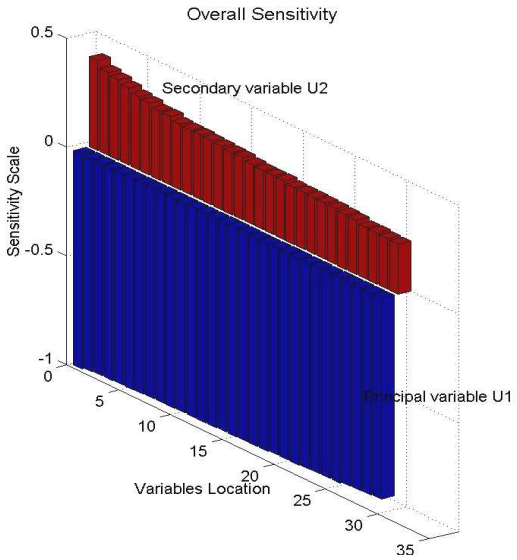

Fig. 5. Sensitivity chart in reduced space

U_1 importance factor	***U_2 importance factor***	***Safety index β.***
- 0.95965	***0.28116***	***9.721010188446312e-001***

Table 2.

Comparative numerical results

Model values [6]		
Safety index β. = 0.977; U_1 -importance factor = - 0.9619; U_2 -importance factor = 0.2733;		
Numerical simulated results		
U_1	U_2	β
8.317475978416375e-001	-1.901175118435460e-001	8.531991179231934e-001
7.812844076073880e-001	-1.831978656824919e-001	8.024754099416677e-001
8.351389158766590e-001	-2.057840513927728e-001	8.601186456642274e-001
8.488781805891856e-001	-2.162520608404962e-001	8.759903648432257e-001
8.858156089383533e-001	-2.386643520747695e-001	9.174039273897269e-001
8.923309629711115e-001	-2.454157566989017e-001	9.254639058942524e-001
9.328863757148401e-001	-2.733192288230011e-001	9.721010188446312e-001
8.236437357911779e-001	-4.928923902097007e-001	9.598603605914141e-001

Associated sensitivity

U_1 importance factor	U_2 importance factor	Safety index β.
-0.97485	0.22282	8.531991179231934e-001
-0.97359	0.22829	8.024754099416677e-001
-0.97095	0.23925	8.601186456642274e-001
-0.96904	0.24686	8.759903648432257e-001
-0.96556	0.26015	9.174039273897269e-001
-0.96419	0.26518	9.254639058942524e-001
-0.95965	0.28116	9.721010188446312e-001
-0.85808	0.31350	9.598603605914141e-001

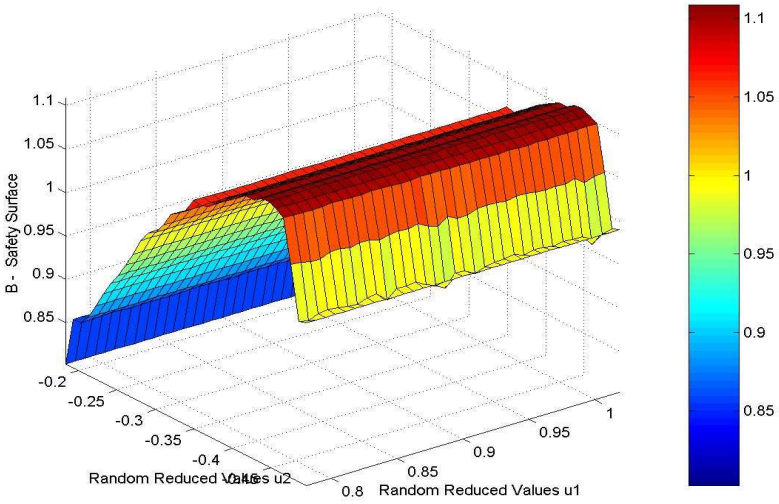

Fig. 5. Safety surface in reduced space

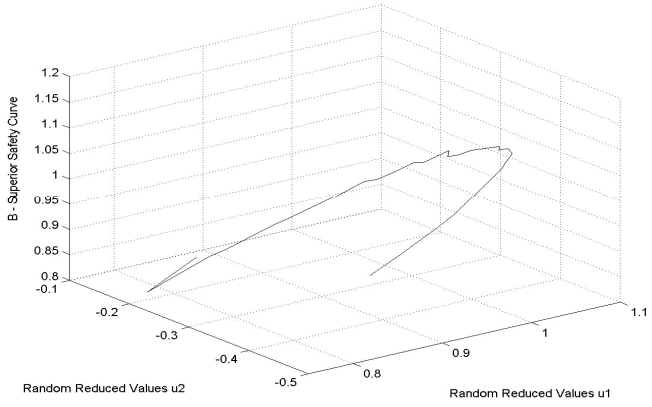

Fig. 6. Safety curve in reduced space

The presented analysis based on the proposed approach produces reasonable accurate results comparatively with the particular model values [6]. Relative errors occur under 1 %. Further the probability of failure obtained using the proposed approach produces not only a single value, butt it produces one inter val of probability values. The bounds of this interval may reflect completeness high uncertainty and variability of variables and may characterize better the probability of failure in the vicinity of tails of real or random variables.

4. CONCLUSIONS

The paper presents a probabilistic cyclic recursive algorithm for calculating the risk of failure, named the risk assessment. Also it accents on the sensitivity analyze as a key factor which could have a profound impact on the risk estimate. The numerical results are observed to be accurate as well as efficient compared with existing methods. The study may offer a greater reliability in life prediction. Highly values for safety factor β lead to low values for the risk of failure. Some approaches, like this, reduce the need for excessive safety margins in design and more cumbersome experimental and analytical approaches. The method can be used to predict the probability of failure, such as the limit-state in risk and reliability analysis. These types of study become not only recommended, but also necessary, for engineers, especially for structural or chemical engineers to work out optimal safety decisions.

REFERENCES

1. L. Z. Rumsiski, *Mathematical Processing of Experimental*, **1980**, Technical Publishing House Bucharest, (In Romanian).
2. **** Standard *RAGS 3A ~ Process For Conducting Probabilistic Risk Assessment* **,** December 1999.
3. D. G. Elms, *Achieving structural safety: theoretical considerations*, Struct. Safety, **1999**, 21, 311-333.
4. St. Ungureanu, Dynamic Systems Sensibility, **1988**, Technical Publishing House Bucharest, (In Romanian).
5. Y. T. Wu, *Computational methods for efficient structural reliability and reliability sensitivity analysis*, AIAA Journal, 32, (8), **1994**, 1717-1723.
6. D. G. Robinson, *A Survey of Probabilistic Methods Used In Reliability, Risk and Uncertainty Analysis: Analytical Techniques I*, Sandia National Laboratories, **1998**, Report SAND98-1189.
7. B. H. Thacker, D. S. Riha, H. R. Millwater, M. P. Enright*, Errors and Uncertainties in Probabilistic Engineering Analysis,* The 39th AIAA Aerospace Sciences Meeting **2001**- Paper no.*AIAA* 2001-1239.
8. A. R. Shouresh, A. H Chaghajerdi, S. J. McCaffery, *Causes Prediction and Prevention of Structural Failures: A State of the Art Report,* 8th ASCE Specialty Conference on Probabilistic Mechanics and Structural Reliability **2000**, Paper no. PMC2000-009.

9. D. Xiaoping, C. Wei, *A Most Probable Point based Method for Uncertainty Analysis*, Proceeding of DETC'00-**ASME 2000** Design Engineering Technical Conference – Paper no. DETC2000/DAC-14263.
10. D. Xiaoping, C. Wei, Collaborative Reliability Analysis for Multidisciplinary Systems Design, The 40th AIAA Aerospace Sciences Meeting **2002**- Paper no.AIAA 2002–5474.
11. M. Di Sciuva, D. Lomario, *A comparison between Monte Carlo and FORMs in calculating the reliability of composite structure*, Composite Structures 59, **2003**, 155–162.
12. L. Zhou1, R. C. Penmetsa1, R. V. Grandhi*, Structural Sysstem Reliability Prediction Using Multi Point Approximations for Design*, 8th ASCE Specialty Conference on Probabilistic Mechanics and Structural Reliability**, 2000***, Paper no.* PMC2000-082.
13. S. Adhikari, S. S. Langly, *Reduction of Random Variables in Structural Reliability Analysis*, Elsevier Science – Scirus Web Information, **2003**.
14. T. Zou1, S. Mahadevan, Z. Mourelatos, *Efficient Reliability Methods for Automotive Structural Systems,* Proceeding of 15th ASCE Engineering Mechanics Conference **2002**, Colombia University NY.
15. V. Sarveswaran, J. W. Smith, D. I. Blockley*, Reliability of corrosion-damaged steel structures using interval probability theory,* Struct. Safety, 20, **1998**, 237-255;
16. C. I. Anghel, R. Iatan, *Probabilistic approach and simulation methods for Risk assessment,* Studia Univ. Babes-Bolyai, CHEMIA, XLIX, 1, **2004**, 111-120;

STUDIA UNIVERSITATIS BABEŞ-BOLYAI, CHEMIA, XLIX, 2, 2004

Dedicated to Professor Valer Fărcăşan
at his 85th anniversary

FLOW GRAPHS IN CHEMICAL KINETICS (II)

MARIUS SOCOL and IOAN BALDEA

Faculty of Chemistry and Chemical Engineering, Babes-Bolyai University,
11 Arany Janos Str., 400028 Cluj-Napoca, Romania

ABSTRACT. Flow graphs used in physics and electronics have been applied to chemical kinetics. Rate laws and expressions of various concentrations of species involved in the mechanisms have been described for several simple systems. Flow graphs were constructed in agreement with the mechanism and differential equations that characterize the time evolution of radicals involved, and the characteristic determinants for the system. Short introduction basic principles of flow graphs, their properties and algebra are also presented. The same results were straightly obtained as those resulted from classical integration or by applying quasi-steady-state approximation.

Keyword: flow graph, differential equations, kinetics and mechanism

1. INTRODUCTION

Graphs and diagrams of various types have been used to depict reaction mechanisms in chemistry as chain processes, catalyzed processes, and enzyme-catalyzed processes [1,2]. Temkin [3-5] has proposed a convenient version of cyclic graphs. These graphs incorporate only intermediate species as vertices. They were used to deduce - in a quite simple way - the concentration of reactive intermediates and the overall reaction rate [6-8]. Numerous chemical chain reactions, photochemical reactions involving propagation of chain as elementary steps, enzyme-catalyzed reactions or even heterogeneous reactions were approached this way. Temkin and Bonchev and their co-workers [9-11] have classified various types of complex mechanisms on the ground of graphs associated with these mechanisms.

Inspired by the flow graphs used in electronics, physics and engineering [12-14], we tried to use flow graphs to associate them with reaction mechanisms in order to obtain some kinetic characteristics of any reaction scheme. Besides the intermediates, these graphs incorporate also the starting chemical species and the main or secondary products. At the same time, we associated determinants to chemical change and construct the graphs on this base. Such a way has the advantage of offering the opportunity to calculate the concentration of any species involved either being in a quasi-steady-state or a transient concentration. These flow graphs can be used for various types of mechanisms with linear sequence, opposing processes, single route chain reactions, homogeneous and heterogeneous catalyzed reactions.

The purpose of this work is to introduce flow graphs and to show how to deal with them in solving some simple reaction mechanisms.

2. SOME BASIC PRINCIPLES OF FLOW GRAPHS

A flow graph is a diagram that represents a set of simultaneous linear algebraic situations (linear differential equations). It is used to represent a system and to obtain the relationships among the system variables. By using the Cramer's method[15] with determinants one could solve the system.

A flow graph consists of a network in which nodes (or vertices) are connected by directed edges (or branches). Each node (vertex) represents a system variable, and each edge connected between two vertices acts as a signal multiplier. An arrow placed on the edge indicates the direction of a signal flow and the multiplication factor is indicated along the edge[16,17]. This multiplication factor is named transmittance and it can be obtained from the coefficients of the equations. The signal flow graph depicts the flow of signals from one point of the system to another and gives the relationships among the signals and it represents the value of the determinant of the system[12].

Definitions related to flow graphs

Before discussing flow graphs certain terms should be defined[18]:

Node (Vertex) is a point representing a variable or a signal. In chemistry it represents a chemical species undergoing some transformation.

Weighting of an edge (transmittance) is a real or complex gain between nodes. Such gains can be expressed in terms of transfer function between two nodes. In chemical kinetics it represents a pseudo-first- or a true first-order rate constant measuring the frequency with which chemical event takes place. By multiplying it with the actual concentration of the species in the vertex of outgoing branch and the volume of the system, the chemical flux, in the indicated direction, is obtained.

Edge (branch) is a directed line segment joining two nodes. The gain of a branch is the transmittance.

Input node or source is a node that has only outgoing edges. This corresponds to an independent variable. In chemical kinetics it represent the reactant species.

Output node or sink is a node that has only incoming edges. This corresponds to a dependent variable. In chemical kinetics, it corresponds to a reaction product.

Mixed (internal) node is a node that has both outgoing and incoming branches.

Path or way is a traversal of connected branches in the direction of the branch arrows.

Forward path (way) is a path from an input node (source) or from a mixed node, if the source is missing, to an output node (sink). The way should not visit any node more than once.

Forward path gain is the product of the branch transmittances of a forward path. A flow graph example is presented in Figure 1.

Properties of flow graphs

A few important proprieties of flow graphs are as follows:

A branch indicates the functional dependence of one signal on another.

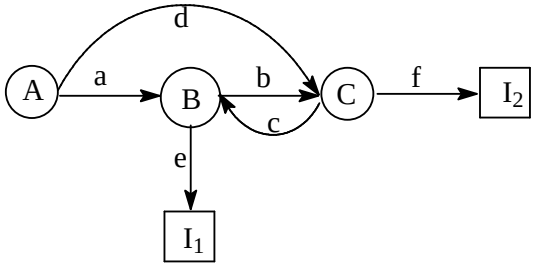

Figure 1. An example of a flow graph. A is an input node (source); I_1 I_2 are output nodes (sinks); a, b, c, d, e, and f are weighting of the edges; B, C are the internal nodes.

A signal passes trough only in the direction specified by the arrow of the branch.

A node adds the signals of all incoming branches and transmits their sum to all outgoing branches.

An interval node, which has both incoming and outgoing branches, may be viewed as an output node by ignoring its outgoing branches. Note, however, that a mixed node never can be a source (input node) in this approach.

For a given system a flow graph is not unique. More than one flow graphs can be drawn for a given system by writing the system equations or the corresponding determinants in a different way[12-14].

3. APPLICATION TO METHANE PYROLYSIS

The first example to be discussed is the methane pyrolysis. The following elementary process represent the simple mechanism, when the reverse reactions are not considered[19]:

$$CH_4 \xrightarrow{k_1} CH_3^{\cdot} + H^{\cdot} \qquad k_1 = 4.3*10^{-6}\ s^{-1}$$

$$CH_3^{\cdot} + CH_4 \xrightarrow{k_2} C_2H_6 + H^{\cdot} \qquad k_2 = 6.57*10^{5}\ L/mol{\cdot}s$$

$$H^{\cdot} + CH_4 \xrightarrow{k_3} CH_3^{\cdot} + H_2 \qquad k_3 = 4*10^{8}\ L/mol{\cdot}s \qquad (1)$$

$$2CH_3^{\cdot} \xrightarrow{k_4} C_2H_6 \qquad k_4 = 9.0125*10^{9}\ L/mol{\cdot}s$$

The accepted values of the rate constants are also given. The stoichiometry is represented by the equation:

$$2CH_4 \rightarrow C_2H_6 + H_2 \qquad (2)$$

In this case, the quasi steady state approximation (QSSA) can be applied for the active radicals. Their steady state concentrations are:

$$[CH_3\cdot] = \sqrt{\frac{k_1}{k_4}[CH_4]} \qquad [H\cdot] = \frac{k_2}{k_3}\sqrt{\frac{k_1}{k_4}}[CH_4]^{\frac{1}{2}} \qquad (3)$$

According to the mechanism (1), the rate law is obtained as the summation of the two steps yielding ethane:

$$r = \frac{d[C_2H_6]}{dt} = k_2[CH_3\cdot][CH_4] + k_4[CH_3\cdot]^2 \tag{4}$$

and therefore

$$r = k_2\sqrt{\frac{k_1}{k_4}}[CH_4]^{3/2} + k_1[CH_4] \tag{5}$$

By taking into account the values of the rate coefficients it simplifies to the form:

$$r = k_2\sqrt{\frac{k_1}{k_4}}[CH_4]^{3/2} \tag{6}$$

An alternative way of dealing with the system is to use the flow graph method.

The differential equations for the reaction system are:

$$\begin{cases} \dfrac{d[CH_3^{\cdot}]}{dt} = 0 = (k_2a + 2k_4x)[CH_3^{\cdot}] - k_3a[H^{\cdot}] - k_1[CH_4] \\ \dfrac{d[H^{\cdot}]}{dt} = 0 = -k_2a[CH_3^{\cdot}] + k_3a[H^{\cdot}] - k_1[CH_4] \end{cases} \tag{7}$$

The following notations are used further on: $[CH_4] = a$ and $[CH_3^{\cdot}] = x$. With these the following equations ca be written:

$$\begin{cases} k_1a = (k_2a + 2k_4x)[CH_3^{\cdot}] - k_3a[H^{\cdot}] \\ k_1a = -k_2a[CH_3^{\cdot}] + k_3a[H^{\cdot}] \end{cases} \tag{8}$$

Here the matrix of the free coefficients represents the matrix of the transmittances of branches outgoing from the input node

$$\begin{array}{c} \\ CH_3^{\bullet} \\ H^{\bullet} \end{array} \begin{array}{c} \begin{array}{cc} CH_3^{\bullet} & H^{\bullet} \end{array} \\ \begin{pmatrix} k_2a+2k_4x & -k_3a \\ -k_2a & k_3a \end{pmatrix} \end{array} \begin{array}{c} \\ \begin{pmatrix} CH_3^{\bullet} \\ H^{\bullet} \end{pmatrix} \end{array} = \begin{array}{c} CH_4 \\ \begin{pmatrix} k_1a \\ k_1a \end{pmatrix} \end{array} \tag{9}$$

$$A \quad \cdot \quad B \quad C$$

The flow graph is the one in which we can transpose the extended determinant, as has been shown above, *obtaining a perfect image of the mechanism* (figure 2).

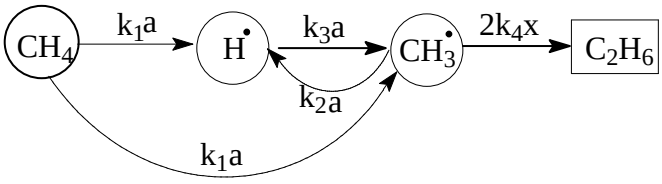

Figure. 2. Flow graph for methane pyrolysis

where C_2H_6 is the final product of termination step (the output node) and CH_4 is the main reactant (the input node). The starting species CH_4, the radical species $CH_3\cdot$ and $H\cdot$ and the final product C_2H_6 represent the nodes and the pseudo-first order rate constants k_1, k_2a, k_3a, and $2k_4[CH_3\cdot]$ represent the branch transmittance, obtained from the coefficients of the system.

The main determinant, or *the global consumption of the radicals' determinant*, is that one of matrix A denoted here by Δ:

$$\text{det. A} = \Delta = \begin{vmatrix} k_2a + 2k_4x & -k_3a \\ -k_2a & k_3a \end{vmatrix} = 2k_4x\,k_3a \qquad (10)$$

The value of main determinant *is also equal with the global gain of the flow graph, without considering the reactant (the input node).* Therefore it can be obtained straight from the graph by multiplying the branch transmittances which are outgoing from radicals to the final product, taking into account every possible ways and every radical involved in the mechanism.

The determinant for $CH_3\cdot$, *the formation determinant* is:

$$\Delta_x = \begin{vmatrix} k_1a & -k_3a \\ k_1a & k_3a \end{vmatrix} = 2k_1ak_3a \qquad (11)$$

The value of the formation determinant *is also equal with the gain of flow graph considering the radical specie an output node*. It is obtained by adding the product of transmittance of the branches, which are outgoing from the reactant CH_4 to the target radical on every possible ways, using the rules of the flow graphs.

The radical concentration CH_3, can be obtained by applying the Cramer's rules in the same way as King and Altman did for enzyme catalyzed reactions[2]:

$$x = [CH_3\cdot] = \frac{\Delta_x}{\Delta} = \frac{2ak_1k_3a}{2k_4xk_3a} \quad ; \quad x = \sqrt{\frac{k_1}{k_4}a} \qquad (12)$$

Thus, the determinant for $H\cdot$(the formation determinant for $H\cdot$ specie) is:

$$\Delta_{H\cdot} = \begin{vmatrix} k_2a + 2k_4x & k_1a \\ -k_2a & k_1a \end{vmatrix} = 2k_1ak_2a + 2k_4xk_1a \qquad (13)$$

$$[H\cdot] = \frac{2ak_1k_2a + 2ak_4xk_1}{2k_4k_3a\sqrt{\frac{k_1}{k_4}a}} \cong \frac{2ak_1k_2a}{2k_4k_3a\sqrt{\frac{k_1}{k_4}a}} = \sqrt{\frac{k_1}{k_4}} \cdot \frac{k_2}{k_3} a^{1/2} \qquad (14)$$

Finally, the rate law,

$$r = k_2\sqrt{\frac{k_1}{k_4}}[CH_4]^{3/2} \qquad (15)$$

identical with the one obtained by the quasi-steady-state approximation.

If we complicate the system by adding the reversible reactions, the decomposition of methane at 1600 degrees is described by the following mechanism[20]:

$$CH_4 \xrightarrow{k_1} CH_3^{\cdot} + H^{\cdot} \qquad k_1=14\ s^{-1}$$

$$H^{\cdot} + CH_4 \xrightarrow{k_2} CH_3^{\cdot} + H_2 \qquad k_2=1.5*10^{12}\ L/mol\cdot s$$

$$H_2 + CH_3^{\cdot} \xrightarrow{k_{-2}} H^{\cdot} + CH_4 \qquad k_{-2}=2.9*10^{10}\ L/mol\cdot s \qquad (16)$$

$$CH_3^{\cdot} + CH_3^{\cdot} \xrightarrow{k_3} C_2H_6 \qquad k_3=2*10^{13}\ L/mol\cdot s$$

$$C_2H_6 \xrightarrow{k_{-3}} CH_3^{\cdot} + CH_3^{\cdot} \qquad k_{-3}=4.5*10^{4}\ s^{-1}$$

$$CH_3^{\cdot} + H^{\cdot} \xrightarrow{k_{-1}} CH_4 \qquad k_{-1}=1.2*10^{13}\ L/mol\cdot s$$

with the global reaction:

$$2CH_4 \rightarrow C_2H_6 + H_2 \qquad (17)$$

The flow graph for this mechanism is a perfect image of it (figure 3). To form this graph we neglect the step of interruption between the hydrogen and methyl radicals because it is insignificant in compression with those of methyl radicals:

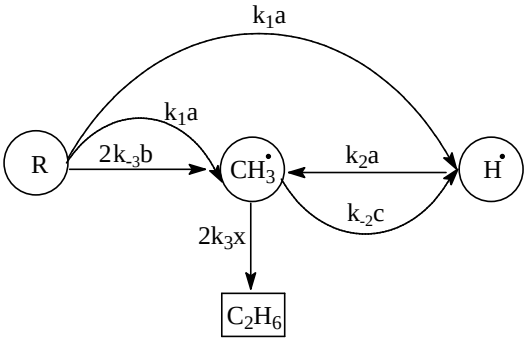

Figure 3. Flow graph for methane pyrolysis

where **R** is the impute node or source of the interested specie, radicals. We note with

x=[$CH_3^{\cdot}$] a=[CH_4] b=[C_2H_6] c=[H_2].

The main determinant is obtained by following the way from the radicals to the output node, the final product:

$$\Delta = k_2 a * 2k_3 x ,$$

which is the consumption determinant because it refers to the consumption of the radicals species in favor of formations of the product.

The formation determinant for the $CH_3^{\cdot}$ species is equal with

$$\Delta_{CH_3^{\cdot}} = \Delta_x = k_2 a(2k_1 a + 2k_{-3} b) \tag{18}$$

which results from the gain of the formation flow graph which is formed by considering the specie $CH_3^{\cdot}$ as a target (figure 4):

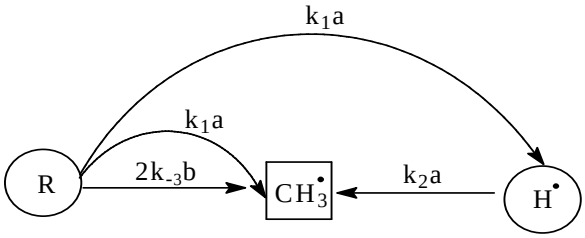

Figure 4. The flow graph for Δ_{CH3}

Taking in account of Cramer's rule the concentration of methyl species is:

$$x = \frac{\Delta_x}{\Delta} = \frac{k_2 a(2k_1 a + 2k_{-3} b)}{k_2 a\ 2k_3 x} \qquad x = \left(\frac{k_1 a + k_{-3} b}{k_3}\right)^{1/2}$$

but we have already considered the QSSA valuable, then the concentration have richen to the equilibrium and in consequence we can neglect the term $k_1 a$.

$$x = \left(\frac{k_{-3} b}{k_3}\right)^{1/2} \tag{19}$$

In the same way we can draw the flow graph corresponding to the formation determinant of the hydrogen radical specie (figure 5):

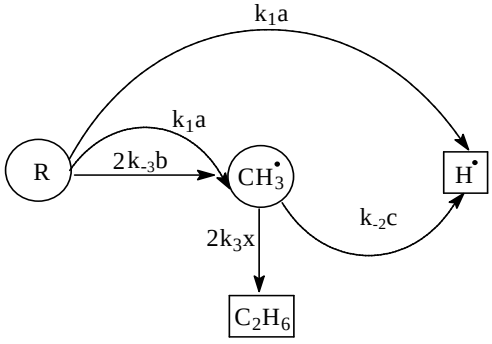

Figure 5. The flow graph for Δ_H

The gain of the flow graph is:

$$\Delta_{H^\cdot} = 2k_1ak_{-2}c + 2k_{-3}bk_{-2}c + 2k_3xk_1a$$

$$[H^\cdot] = \frac{2k_{-2}c(k_1a + k_{-3}b) + 2k_3x\ k_1a}{2k_3x\ k_2a} = \frac{k_{-2}c\ k_{-3}b}{k_2a\ k_3x} + \frac{k_1}{k_2} \qquad (20)$$

To find the dependence of the methane concentration to time we have to write the differential equation:

$$\frac{d[CH_4]}{dt} = k_{-2}[CH_3^\cdot][H_2] + k_{-1}[H^\cdot][CH_3^\cdot] - k_2[H^\cdot][CH_4] - k_1[CH_4] \qquad (21)$$

$$\frac{d[CH_4]}{dt} = k_{-1}[H^\cdot][CH_3^\cdot] - 2k_1[CH_4] \qquad (22)$$

$$\frac{da}{dt} = 130.25 \cdot \frac{(C_{A0} - a)^2}{a} + 3.75 \cdot 10^{-3} \cdot (C_{A0} - a)^{1/2} - 2k_1a \qquad (23)$$

If the numerical integration is applied the profile methane concentration – time was obtained. If we consider the fact that in calculation of species concentrations we didn't take in evidence the reaction $H + CH_3 \rightarrow CH_4$, we'll make the correction with factor $1 + \frac{k_{-1}k_{-2}}{k_3k_2}\frac{c}{a} + \frac{2k_{-1}}{k_2}\frac{x}{a}$ which represent the error made in finding the value of [H] concentration, by not considering the reaction $H + CH_3 \rightarrow CH_4$.

The numerical integration and calculation of all concentrations species was made by a Matlab program which is presented in the following, considering the QSSA:

```
t=0:0.0001:0.03;h=0.0001;y=zeros(1,301);y(1)=1e-6;
for i=1:300
y(i+1)=y(i)+h*(130.25*((y(1)-y(i))^2)/y(i)+3.75e-3*((y(1)-
y(i))^0.5)-28*y(i));
end
w=1e-6-y;x=3.35e-5*(w.^0.5);u=3.24*1e-
7*((w.^1.5)./y)+9.333*1e-
12;d=x./y;e=1+16*d;v=u./e;z=zeros(1,301);z(1)=1e-6;
for i=1:300
z(i+1)=z(i)+h*((130.25*((z(1)-z(i))^2)/z(i)+3.75e-
3*((z(1)-z(i))^0.5))*e(i)-28*z(i));
end
figure plot(t,(z*1e7),'m')
hold on plot(t,(l*1e8),'m')
hold on   plot(t,(v*1e11),'m')
xlabel('t[s]')
ylabel('Methane,Methil,Hidrogen concentrations')
hold off
```

This profiles are comparable with those obtained by Skinner[20] solving with a Fortran programe the differential equations system, and not considering the QSSA.

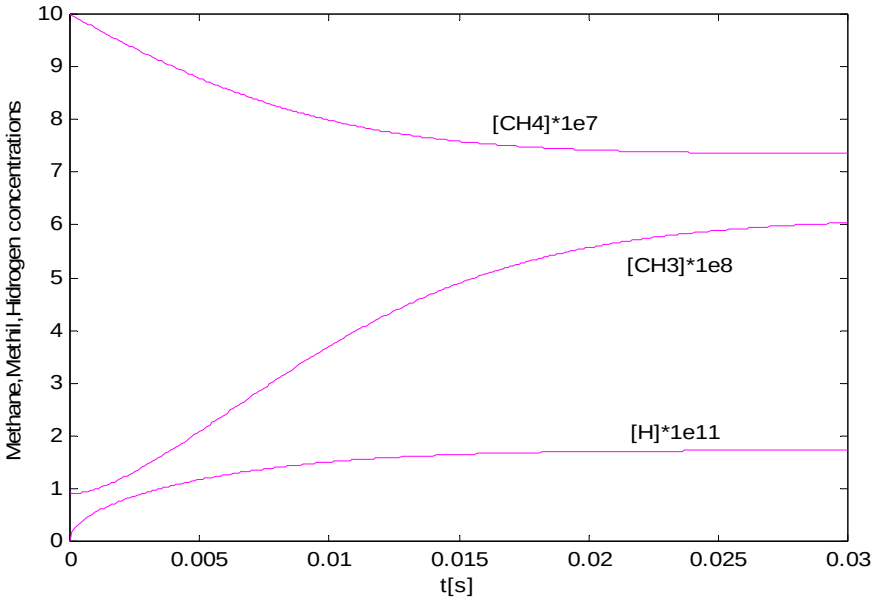

Figure 6. Concentration dependence of time for methane pyrolysis

4. THE PYROLISIS OF 1,3-DIPHENILPROPANE

The second example refers to 1,3-diphenilpropane pyrolysis and it's a kind of Rice-Herzfeld mechanism[21]:

$$\underset{(a)}{Ph-CH_2-CH_2-CH_2-Ph} \xrightarrow{k_1} \underset{(R_1)}{Ph-CH_2^{\bullet}} + \underset{(R_2)}{Ph-CH_2-CH_2^{\bullet}} \quad \text{initiation} \quad (24)$$

$$\underset{(R_1)}{Ph-CH_2^{\bullet}} + Ph-CH_2-CH_2-CH_2-Ph \xrightarrow{k_H} Ph-CH_3 + \underset{(R_3)}{Ph-CH^{\bullet}-CH_2-CH_2-Ph} \quad (25)$$

$$Ph-CH^{\bullet}-CH_2-CH_2-Ph \xrightarrow{k_\beta} Ph-CH_2^{\bullet} + Ph-CH=CH_2 \quad (26)$$

$$R_3 + R_3 \xrightarrow{k_{T_1}} Product_2 \quad \text{termination} \quad (27)$$

$$R_3 + R_1 \xrightarrow{k_{T_2}} Product_1 \quad \text{termination} \quad (28)$$

$$R_1 + R_1 \xrightarrow{k_{T_3}} Product_3 \quad \text{termination} \quad (29)$$

The representative flow graph (figure 7) for the mechanism is as follows:

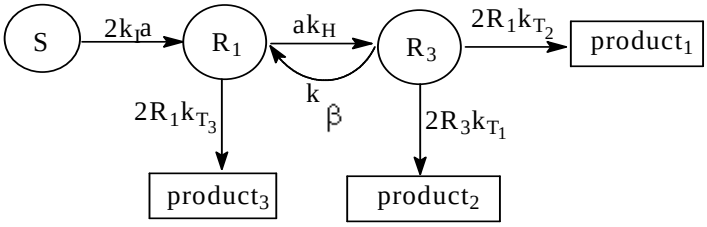

Figure 7. Flow graph for 1,3-diphenilpropane pyrolysis

the rate law is:

$$r = ak_H R_1 \tag{30}$$

The mechanism system is as follows:

$$\begin{array}{c} \\ R_1 \\ R_3 \end{array} \begin{array}{c} \begin{array}{cc} R_1 & R_3 \end{array} \\ \begin{pmatrix} ak_H+2R_1k_{T_3} & -k_\beta \\ -ak_H & 2R_1k_{T_2}+2R_3k_{T_1}+k_\beta \end{pmatrix} \end{array} \cdot \begin{array}{c} a \\ \begin{pmatrix} R_1 \\ R_3 \end{pmatrix} \end{array} = \begin{pmatrix} 2k_1a \\ 0 \end{pmatrix} \tag{31}$$

$$\Delta = (ak_H + 2R_1k_{T_3})(2R_1k_{T_2} + 2R_3k_{T_1} + k_\beta) - ak_Hk_\beta = \\ = ak_H(2R_1k_{T_2} + 2R_3k_{T_1}) + 2R_1k_{T_3}(2R_1k_{T_2} + 2R_3k_{T_1} + k_\beta) \tag{32}$$

The value of this determinant (the global consumption radical) is also equal with the global gain of flow graph without considering the reactant (the input node) following the given rules of the flow graphs.

Taking in account that: $2R_1k_{T_2} + 2R_3k_{T_1} << k_\beta$

$$\Delta = ak_H(2R_1k_{T_2} + 2R_3k_{T_1}) + 2R_1k_{T_3}k_\beta \tag{33}$$

Also, using the same proprieties of the flow graphs (following the branch way, starting from the reactant, to the aimed radical) we obtain:

$$\Delta_{R_1} = a2k_Ik_\beta \quad \text{and} \quad \Delta_{R_3} = 2ak_Iak_H \tag{34}$$

According with Cramer's method, we have:

$$\frac{R_3}{R_1} = \frac{\Delta R_3}{\Delta R_1} = \frac{ak_H}{k_\beta} \qquad R_3 = \left(\frac{ak_H}{k_\beta}\right)R_1$$

$$R_1 = \frac{\Delta R_1}{\Delta} = \frac{2ak_I \cdot k_\beta}{2ak_HR_1k_{T_2} + 2ak_Hk_{T_1}R_3 + 2R_1k_{T_3}k_\beta}$$

$$R_1^2 = \frac{a \cdot k_I}{\frac{ak_H}{k_\beta} \cdot k_{T_2} + \left(\frac{ak_H}{k_\beta}\right)^2 \cdot k_{T_1} + k_{T_3}}$$

$$R_1 = \left(\frac{ak_I}{\frac{ak_H}{k_\beta} \cdot k_{T_2} + \left(\frac{ak_H}{k_\beta}\right)^2 \cdot k_{T_1} + k_{T_3}} \right)^{1/2} \tag{35}$$

knowing that $r = ak_H R_1$ it results

$$r = ak_H \left(\frac{ak_I}{\frac{ak_H}{k_\beta} \cdot k_{T_2} + \left(\frac{ak_H}{k_\beta}\right)^2 \cdot k_{T_1} + k_{T_3}} \right)^{1/2} \tag{36}$$

Equation (36) is the same with that one obtained by applying quasi-steady state approximation (QSSA)[22,23] and long-chain approximation (LCA)[24].

5. THE PYROLISIS OF PROPANE

An example illustrating a very complex mechanism is the one referring at thermal decomposition of propane[25]. Homogenous pyrolysis of propane between 1050 – 1250 K has been chosen as an example because every proposed mechanism in last few years[26-28] are obeying the mechanism formed from eleven reactions, proposed by Lifshitz and Frenklach[29], although there are some inconcordances by means of rate constants values for some reaction

The described mechanism is as follows:

$C_3H_8 \xrightarrow{k_1} CH_3^\bullet + C_2H_5^\bullet$	$k_1 = 1.168\ s^{-1}$
$CH_3^\bullet + C_3H_8 \xrightarrow{K_2} CH_4 + i-C_3H_7^\bullet$	$k_2 = 10^7$ L/mol·s
$CH_3^\bullet + C_3H_8 \xrightarrow{K_3} CH_4 + n-C_3H_7^\bullet$	$k_3 = 1.21 \times 10^7$ L/mol·s
$H^\bullet + C_3H_8 \xrightarrow{k_4} H_2 + i-C_3H_7^\bullet$	$k_4 = 7.31 \times 10^8$ L/mol·s
$H^\bullet + C_3H_8 \xrightarrow{k_5} H_2 + n-C_3H_7^\bullet$	$k_5 = 8.84 \times 10^8$ L/mol·s
$i-C_3H_7^\bullet \xrightarrow{k_6} C_2H_4 + CH_3^\bullet$	$k_6 = 1.35 \times 10^5\ s^{-1}$ (37)
$n-C_3H_7^\bullet \xrightarrow{k_7} C_2H_4 + CH_3^\bullet$	$k_7 = 1.61 \times 10^7\ s^{-1}$
$i-C_3H_7^\bullet \xrightarrow{k_8} C_3H_6 + H^\bullet$	$k_8 = 1.23 \times 10^6\ s^{-1}$
$n-C_3H_7^\bullet \xrightarrow{k_9} C_3H_6 + H^\bullet$	$k_9 = 1.81 \times 10^6\ s^{-1}$

$$C_2H_5^{\bullet} \xrightarrow{k_{10}} C_2H_4 + H^{\bullet} \qquad k_{10} = 2.58 \times 10^5\ s^{-1}$$

$$CH_3^{\bullet} + CH_3^{\bullet} \xrightarrow{k_{11}} C_2H_6 \qquad k_{11} = 9.00 \times 10^9\ L/mol{\cdot}s$$

For such a mechanism, the calculation is very difficult and it takes a long time and attention. That's why we appeal to the method of flow graph.

The flow graph (figure 8) is as follows:

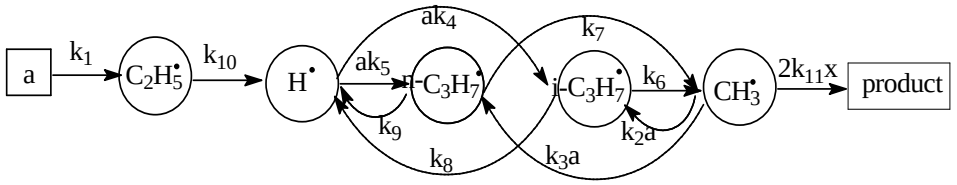

Figure 8. Flow graph for propane pyrolysis

we note: a = $[C_3H_8]$ and $x = [CH_3^{\bullet}]$; Using the proprieties of the flow graphs we obtain:

$$\Delta = k_{10}ak_4k_6k_9 2k_{11}x + k_{10}ak_5k_7 2k_{11}xk_8 + k_{10}ak_4k_6 2k_{11}xk_7 + k_{10}ak_5k_7k_6 2k_{11}x = 2k_{10}k_{11}xa[k_4k_6(k_7+k_9) + k_5k_7(k_6+k_8)] \quad (38)$$

$$\Delta_x = 2a^2k_1k_{10}[k_4k_6(k_7+k_9) + k_5k_7(k_6+k_8)] \quad (39)$$

$$\Delta_{H\cdot} = 2ak_1k_{10}[k_8k_7k_2a + k_8k_2ak_9 + k_3ak_9k_8 + k_3ak_9k_6 + k_{11}x(k_6k_7 + k_7k_8 + k_9k_6 + k_8k_9)] \quad (40)$$

$$\Delta_{C_2H_5\cdot} = 2a^2k_1k_{11}x(k_5k_6k_7 + k_4k_6k_7 + k_5k_7k_8 + k_4k_6k_9) \quad (41)$$

$$\Delta_{i-C_3H_7\cdot} = 2a^2k_1k_4k_{10}[k_3ak_9 + k_2ak_9 + k_2ak_7 + k_{11}x(k_7+k_9)] \quad (42)$$

$$\Delta_{n-C_3H_7\cdot} = 2a^2k_1k_5k_{10}[k_2ak_8 + k_3ak_8 + k_3ak_6 + k_{11}x(k_6+k_8)] \quad (43)$$

Using the Cramer's rules we obatin:

$$[CH_3\cdot] = \frac{\Delta_x}{\Delta} \quad (44)$$

$$[H\cdot] = \frac{\Delta_{H\cdot}}{\Delta} \quad (45)$$

$$[C_2H_5\cdot] = \frac{\Delta_{C_2H_5\cdot}}{\Delta} \quad (46)$$

$$[i-C_3H_7\cdot] = \frac{\Delta_{i-C_3H_7\cdot}}{\Delta} \quad (47)$$

$$[n-C_3H_{7^\cdot}] = \frac{\Delta_{n-C_3H_{7^\cdot}}}{\Delta} \tag{48}$$

with the rate law:

$$-\frac{d[C_3H_8]}{dt} = k_1[C_3H_8] + (k_2 + k_3)[CH_3^\cdot][C_3H_8] + (k_4 + k_5)[H^\cdot][C_3H_8] \tag{49}$$

Using these equations we obtain:

$$[CH_3^\cdot] = 1.14*10^{-5}*\sqrt{a}\ ,\ [H^\cdot] = 1.346*10^{-9}*(10^2*\sqrt{a}+1)\ ,[C_2H_5^\cdot] = 4.535*10^{-6}*a$$
$$[i-C_3H_7^\cdot] = 7.23*10^{-7}*a*(110*\sqrt{a}+1) \tag{50}$$
$$[n-C_3H_7^\cdot] = 6.68*10^{-8}*a*(205.5*\sqrt{a}+1)$$

and for initial concentration of propane by 10^{-6} mol/l we obtain:

$[CH_3]=1.14*10^{-8}$;$[H]=1.485*10^{-9}$; $[C_2H_5]=4.535*10^{-12}$; (51)
$[i\text{-}C_3H_7]=8.025*10^{-13}$; $[n\text{-}C_3H_7]=8.056*10^{-14}$;

The program in Matlab which solves the differential system without any approximation (QSSA) using the numerical methods is:

```
t=0:1e-7:0.03;h=1e-7;
k1=1.168;k2=1e7;k3=1.21e7;k4=7.31e8;k5=8.84e8;k6=1.35e5;
k7=1.61e7;
k8=1.23e6;k9=1.81e6;k10=2.58e5;k11=9e9;
y=zeros(1,(3e5+1));z=zeros(1,(3e5+1));w=zeros(1,(3e5+1));u=z
eros(1,(3e5+1)); v=zeros(1,(3e5+1));r=zeros(1,(3e5+1));
y(1)=1e-6;z(1)=0;w(1)=0;u(1)=0;v(1)=0;r(1)=0;
for i=1:3e5
   y(i+1)=y(i)-
h*(k1*y(i)+(k2+k3)*r(i)*y(i)+(k4+k5)*y(i)*w(i));
   z(i+1)=z(i)+h*(k1*y(i)-k10*z(i));
   w(i+1)=w(i)+h*(k8*v(i)+k9*u(i)+k10*z(i)-
(k4+k5)*y(i)*w(i));
   u(i+1)=u(i)+h*(k3*r(i)*y(i)+k5*w(i)*y(i)-(k7+k9)*u(i));
   v(i+1)=v(i)+h*(k2*r(i)*y(i)+k4*w(i)*y(i)-(k6+k8)*v(i));
   r(i+1)=r(i)+h*(k1*y(i)+k6*v(i)+k7*u(i)-
(k2+k3)*y(i)*r(i)-k11*r(i)*r(i));
end
figure
plot(t,(y*1e7))
hold on
plot(t,(z*1e12))
hold on
plot(t,(w*1e9))
hold on
plot(t,(u*1e14))
hold on
plot(t,(v*1e13))
hold on
```

```
plot(t,(r*1e8))
xlabel('t[s]') ylabel('Propane,Ethil,Hidrogen,n-Propil,
i-Propil,Methil concentrations')
hold off
```

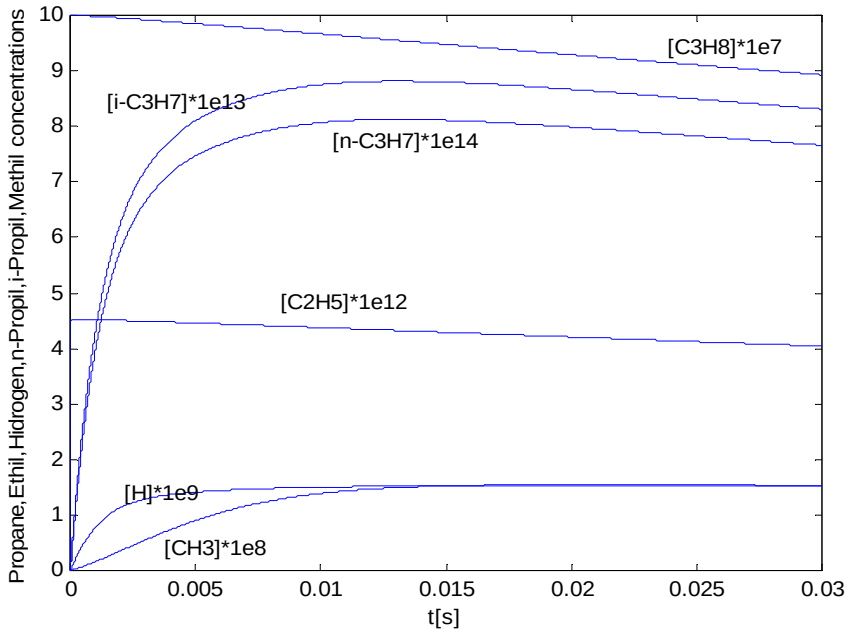

Figure 9. Concentration dependence of time for propane pyrolysis

It is observed that the stationary concentrations obtained are approximately the same with those obtained with graph theory using QSSA approximation.

REFERENCES

1 M.Boudart, *Kinetics of Chemical Processes*, Prentice Hall, Englewood Cliffs New-Jersey, 1968, 100.

2. E. L. King, C. Altman, *Phys. Chem.*, 1956, 60, 1375

3. M. I. Temkin , *Dokl. Akad. Nauk SSSR,* 1963, 152, 156-159.

4. M. I. Temkin, *Dokl. Akad. Nauk SSSR,* 1965, 165, 615-618.

5. M. I. Temkin, *Mechanism and Kinetics of Complicated Reactions*, S. Z. Roginski, Moscow, 1970, p. 57.

6. E. Segal, *Ann. Univ. Bucuresti* 2003.

7. E. Segal, *Progress in Catalysis,* 1997, *6,* 135-141.
8. E. Segal, *Progress in Catalysis,* 1998, *7,* 1-4.
9. O. N. Temkin, D. G. Bonchev, *J. Chem. Edu.,* 1992, 69, 544-550.
10. A. V. Zeigarnik, O. N. Temkin, D. G. Bonchev, *J. Chem. Inf .Comput .Sci,* 1995, 35, 729-737.
11. A. V. Zeigarnik, O. N. Temkin, D. G. Bonchev, *J. Chem. Inf. Comput. Sci,* 1996, 36, 973-981.
12. K. Ogata, *Modern Control Engineering,* Prentice Hall International, New Jersey, 1995.
13. N. S. Nice, *Control System Engineering,* Addison-Westley Publishing Company, 1995, p. 240-260, 268-275.
14. R. C. Dorf, R. H. Bihop, *Modern Control System*, Prentice Hall International, New Jersey, 2001, p. 66-80,118-158.
15. A. C. Aitken, *Determinants and Matrices,* Oliver and Boyd, Edinburgh, 1939, Chap. 2.
16. M. V. Diudea, O. Ivanciuc, *Topologie Moleculara*, Ed. Comprex, Cluj, 1995, p. 37.
17. T. Ionescu, *Grafuri. Aplicatii. Vol 1.* Ed. Didactica si Pedagogica, Bucuresti, 1973, p. 198-207.
18.M. Socol, I. Baldea, *Stud. Univ. Babes-Bolyai, Chemia,XLVIII,* 1, 2003, p. 109-128.
19. K. H. Ebert, H, J. Ederer, G. Isbarn, *Int. J. of Chemical Kinetics***,** 1983**,** 15(5)**,** 486-493.
20. G. B. Skinner, *Introduction to Chemical Kinetics***,** Academic Press, New York, 1974**,** 87-94.
21 P. E. Savage, *J. Anal. Appl. Pyrolysis*, 2000*, 54***,** 109-126.
22 G. Come, *J. Phys. Chem.*, 1977**,** *81***,** 2560**.**
23 T.Turányi, A. S. Tomlin, M. J. Pilling, *J. Phys. Chem.*, 1993**,** *97***,** 163**.**
24 G. R. Gavalas, *Chem. Eng. Sci*., 1966*, 21***,** 133**.**
25 D. Miller, M. Frenklach, *Int. J. Chem. Kinet.*, 1983*, 15***,** 677-696**.**
26 J. Bradley, *J. Chem. Soc., Faraday Trans.,* 1979*, 75*, 2819.
27 J. M. Simmie, W. C. Gardiner, Jr., C. S. Eubank, *J. Phys. Chem.*, 1982**,** *86,* 799.
28 C. C. Chiang, G. B. Skiner, *"18th Symp. (International) on Combustion", The Combustion Institute,* 1981**,** 915.
29 A Lifshitz, M. Frenklach, *J. Phys. Chem*., 1975**,** *79***,** 686.

STUDIA UNIVERSITATIS BABEŞ-BOLYAI, CHEMIA, XLIX, 2, 2004

Dedicated to Professor Valer Fărcăşan at his 85th anniversary

GALVANOSTATIC H_2O_2 ELECTROSYNTHESIS ON RETICULATED GLASSY CARBON ELECTRODE

OLIVIA SERDAN and PETRU ILEA

Department of Physical Chemistry, Babes-Bolyai University,11 Arany Janos Str. 400028 Cluj-Napoca, Romania. E-mail:pilea@chem.ubbcluj.ro

ABSTRACT. The influence of experimental parameters (electrolyte concentration, current density and air flow rate) on the current efficiency and specific energy consumption for H_2O_2 electrosynthesis by cathodic reduction of oxygen on reticulated glassy carbon electrode was investigated. The optimum results, consisting in high H_2O_2 concentration and current efficiency associated with low specific energy consumption, were obtained at 0.392 mA cm^{-2} current density and 60 l h^{-1} air flow rate when a 1 M NaOH solution was used as electrolyte.

Keywords: H_2O_2 electrosynthesis, partial oxygen reduction, reticulated glassy carbon electrode.

INTRODUCTION

The pulp and paper industry remains a promising market for H_2O_2, primarily due to environmental concerns over chlorine based processing [1, 2]. Thus, the use of hydrogen peroxide has become an attractive alternative. Among the various ways of producing hydrogen peroxide, the synthesis by partial electroreduction of dissolved oxygen in alkaline media [3]:

$$O_2 + H_2O + 2e^- \rightarrow HO_2^- + HO^- \qquad \varepsilon^\circ = -0.065\ V \qquad (1)$$

has received much attention. However, this reaction has limited applicability due to the low oxygen solubility, the low reaction rate and the reduction of oxygen to HO^- [3]:

$$O_2 + 2H_2O + 4e^- \rightarrow 4\ HO^-, \qquad \varepsilon^\circ = -0.401\ V \qquad (2)$$

Carbonaceous materials are often selected as electrode materials because of their intrinsic electrocatalytic properties for the partial electroreduction of the dissolved oxygen. The high porosity of carbonaceous materials as well as the possibility to fabricate them at desired porosity (e.g. the reticulated carbon electrode) assure a high active surface necessary to increase the reaction rate for H_2O_2 electrosynthesis (expressed for the volume unit of the electrochemical reactor).

The low solubility of O_2 in aqueous solutions determines a low mass transfer limiting current density and requires the use of a 3D electrode. The reticulated glassy carbon electrode has an exceptionally high void volume, a high surface area combined with self-supporting rigidity, a low resistance to fluid flow, a

good resistance to very high temperatures in non-oxidizing environments and is very inexpensive compared to solid glassy carbon [4, 5]. The reticulated glassy carbon may easily be machined into various geometric shapes and mounted in various cell configurations. Holes, tubes, disks or rings are also produced [5, 6].

In this context, the aim of the present work was to investigate the influence of different experimental parameters (electrolyte concentration, current density and air flow rate) on the current efficiency and specific energy consumption for H_2O_2 electrosynthesis process by cathodic reduction of oxygen from NaOH alkaline solutions, on reticulated glassy carbon electrode.

EXPERIMENTAL SECTION

Chemicals

The electrolyte was a NaOH aqueous solution (*Lachema, Czech Republic*) of different concentrations: 1 M, 2 M or 4 M.

The quantity of H_2O_2 obtained during the electrosynthesis process was measured by titration with a 0.0117 N $KMnO_4$ solution.

Experimental equipment

The experimental set up used for H_2O_2 galvanostatic electrolysis on reticulated glassy carbon electrode is presented in fig 1.

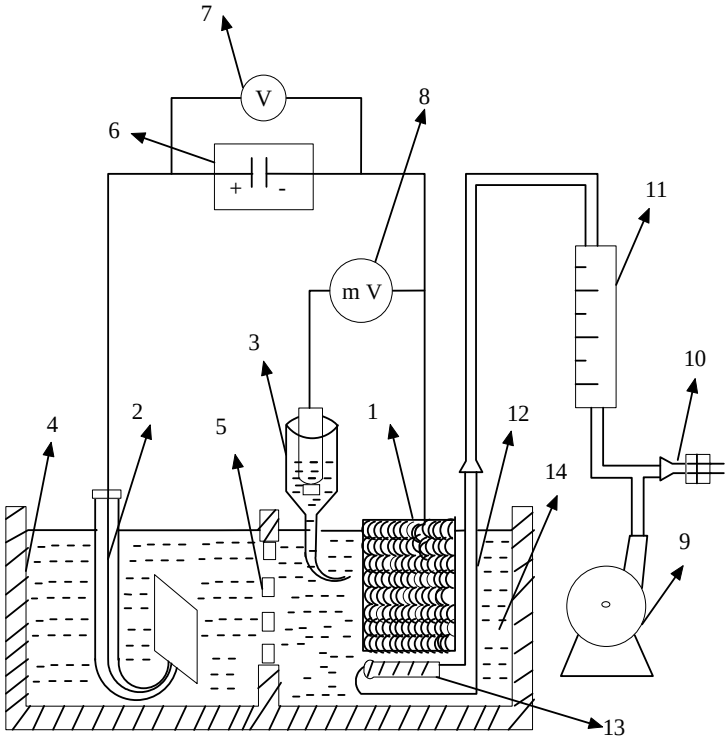

Fig. 1. The experimental set up for galvanostatic electrolysis.

The set up for galvanostatic electrolysis was composed from: 1- reticulated glassy carbon electrode as cathode; 2 - Pt as anode; 3 - saturated calomel electrode (SCE) as reference electrode; 4 - plexiglass electrosynthesis cell (2 compartments, working volume: 2 x 150 ml); 5 - ion exchanging membrane, Nafion® type; 6 - d.c. power source; 7 - voltmeter; 8 - digital milivoltmeter; 9 - air pump; 10 - tap to adjust the air flow rate; 11 - flow rate meter; 12 - air bubbling; 13 - frit; 14 - electrolyte solution (NaOH).

The specific surface of the cathode was 17 cm^2/cm^3. The cathode volume was 7.5 cm^3, which corresponds to a real active surface of the cathode of $17 \cdot 7.5 = 127.5$ cm^2.

RESULTS AND DISCUSSION

In order to determine the current efficiency and the specific energy consumption, preliminary, the experimental quantity of H_2O_2 was evaluated and the theoretical quantity of the electrosynthesized H_2O_2 was calculated.

The experimental quantity of H_2O_2 (m_{exp,H_2O_2}), obtained from the electrosynthesis process, was evaluated according to the following relation:

$$m_{exp,H_2O_2} = C_{KMnO_4} \cdot V_{KMnO_4} \cdot \frac{V_{NaOH}}{V_{sample}} \cdot E_{H_2O_2} \quad \text{(g)} \qquad (3)$$

where: C_{KMnO_4} is the normal concentration of the $KMnO_4$ solution; V_{KMnO_4} is the permanganate volume used for the titration (ml); V_{sample} is the sample volume from the cathodic compartment (ml); V_{NaOH} is the electrolyte volume from the cathodic compartment (ml), $E_{H_2O_2}$ is the equivalent of H_2O_2.

The theoretical quantity of H_2O_2 (m_{th,H_2O_2}) was calculated based on Faraday's law:

$$m_{th,H_2O_2} = I \cdot t \cdot E_{H_2O_2} \cdot \frac{1}{F} \quad \text{(g)} \qquad (4)$$

where: I is the current intensity (A), t is the time of electrosynthesis (s), F is the Faraday constant (96500 C).

The current efficiency of the electrosynthesis process was calculated as the ratio of the experimental and theoretical quantities as H_2O_2:

$$r_F = \frac{m_{exp,H_2O_2}}{m_{th,H_2O_2}} \cdot 100 \quad (\%) \qquad (5)$$

On the other hand, the energy consumption (W) and the specific energy consumption (W_s) were calculated as follows:

$$W = E_B \cdot I \cdot t \qquad (W\ s) \qquad (6)$$

$$W_s = \frac{W}{m_{exp,H_2O_2}} \qquad (kWh/kg\ H_2O_2) \qquad (7)$$

where: E_B represents the cell voltage (V); the meaning of the other symbols has been already presented.

The first experiment was made at constant current density (i = 0.196 mA cm^{-2}) and at constant air flow rate (Q_{air} = 25 l h^{-1}) for three different concentrations of the NaOH electrolyte (1, 2 and 4 M). The obtained results are presented in fig 2.

It can be observed from fig. 2 that the H_2O_2 concentration increases in time for all electrolyte concentrations. However, the increase of NaOH concentration leads to a slower increase of the H_2O_2 concentration. On the other hand, when the electrolyte concentration increases a decrease of the current efficiency corresponding to the electrosynthesis process (fig. 2 B) and, obviously, an increase of the specific energy consumption (fig. 2 C) were observed, due to the decrease of air solubility [3]. This means that it is better to use moderate concentrations of electrolyte in order to obtain a high current efficiency and low energy consumption.

Next, the influence of the current intensity on the H_2O_2 concentration, current efficiency and specific energy consumption obtained at different moments of the electrosynthesis process in NaOH 1M was studied (fig. 3).

The experimental results show that when the current density increases the reaction rate increases and, consequently, a larger quantity of hydrogen peroxide is obtained (fig. 3A). The current efficiency of the process exhibits a flattened maximum at a current intensity of ~ 50 mA. Above this value, the current efficiency decreases, probably due to the side cathodic reaction (hydrogen evolution reaction or complete oxygen reduction to HO^-) (fig. 3B). In the range of high values of current intensities (I > 40 mA) the specific energy consumption reaches a plateau (fig. 3C).

Further, the influence of the air flow rate on the process parameters at two values of the current intensities, 25 and 50 mA, was investigated (fig. 4). Three values of air flow rate were used: 25, 40 and 60 l h^{-1}.

The experimental results show that at 50 mA the increase of the air flow rate has a favourable effect on the H_2O_2 concentration, as well as on the current efficiency and specific energy consumption (fig. 4). Thus, as it can be observed in figure 4 at a current intensity of 50 mA the increase of the air flow rate involves an increase of H_2O_2 concentration and current efficiency, while the specific energy consumption decreases. The best values for the current efficiency were obtained at an air flow rate of 60 l h^{-1}, while the specific energy consumption presents convenient values.

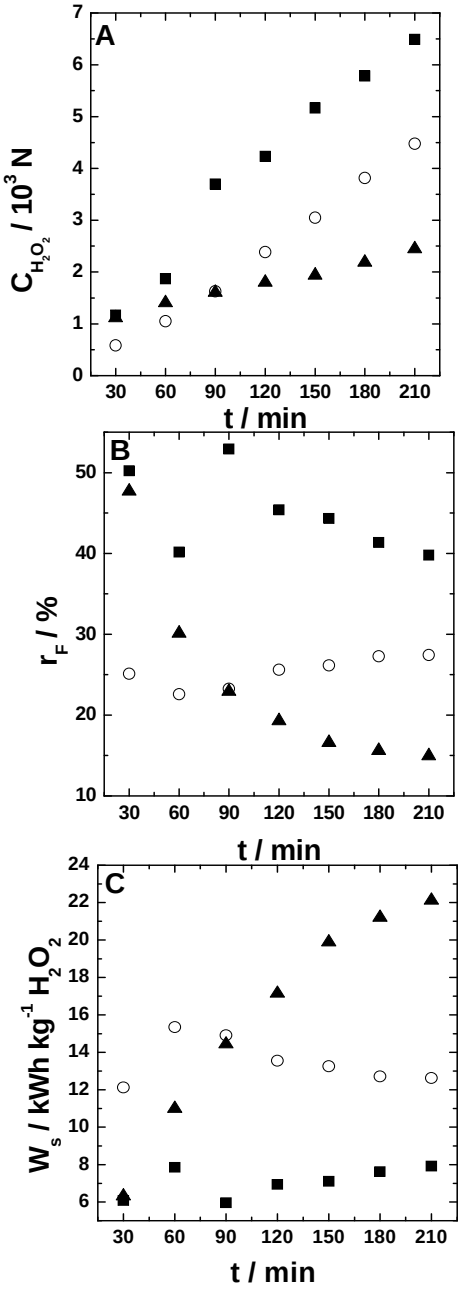

Fig. 2. Evolution of H_2O_2 concentration (A), current efficiency (B) and specific energy consumption (C) during the H_2O_2 electrosynthesis for different NaOH electrolyte concentrations (■ = 1M; ○ = 2M; ▲ = 4M). Experimental conditions: i = 0.196 mA cm^{-2}; Q_{air} = 25 l h^{-1}; room temperature.

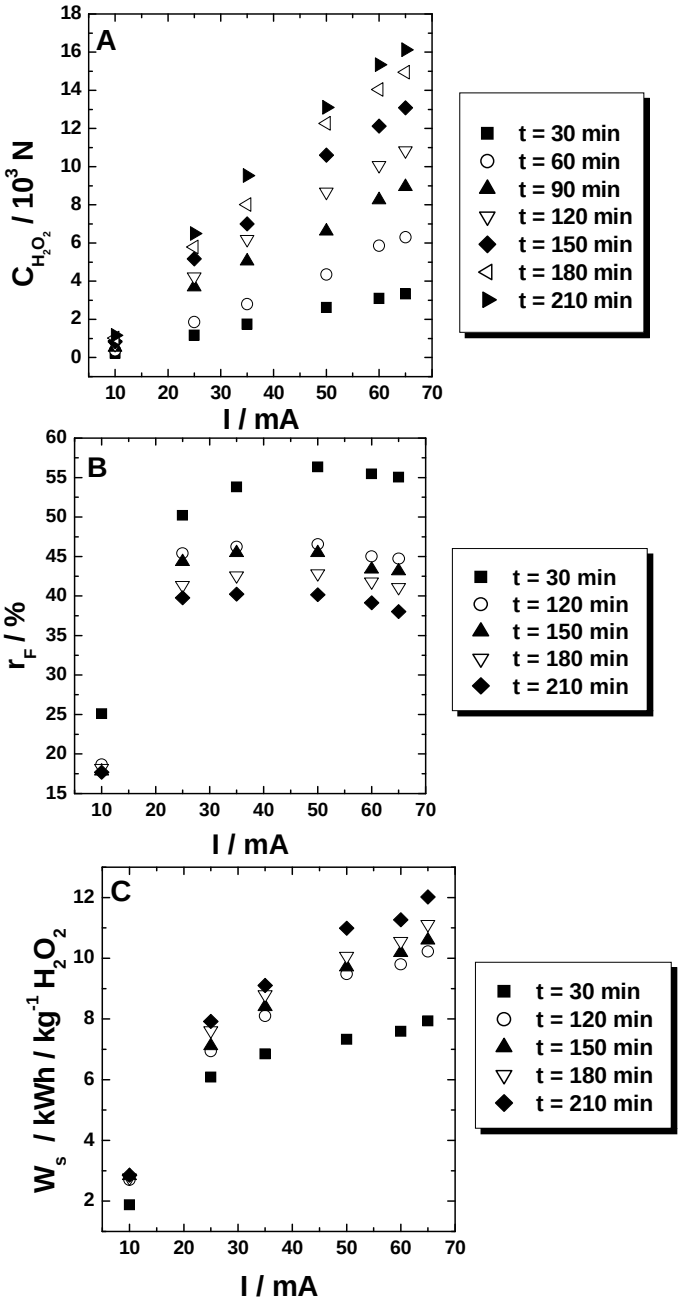

Fig. 3. Influence of the H_2O_2 concentration (A), current efficiency (B) and energy consumption (C) on the current intensity, at different moments of the H_2O_2 electrosynthesis process.
Experimental conditions: electrolyte, 1M NaOH; Q_{air} = 25 l h^{-1}; room temperature.

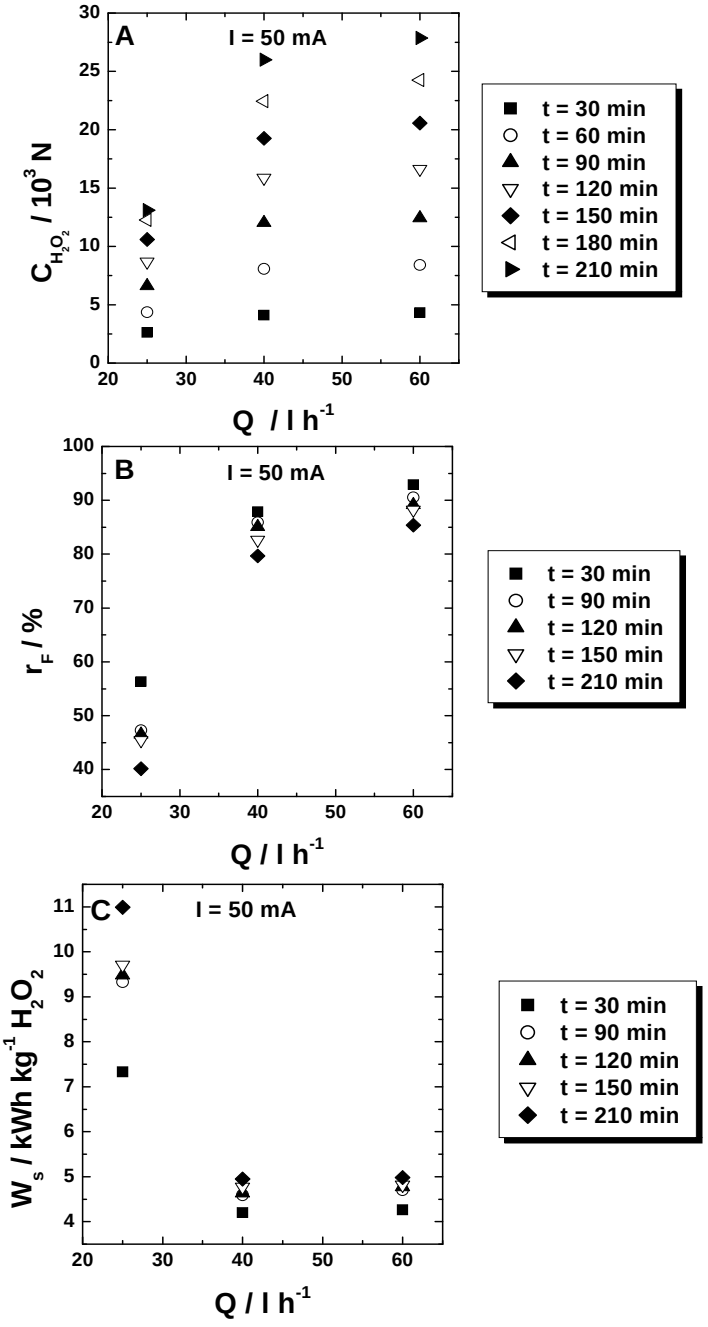

Fig. 4. The dependence of H_2O_2 concentration (A), current efficiency (B) and energy consumption (C) on the air flow rate, at different moments of the electrolysis process. Experimental conditions: electrolyte, NaOH 1M; ambient temperature.

CONCLUSIONS

The study of the H_2O_2 electrosynthesis process by cathodic reduction of oxygen on reticulated glassy carbon electrode in alkaline electrolyte allows formulating the following conclusions:

- The best results (high values of H_2O_2 concentrations and current efficiencies associated with low specific energy consumption) were obtained for a current density of 0.392 mA cm^{-2} and an air flow rate of 60 l h^{-1} when a 1M NaOH solution was used as electrolyte.
- The increase of the current efficiency with the current density and air flow rate is limited by the inherent increase of the specific energy consumption [7].

ACKNOWLEDGEMENTS

Authors thank Professor I. C. Popescu, Department of Physical Chemistry, Babes-Bolyai University, Cluj-Napoca (Romania) for valuable discussions.

REFERENCES

[1] E. E. Kalu, C. Oloman, *J. Appl. Electrochem*., **1990**, 20, 932.

[2] P. Ilea, S. Dorneanu, I. C. Popescu, *J. Appl. Electrochem*., **2000**, 30, 187.

[3] K. Kinoshita, "Electrochemical Oxygen Technology" (J. Wiley & Sons, New York), **1992**, 9, 32.

[4] C. Oloman, "Electrochemical processing for the pulp & paper industry" (The Electrochemical Consultancy, England), **1996**, 145.

[5]. J. Wang, *Electrochim. Acta*, **1981**, 12, 1721.

[6] J. M. Friedrich, C. Ponce-de-Leon, G. W. Reade, F. C. Walsh, *J. Electroanal. Chem*., **2004**, 561, 203.

[7] O. Serdan, PhD Thesis, "Babes-Bolyai" University, Cluj-Napoca, **2004**.

STUDIA UNIVERSITATIS BABEŞ-BOLYAI, CHEMIA, XLIX, 2, 2004

Dedicated to Professor Valer Fărcăşan at his 85th anniversary

REACTIONS OF THE 3-CYANO-10-METHYL-PYRIDO[3,2-g]QUINOLIN-4-ONE

CLAUDIA MOLDOVAN[1], CASTELIA CRISTEA[1], IOAN A. SILBERG[1], ABDALLAH MAHAMOUD[2], CALIN DELEANU[3] and JACQUES BARBE[2]

[1] *"Babeş-Bolyai" University, Faculty of Chemistry and Chemical Engineering, Organic Chemistry Department, Cluj-Napoca, Ro- 400028, Romania*
[2] *Université de la Méditerranée, GERCTOP-UMR CNRS 6009, Marseille, France*
[3] *Institute of Organic Chemistry, National NMR Laboratory, Bucharest, Romania*

ABSTRACT. The reaction of 3-cyano-10-methyl-pyrido[3,2-g]quinoline-4-one **1** with alkylhalides in alkaline conditions under PTC conditions is described. A mixture of N-alkyl- and O-alkyl-3-cyano-10-methyl-pyrido[3,2-g]quinoline was obtained in low yields as a consequence of an ambident nucleophile generated by **1,** while the main competitive reaction appears to be the hydration of the carbonyl bond in alkaline medium.

INTRODUCTION

Interesting biological activity of symmetrically 4,6-bis-alkylated-pyrido[3,2-g]quinoline derivatives was previously reported [1-5]. The chemical synthesis of these compounds was performed starting with 2,8,10-trimethyl-pyrido[3,2-g]quinoline-4,6-dione and various alkylhalides under phase transfer catalysis (PTC) conditions.

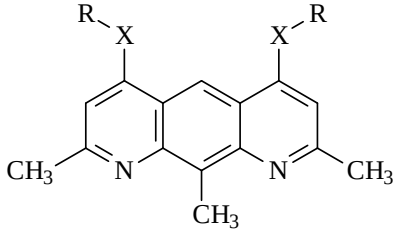

X = O, N, S
R = $-CH_2-CH_2-CH_2-N(CH_3)_2$
$-CH_2-CH_2-N(C_2H_5)_2$

Attempts to synthesize new 4-alkoxy-3-cyano-10-methylpyrido[3,2-g]quinoline **4** by the same method (S_N reaction of alkylhalides using 3-cyano-10-methylpyrido[3,2-g]quinoline-4-one **1** as a nucleophile under PTC conditions) are discussed.

RESULTS AND DISCUSSIONS

3-Cyano-10-methyl-pyrido[3,2-g]quinoline-4-one **1**, synthesized as previously reported and analyzed by NMR and IR spectroscopy [6], was found to present in DMSO solution only one of the two possible tautomeric forms shown in Scheme 1.

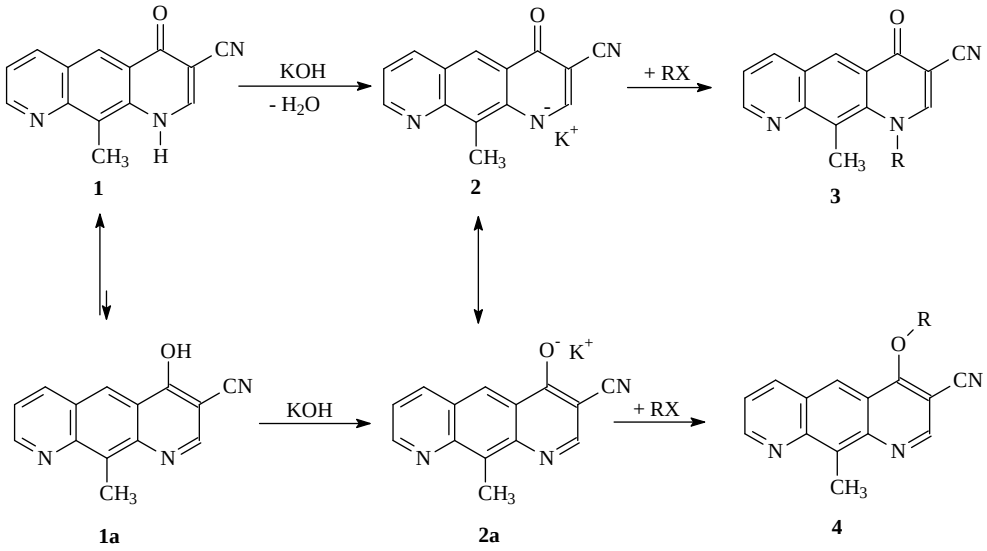

Scheme 1

The acidity of **1**, suggested by the low field signal of the proton (δ = 12.2 ppm in DMSO-d_6 solution) enabled us to propose the formation of the two potassium salts **2** and **2a** (Scheme 1). A high electron density could be expected either to the nitrogen atom in structure **2** or to the oxygen atom in the resonance structure **2a**. This ambident nucleophile could be the reagent in S_N reaction of several alkylchlorides.

The alkylation reaction of **1** was experimented under PTC conditions, using aromatic hydrocarbon solvent (toluene, xylene), concentrated aqueous potassium hydroxide and tetrabutylamonium bromide (TBAB) as phase transfer agent. From the organic layer of the PTC reaction mixture, two alkyl-derivatives were identified by TLC chromatography and analyzed by means of ^{1}H-NMR spectroscopy. After 72 hours reaction time, a mixture of alkyl-derivatives **3** and **4** was obtained (table 1). The overall yield of the alkylation reaction was found to be very low (5%).

Table 1.

Alkylation of **1** under PTC conditions

Alkyl halide RX	**4** :**3** ratio	Solvent (reaction temperature)
Cl-CH_2-CH_2-N(Et)$_2$	1 : 3	toluene (110ºC)
	1 : 3	xylene (130ºC)

In contrast, a large amount of another reaction product separated as a precipitate between the two layers of the PTC reaction mixture. After filtration the precipitate was found to be highly soluble in water. The ^{1}H-NMR analysis of

this reaction product revealed a mixture of two compounds with similar coupling patterns characteristic to 4-substituted-3-cyano-10-methyl-pyrido[3,2-g]quinoline structures separated by slightly different shielding effects ($\Delta\delta_{similar\ H}$= 0.1 ppm) These two compounds, **6** and **2**, were found in 5:1 ratio according to their ^{1}H-NMR signals integrals. A detail containing the aromatic protons region of ^{1}H-NMR spectrum is shown in fig. 1.

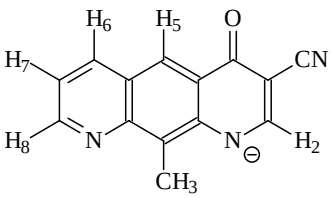

2

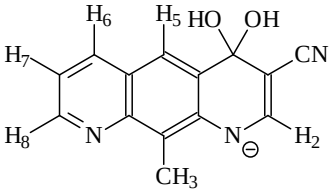

6

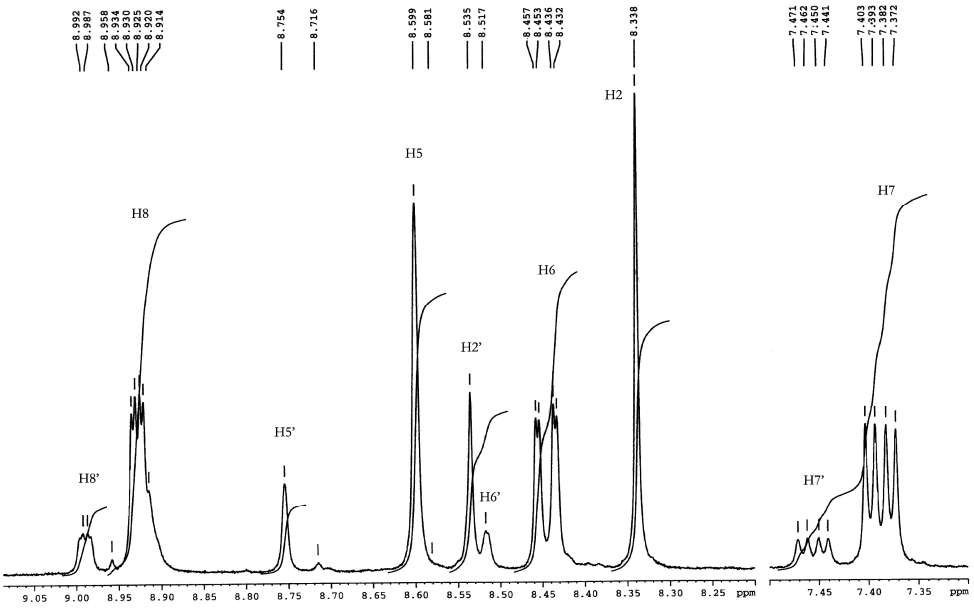

Fig. 1. 400 MHz ^{1}H-RMN of the by-products of PTC reaction.

The two compounds in the mixture are: the potassium salt **2** (scheme 1) and the *geminal*-diol **6** (scheme 2), both obtained in the presence of KOH strong base used in PTC reaction. The hydration of the heterogenous C=O bond could be taken into account, due to the stabilizing effect of the nitrile group which lies in the neighboring position and the electron withdrawing effect of the quinoline moiety in the structure of compound **6**.

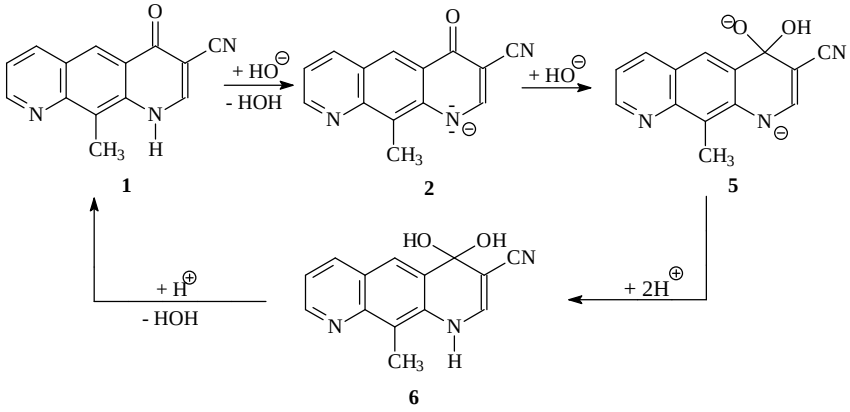

Scheme 2

The diagnosis of hydration was proved by supplementary experimental data. Thus, by the titration of the mixture with NaOH and back titration with HCl a curve with the aspect of a hysteresis loop was obtained (fig. 2).

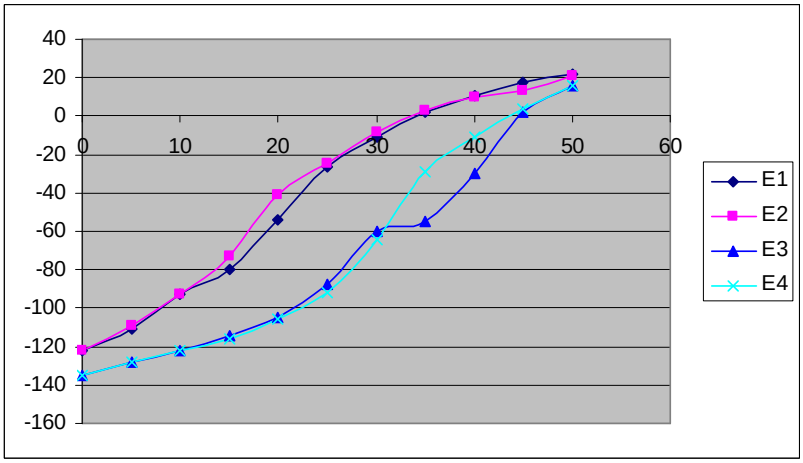

Fig. 2. Titration curve of reaction mixture. E_1: HCl 0,001N titration curve; E_2: HCl 0,001N titration curve registered after 5 min. equilibration time; E_3: NaOH 0,001N titration curve; E_4: NaOH 0,001N titration curve registered after 5 min. equilibration time.

The acido-basic properties of **1** make possible the anion structure **2** to be obtained by the ionization of the acidic N-H group in the presence of one equivalent of NaOH. Subsequently the nucleophilic addition of a OH^- to the heterogenous carbonyl double bond of **2,** may produce the hydrated 3-cyano-10-methyl-pyrido[3,2-g]quinoline-4-one anion **5**. During the back titration, in acidic media, the anion **5** is neutralized to 3-cyano-10-methyl-pyrido[3,2-g]dihydroquinolin-4,4-diol **6**, which regenerates the starting compound **1** by water elimination.

The recorded UV spectrum of the neutral solution (obtained by titration) contains three absorption bands situated at 198, 247 and 279 nm. The same pattern was obtained for the absorption bands of the solution in basic medium. In acidic medium a batochromic shift of 9 nm was recorded for the position of the absorption band situated at the highest wavelength (fig. 3).

According to these UV data we suggest the formation of compound **6** in acidic media; the batochromic shift could be expected for the structure **6** as compared to structures **1** and **2** because of the fact that the cross conjugation of the lone pair of electrons from the nitrogen atom with the carbonyl and nitrile groups is altered.

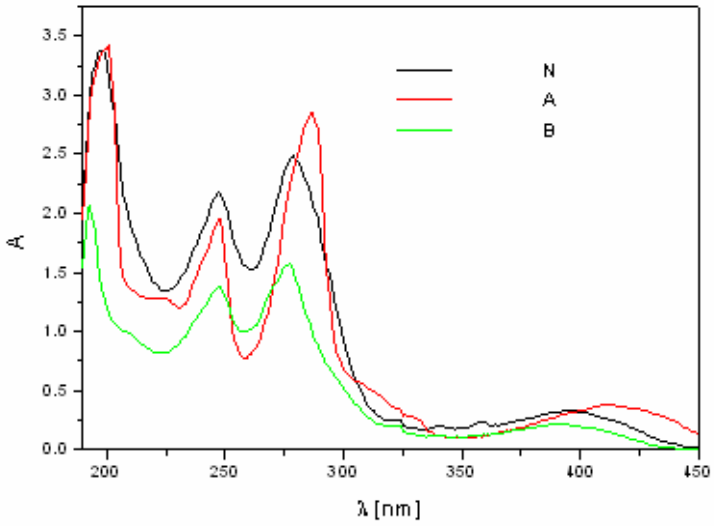

Fig. 3. UV-spectrum of compounds 1, 2 and 6.
N (neutral solution, pH 7), λ[nm] / (ε): 193 (2059), 248 (1373), 277 (1571)
A (acidic solution, pH 1), λ[nm] / (ε): 201 (3424), 248 (1956), 286 (2850)
B (basic solution pH 10), λ[nm] / (ε): 198 (3367), 247 (2174), 279 (2448)

The alkylation reaction of **1** performed under classical conditions (using alkylhalides in the presence of K_2CO_3 in DMF solvent) generated a product completely soluble in water, a fact that enabled us to suggest that a hydration reaction took place.

CONCLUSIONS

Under PTC conditions, in the presence of strong bases such as KOH and NaOH, the hydration of the carbonyl bond in the substrate **1** occurs as the main reaction. As a consequence of an ambident nucleophile structure generated by **1**, the alkylation reaction generates a mixture of N- and O-alkyl-derivatives in low yields.

EXPERIMENTAL

*General procedure for hydration/alkylation reaction of **1** under PTC conditions*

Compound **1** (5 mmol), 2-diethylamino-ethylchlorid hydrochlorid (7 mmol), TBAB (0.2g) were solved in aromatic hydrocarbon solvent (50 mL) and mixed with 25 mL KOH 50% aqueous solution. The reaction mixture was heated under vigorous stirring for 72 hours. After cooling, the abundant precipitate separated between the two layers was filtered off. A white powder (1.03 g, 80% yields) was obtained and it was found to be highly soluble in water.

The two layers of the reaction mixture were separated. The organic layer was washed with water, then dried over anhydrous $MgSO_4$ and the solvent was evaporated in vacuum. 0.08 g, yield 5% crude reaction product was obtained.

3-cyano-10-methyl-pyrido[3,2-g]dihydroquinolin-4,4-diol 6

^{1}H-NMR (DMSO-d_6 solution): 3.01 ppm (s, 3H, -CH_3), 8.92 ppm (dd, 1H, H_8), 7.38 ppm (m, 1H, H_7), 8.44 ppm (dd, 1H, H_6), 8.59 ppm (s, 1H, H_5), 8.33 ppm (s, 1H, H_2)

3-Cyano-1-(2'-diethylaminoethyl)-10-methyl-pyrido[3,2-g]quinolin-4-one 3

^{1}H-RMN ($CDCl_3$ solution): 2.49 ppm (s, 3H, -CH_3), 8.65 ppm (dd, 1H, H_8), 6.92 ppm (m, 1H, H_7), 7.8 ppm (dd, 1H, H_6), 7.42 ppm (s, 1H, H_5), 7.40 ppm (s, 1H, H_2), 3.55 ppm (t, 2H, -CH_2), 3.05 ppm (t, 2H, -CH_2), 2.95 ppm (q, 4H, -CH_2), 2.99 ppm (t, 6H, -CH_3).

3-Cyano-4-(2'-diethylaminoethoxy)-10-methyl-pyrido[3,2-g]quinoline 4

^{1}H-NMR ($CDCl_3$ solution): 2.99 ppm (s, 1H, -CH_3), 8.9 ppm (dd, 1H, H_8), 7.3 ppm (m, 1H, H_7), 8.19 ppm (dd, 1H, H_6), 8.62 ppm (s, 1H, H_5), 8.75 ppm (s, 1H, H_2), 4.4 ppm (t, 2H, -CH_2), 2.38 ppm (t, 2H, -CH_2), 2.14 ppm (q, 4H, -CH_2), 0.51 ppm (t, 6H, -CH_3).

The hysterezis curve was obtained by potentiometric titration of 0.117 g precipitate solved in 50 mL of distilled water, with HCl solution (0.001N). The back titration was performed with NaOH solution 0.001N.

The UV spectra were recorded on a UNICAM Helios β spectrophotometer.

NMR spectra were recorded on a 400 MHz Bruker spectrometer.

ACKNOWLEDGMENT

Agence Universitaire de la Francofonie (AUF) is greatly acknowledged for financial support (FICU 2001/PAS21)

REFERENCES

1. Molock F., Boykin D.W. The synthesis of pyridoquinolines with di-alkylaminopropylamine side chains. *J. Heterocycl. Chem.* **1983**, 20, 681-686.
2. A. Mahamoud, M. Kayirere, J. P. Galy, J. Barbe, D. Sharples, M. Richardson, G. Atassi, Synthesis, intercalation into DNA and anticancer activity of some 4,6-dialkoxy-10-methyl-pyrido[3,2-g]quinolines, *Heterocycl. Commun*. **1994**, 1, 47-50.
3. Matias C., Mahamoud A., Barbe J., Pradines B., Doury J.C. Synthesis and antimalarial activity of new 4,6-dialkoxy and 4,6-bis(alkylthio)pyrido[3,2-*g*]quinoline derivatives. *Heterocycles* **1996**, 43, 1621-1632.
4. Chevalier J., Atifi S., Eyraud A., Mahamoud A., Barbe J., Pages J.M. New pyridoquinoline derivatives as potential inhibitors of the fluoroquinolone efflux pump in resistant Enterobacter aerogenes strains. *J. Med. Chem.* **2001**, 44, 4023-4026.
5. S. Gallo, S. Atifi, A. Mahamoud, C. Santelli-Rouvier, K. Wolfart, J. Molnar, J. Barbe, Synthesis of aza mono, bi and tricyclic compounds. Evaluation of their anti MDR activity, *Eur. J. Med. Chem.* **2003**, 38, 19-26.
6. C. Moldovan, C. Cristea, I. A. Silberg, A. Mahamoud, C. Deleanu, J. Barbe, A convenient route to 1,4-dihydro-3-cyano-10-methyl-pyrido[3,2-g]-quinoline derivatives as key-intermediates for the synthesis of novel MDR reversal agents, sent to *Heterocycl. Commun.* **2003**.

STUDIA UNIVERSITATIS BABEŞ-BOLYAI, CHEMIA, XLIX, 2, 2004

Dedicated to Professor Valer Fărcăşan at his 85th anniversary

GRAPHITE ELECTRODE MODIFIED BY CHARGE TRANSFER COMPLEX BETWEEN TETRACYANOQUINODIMETHANE AND 16*H*,18*H*-DIBENZO[c,1]-7,9-DITHIA-16,18-DIAZAPENTACENE USED FOR NADH ELECTRO-OXIDATION

DELIA GLIGOR[a], MARIUS SOCOL[a], IONEL CATALIN POPESCU*[a], CASTELIA CRISTEA[b], IOAN ALEXANDRU SILBERG[b]

[a]Department of Physical Chemistry, [b]Department of Organic Chemistry, Faculty of Chemistry and Chemical Engineering, Babes-Bolyai University of Cluj, 11 Arany Janos Str., 400028 Cluj-Napoca, Romania. E-mail: cpopescu@chem.ubbcluj.ro

ABSTRACT. The electrochemical behavior of a new charge transfer complex between 7,7,8,8-tetracyanoquinodimethane and 16*H*,18*H*-dibenzo[c,1]-7,9-dithia-16,18-diaza-pentacene adsorbed on spectrographic graphite has been investigated. Cyclic voltammetry measurements, performed in aqueous buffer solutions at different potential scan rates and pH values, pointed out to a quasi-reversible, surface confined redox process. The voltammetric response involves the transfer of $1e^-/1H^+$, with a heterogeneous rate constant of 26.8 s^{-1} (pH 7.0). The modified electrodes showed a good electrochemical stability as well as moderate electrocatalytic activity toward NADH electro–oxidation.

Keywords: NADH oxidation, charge transfer complex, modified electrodes, TCNQ, phenothiazine derivatives.

INTRODUCTION

The electrochemical oxidation of β-nicotinamide adenine dinucleotide (NADH) has been extensively investigated, its efficient and reversible recycling being of particular interest for the construction of NADH-dependent dehydrogenase based amperometric biosensors and for energy conversion *via* biofuel cell [1-3].

It is known that the direct electro-oxidation of NADH at many bare electrodes is complicated and requires a large overvoltage [4-6], which results in the interference from more easily oxidizable species. Additionally, the adsorbed molecules of NAD^+ could cause electrode fouling at NADH concentration above 0.1 mM [1]. The most efficient way to realize the NADH electro-oxidation at low overvoltages is the use of mediators immobilized on the electrode surface.

Many redox couples could be used as mediators for NADH oxidation, because of the low value of the formal potential ($E^{0'}$) of NAD^+/NADH redox couple (–315 mV *vs.* NHE, at pH 7 and 25^0 C) [7]. In spite of this, only a restricted number of compounds have been selected in order to obtain modified electrodes for electrocatalytic oxidation of NADH [1,2,8,9]. Among these, organic dyes, i.e. phenazines, phenoxazines and phenothiazines derivatives, were used frequently to design efficient electrocatalytic schemes for NADH recycling [10-14]. However, these mediators suffer because of their chemical/electrochemical instability, especially at high pH values [8].

In order to improve the operational stability of NADH sensors, two different approaches have been proposed: (i) more efficient immobilization of the mediator by its electropolymerization [15], by using a polymeric film as an entrapment matrix [8,16] or as a diffusion barrier [1,17]; (ii) improvement of the mediator behavior, as for example by decreasing the mediator reactivity *via* enlarging the intramolecular conjugation system [18,19], by introduction of withdrawing (-I) substituents [20,21], or using charge-transfer complexes between a component, acting as electron donor and an electronegative component acting as an electron acceptor [8].

In this context, based on the fact that the phenothiazine and its derivatives are good electron donors, suitable for forming numerous charge transfer complexes with different electron acceptors, in this work a charge transfer complex (CTC) between 7,7,8,8-tetracyanoquinodimethane (TCNQ) and 16*H,*18*H*-dibenzo[c,1]-7,9-dithia-16,18-diaza-pentacene (DDDP) was investigated as a redox mediator for NADH electro-oxidation. The electrochemical behavior and stability of the CTC adsorbed on spectrographic graphite were investigated by cyclic voltammetry (CV) in different experimental conditions (various potential scan rates and pH values). Finally, using CV measurements, the CTC modified graphite electrodes were examined for their electrocatalytic activity toward NADH oxidation.

EXPERIMENTAL SECTION

Materials

The charge transfer complex (CTC) between 7,7,8,8-tetracyanoquinodimethane (TCNQ) and 16*H,*18*H*-dibenzo[c,1]-7,9-dithia-16,18-diaza-pentacene (DDDP) (see Scheme 1) was synthesized according to a previously published procedure [22].

β-Nicotinamide adenine dinucleotide, reduced form (NADH), was purchased from Sigma (St. Louis, MO, USA) as disodium salt. Phosphate buffer solutions were prepared using $Na_2HPO_4 \cdot 2H_2O$ and $NaH_2PO_4 \cdot H_2O$ from Merck (Darmstadt, Germany). All other reagents were of analytical grade and used as received.

The supporting electrolyte was a 0.1 M phosphate buffer solution. The pH value was adjusted using the appropriate H_3PO_4 or NaOH solutions.

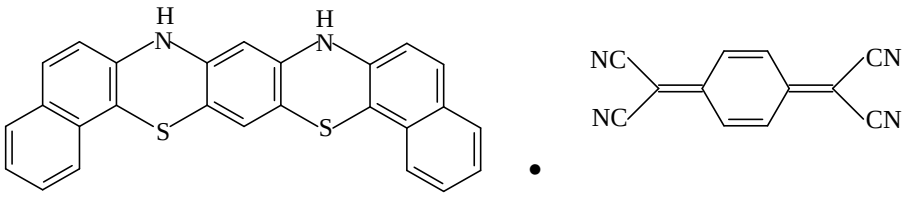

DDDP **TCNQ**

Scheme 1. CTC of DDDP-TCNQ formula.

Electrode preparation

A spectrographic graphite rod (Ringsdorff-Werke, GmbH, Bonn-Bad Godesberg, Germany), of ~3 mm diameter, was wet polished on fine (grit 400 and 600) emery paper (Buehler, Lake Bluff, Ill., USA). Then, a graphite piece of suitable length was carefully washed with doubly distilled water, dried, and finally press-fitted into a PTFE holder in order to obtain a graphite electrode, having in contact with the solution a flat circular surface of ~ 0.071 cm^2.

The modified graphite electrodes were obtained by spreading onto the electrode surface 5 µl of 10 mM CTC solution in dimethylformamide, and leaving them for 20 minutes at room temperature to evaporate the solvent. Before immersion in the test solution, the modified electrodes were carefully washed with doubly distilled water.

For each electrode, the surface coverage (Γ, mol cm^{-2}) was estimated from the under peak areas, recorded during the CV measurements at low scan rate ($v < 10$ mV s^{-1}), and considering the surface redox valence equal to unity [23]. All presented results are the average of at least 3 identically prepared electrodes, if not otherwise mentioned.

Electrochemical measurements

CV measurements were carried out in a conventional three-electrode electrochemical cell. A saturated calomel electrode (SCE) and a coiled Pt wire served as reference and counter electrode, respectively. The cell was connected to a computer-controlled voltammetric analyzer (Autolab-PGSTAT10, Eco Chemie, Utrecht, The Netherlands).

RESULTS AND DISCUSSION

1. Electrochemical behavior of the CTC-modified graphite electrode

The electrochemical behavior of CTC adsorbed on spectrographic graphite (G/CTC) was investigated using CV measurements, performed in different experimental conditions. As can be seen from Figure 1, the cyclic voltammogram recorded for G/CTC electrode is similar with that recorded for DDDP, presenting one wave with the formal standard potential placed at ~ 265 mV *vs.* SCE (pH 7.0). This similarity proves a reduced intermolecular interaction between DDDP and TCNQ in CTC.

The electrochemical parameters for different pH values, summarized in Table 1, point to a quasi-reversible, one-electron process. The discrepancies

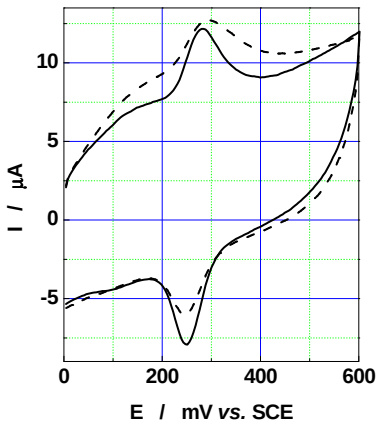

Fig. 1. Voltammetric response of CTC (—) and DDDP (---) adsorbed on spectrographic graphite. Experimental conditions: starting potential, 0 mV *vs.* SCE; scan rate, 50 mV s^{-1}; supporting electrolyte, 0.1 M phosphate buffer, pH 7.0; surface coverage, see Table 1.

between the theoretical value of the peak width at half peak height (E_{FHWM} = 90.6/n mV) and the corresponding experimental values as well as $\Delta E_p \neq 0$ (Table 1) prove the existence of some interactions between the surface-confined redox species [24,25].

Table 1.

Electrochemical parameters of the voltammetric response of CTC, adsorbed on spectrographic graphite. Experimental conditions: as in fig. 1.

pH	ΔE_{peak} (mV)	E_{FWHM} (mV)		I_{pa}/I_{pc}	Surface coverage (nmol cm^{-2})
		anodic	cathodic		
3	38	95	91	1.09	0.9
5	53	124	87	0.69	0.7
7	37	95	70	0.68	0.7
9	57	124	111	1.01	1.3

As expected for surface confined redox active species [25], the cyclic voltammograms recorded for a wide range of potential scan rates (0.01 – 3.2 V s^{-1}) showed a linear dependence of the peak currents (I_p) on the electrode potential scan rate (v) (Figure 2, Table 2). Also, the slope of log I_p *vs.* log v dependence was close to one, confirming once more the existence of adsorbed species. The number of electrons involved in the redox process, estimated from the I_p *vs.* v dependence [26], was found close to 1 (within ± 10 %), in accordance with the predicted value for the cation radical formation.

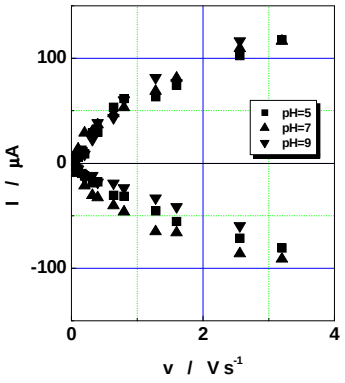

Fig. 2. Peak current dependence on the potential scan rate for the voltammetric response of CTC-modified graphite electrodes. Experimental conditions: starting potential, –1000 mV *vs.* SCE; scan rate, 50 mV s^{-1}; supporting electrolyte, 0.1 M phosphate buffer, pH 7.0; surface coverage, see Table 2.

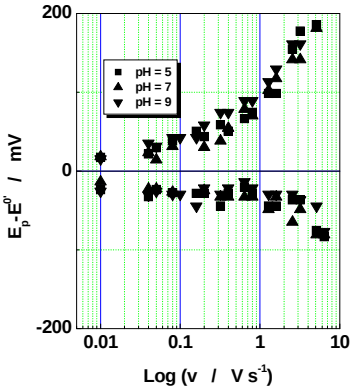

Fig. 3. (E_p - $E^{o'}$) *vs.* logarithm of the scan rate dependence for CTC adsorbed on spectrographic graphite. Experimental conditions: surface coverage, see Table 3; other conditions, see Fig. 1.

Table 2.

Linear regression parameters for the dependence of the peak current on the potential scan rate (0.01 to 0.64 V s^{-1}), observed for CTC-modified graphite electrodes. Experimental conditions: as in fig. 2.

pH	Slope (10^6 A V s^{-1})		R / no. of exp. points		Surface coverage (nmol cm^{-2})
	oxidation	reduction	oxidation	reduction	
3	29.9 ± 2.2	-46.6± 2.8	0.971 / 13	0.981 / 13	0.7 ± 0.2
5	81.1 ± 3.4	-39.8 ± 3.0	0.992 / 11	0.981 / 11	2.2 ± 0.3
7	64.9 ± 6.0	-49.4 ± 6.0	0.967 / 10	0.945 /10	1.1 ± 0.3
9	67.2 ± 3.6	-24.4 ± 2.3	0.985 / 12	0.959 / 12	1.6 ± 0.5

Table 3.

Kinetic parameters for the heterogeneous electron transfer at CTC-modified graphite electrodes. Experimental conditions: as in fig. 3.

pH	k_s (s^{-1})	α	R / no. of exp. points		Surface coverage (nmol cm^{-2})
			oxidation	reduction	
3	38.6	0.44	0.918 / 4	0.966 / 4	1.3 ± 0.4
5	37.5	0.65	0.956 / 5	0.972 / 4	0.5 ± 0.02
7	26.8	0.43	0.979/ 5	0.999 / 5	0.5 ± 0.1
9	42.3	0.65	0.982 / 6	0.986 / 3	1.3 ± 0.4

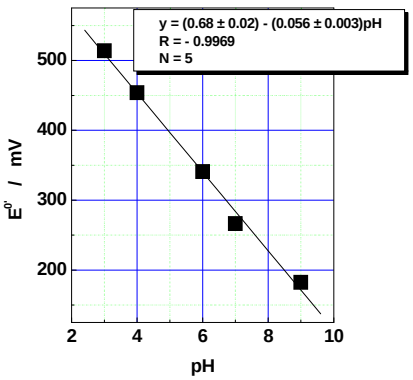

Fig. 4. pH dependence of the standard formal potential for CTC-modified electrodes. Experimental conditions: starting potential, -1000 mV *vs.* SCE; scan rate, 50 mV s^{-1}; supporting electrolyte, 0.1 M phosphate buffer.

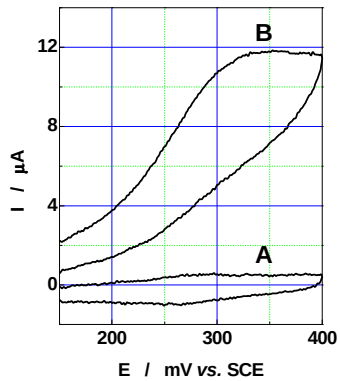

Fig. 5. Electrocatalytic oxidation of NADH at CTC-modified graphite electrode: (A) 0.1 M phosphate buffer, pH 7.0; (B) 0.1 M phosphate buffer containing 5 mM NADH. Experimental conditions: starting potential, +150 mV *vs.* SCE; scan rate, 5 mV s^{-1}; surface coverage, ~ 2.2·nmol cm^{-2}.

The heterogeneous electron transfer rate constant (k_s, s^{-1}) was estimated at different pH values (Table 3) using the treatment proposed by Laviron [27] (Figure 3). Within the experimental error, the heterogeneous electron transfer rate constant (k_s) and the transfer coefficient (α) are not significantly affected by the pH, being equal to 26.8 s^{-1} and 0.43, respectively (pH 7). The k_s value is close to that obtained for DDDP (30.1 s^{-1}) [19], indicating the weak influence of TCNQ presence on the redox behavior of DDDP.

As expected for the redox behavior of an N-unsubstituted phenothiazine moiety-containing compound [28], the CTC formal redox potential ($E^{0'}$, estimated as the average of cathodic and anodic peak potentials) was found to be pH-dependent (Figure 4). The slope (~ 56 mV/ΔpH) of the regression line, corresponding to the $E^{0'}$ – pH dependence, obtained from the experimental data within a wide pH range (3 – 9), proved that in the redox process is involved an equal number of electrons and protons. Therefore, the voltammetric response corresponding to the formation of the CTC cation radical, involves a $1e^-/1H^+$ transfer.

2. Electrocatalytic activity of the CTC-modified graphite electrode

Starting from the favorable electrochemical behavior of CTC adsorbed on graphite, its electrocatalytic activity was tested by cyclic voltammetry. Figure 5 presents the cyclic voltammograms (v = 5 mV s^{-1}) obtained for G/CTC electrodes in the absence and in the presence of 5 mM NADH. In the presence of NADH it can be observed a remarkable enhancement of the anodic peak current, associated with the progressive diminishing of the cathodic one, proving good CTC electrocatalytic effect for NADH oxidation. The electrocatalytic efficiency, estimated as the $(I_{cat})_{NADH}/(I_{cat})$ ratio, at an applied potential of +300 mV *vs.* SCE, was found equal to 28. This value is comparable with that obtained for DDDP (24.3, measured at + 320 mV *vs.* SCE), reflecting again the reduced influence of TCNQ in CTC complex. Taking as reference the potential for NADH electro-oxidation at bare graphite electrodes [5,29,30], an overpotential decrease higher than 100 mV was noticed.

3. Chemical and electrochemical stability of the CTC-modified graphite electrode

The stability of modified electrodes was tested by measuring the variation of mediator electrochemical signal in a defined time range. It is known that the immobilization stability of a mediator on graphite electrodes is decided by the number of conjugated aromatic rings from molecule, therefore the mediator which contains more aromatic rings will lead to the obtaining of a more stable modified electrode. Additionally, the strong interaction between the graphite surface and phenothiazine derivatives (the superposition between π electrons of graphite and the mediator) determines a fast charge transfer between the electrode and mediator [10,31]. The stability of G/CTC electrodes was tested chemically and electrochemically.

Chemical stability of G/CTC electrodes was studied by keeping the electrode at room temperature, and during the time the electrodes were periodically tested. The CTC-modified electrodes presented a voltammetric response after 7 days, but a weak decrease of the surface coverage (~ 85 %) could be observed.

This result proves the utility of CTC strategy in order to increase the stability of DDDP-modified electrodes [32].

Several reasons could be responsible for the electrochemical instability of the G/CTC-modified electrode: (i) the CTC intrinsic electrochemical instability enhanced by the pH increase and applied potential and (ii) the mediator desorption.

The electrochemical stability tests of the G/CTC were realized in potentiodynamic conditions: the electrode potential was continuously cycled within the potential range covering the domain of the mediator redox activity, at different pH values of the contact solution. From the recorded voltammograms a progressive decrease of the electrode surface coverage was observed, while the voltammogram shape remains invariant (results not shown). This behavior proves both the good CTC electrochemical stability in the potential range used for the NADH recycling, and its relatively strong adsorption on the graphite surface.

The kinetic interpretation of the deactivation process showed that it obeys a first-order kinetics. The slopes of kinetic plots were used to determine the values of the deactivation rate constants, as an average of the anodic and cathodic processes (Table 4). Surprisingly, as can be seen from Table 4, at higher pH values the deactivation process is slower, recommending CTC modified electrodes as very useful for the development of NADH amperometric sensors. However, the electrochemical stability of CTC was inferior to that observed for DDDP ($1.8 \cdot 10^{-14}$ mol cm^{-2} s^{-1}; phosphate buffer pH 7). This higher instability of the CTC-modified graphite electrodes could be due to a weaker adsorption of CTC on graphite surface in comparison with DDDP [32].

Table 4.

Deactivation rate constants for CTC-modified graphite electrodes. Experimental conditions: scan rate, 50 mV s^{-1}; supporting electrolyte, 0.1 M phosphate buffer, pH 7.0; time range, 0 - 500 s.

pH	$\Gamma_{(t=0)}$ (10^{10} mol cm^{-2})		k_{deact} (10^{14} mol cm^{-2} s^{-1})	R / no. of exp. points	
	anodic	cathodic		anodic	cathodic
4	9.1 ± 0.5	3.9 ± 0.1	75.1	0.9740 / 5	0.9331 / 5
7	9.9 ± 0.1	8.01 ± 0.05	12.3	0.9053 / 5	0.9799 / 5
8	10.9 ± 0.04	9.07 ± 0.01	4.5	0.8509 / 4	0.9970 / 4

CONCLUSIONS

The adsorption on graphite of a charge transfer complex between 7,7,8,8-tetracyanoquinodimethane and 16*H*,18*H* dibenzo[c,1]-7,9-dithia-16,18-diazapentacene resulted in modified electrodes for NADH oxidation.

The linear dependence between peak current (I_p) and the potential scan rate (v), corroborated with the slope of standard formal potential linear regression ($E^{0'}$) *vs.* pH, proves the existence of a redox couple adsorbed on electrode surface involving $1e^-/1H^+$.

The study of chemical and electrochemical stability of CTC adsorbed on graphite evidences a higher chemical stability of CTC in comparison with DDDP, confirming the proposed strategy to increase the stability of modified electrodes.

The CTC-modified graphite electrodes present a moderate electrocatalytic activity towards NADH oxidation, the electrocatalytic efficiency suggesting the possibility of using them as amperometric sensors for NADH.

ACKNOWLEDGEMENTS

Financial support from the Romanian Academy (Grant 43/2003) and CNCSIS (Grant A – 32/1716 – 2003) is gratefully acknowledged.

REFERENCES

[1] I. Katakis, E. Domínguez, *Mikrochim. Acta*, **1997**, 126, 11.
[2] M. J. Lobo, A. J. Miranda, P. Tunon, *Electroanalysis*, **1997**, 9, 191.
[3] G. T. R. Palmore, H. Bertschy, S. H. Bergens, G. M. Whitesides, *J. Electroanal. Chem.*, **1998**, 443, 155.
[4] H. Jaegfeldt, *J. Electroanal. Chem.*, **1980**, 110, 295.
[5] J. Moiroux, P. J. Elving, *Anal. Chem.*, **1978**, 50, 1056.
[6] Z. Samec, P. J. Elving, *J. Electroanal. Chem.*, **1983**, 144, 217.
[7] H. K. Chenault, G. M. Whitesides, *Appl. Biochem. Biotechnol.*, **1987**, 14, 147.
[8] L. Gorton, *J. Chem. Soc., Faraday Trans. 1*, **1986,** 82, 1245.
[9] P. N. Bartlett, P. Tebbutt, R. G. Whitaker, *Prog. Reaction Kinetics*, **1991**, 16, 55.
[10] L. Gorton, A. Torstensson, H. Jaegfeldt, G. Johansson, *J. Electroanal. Chem*., **1984**, 161, 103.
[11] J. Kulys, G. Gleixner, W. Schuhmann, H. -L. Schmidt, *Electroanalysis*, **1993**, 5, 201.
[12] L. T. Kubota, L. Gorton, *Electroanalysis*, **1999**, 11, 719.
[13] L. Gorton, E. Dominguez, *Rev. in Mol. Biotechnol.*, **2002**, 82, 371.
[14] L. Gorton, E. Dominguez, "*Electrochemistry of NAD(P)+/NAD(P)H"*, in *"Encyclopedia of Electrochemistry"*, G. S. Wilson (ed.), J. Wiley, New York, **2002**, vol. 9, pp. 67-143.
[15] A. A. Karyakin, E. E. Karyakina, W. Schuhmann, H.-L. Schmidt, S. D. Varfolomeyev, *Electroanalysis*, **1994**, 6, 821.
[16] C. Degrand, L. L. Miller, *J. Am. Chem. Soc.*, **1980**, 102, 5728.
[17] M. J. Lobo, A. J. Miranda, P. Tunon, *Electroanalysis*, **1996**, *8*, 591.
[18] N Urasaki, S. Yoshida, T. Ogawa, K. Kozawa, T. Uchida, *Bull. Chem. Soc. Jpn.*, **1994**, 67, 2024.
[19] D. Dicu, L. Muresan, C. Cristea, I. A. Silberg, I. C. Popescu, *Electrochim. Acta*, **2000**, 45, 3951.
[20] D. Gligor, L. Muresan, I. C. Popescu, I. A. Silberg, *Rev. Roum. Chim.*, **2002**, 47(10-11), 953.
[21] D. Gligor, L. Muresan, I. C. Popescu, I. A. Silberg, *Rev. Roum. Chim.*, **2003**, 48(6), 463.
[22] C. Cristea, I. A. Silberg, *Stud. Univ. Babes-Bolyai, Chemia*, **1997,** *42*, 111.
[23] H. Huck, *Phys. Chem. Chem. Phys.*, **1999**, 1, 855.
[24] E. Laviron, L. Roulier, *J. Electroanal. Chem*,. **1980,** 115, 65.
[25] R.W. Murray, *"Introduction to the Chemistry of Molecularly Designed Electrode Surfaces"*, in "*Techniques of Chemistry*", W.H. Saunders, Jr., (ed.), J. Wiley **1992**, vol. XXII, pp. 9.
[26] R.W. Murray, *"Chemically Modified Electrodes"*, in *"Electroanalytical Chemistry*", A. J. Bard (ed.), M. Dekker, New York, **1983**, vol. 13, pp. 191.
[27] R. Laviron, *J. Electroanal. Chem.*, **1979**, 101, 19.
[28] G. Cauquis, A. Deronzier, J.-L. Lepage, D. Serve, *Bull. Soc. Chim. France*, **1977**, 295.
[29] H. Jaegfeldt, T. Kuwana, G. Johansson, *J. Am. Chem. Soc.*, **1983**, 105, 1805.
[30] A. Torstensson, L. Gorton, *J. Electroanal. Chem.*, **1981**, 130, 199.
[31] L. Gorton, G. Johansson, A. Torstensson, *J. Electroanal. Chem.*, **1985**, 196, 81.
[32] D. Gligor, "*PhD thesis"*, University "Babes-Bolyai" Cluj-Napoca, **2002**.

STUDIA UNIVERSITATIS BABEŞ-BOLYAI, CHEMIA, XLIX, 2, 2004

Dedicated to Professor Valer Fărcăşan
at his 85th anniversary

NEW MACROCYCLES INCLUDING SPIRO-1,3-DIOXANE UNITS AS IONOPHORES FOR CATION SELECTIVE ELECTRODES

LILIANA OLENIC[1], GHEORGHE MIHĂILESCU[1], STELA PRUNEANU[1], ION GROSU[2], ELENA BOGDAN[2], LUMINITA DAVID[2], SIMINA DREVE[1]

[1] National Institute for R&D of Isotopic and Molecular Technologies, Donath Street, no. 71-103, POBox 700, R-400293, Cluj-Napoca, Romania
[2] "Babeş-Bolyai" University, Organic Chemistry Department, 11 Arany Janos Street, 400028 Cluj-Napoca, Romania

ABSTRACT. The paper is concerned with preliminary studies on new macrocycles-"monomers and dimers"-containing spiro-1,3-dioxane units as ionophores for poly(vinyl chloride) membranes for potentiometric sensing of sodium, potassium, calcium and magnesium ions. The best macrocycles were evaluated for each cation.

The optimum membrane composition and the appropriate preparation procedure for obtaining the electrodes with good electrochemical characteristics were closely followed.

INTRODUCTION

A large and diverse range of ligands[1] (hosts for metal ions and neutral molecules) has been prepared, exhibiting both remarkable selectivity and useful reactivity properties. The crown ethers are among the simplest and most appealing macrocyclic (large ring) ligands.

The interplay of complex stability and cation exchange kinetics is very important in the uses of supramolecular cation hosts. On the basis of their behaviour, we may distinguish between cation receptors (slow kinetics, large stability constants) and cation carriers (fast kinetics, lower stability). The crown ethers[2] are among the important ionophores for ion-selective electrodes.

This type of electrodes is widely used for blood-electrolyte analysis[3].

Some papers[4] has indicated that the hospitals would carry out 50-200 analyses of cations on each working day.

In view of medical applications or environmental analysis the development of cheap and small Na^+, K^+, Ca^{2+}, Mg^{2+}- sensors[5] are of interest.

Many authors[6-8] achieve low detection limits for determination of these cations.

Our paper is concerned with preliminary studies on new synthesized ligands as ionophores for potentiometric sensing of cations (sodium, potassium, calcium and magnesium).

EXPERIMENTAL

Materials:

The reagent and materials used were obtained from: potassium tetrakis(4-chlorophenyl)borate and 2-nitrophenyl octyl ether (NPOE)- Fluka, Switzerland; sodium chloride p.a., potassium chloride p.a., calcium nitrate p.a., magnesium nitrate p.a., poly(vinylchloride) (PVC-high molecular weight), ionophores - Romania, tetrahydrofuran (THF) p.a.- Carlo Erba, Italy. The THF was distilled before use for removing 2,6-di-*tert*-butyl-*p*-cresol.

The ionophores were synthesized as described previously[9] (Figure 1). The monomeric and dimeric macrocycles **2b**, **3b**, **4a**, **4b**, **5a**, **5b**, **6a** and **7a** were used in our experiments as ligands for cations[10].

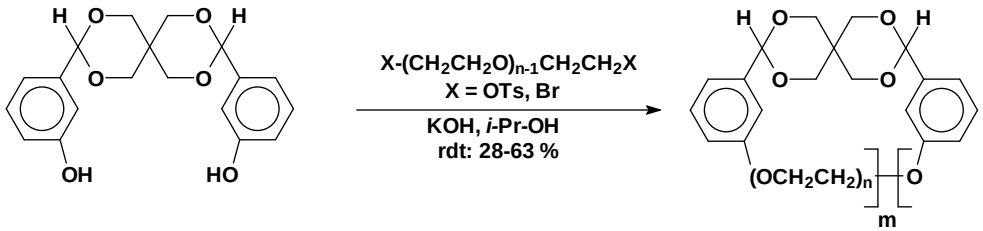

1

n = 1, m = 2	**2b**	
n = 2, m = 2	**3b**	
n = 3, m = 1	**4a**; m = 2	**4b**
n = 4, m = 2	**5a**; m = 2	**5b**
n = 5, m = 2	**6a**; m = 2	**6b**
n = 6, m = 2	**7a**; m = 2	**7b**

Figure 1

Preparation of membranes:

PVC membranes were prepared by a standard procedure using the following compositions as presented in Table 1.

Table 1

PVC membranes compositions

Composition	Cation			
	Sodium	Potassium	Calcium	Magnesium
Ionofor (%)	6,50	1,00	1,00	1,40
2-Nitrophenyl octyl ether (%)	66,70	67,00	65,60	64,50
PVC (%)	26,80	31,70	32,80	33,10
Potasiumtetrakis(4-chlorophenyl)borate (%)	-	0,30	0,60	1,00

The membrane components were dissolved in THF and the resulting solution poured into a teflon mould. Upon evaporation (24 h), homogeneous, transparent PVC membranes with a thickness of about 0.2 mm were obtained. Disks of the appropriate diameter are cut out with a punch. For each membrane composition two electrodes were prepared. The membranes were glued on teflon electrod body.

Cell potentials were measured relative to a double junction calomel reference electrode (with internal reference solution 0.1M calcium nitrate for sodium, potassium and magnesium ion determination and 0.1M potassium chloride for calcium ion determination) with an ionometer DXC-91 (Datronix Computer). All potentiometric measurements were carried out at 20±0.5^{0}C.

Calibrated solutions were prepared by serial dilution of 0.1 M XCl (X= Na^+, K^+) and 0.1 M $X(NO_3)_2$ (X= Ca^{2+}, Mg^{2+}) stock solutions to 10^{-6} M, with deionizer water.

Before the experiment to be performed and between the experiments, membranes were conditioned and stored in the same stock solutions.

RESULTS AND DISCUSSION

Membranes were evaluated by studying their behavior in various test solutions. The calibration functions are represented in Figure 2 and their slopes/ linear calibration ranges are presented in Table 2.

Table 2

The slopes and the linear response range for ion-selective membranes

Membrane	S [mV/pE]/ linear response range			
	Cation			
	Na	K	Ca	Mg
2b (dimer)	40 10^{-3}-10^{-1}	62 10^{-4}-10^{-1}	25 10^{-6}-10^{-1}	20 10^{-4}-10^{-1}
3b (dimer)	14 10^{-2}-10^{-1}	67 10^{-5}-10^{-1}	20 10^{-5}-10^{-1}	29 10^{-3}-10^{-1}
4a (monomer)	28 10^{-4}-10^{-1}	74 10^{-5}-10^{-1}	23 10^{-5}-10^{-1}	41 10^{-5}-10^{-1}
4b (dimer)	47 10^{-3}-10^{-1}	69 10^{-5}-10^{-1}	39 10^{-5}-10^{-1}	26 10^{-3}-10^{-1}
5a (monomer)	47 10^{-4}-10^{-1}	72 10^{-5}-10^{-1}	19 10^{-5}-10^{-1}	24 10^{-5}-10^{-1}
5b (dimer)	34 10^{-3}-10^{-1}	66 10^{-5}-10^{-1}	34 10^{-4}-10^{-1}	15 10^{-5}-10^{-1}
6a (monomer)	55 10^{-3}-10^{-1}	72 10^{-5}-10^{-1}	24 10^{-5}-10^{-1}	27 10^{-4}-10^{-1}
7a (monomer)	51 10^{-3}-10^{-1}	57 10^{-5}-10^{-1}	24 10^{-5}-10^{-1}	23 10^{-5}-10^{-1}

In order to asses the membranes lifetime the slope over the above range was measured each week over a period of 3 months, while the electrode was in continual use.

The membranes continued to function in a reproducible manner for approximately three months, after a small decline in slope. The initial potential is changed between two sets of measurements. The process governing the lifetime of cation selective electrodes include the loss of the active site, of the additives and of the plasticizer, particularly by diffusion into the sample solution.

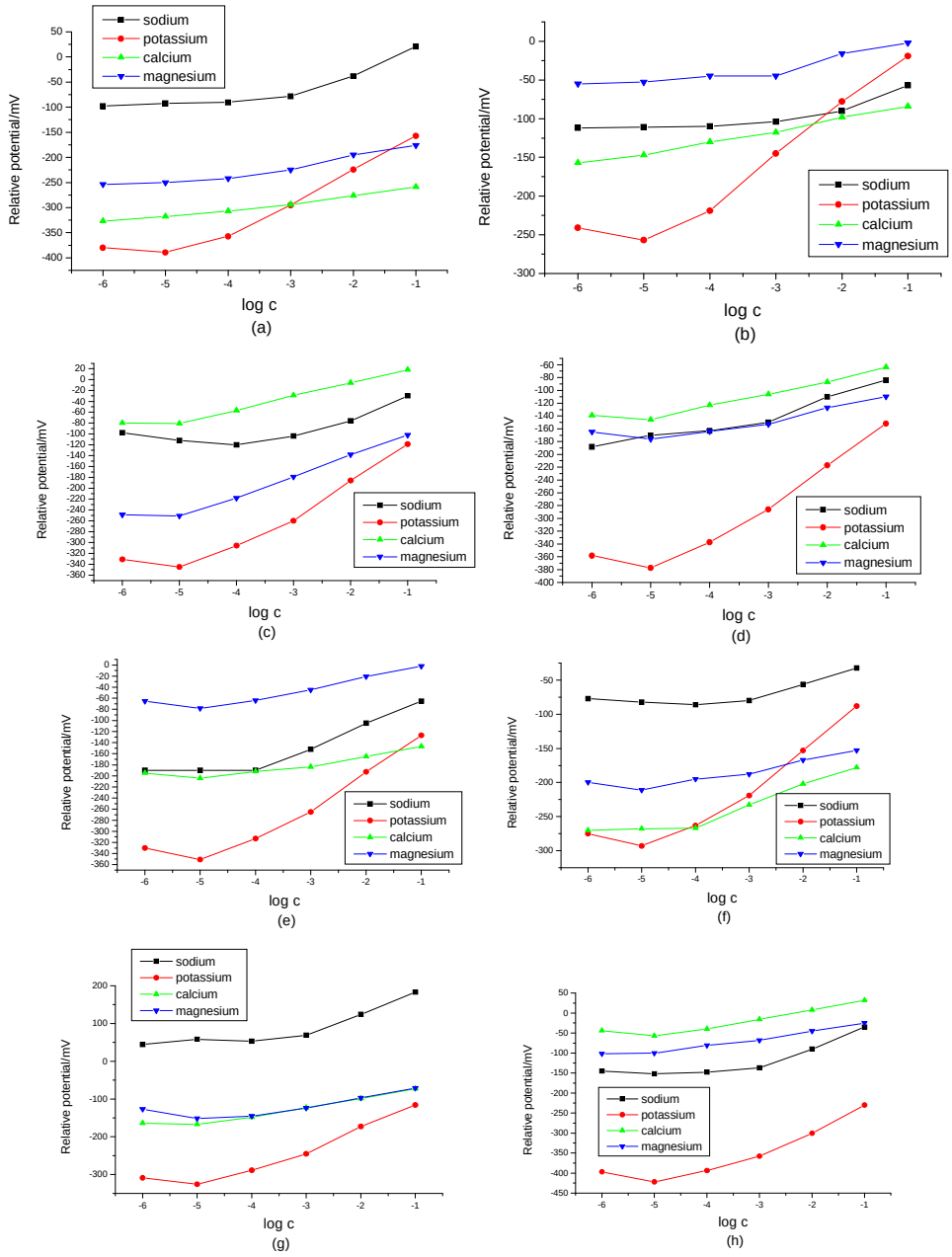

Figure 2. The calibration functions for cations. Membrane:(a) 2b; (b) 3b; (c) 4a; (d) 4b; (e) 5a; (f) 5b; (g) 6a; (h) 7a

The results of cations determination are presented in Table 3.

Table 3

The ion-selective membranes electrochemical response

electrochem respons	Membranes							
	2b d	**3b** d	**4a** m	**4b** d	**5a** m	**5b** d	**6a** m	**7a** m
excellent	**Ca**	**K** **Mg**	**K** **Mg**	**K** **Ca**	**K**	**K** **Ca**	**K** **Na** **Mg**	**K**
good	**K**			**Mg**	**Mg**		**Ca**	**Na** **Ca**
poor	**Mg**		**Ca**		**Na**			**Mg**
very poor		**Na** **Ca**	**Na**		**Ca**	**Mg**		

The response of membranes is rapid (<10 sec).

The metal binding ability of such ligands is effective by virtue of the chelate and macrocyclic effects. The selectivity for cations is very much improved for macrocyclic cavities, more rigid and restricted so that they are unable to constrict sufficiently to bind cations that are too small for the cavity; they cannot expand to accommodate cations with radii greater than the optimum size fit. A successful host exhibits a strong affinity for one particular guest and a much lower affinity for other cations. The selectivity is governed by an enormous number of factors: size match between cation and host cavity, electrostatic charge, coordinating ability, cation binding kinetics, chelate ring size, etc. That is why to designate a particular ligand to be highly selective for a given cation is very complicated.

In our case we can conclude that all ligands are selective for K^+ having very good electrochemical response but only 6a and 7a monomers have good electrochemical response for Na^+. The monomers have a good electrochemical response for calcium ion while the dimers have a good electrochemical response for magnesium ion.

The solid-state molecular structure was determined for some monomers[9]. The structures revealed different orientation of the aromatic rings and the collapse of the middle part of the macrocycle. This suggests that these compounds may be able to coordinate as a ditopic “host” molecule.

The selectivity of ligands also depend on the ability of the large, flexible parts (the length of the polyethoxylated chain) of macrocycles to “wrap” around the metal cation, effectively enclosing it almost entirely within an organic sheath.

We conclude that there is no rule concerning the electrochemical response of the ligands for these cations.

The research will be continued with studies on selectivity and improving the detection limit of the best ligands as ionophores.

CONCLUSIONS

The new series of ligands was used as ionophores for polymeric membranes for Na^+, K^+ , Ca^{2+},Mg^{2+} determination having good electrochemical characteristics.

These membranes could be used in clinical determination of cations where the concentration in human blood plasma is between: 135-145 mmol/l for Na^+, 3.5-5 mmol/l for K^+, 1-1.3 mmol/l for Ca^{2+} and 0.6-0.9 mmol/l for Mg^{2+}

REFERENCES

1. Jonathan W. Steed, Jerry L. Atwood, *Supramolecular Chemistry*, **2000**, Ed. J. Wiley & Sons. Ltd, Chaper 3, pg. 87-195.
2. C.J. Moody, Bahruddin S. Saad şi J.D.R. Thomas, *Analyst*, **1989**, 114, 15-19
3. Robert W. Burnett şi alţii, *Clin. Chem. Lab Med,* **2000**; 38(4):363-370
4. Worth, H.G.J., *Analyst,* **1988**, 113, 373
5. F. Kauffmann, B. Hoffmann şi R. Erbach, *Sensors and Actuators B,* 18-19 (**1994**) 60-64.
6. Sokalski şi altii, “Low Detection Limit Ion Selective Membrane Electrodes” Patent Nr. 6,126,801 din oct. 3, **2000**.
7. A. Ceresa, A. Radu, S. Peper, E. Bakker, E. Pretsch, *Anal. Chem.*, **2002**, 74, 4027-4036.
8. A. Malon, A. Radu, N. Qin, Y. Qin, A. Cerese, M. Maj-Zvranska, E. Bakker, E. Pretsch, *Anal.Chem*., **2003**, 75, 3865-3871.
9. Ion Grosu, Elena Bogdan, Gerard Ple, Loic Toupet, Yvan Ramondenc, Eric Condamine, Valerie Peulon-Agasse, Mirela Balog, *Eur*. *J. Org. Chem.,* **2003**, 3153-3161.
10. L. Olenic, S. Pruneanu, Gh. Mihailescu, I. Badescu, E. Bogdan, I. Grosu, *The 2nd International Symposium on Electrochemistry,* Bucharest, Romania, September 13-15, **2001**.

STUDIA UNIVERSITATIS BABEŞ-BOLYAI, CHEMIA, XLIX, 2, 2004

Dedicated to Professor Valer Fărcăşan at his 85th anniversary

ELECTRODEPOSITION OF CdS THIN FILMS

DELIA GLIGOR, LIANA MURESAN*, LIVIU BOBOS, IONEL CATALIN POPESCU

*Faculty of Chemistry and Chemical Engineering, Babes-Bolyai University of Cluj, 11 Arany Janos Str., 400028, Cluj-Napoca, Romania. *E-mail:limur@chem.ubbcluj.ro*

ABSTRACT. CdS thin films were obtained by potentiostatic electrodeposition on platinum and ITO electrodes from solutions containing $CdSO_4$ and $Na_2S_2O_3$ at concentration ratios higher than 1. The influence of deposition time, temperature and $Cd^{2+}/S_2O_3^{2-}$ ratio on CdS thin film electrodeposition on platinum electrodes, as well as the film composition were investigated electrochemically, by stripping voltammetry. The morphology and the composition of CdS films obtained on ITO supports were determined by SEM and EDS. It was concluded that the CdS film formation is favored by the increase of electrodeposition duration and electrolyte temperature, as well as by acid media (pH 3) and high $Cd^{2+}/S_2O_3^{2-}$ ratios (200/1).

Keywords: CdS electrodeposition, Pt and ITO electrodes, stripping voltammetry.

INTRODUCTION

The electrochemical deposition of thin films of metallic chalcogenides represents a subject of great interest, due to the semiconducting properties of these materials. Among these, CdS has gained considerable attention, being an n-type semiconductor with an optical band gap of 2.4 eV at room temperature. Thin films of CdS are used as detectors of light and window materials for CdS/CdTe solar cells of high efficiency (more than 7%) [1].

The electrodeposition represents a successful way to prepare CdS, being a low-cost process, well suited to the manufacture of film solar cells. Recently, several papers have been published referring to the CdS electrodeposition conditions and to methods of its electrochemical characterization [2, 3].

The electrodeposition of thin films of metallic chalcogenides can be realized in many ways, but the most successful methodologies are:

(i) co-deposition, where both elements are deposited at the same time from the same solution. Stoichiometry is maintained by having the more noble element as the limiting reagent, and poising the potential where the less noble element will be underpotentially deposited only on the more noble element [4-7].

(ii) precipitation, which consists in electrochemical generation of the precursor of one of the elements, the other being in solution. The reaction takes place in homogeneous phase, but because one of the reactants is forming directly on the electrode surface, the greatest part of the product precipitates on the surface and the thickness of the deposited film is controlled by the quantity of electrogenerated forerunner.

In both cases, the electrodeposition of CdS films on conductive substrates is a process difficult to control and frequently the quality of the obtained film is relatively poor [2, 8]. Moreover, there is a tendency towards the incorporation of some minority components from solution into the CdS film, which can result in greatly altered solid-state properties [9].

In this context, in order to optimize the obtaining of CdS films on different supports, the aim of this work was to investigate the influence of deposition time, temperature, pH, and $Cd^{2+}/S_2O_3^{2-}$ ratio on the characteristics of the thin CdS films prepared by potentiostatic electrodeposition on platinum and on indium tin oxide (ITO) electrodes.

Stripping voltammetry was used to estimate the nature and the amount of the film components, being one of the methods that could furnish interesting information about the phase composition of chalcogenides, particularly of sulfide materials. On the other side, it gives the possibility to discriminate between the electrochemical processes associated with transformation of the metal and that of metallic sulfides [3]. The electrochemical behavior of sulfides depends on their nature (Gibbs energy, crystal lattice energy, chemical interaction with electrolyte solutions) and the greater the crystal lattice energy, the more positive potential is required for the compound oxidation.

The morphology and the structure of CdS films were investigated using Scanning Electron Microscopy (SEM) and Energy Dispersive X Ray Spectroscopy (EDS).

EXPERIMENTAL SECTION

Reagents

Chemically purified 3 M $CdSO_4$, 2.7 M $Na_2S_2O_3$ and 0.1 M H_2SO_4 were obtained at “Raluca Ripan” Institute of Chemistry Cluj-Napoca. Na_2SO_4 was purchased from Chimopar, Bucharest.

CdS film electrodeposition

In a first step, the deposition process was achieved in solutions containing $CdSO_4$ and $Na_2S_2O_3$ ($Cd^{2+}/S_2O_3^{2-}$ ratios of 2/1 and 200/1), at pH 3, using a thermostated parallel plates cell equipped with a Pt cathode and a Pt anode. The deposition potential was chosen in the range corresponding to very low cathodic currents, where Cd nucleation starts, and the rate of deposition process is small. This condition assures the limitation of atoms number, which are deposited in a defined time range, as well as atoms diffusion on the surface towards optimum incorporation positions in crystalline network [4].

Next, the electrodeposition was achieved on ITO glass previously cleaned by ultrasonnation during 15 minutes, in a 1:1 acetone-ethanol mixture.

Electrochemical measurements

The electrodeposited CdS film was cathodically stripped. Stripping voltammetry measurements were carried out in a conventional three-electrode electrochemical cell by recording the voltammogram corresponding to the previously

electrodeposited CdS, after replacing the solution used during deposition by 0.5 M Na_2SO_4 (pH 3). A saturated calomel electrode (SCE) and a coiled Pt wire served as reference and counter electrode, respectively. The cell was connected to a computer-controlled voltammetric analyzer (Autolab-PGSTAT10, Eco Chemie, The Netherlands). The scan rate was 50 mV s^{-1}.

Characterization of electrodeposited CdS films

Morphological examination of CdS deposits on ITO prepared in the parallel plates cell, was carried out with a Cambridge S 250 scanning electronic microscope (SEM). The chemical composition of the samples was obtained by using a Princeton Gamma Tech. energy dispersive X-ray analyzer coupled with the SEM.

RESULTS AND DISCUSSION

Influence of deposition time

The electrodeposition was achieved at potentials placed in the equilibrium proximity (-750 mV *vs.* SCE), where the deposition rate is low and the exchange current density is high, the numbers of atoms that are deposited being a little greater than those which are dissolved in a certain time range.

In each solution, the deposition was performed at the above mentioned potential, during 30 and 60 minutes. The cathodic current decay observed during the electrodeposition time proves that a resistive film is formed on the electrode surface.

For electrochemical characterization of deposited films, a cathodic stripping Figure 1) of CdS covered electrodes, immersed in a solution of 0.5 M Na_2SO_4 (pH 3), was used.

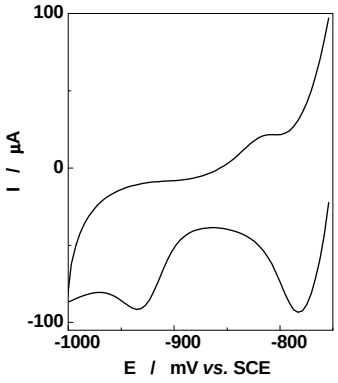

Fig. 1. Cathodic stripping of previously electrodeposited CdS film on Pt electrode. Experimental conditions: 0.5 M Na_2SO_4 (pH 3); scan rate, 50 mV s^{-1}; deposition electrolyte, 0.2 M $CdSO_4$ + 0.1 M $Na_2S_2O_3$ (pH 3); deposition potential, -750 mV *vs.* SCE; deposition time, 30 min.; working temperature, 20^0 C.

The two peaks observed during the cathodic scanning, were attributed to the following processes:

$Cd^{2+} + 2e^- \rightarrow Cd$ (E = -780 mV *vs.* SCE) (1)

$S + 2e^- \rightarrow S^{2-}$ (E = -932 mV *vs.* SCE) (2)

The first peak appears because, during the CdS deposition on Pt electrode, beside CdS, metallic Cd was deposited, too. In contact with the Na_2SO_4 solution (pH 3) the electrodeposited metallic Cd is partially dissolved, and is subsequently redeposited during the cathodic scanning. This fact was experimentally confirmed by the increase of this peak height after Cd^{2+} addition in the Na_2SO_4 solution (results not shown).

The second reaction is the result of $S_2O_3^{2-}$ decomposition in acid medium, when elemental sulphur, able to be reduced to S^{2-}, is formed [1]. The corresponding voltammetric peak appears as well on the cyclic voltammogram recorded on Pt electrode in a Na_2SO_4 solution of pH 3 containing only thiosulphate (results not shown).

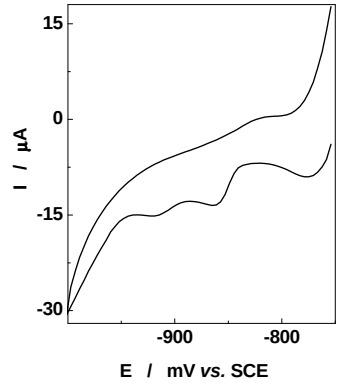

Fig. 2. Cathodic stripping of previously electrodeposited CdS film. Experimental conditions: Pt electrode; deposition time, 60 min; for the other conditions, see Fig. 1.

As it can be seen from Figure 2, the increase of deposition time from 30 to 60 minutes led to the appearance of a supplementary peak (placed between the two peaks already discussed) during the cathodic stripping. This supplementary reduction peak (placed at E = -860 mV *vs.* SCE) was attributed to the CdS reduction following the reaction:

$$CdS + 2e^- \rightarrow Cd + S^{2-} \quad (3)$$

CdS formation is favored by the increase of the deposition time.

A supplementary proof supporting this conclusion is the fact that, when CdS (prepared from $CdSO_4$ solution by precipitation with Na_2S, followed by filtration and drying) was mechanically immobilized on a graphite electrode, the corresponding cyclic voltammogram exhibited a single reduction peak at -875 mV *vs.* SCE (results not shown).

Influence of temperature

CdS formation is favored by the temperature increase [3], when the superficial diffusion of adatoms (which is slow at ambient temperature) is enhanced. The results obtained by stripping of deposits obtained on Pt electrode, at temperatures around 90^0C from solutions of 0.2 M $CdSO_4$ + 0.1 M $Na_2S_2O_3$

(pH 3) presented in Figure 3, confirm this affirmation. Thus, during cathodic stripping only one peak appears, at a potential of about -880 mV *vs.* SCE, being ascribed to CdS reduction. A comparison of this stripping voltammogram with that recorded in the same solutions at room temperature, allowed to conclude that CdS formation is clearly favored by the temperature increase.

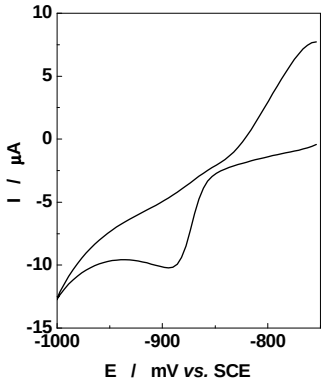

Fig. 3. Cathodic stripping of previously electrodeposited CdS film at high temperature. Experimental conditions: Pt electrode; deposition time, 30 min.; working temperature, 90^0 C; for the other conditions, see Fig. 1.

Influence of Cd^{2+}/ $S_2O_3^{2-}$ ratio

High concentrations of $S_2O_3^{2-}$ favor the formation of colloidal S, which disturbs the reduction of S to S^{2-} and contribute to the obtaining of CdS films of poor quality [1].

In this context, the influence of $Cd^{2+}/S_2O_3^{2-}$ ratio upon the CdS film formation was initially examined at room temperature.

Comparing the stripping voltammogram recorded for CdS film deposited when the $Cd^{2+}/S_2O_3^{2-}$ ratio was 200/1 (results not shown) with that obtained in the same experimental conditions, but for a $Cd^{2+}/S_2O_3^{2-}$ ratio of 2/1 (Figure 1), it was noticed that the peak corresponding to CdS reduction becomes visible only in the first case. The fact that high $Cd^{2+}/S_2O_3^{2-}$ ratio is beneficial for CdS film formation was more evident, examining the results obtained at 90^{0}C and 60 minutes deposition time (Figure 4).

Based on the above mentioned experiments it was concluded that the best conditions for CdS film deposition on Pt electrode were the following: deposition electrolyte, 0.2 M $CdSO_4$ + 1 mM $Na_2S_2O_3$, pH 3; deposition time, 60 minutes; working temperature, 90^0 C. Extrapolating these results, ITO glass was used as substrate for CdS film deposition.

Morphology of electrodeposited CdS films

The morphology of CdS films obtained on ITO glass at 90^0 C, 60 minutes deposition time and $Cd^{2+}/S_2O_3^{2-}$ ratio of 200/1 was investigated by SEM. In these conditions, in the absence of any previous activation of ITO glass, the CdS film consisted of insular growths on the electrode surface, suggesting the existence of a limited number of active sites on the ITO surface (Figure 5A). Consequently,

an activation treatment of the ITO support was performed before electrodeposition, by cathodic polarization at -300 mV *vs.* SCE, during 10 s, in a 0.1 M H_2SO_4 solution. As expected, the CdS deposits become more uniform and small grained (Figure 5B).

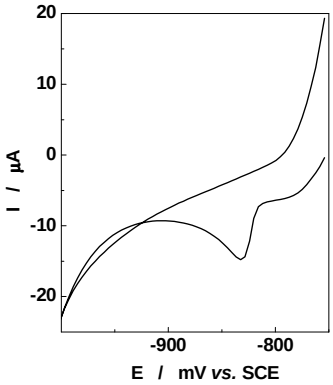

Fig. 4. Cathodic stripping of electrodeposited CdS film. Experimental conditions: Pt electrode; deposition solution, 0.2 M $CdSO_4$ + 1 mM $Na_2S_2O_3$ (pH 3); deposition time, 60 min.; working temperature, 90^0 C; for the other conditions, see Fig. 1.

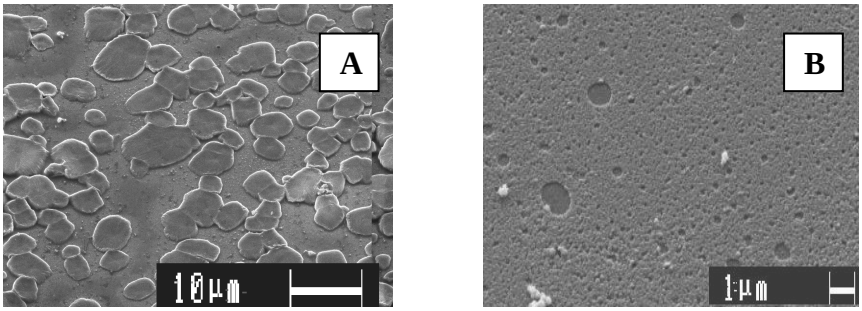

Fig. 5. SEM micrographs of CdS film electrodeposited on ITO electrode unactivated (A) and previously activated by cathodic polarization (B). Experimental conditions: activation potential, -300 mV *vs.* SCE; activation time, 10 s; supporting electrolyte, 0.1 M H_2SO_4; deposition solution, 0.2 M $CdSO_4$ + 1 mM $Na_2S_2O_3$ (pH 3); deposition time, 60 min.; working temperature, 90^0 C; deposition potential, -750 mV *vs.* SCE.

The EDS spectrum recorded for CdS deposited film (Figure 6) pointed out to a chemical composition of ~50% Cd and 50% S, with a slight excess of S (Table 1).

Table 1.

Chemical composition corresponding to EDS spectrum of the electrodeposited CdS film on ITO electrode. Experimental conditions, as in Fig. 6.

Element	Composition		χ^2	P:B Ratio
	Wt%	At%		
Cd	77.2	49.2	4.4	8.2
S	22.8	50.8	2.1	8.0
Total	**100.0**	**100.0**	**-**	**-**

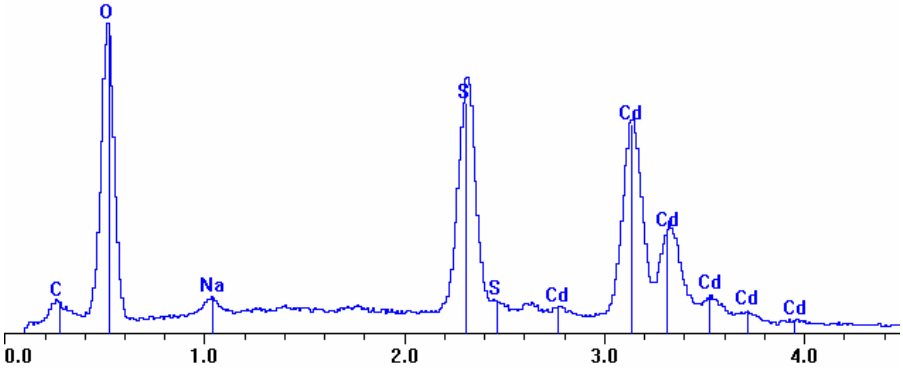

Fig. 6. EDS spectrum of CdS film electrodeposited on unactivated ITO electrode. Experimental conditions: electrodeposition conditions as in Fig. 5; live time, 100.00; beam voltage, 10.00; count rate, 2841; beam current, 1.00; dead time, 24.36 %; takeoff angle, 38.84.

CONCLUSIONS

Based on the obtained results, the following conclusions can be formulated:

- CdS film electrodeposition is promoted by temperatures around 90^0 C, acid media (pH 3), long electrodeposition time (1h) and high $Cd^{2+}/S_2O_3^{2-}$ ratios (200/1).
- The morphology and the structure of the CdS films obtained on ITO electrodes without a previous activation of the support indicates the existence of a limited number of active sites on the surface, but a short cathodic polarization significantly improves the CdS film quality.

ACKNOWLEDGEMENTS

The authors thank Dr. G. Maurin, from UPR 15 du CNRS, Université "Pierre et Marie Curie" Paris, France, for scanning electron micrographs and for EDS spectrum and Dr. E. J. Popovici, from "Raluca Ripan" Institute of Chemistry Cluj-Napoca, for providing the ITO glass and the reagents.

The research was partially supported by the CNCSIS (Grant CERES 28/2003).

REFERENCES

[1] L. M. Peter, *Electrochim. Acta*, **1978**, 23, 165.

[2] J. Nishino, S. Chatani, Y. Uotami and Y. Nosaka, *J. Electrochem. Soc.*, **1999**, 473, 217.

[3] Kh. Brainina, E. Neyman, *Electroanalytical Stripping methods,* in "Chemical Analysis", vol. 126, p. 123, Wiley Interscience, N. York, **1993**.

[4] J. L. Stickney, *Electrochemical Atomic Layer Epitaxy (EC-ALE): Nanoscale Control in the Electrodeposition of Compound Semiconductors,* in "Advances in Electrochemical

Science and Engineering", vol. 7, p. 5, R. Alkire and D. Kolb (editors), Wiley-VCH Verlag GmbH, **2001**.

[5] T. Torimoto, Sh. Nagakubo, M. Nishizawa, H. Yoneyama, *Langmuir*, **1998**, 14 (25), 7077.

[6] A. Gichuhi, B. Edwards Boone, C. Shannon, *Langmuir*, **1999**, 15, 763.

[7] L. P. Colletti, B. H. Flowers,Jr., J. L. Stickney, *J. Electrochem. Soc.*, **1998**, 145 (5), 1442.

[8] S. Denisson, *J. Mater. Chem.*, **1994**, 4(1), 41.

[9] V. I. Birss, L. E. Kee, *J. Electrochem. Soc.*, **1986**, 133, 2097.

STUDIA UNIVERSITATIS BABEŞ-BOLYAI, CHEMIA, XLIX, 2, 2004

Dedicated to Professor Valer Fărcăşan
at his 85th anniversary

ELECTROANALYTICAL CHARACTERIZATION OF A Co(II) -PHTALOCYANINE MODIFIED CARBON PASTE ELECTRODE

GRAZIELLA L. TURDEAN[1], AMELIA F. PALCU[1,2], CAMELIA FĂRCAŞ[1,3] and IONEL CĂTĂLIN POPESCU[1]

[1] *Department of Physical Chemistry, Faculty of Chemistry and Chemical Engineering, "Babes-Bolyai" University of Cluj, 11 Arany Janos St., 400028 Cluj-Napoca, Romania; E-mail: gturdean@chem.ubbcluj.ro*
[2] *Grup Scolar Agricol Chisineu-Cris, 5 P-ta Avram Iancu, 315100 Chisineu-Cris (Arad), Romania*
[3] *Seminarul Teologic Liceal Roman Unit "Inochentie Micu", 26 Calea Motilor St., 400001 Cluj-Napoca, Romania*

ABSTRACT. An effective strategy for circumventing problems of high applied potential on metal electrodes for detecting species of medical or environmental importance is the use of metallophthalocyanines (e.g. Co(II)- phthalocyanine, CoPC) as electrocatalyst. A carbon paste matrix modified with CoPC was used to obtain an amperometric transducer, working at an applied potential lowered with 0.6 V than the corresponding unmodified carbon paste electrode. The electroanalytical parameters estimated from the amperometric calibration curves have values much higher than in the case of unmodified electrode.

Keywords: amperometric transducer, glucose, thiocholine, carbon paste electrode, cobalt phthalocyanine.

INTRODUCTION

Carbon paste (CP) is a mixture of graphite powder and an organic liquid, which is immiscible in aqueous solutions. One of the most important composite electrodes is based on CP (CPEs) and was proposed by Adams in 1958 [1]. CPEs are characterized by: (i) exceptionally low background currents, (ii) a wide operating potential range, (iii) convenient modification procedure, (iv) renewability of the surface, (v) miniaturization possibility and (vi) low cost [2]. The pasting liquid serves not only to maintain a firm electrode shape and to fill up the crevices between the graphite particles, but also insulates the graphite from the contacting aqueous solution and acts as a medium for the entrapment of different compounds.

The use of electrochemical methods for glucose or thiocholine analysis has been limited by the high potentials required for their oxidation at conventional electrodes. As a consequence, CPEs have been widely applied as a substitute for noble metal electrodes.

Remarkable progresses in lowering significantly the oxidation potential are obtained by modification of CPEs with electrocatalysts from the metallophthalocyanines class (e.g. Co(II)-phthalocyanines, CoPC) [3]. Phthalocyanines are a class of benzoporphyrins that have strong pigmenting power, forming a family of dyes [4].

The electrochemistry of phthalocyanines has received a great deal of attention due to good catalytic behavior [5]. Devices using CoPC-modified CPEs have been investigated, mainly with regard to their catalytic oxygen reduction activity or the possibility of decreasing the effective oxidation potential for a variety of organic compounds: cysteine [6], thioglycolic acid [7], secondary alcohols [8], hydrazine [9].

The aim of this work is to investigate by electrochemical methods (i.e. cyclic voltammetry, rotating disc electrode and amperometry), the electrochemical and electroanalytical behavior of CoPC modified carbon paste electrodes, in view to obtain an amperometric transducer for glucose or thiocholine detection, operated at a low potential value.

EXPERIMENTAL

Chemicals

Glucose oxidase (Gox) (E.C 1.1.3.4., type VII, isolated from Aspergillus niger, 88,2 U/mg), acetylcholinesterase (AChE) (E.C. 3.1.1.7, type V-S, from *Electric eel*, 970 U/mg solid), acetylthiocholine chloride (ASChCl) were purchased from Sigma (St. Louis, Mo, USA). Cobalt phtalocyanine, graphite powder (99.9% purity) and paraffin oil were obtained from Fluka (Buchs, Switzerland). The supporting electrolyte was a 1/15 M phosphate buffer (pH 8) prepared by mixing the necessary volumes of $Na_2HPO_4.12H_2O$ and KH_2PO_4 solutions.

The glucose obtained from Reactivul (Bucuresti, Romania) was used to prepare stock solution, which are let to mutarotate at room temperature overnight before use.

The thiocholine solution was freshly prepared just before using, by dissolving the appropriate amounts of enzyme (AChE) and substrate (ASChCl) salts into the phosphate buffer (pH 8) solution.

All other chemicals were of analytical grade and were used without further purification. All solutions were prepared with distilled water.

Preparation of the CoPC/Gox/CP bioelectrodes for glucose detection

Unmodified carbon pastes were prepared by mixing 3 g of graphite powder with 2.2. ml of paraffin oil. The CoPC-modified carbon paste was prepared by thoroughly mixing 0.15 g of unmodified carbon paste with 0.01 g CoPC (7%). The CoPC/Gox/CPE was prepared by mixing 0.16 g of unmodified carbon paste with 0.01 g CoPC (7%) and 0.035 g Gox (≈ 3100 U Gox).

The CPEs were fabricated by pressing the obtained unmodified carbon paste mixture into the end of a plastic syringe having a geometric surface area of 0.03 cm^2. Its inner end was connected to a silver wire. The tip of the syringe was filled with CoPC-modified paste or with CoPC+Gox, in view to obtain the CoPC/CP or CoPC/Gox/CP electrodes, respectively. Before use the surface of all CPEs was smoothed manually on a clean filter paper.

Preparation of the CoPC/CP electrodes for thiocholine detection

Unmodified carbon paste was prepared by mixing 0.15 g of graphite powder with 0.06 ml of paraffin oil. The CoPC-modified carbon paste was prepared by thoroughly mixing 0.15 g of unmodified carbon paste with 0.015 g

CoPC (10 %). The CPEs were fabricated by pressing the obtained unmodified carbon paste mixture into the end of a plastic syringe having a geometric surface aria of 0.07 cm^2. Its inner end was connected to a silver wire. The tip of the syringe was filled with CoPC-modified carbon paste, in view to obtain the CoPC/CPE. Before use, the modified and unmodified CPEs were smoothed manually on a clean filter paper.

Electrochemical measurements

Cyclic voltammetry experiments were carried out using a typical undivided three-electrode cell equipped with a SCE or an Ag|AgCl, KCl_{sat} as reference electrode and a platinum plate as counter electrode. As working electrodes unmodified CPEs and CoPC/CPEs were employed.

Data for the electrochemical oxido-reduction process at unmodified and modified electrodes were collected using a custom-made computer controlled cyclic voltammetry set-up, including a low current potentiostat (Polarograph LP7e, Praha, Czech Republic) and a data acquisition interface (AT MOI-16F, National Instruments, USA). LabView 3.1 software was used to monitor the cyclic voltammetry measurements. All experiments were conducted at ambient temperatures (20 ± 2℃). When necessary, the electrolyte solution was deaerated by argon bubbling. The rotating disc electrode (PINE - Instruments Company, USA) measurements were made using the custom made installation described above.

Batch amperometric measurements with the unmodified and modified electrodes were performed in a thermostated (30° C) and stirred solution of 1/15 M phosphate buffer (different pH), by addition of increasing volumes of substrate solution. A stable potential (values specified in figures) between the working electrode and the reference electrode was maintained with a polarograph (type OH-105, Radelkis, Budapest, Hungary).

RESULTS AND DISCUSSION

1. Electrochemical behavior of the CoPC/Gox/CP bioelectrodes for glucose detection

It is well-know that Gox catalyses the oxidation of glucose to gluconolactone and this reaction is used in the fabrication of amperometric biosensors. On the basis of the structural feature of the electrode matrix, two possible catalytic mechanisms may be considered [5]:

Mechanism I. The CoPC behaves as a mediator for the electron transport from the enzyme redox center to the electrode, following the reactions:

$$\text{Glucose}_{(sol)} + \text{Gox}_{(m)}(ox) \rightarrow \text{gluconic acid}_{(sol)} + \text{Gox}_{(m)}(red) \quad (1)$$

$$\text{Gox}_{(m)}(red) + \text{CoPC}_{(m)}(ox) \rightarrow \text{Gox}_{(m)}(ox) + \text{CoPC}_{(m)}(red) \quad (2)$$

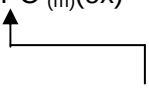

$$\text{CoPC}_{(m)}(red) \rightarrow \text{CoPC}_{(m)}(ox) + e^- \quad (3)$$

where: sol means solution and m means electrode matrix.

Mechanism II. The enzyme catalyses the oxidation of the substrate in the presence of oxygen, and the CoPC catalyses the oxidation of H_2O_2, which is the product of the enzyme-substrate reaction, following the reactions 4 - 5:

$$\text{glucose}_{(sol)} + O_{2\,(sol)} \xrightarrow{\text{Gox(m)}} \text{gluconic acid}_{(sol)} + H_2O_{2\,(m)} \quad (4)$$

$$\text{CoPC}_{(m)}(ox) + H_2O_{2\,(m)} \rightarrow 2H^+ + O_2 + \text{CoPC}_{(m)}(red) \quad (5)$$

$$\text{CoPC}_{(m)}(red) \rightarrow \text{CoPC}_{(m)}(ox) + e^- \quad (6)$$

In both mechanisms the electrode reaction involves the electrochemical oxidation of the CoPC from the electrode matrix (equations 3 and 6). However, the main difference between mechanism I and mechanism II is that oxygen is involved in the enzyme reaction of mechanism II and the reaction takes place only in the presence of O_2. On the other hand, mechanism I will not be affected by oxygen and in the mechanism II, the CoPC should have a good catalytic behavior towards H_2O_2.

The cyclic voltamogramms for a CoPC/CPE immersed both in phosphate buffer blank solution and in the same solution in the presence of H_2O_2 are shown in figure 1A. It can be seen that H_2O_2 can be oxidized at ≈ 0.7 V *vs.* SCE on CoPC/CPE, while on bare CPE it is oxidized at ≈ +1.3 V *vs*. SCE (results not shown). The oxidation potential of H_2O_2 shifted negatively with almost 0.6 V suggesting that the CoPC is a good electrochemical catalyst for the H_2O_2 oxidation.

The cyclic voltamogramms of the CoPC/Gox/CP bioelectrode in the absence and the presence of glucose is presented in figure 1B. The addition of glucose induces the appearance of a peak placed, at ≈ 0.7 V *vs.* SCE, which confirms that the detection of glucose is based on the action of CoPC as electrocatalyst of H_2O_2 oxidation (mechanism II).

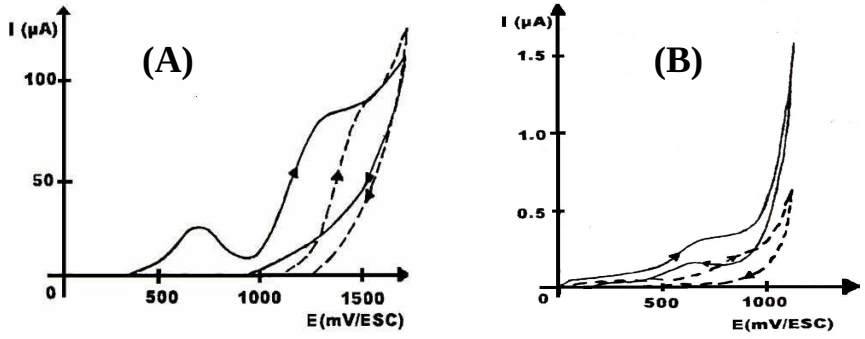

Figure 1. Cyclic voltammetry on CoPC/CP (**A**) and CoPC/Gox/CP (**B**) electrodes in the absence and presence of 83 mM H_2O_2 (**A**) and 11.4 mM glucose (**B**). Experimental conditions: phosphate buffer 1/15 M, pH 7; scan rate, 25 mVs^{-1}; room temperature.

A large excess of enzyme in the electrode configuration decreases the effect of pH variations on the biosensor functionality. Therefore, the pH profiles in the linear measuring range under diffusion control should be substantially less sharp than those for the respective enzyme in solution. Generally, the optimum pH of immobilized Gox is shifted with 0.9 pH toward more alkaline pHs than in the case of the dissolved enzyme [10]. This is due to the formation of gluconic acid within the enzyme matrix, which causes a local pH decrease, resulting in a shift of the optimum pH to higher values than in solution. In this context, the optimum pH of an unmodified Gox/CPE is placed at pH 8 (figure 2), and the presence of CoPC shifts the optimum pH from pH 8 to pH 7 (results not shown).

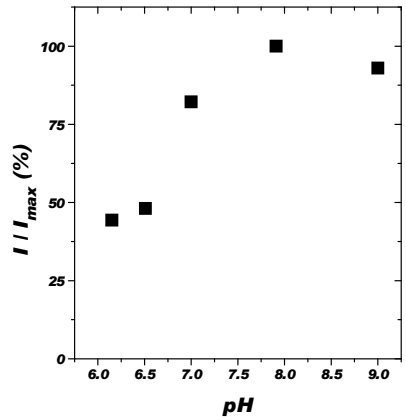

Figure 2. Influence of pH on the electrochemical response of Gox/CPEs. Experimental conditions: phosphate buffer 1/15 M; substrate concentration, 0.6 mM glucose; applied potential, 0.7 V *vs*. SCE; continuos stirring; room temperature.

Electroanalytical parameters of the CoPC/Gox/CP bioelectrode are presented in table 1. As observed, the presence of CoPC enhance the analytical performance (sensitivity and detection limit) of the realized device.

2. Electrochemical behavior of the CoPC/CPEs for thiocholine detection

The thiocholine is an intermediary obtained in the hydrolyse reaction of acetylthiocholine in the presence of acetylcholinesterase [11, 12]:

$$\text{acetylthiocholine} + H_2O \xrightarrow{\text{AChE}} \text{thiocholine} + \text{acetic acid} \quad (7)$$

$$2\ \text{thiocholine} \xrightarrow{\text{oxidation}} \text{dithio-bis-choline} + 2H^+ + 2e^- \quad (8)$$

This reaction pathway is used to evaluate the environmental pollution by indirect measurement of the inhibited acetylcholinesterase activity induced by organophosphorous pesticides.

Oxidation of thiocholine on CoPC/CPE is believed to be a two-step electrocatalytic process. This is initiated by the electrochemical oxidation of the central metal from CoPC species, followed by the chemical oxidation of thiocholine and the regeneration of the original CoPC complex, as described in the following reactions [13, 14]:

$$Co(II)PC \xrightarrow{\text{electrode}} Co(III)PC + e- \quad (9)$$

$$2\ Co(III)PC + 2\ R\text{-}SH \rightarrow 2\ Co(II)PC + RSSR + 2H^{+} \quad (10)$$

where: R-SH is the thiocholine and RSSR is the dithio-bis-choline.

In this context, cyclic voltametry measurements performed on CPE and on CoPC/CPEs in contact with both phosphate buffer (pH 8) and phosphate buffer containing enzymatically prepared thiocholine are presented in figure 3. As expected, the presence of CoPC in the electrode matrix induces the shift of thiocholine oxidation peak potential with 0.6 V (from ≈ 0.8 V *vs*. Ag/AgCl, KCl_{sat} on CPE, to ≈ 0.2 V *vs*. Ag/AgCl, KCl_{sat} on CoPC/CPE). Because the process is an irreversible one, no cathodic response was observed on the reverse scan. Also, an increase of the current intensity is observed in the presence of CoPC. These facts confirm the electrocatalytical effect of the CoPC in the electrode matrix.

For the first time, about our knowledge, the RDE measurements of thiocholine oxidation on CoPC/CPE served for the estimation of the kinetic current ($0.12*10^{-4}$ A) and of the diffusion coefficient ($0.67*10^{-6}$ $cm^2{}_*s^{-1}$) using the classically Koutecky-Levich plot (figure 4), obtained under mixed control (charge transfer and mass transport).

As in the case of glucose detection, the analytical parameters of the CoPC/CPE used for the detection of thicholine were enhanced, proving the electrocatalytical properties of the studied CoPC (table 1).

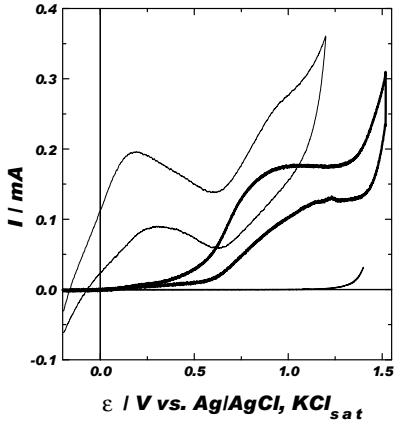

Figure 3. Voltammetric response of 0.03 M SCh at CPE (▬▬) and at CoPC/CPE (- - - - - -) in comparison with buffer solution (——). Experimental conditions: phosphate buffer 1/15 M, pH 8; scan rate 5 mVs^{-1}.

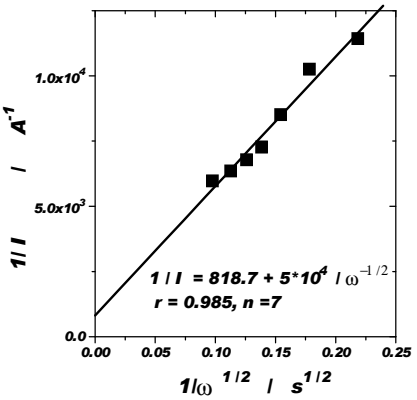

Figure 4. Koutecky-Levich plot for thiocholine oxidation on a CoPC/CPE. Experimental conditions: phosphate buffer 1/15 M, pH 8; thiocholine concentration, 7.15 mM; measurement potential, 0.2 V *vs*. Ag/AgCl, KCl_{sat}.

Table 1.
Analytical parameters of the investigated amperometric transducers.

Analyte*	Working electrode Applied potential	Sensitivity R	Linear range	Detection limit / mM
Glucose	CPE 1.3 V *vs*. SCE	0.14 μA/mM 0.999	0-1.4 mM	0.05
	CoPC/CPE 0.7 V *vs*. SCE	3.02 μA/mM 0.998	0-1.4 mM	0.03
Thiocholine	CPE 0.8-1 V *vs*. Ag/AgCl, KCl_{sat}	3.53 mA/M 0.991	0 - 0.05 M	1
	CoPC/CPE 0.2 V *vs*. Ag/AgCl, KCl_{sat}	6.65 mA/M 0.989	0 - 0.03 M	0.45

* detection at pH 8

CONCLUSIONS

The use of carbon paste as substitute for noble metal electrodes offers several distinct advantage in solid electrode voltammetry. The presented results clearly prove that carbon paste electrodes can be widely applied in their modified form. Good selective amperometric devices for glucose and thiocholine detection were obtained by using CoPC as electrocatalyst. In both cases, for glucose and thiocholine detection, the presence of CoPC improve the electroanalytical parameters, by increasing the sensitivity and decreasing the limit of detection. This type of devices open the way of developing the area of biosensors by realization of enzyme based amperometric electrodes.

ACKNOWLEDGEMENTS

Financial support from CNCSIS Grants is gratefully acknowledged.

REFERENCES

[1] Q. Chi, W. Gopel, T. Ruzgas, L. Gorton, P. Heiduschka, *Electroanal*. **1997**, 9(5), 357.

[2] J. Kulys, L. Gorton, E. Dominguez, J. Emneus, H. Jarskog, *J. Electroanal. Chem*., **1994**, 372, 49.

[3] M. Sekota, T. Nyokong, *Electroanal*. **1997**, 9(6), 1257.

[4] I. Rosen-Margalit, A. Bettelheim, J. Rishpon, *Anal. Chim. Acta*., **1993**, 281, 327.

[5] Z. Sun, H. Tachikawa, *Anal. Chem*., **1992**, 64, 1112-1117.

[6] M. K. Halbert, R. P. Baldwin, *Anal. Chem*., **1985**, 57, 591.

[7] S. Shahrokhian, J. Yazdani, *Electrochim. Acta,* **2003**, 48(28), 4143.

[8] V. B. Sharma, S. L. Jain, B. Sain, *Tetrahedron Letts*., **2003**, 44(2), 383.

[9] X. Li, S. Zhang, C. Sun, *J. Electroanal. Chem*., **2003**, 553, 139.

[10] H.-L. Schmidt, W. Schuhmann, F. W. Scheller, F. Schubert, “Specific features of biosensors, in “Sensors. A comprehensive survey” (edited by W. Gopel, J. Hesse, J. N. Zemal), vol. 3 “Chemical and Biochemical Sensors”, Part II (edited by W. Gopel, T.A Jones, M. Kleitz, I. Lundstrom, T. Seiyama), VCH, Weiheim, **1992**, p. 772.

[11] I. C. Hartley, J. P. Hart, *Anal. Prooced. Anal. Commun*, **1994**, 31, 333.

[12] G. L. Turdean, I.C. Popescu, L. Oniciu, D. R. Thevenot, *J. Enzy. Inhib. Med. Chem*., **2002**, 17(2), *107-115*.

[13] J. P. Hart, I. C. Hartley, *Analyst*, **1994**, 119, 259.

[14] G. L. Turdean, C. S. Mosneag, I. C. Popescu, *ACH-Models in Chemistry*, **2000**, 137(4), 519.

STUDIA UNIVERSITATIS BABEŞ-BOLYAI, CHEMIA, XLIX, 2, 2004

Dedicated to Professor Valer Fărcăşan at his 85th anniversary

SPINEL OXIDE COMPOSITE ELECTRODES. I. $CuCo_2O_4$ AND $Li_{0.1}Cu_{0.9}Co_2O_4$ CARBON PASTE ELECTRODES FOR H_2O_2 OXIDATION/REDUCTION

OLIVIA SERDAN[1], PETRU ILEA[1], BENOIT MARSAN[2] and IONEL CATALIN POPESCU[1]

[1]Department of Physical Chemistry, Babes-Bolyai University, 400028 Cluj-Napoca, Romania;
[2] Department of Chemistry, Universite du Quebec a Montreal, Montreal, Canada.
E-mail:pilea@chem.ubbcluj.ro

ABSTRACT. A new method to obtain composite electrodes based on **$CuCo_2O_4$** and **$Li_{0.1}Cu_{0.9}Co_2O_4$** spinel-type oxides, is presented. Both oxides were prepared as powders by thermal decomposition of nitrate precursors. In the anodic potentials domain, cyclic voltammetry measurements performed on **$CuCo_2O_4$**-carbon paste electrodes (**CPEs**) showed the presence of Co(IV/III) and Co(III/II) quasi-reversible redox transitions, while in the cathodic potentials domain Cu(II/I) and Cu(I/0) transitions were observed. Contrarily, at **$Li_{0.1}Cu_{0.9}Co_2O_4$-CPEs,** only Co(III/II) transition was noticed. The electrochemical response of both electrodes, recorded in the presence of H_2O_2, proved a moderate electrocatalytic activity toward H_2O_2 oxidation/reduction.

Keywords: copper-cobalt oxide, **$Li_{0.1}Cu_{0.9}Co_2O_4$** oxide, carbon paste electrode, H_2O_2 oxidation/reduction.

INTRODUCTION

Transition metal oxides, especially spinel-type oxides, represent versatile materials for electrocatalysis [1,2]. Studies on the physico-chemical and electrochemical catalytic properties of complex oxides with spinel structure have received considerable attention during recent years [3-7], as they are low-cost, easily available, reasonably stable and catalytically active materials.

Among spinel-type oxides, copper-cobalt spinels are of interest for CO oxidation in the presence of O_2 as well as for the conversion of synthesis gas ($CO/CO_2/H_2$) to higher alcohols [8]. $CuCo_2O_4$ and $NiCo_2O_4$ are highly effective in removing CO, NO and hydrocarbons from waste and exhaust gases in the absence of oxygen at 350ºC [1]. $CuCo_2O_4$ has a high catalytic activity for xylene complete oxidation [9]. It was shown that the intercalation of Cu^{2+} into the Co_3O_4 matrix enhances the electrocatalytic activity of the spinel oxide for anodic oxygen evolution [8]. Additionally, it has been demonstrated that Li-doping increases the electrical conductivity and electrocatalytic properties of spinel oxides [5]. Their electrochemical characterization has been carried out especially on thin films obtained on suitable substrates (either conducting or non-conducting) [10-13].

Spinel oxides powders have been obtained using various methods of preparation such as (i) thermal decomposition of mixed nitrates, carbonates or hydroxides [3, 14, 15]; (ii) sol-gel method [16]; and (iii) freeze drying method [17]. Spinel oxides thin films have been prepared by chemical spray pyrolysis [18] or by cathodic sputtering [19].

Continuing our preoccupations in the domain of spinel oxides-modified electrodes [20], in this paper a new method to obtain composite electrodes based on powders of spinel-type oxides is presented. The method exploits the major advantages of carbon paste electrodes, which consist in using small amounts of substances, renewability, exceptionally low background currents, a wide operating potential window, a convenient modification, miniaturization and low-cost [21]. The composite electrodes were obtained by hand-mixing $\mathbf{CuCo_2O_4}$ or $\mathbf{Li_{0.1}Cu_{0.9}Co_2O_4}$ with graphite powder and paraffin oil. The investigated oxides were prepared as powders by thermal decomposition of nitrate precursors. The morphological studies on the obtained spinel oxides powders were done using scanning electron microscopy (SEM). The surface composition was assessed through semiquantitative energy dispersive analysis of X-rays (EDAX), while the crystalline structure of the oxides was determined by X-ray diffraction. The electrochemical behaviour of the composite electrodes was studied by cyclic voltammetry, performed in 1 M NaOH solutions. The electrocatalytic response in the presence of H_2O_2 was also investigated.

EXPERIMENTAL SECTION

Materials

The $\mathbf{CuCo_2O_4}$ and $\mathbf{Li_{0.1}Cu_{0.9}Co_2O_4}$ oxides were obtained as powders by evaporating the aqueous solutions of the corresponding metals nitrates, $Cu(NO_3)_2 \cdot 2.5\ H_2O$ (*Fisher Scientific, ACS*) and $Co(NO_3)_2 \cdot 6H_2O$ (*Fisher Scientific, ACS*), followed by the thermal decomposition of the obtained mixtures at 350^{o}C, in a triple-zone quartz furnace (Lindberg 59744) under air atmosphere.

Graphite powder and paraffin oil were purchased from *Fluka* and used as received. The supporting electrolyte was a solution of 1 M NaOH (*Lachema, Czech Republic*).

Electrode preparation

The carbon paste electrodes (**CPEs**) modified with $\mathbf{CuCo_2O_4}$ (**$\mathbf{CuCo_2O_4}$-CPE**) or $\mathbf{Li_{0.1}Cu_{0.9}Co_2O_4}$ (**$\mathbf{Li_{0.1}Cu_{0.9}Co_2O_4}$-CPE**) were prepared by mixing 50 mg of graphite powder and 50 mg of oxide powder with 40 µL of paraffin oil.

A portion of the resulting paste was packed firmly into the cavity of a Teflon tube electrode (3 mm diameter). The electric contact was established *via* a copper wire. The surface of the resulting carbon paste electrode was manually smoothed on a clean paper.

Morphology/structure investigation

Surface morphology of the oxide powders was examined with a scanning electron microscope (Hitachi, model S-2300) and the surface composition was assessed using an energy dispersive spectrometer.

X-ray diffraction patterns of the oxide powders were obtained using a Siemens model D5000 instrument with Co-K_α radiation (λ=1.789Å).

Electrochemical measurements

The cyclic voltammetry measurements were performed in a classical three-electrode electrochemical cell, containing the working electrode (the composite electrode), the reference electrode (a saturated calomel electrode, SCE) and Pt wire as counter-electrode (~1 cm^2). The electrochemical cell was connected to a computer-controlled potentiostat (Autolab-PGSTAT10, Eco Chemie, Netherlands).

RESULTS AND DISCUSSION

In order to estimate the dimensions of the oxide particles, morphological studies on the prepared spinel oxides powders (**$CuCo_2O_4$**, **$Li_{0.1}Cu_{0.9}Co_2O_4$**) were carried out using scanning electron microscopy (SEM). The surface composition was established through semiquantitative EDAX analysis.

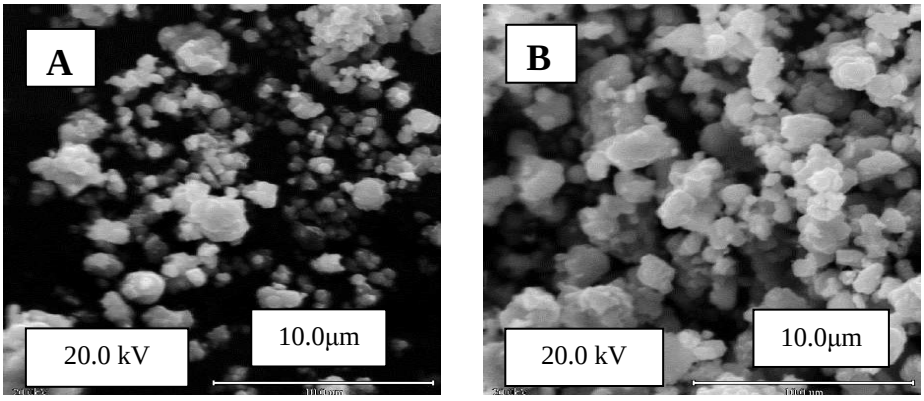

Fig. 1. SEM micrographs of **$CuCo_2O_4$** (A) and **$Li_{0.1}Cu_{0.9}Co_2O_4$** (B) powders (x5000)**.**

The **$Li_{0.1}Cu_{0.9}Co_2O_4$** powder (Fig. 1) was more porous and more uniform than **$CuCo_2O_4$** powder. EDAX analysis indicated a Cu:Co atomic ratio of 0.51 for **$CuCo_2O_4$** and of 0.46 for **$Li_{0.1}Cu_{0.9}Co_2O_4$**, proving a composition very close to that corresponding to the expected stoichiometric ratio.

The X-ray diffraction analysis (Fig. 2) performed on the oxides powders (**$CuCo_2O_4$**, **$Li_{0.1}Cu_{0.9}Co_2O_4$**) pointed out to the existence of a face-centered cubic spinel structure.

The positions of the diffraction lines and their relative intensity for the copper-cobalt oxide powder are in good agreement with data for $Cu_{0.95}Co_{2.05}O_4$ [22]. A partial substitution (10%) of copper with lithium led to an increase of t he peaks diffraction intensity, indicating an increase of the oxide cristallinity. In the same time, the diffraction peaks for **$Li_{0.1}Cu_{0.9}Co_2O_4$** oxide were slightly shifted toward higher values of Bragg angles, showing a decrease of the lattice parameter.

The voltammetric responses of the carbon paste electrodes incorporating the two spinel oxides, **$CuCo_2O_4$** and **$Li_{0.1}Cu_{0.9}Co_2O_4$**, usually considered as an electrochemical "fingerprint" of the electroactive compound, are presented in Fig. 3.

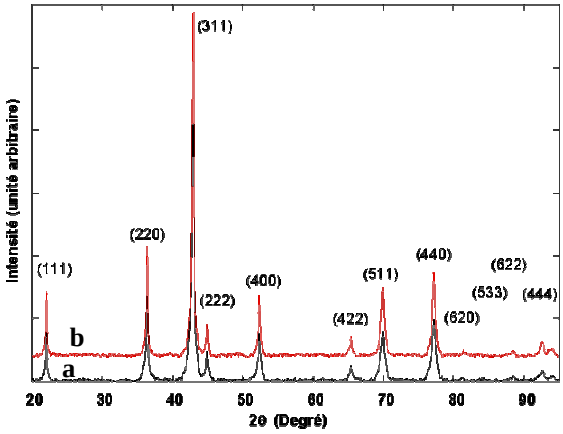

Fig. 2. X-ray diffractograms of **$CuCo_2O_4$** (a) and **$Li_{0.1}Cu_{0.9}Co_2O_4$** (b) powders.

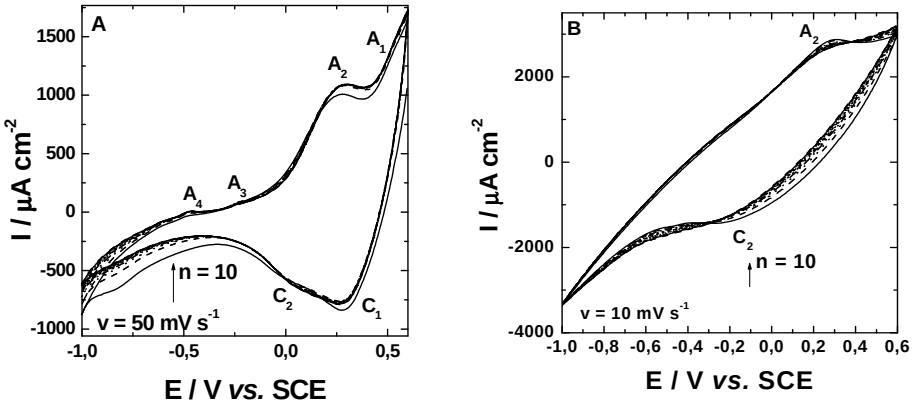

Fig. 3. Repetitive cyclic voltammograms recorded at **$CuCo_2O_4$-CPE** (A) and **$Li_{0.1}Cu_{0.9}Co_2O_4$-CPE** (B). Experimental conditions: supporting electrolyte, 1 M NaOH; starting potential, +0.6 V *vs.* SCE; n-cycle number.

A minor variation of the current intensity observed during repetitive potential cycling in the potential domain where the investigated oxide is electrochemically active, proved the stability of the studied electrodes.

In the positive potentials region, the voltammetric response of **$CuCo_2O_4$-CPE** showed the presence of two quasi-reversible redox transitions (A_1/C_1 and A_2/C_2, see Fig. 3A). The first transition was attributed to the Co(IV/III) couple, involved in the following process [23]:

$CoO_2 + H_2O + e^- \Leftrightarrow CoOOH + OH^-$ (A_1/C_1)

The second transition was attributed to the Co(III/II) redox couple:

$CoOOH + H_2O + e^- \Leftrightarrow Co(OH)_2 + OH^-$ (A_2/C_2)

In the negative potentials region, the voltammetric response of **$CuCo_2O_4$-CPE** showed the presence of two redox transitions (A_3 and A_4 from Fig. 3A). The first transition was attributed to Cu(II/I) redox couple [24]:

$2\ Cu(OH)_2 + 2\ e^- \Leftarrow Cu_2O + H_2O + 2\ OH^-$ (A_3)

The second transition was attributed to Cu(I/0) [24]:

$Cu_2O + H_2O + 2\ e^- \Leftarrow 2\ Cu + 2\ OH^-$ (A_4)

The cyclic voltammogram recorded at **$Li_{0.1}Cu_{0.9}Co_2O_4$-CPE** (Fig. 3B) presented only one peak pair (A_2/C_2) corresponding to the Co(III/II) redox transition.

The voltammetric responses recorded in the presence of H_2O_2 for both **$CuCo_2O_4$-CPE** and **$Li_{0.1}Cu_{0.9}Co_2O_4$-CPE** are presented in Fig. 4.

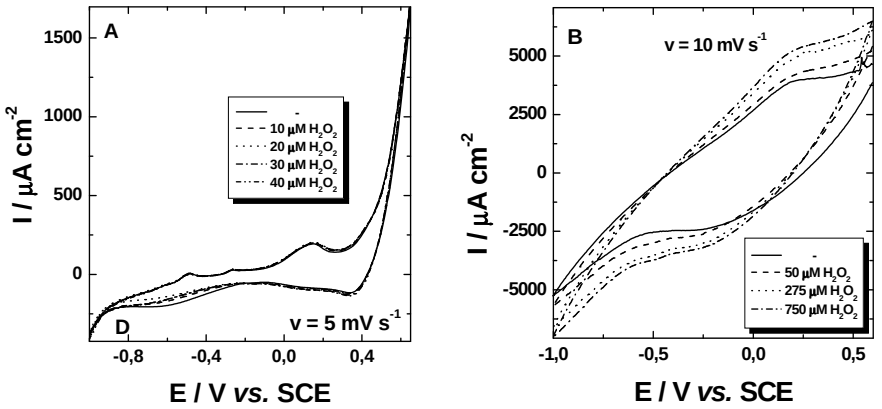

Fig. 4. Cyclic voltammograms recorded at **$CuCo_2O_4$– CPE** (A) and **$Li_{0.1}Cu_{0.9}Co_2O_4$-CPE** (B) in the absence and in the presence of H_2O_2. Experimental conditions: supporting electrolyte, 1 M NaOH; starting potential, +0.65 V *vs.* SCE (A) and +0.6 V *vs.* SCE (B).

The addition of 40 μM H_2O_2 in the electrolyte solution does not change significantly the cyclic voltammograms of **$CuCo_2O_4$-CPE** (Fig. 4A), while the addition of almost the same concentration of H_2O_2 (50 μM) induced an important increase of both oxidation and reduction peak currents for **$Li_{0.1}Cu_{0.9}Co_2O_4$-CPE** (Fig. 4B). Additionally, for this electrode, further increases of peak currents with the increase of H_2O_2 concentration were observed. These results indicate that **$Li_{0.1}Cu_{0.9}Co_2O_4$-CPE** has a moderate electrocatalytic activity toward H_2O_2 oxidation/reduction, described by the following reactions:

$HO_2^- + OH^- \rightarrow O_2 + H_2O + 2\ e^-$ (1)

$HO_2^- + H_2O + 2\ e^- \rightarrow 3\ OH^-$ (2)

CONCLUSIONS

The physico-chemical and electrochemical characterization of **$CuCo_2O_4$-CPE** and **$Li_{0.1}Cu_{0.9}Co_2O_4$-CPE** led to the following conclusions:

- The SEM micrographs showed that **$Li_{0.1}Cu_{0.9}Co_2O_4$** powder is more porous than **$CuCo_2O_4$** powder.
- The analysis of the investigated oxide powders by X-ray diffraction proved the existence of a face-centered cubic spinel structure.
- Cyclic voltammetry measurements performed at **$CuCo_2O_4$-CPEs** indicated the presence of the quasi-reversible redox transitions Co(IV/III) and Co(III/II) in the anodic potentials domain, and the transitions Cu(II/I) and Cu(I/0) in the cathodic potentials domain. For **$Li_{0.1}Cu_{0.9}Co_2O_4$-CPE**, only one peak pair due to the Co(III/II) redox transition was observed.
- **$Li_{0.1}Cu_{0.9}Co_2O_4$-CPE** presented a better electrocatalytic activity toward H_2O_2 oxidation/reduction than **$CuCo_2O_4$-CPE**.

ACKNOWLEDGEMENTS

Authors acknowledge the assistance of Mr. M. Preda (Universite du Quebec a Montreal, UQAM, Montreal (Canada)) for recording the X-ray diffraction patterns and Mr. R. Mineau (UQAM) for the SEM and EDAX analyses.

REFERENCES

[1] E. Rios, H. Nguyen-Cong, J. F. Marco, J. R. Gancedo, P. Chartier, J. L. Gautier, *Electrochim. Acta*, **2000**, 45, 4431.
[2] E. Rios, J. L. Gautier, G. Poillerat, P. Chartier, *Electrochim. Acta*, **1998**, 44, 1491.
[3] A. C. Tavares, M. A. M. Cartaxo, M. I. da Silva Pereira, F. M. Costa, *J. Solid State Electrochem.*, **2001**, 5, 57.
[4] M. Longhi, L. Formaro, *Electrochem. Comm.*, **2002**, 4, 123.
[5] F. Svegl, B. Orel, I. Grabec-Svegl, V. Kaucic, *Electrochim. Acta*, **2000**, 45, 4359.
[6] R. N. Singh, J. P. Pandey, N. K. Singh, B. Lal, P. Chartier, J. F. Koenig, *Electrochim. Acta*, **2000**, 45, 1911.
[7] A. Restovic, E. Rios, S. Barbato, J. Ortiz, J. L. Gautier, *J. Electroanal. Chem.*, **2002**, 522, 141.
[8] N. Fradette, B. Marsan, *J. Electrochem. Soc.*, **1998**, 145, 2320.
[9] J. L. Gautier, E. Trollund, E. Rios, P. Nkeng, G. Poillerat, *J. Electroanal. Chem.*, **1997**, 428, 47.
[10] R. Boggio, A. Carugati, S. Trasatti, *J. Appl. Electrochem.*, **1987**, 17, 828.
[11] I. Vartires, V. Popescu, A. Mihelis, N. Spataru, *Rev. Roum. Chim.*, **1987**, 32, 551.
[12] P. Rasiyah, A. C. Tseung, *J. Electrochem. Soc.*, **1983**, 130, 365.
[13] L. D. Burke, M. McCarthy, *J. Electrochem. Soc.*, **1983**, 130, 372.
[14] I. Nikolov, R. Darkaoui, E. Zhecheva, R. Stoyanova, N. Dimitrov, T. Vitanov, *J. Electroanal. Chem.*, **1997**, 429, 157.
[15] J. Haenen, W. Visscher, E. Barendrecht, *J. Electroanal. Chem.*, **1986**, 208, 273.
[16] F. Svegl, B. Orel, M. G. Hutchins, K. Kalcher, *J. Electrochem. Soc.*, **1996**, 143, 1532.
[17] P. Rasiyah, A. C. Tseung, *J. Electrochem. Soc.*, **1983**, 130, 2384.
[18] R. N. Singh, J. F. Koenig, G. Poillerat, P. Chartier, *J. Electroanal. Chem.*, **1991**, 314, 241.
[19] P. Nkeng, G. Poillerat, J. Koenig, P.Chartier, B. Lefez, J. Lopitaux, M. Lenglet, *J. Electrochem. Soc.*, **1995**, 142, 1777.
[20] O. Serdan, P. Ilea, I. C. Popescu, *Rev. Roum. Chim.*, **2004**.
[21] Q. Chi, W. Gopel, T. Ruzgas, L. Gorton, P. Heiduschka, *Electroanalysis*, **1997**, 9, 357.
[22] JCPDS-International Centre of Diffraction Data, fiche#78-2177 **1995**.
[23] A. Ait Addi, J. Douch, M. Hamdani, *Ann. Chim. Sci. Mat.*, **1998**, 23, 589.
[24] O. Serdan, M. Rauliuc, B. Marsan, P. Ilea, L. Muresan, I. C. Popescu, *Journees d'electrochimie*, Poster 4A-133, Poitiers, Franta, 3-6 juin 2003.

STUDIA UNIVERSITATIS BABEŞ-BOLYAI, CHEMIA, XLIX, 2, 2004

Dedicated to Professor Valer Fărcăşan at his 85th anniversary

SPINEL OXIDE COMPOSITE ELECTRODES. II. PREPARATION, PHYSICO-CHEMICAL PROPERTIES AND ELECTROCHEMICAL BEHAVIOUR OF $CuCo_2O_4$ AND $Li_{0.1}Cu_{0.9}Co_2O_4$ DEPOSITED ON Ni ELECTRODES

OLIVIA LAZAR[1], PETRU ILEA[1], BENOIT MARSAN[2] and IONEL CATALIN POPESCU[1]

[1]Department of Physical Chemistry, Babes-Bolyai University, 400028 Cluj-Napoca, Romania;
[2]Department of Chemistry, Quebec University, Montreal, Canada. E-mail:pilea@chem.ubbcluj.ro

ABSTRACT. **$CuCo_2O_4$** and **$Li_{0.1}Cu_{0.9}Co_2O_4$** deposited on Ni electrodes (**Ni/$CuCo_2O_4$**, **Ni/$Li_{0.1}Cu_{0.9}Co_2O_4$**) were prepared by thermal decomposition of nitrate precursors deposited on Ni grating. The physico-chemical characterization showed that these oxides have a spinel structure. In the anodic potentials domain, cyclic voltammetry measurements performed on both **Ni/$CuCo_2O_4$** and **Ni/$Li_{0.1}Cu_{0.9}Co_2O_4$** electrodes showed the presence of the Co(IV/III) quasi-reversible redox transition, while in the cathodic potentials domain the Cu(II/I) transition was observed. The highest roughness factor (666) was obtained for **Ni/$Li_{0.1}Cu_{0.9}Co_2O_4$** electrode. The heterogeneous electron transfer rate constant values pointed out that the Co(IV/III) transition is faster on **Ni/$Li_{0.1}Cu_{0.9}Co_2O_4$** electrode.

Keywords: spinel oxide, copper-cobalt oxide, lithium-copper-cobalt oxide, composite electrodes.

INTRODUCTION

Cheap and easily prepared spinel-type oxides have been investigated extensively as electrodes for electrocatalytic processes, such as evolution and reduction of oxygen, as well as chlorine evolution [1, 2]. In these compounds, the cations of mixed valences favour the reversible adsorption of oxygen by providing donor-acceptor sites for its chemisorption [3]. Cobaltite binary oxides ($M_xCo_{3-x}O_4$ with M = Co, Ni, Mn, Cu, Zn, Li) have been obtained using various methods and conditions of preparation such as thermal decomposition [4-6], sol-gel synthesis [7] and cryochemical synthesis [8]. An effect of the nature of the substrate (Pt, Ni, Ti) was also put in evidence [9-11]. It was shown that the intercalation of Cu^{2+} into the Co_3O_4 matrix enhances the electrocatalytic activity of the spinel oxide [1]. Additionally, it has been demonstrated that Li-doping increased electrical conductivity and electrocatalytic properties of spinel oxides [11].

Continuing our preoccupations on the electrochemistry of composite electrodes [12, 13], in this paper **$CuCo_2O_4$** / **$Li_{0.1}Cu_{0.9}Co_2O_4$** deposited on Ni grating electrodes were prepared by thermal decomposition of nitrate precursors deposited on a substrate of Ni grating. The morphological studies on the **Ni/$CuCo_2O_4$** and **Ni/$Li_{0.1}Cu_{0.9}Co_2O_4$** electrodes were done using scanning

electron microscopy (SEM). The surface composition was assessed through semiquantitative energy dispersive analysis of X-rays (EDAX), while the crystalline structure of the oxides was determined by X-ray diffraction. The electrochemical behaviour of the composite electrodes was studied by cyclic voltammetry, performed in 1 M NaOH solutions.

EXPERIMENTAL SECTION

Electrode preparation

$CuCo_2O_4$ / **$Li_{0.1}Cu_{0.9}Co_2O_4$** deposited on Ni grating electrodes were prepared by thermal decomposition of nitrate precursors, deposited on a substrate of Ni grating. In this procedure, $Cu(NO_3)_2 \cdot 2.5\ H_2O$ (*Fisher Scientific, ACS*) and $Co(NO_3)_2 \cdot 6H_2O$ (*Fisher Scientific, ACS*) were dissolved in the solvent mixture isopropanol : nanopure water (4 : 1), with the appropriate atomic ratio (Cu : Co) and concentration. The solution was deposited uniformly onto a Ni grating which had been previously degreased in dichloromethane (*Anachemia, ACS*) and thoroughly washed with nanopure water. The solvent was then evaporated at 100˚C and the nitrate coating was heated for 15 min in a triple-zone quartz furnace (Lindberg 59744) under air atmosphere at 350˚C. The procedure was repeated four times until the desired catalyst loading was achieved, and the electrodes were thereafter annealed over 1 h under the same conditions.

Morphology/structure investigation

Surface morphology of the oxide powders was examined with a scanning electron microscope (Hitachi, model S-2300) and the surface composition was assessed using an energy dispersive spectrometer.

X-ray diffraction patterns of the oxide powders were obtained using a Siemens model D5000 instrument with Co-K_α radiation (λ=1.789Å).

Electrochemical measurements

The cyclic voltammetry measurements were performed in a classical three-electrode electrochemical cell, containing: the working electrode (the composite electrode), the reference electrode (a saturated calomel electrode, SCE) and Pt as counter electrode (~1 cm^2). The electrochemical cell was connected to a computer-controlled potentiostat (Autolab-PGSTAT10, Eco Chemie, Netherlands). The supporting electrolyte was a solution of 1 M NaOH (*Lachema, Czech Republic*).

RESULTS AND DISCUSSION

In order to estimate the degree of coverage of Ni grating electrodes with spinel oxides (**$CuCo_2O_4$**, **$Li_{0.1}Cu_{0.9}Co_2O_4$**), morphological studies on the prepared electrodes were carried out using a scanning electron microscopy (SEM) (Fig. 1). The surface composition was established through semiquantitative EDAX analysis.

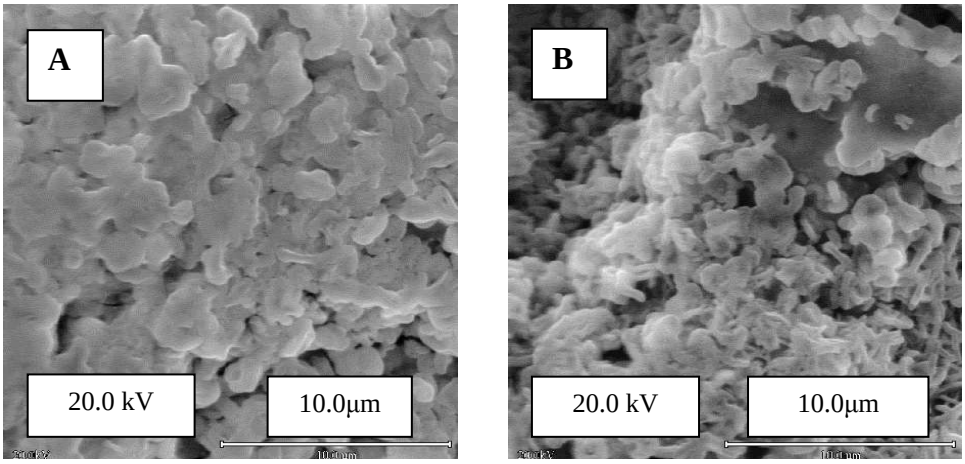

Fig. 1. SEM micrographs of **Ni/CuCo$_2$O$_4$** (A) and **Ni/Li$_{0.1}$Cu$_{0.9}$Co$_2$O$_4$** (B) electrodes**,** x5000.

The **Ni/Li$_{0.1}$Cu$_{0.9}$Co$_2$O$_4$** electrode was more porous than **Ni/CuCo$_2$O$_4$** electrode, which is in agreement with the observation made for the corresponding powders [13]. It is important to mention that Ni electrodes are completely covered by oxides for both investigated electrodes, assuring that only the oxide layer will dictate their electrochemical behaviour. EDAX analysis indicated the atomic ratio Cu : Co for **Ni/CuCo$_2$O$_4$** of 0.51 and for **Ni/Li$_{0.1}$Cu$_{0.9}$Co$_2$O$_4$** of 0.47, proving a composition very close to that corresponding to a stoichiometric ratio.

The X-ray diffraction analysis (Fig. 2) performed on **Ni/CuCo$_2$O$_4$** and **Ni/Li$_{0.1}$Cu$_{0.9}$Co$_2$O$_4$** electrodes pointed out the existence of a cubic spinel structure of the investigated oxides.

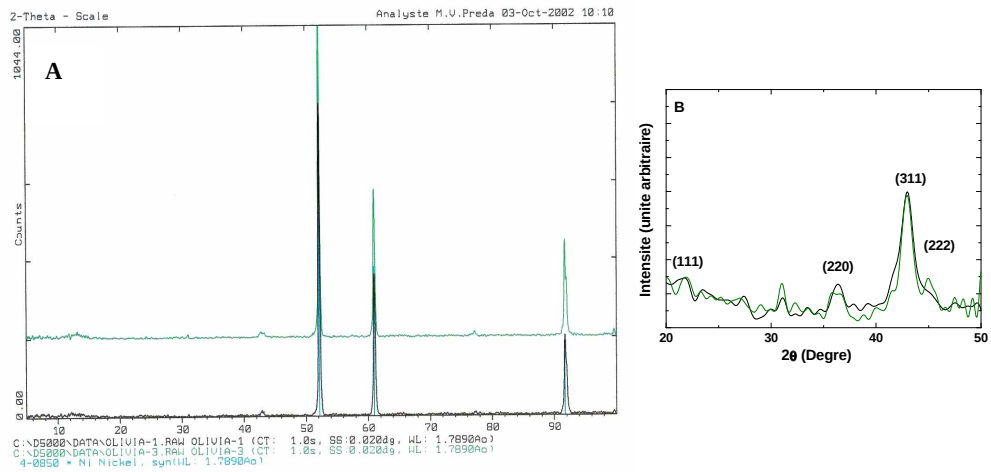

Fig. 2. X-ray diffractograms of **Ni/CuCo$_2$O$_4$** (-) and **Ni/Li$_{0.1}$Cu$_{0.9}$Co$_2$O$_4$** (**-**) electrodes.

The X-ray diffractograms (Fig. 2A) presents three well defined diffraction lines for Ni, at values of Bragg angles (2θ) of ~52, ~61 and ~92, due to the formation of a thin layer of spinel oxide on the Ni substrate. Diffractograms are limited to Bragg angles lying between 20º and 50º (Fig. 2B) because of the high intensity of the diffraction lines of the nickel substrate in comparison to those of the oxide phase in the region 50º-90º. The positions of the diffraction lines and their relative intensity in the copper-cobalt oxide powder were in good agreement with data for $Cu_{0.92}Co_{2.08}O_4$ [14].

The electrochemical behavior for **Ni/$CuCo_2O_4$** and **Ni/$Li_{0.1}Cu_{0.9}Co_2O_4$** electrodes was investigated by cyclic voltammetry measurements at different scan rates (Fig. 3).

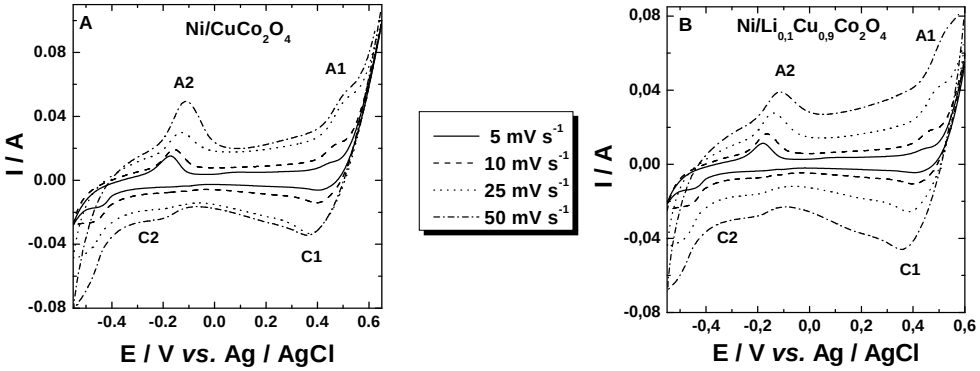

Fig. 3. Influence of potential scan rate on the electrochemical behaviour of **Ni/$CuCo_2O_4$** (A) and **Ni/$Li_{0.1}Cu_{0.9}Co_2O_4$** (B) electrodes . Experimental conditions: starting potential, 0.65 V vs. Ag/AgCl (A), 0.6 V vs. Ag/AgCl (B); supporting electrolyte, 1 M NaOH.

The cyclic voltammograms of **Ni/$CuCo_2O_4$** and **Ni/$Li_{0.1}Cu_{0.9}Co_2O_4$** (Fig. 3) showed in the positive potential region the presence of the redox cuasi-reversible transitions Co(IV/III) (A1/C1, equation 1) [15] and in the negative potential region, the transitions Cu(II/I) (A2/C2, equation 2) [16]:

$$CoO_2 + H_2O + e^- \leftrightarrow CoOOH + OH^- \quad (1)$$

$$2\ Cu(OH)_2 + 2\ e^- \leftrightarrow Cu_2O + H_2O + 2\ OH^- \quad (2)$$

The roughness factor (R_F), defined as the ratio of the real surface area to the geometric area of a rugous film, was measured as the ratio between the double-layer capacitance for the investigated oxide/electrolyte interface (C_{dl}) and the double-layer capacitance for an ideally smooth oxide surface 60 μF cm^{-2} [17]. The double-layer capacitance for the investigated oxide/electrolyte interface was estimated using cyclic voltammograms recorded at different scan rates in the capacitive region, by assuming no adsorption pseudo-capacitance. C_{dl} was calculated from the slope of the linear curve I_{cap} *vs.* scan rate (Fig. 4) [9]:

$$C_{dl} = \frac{di_{cap}}{d(\frac{\delta E}{\delta t})} \quad (3)$$

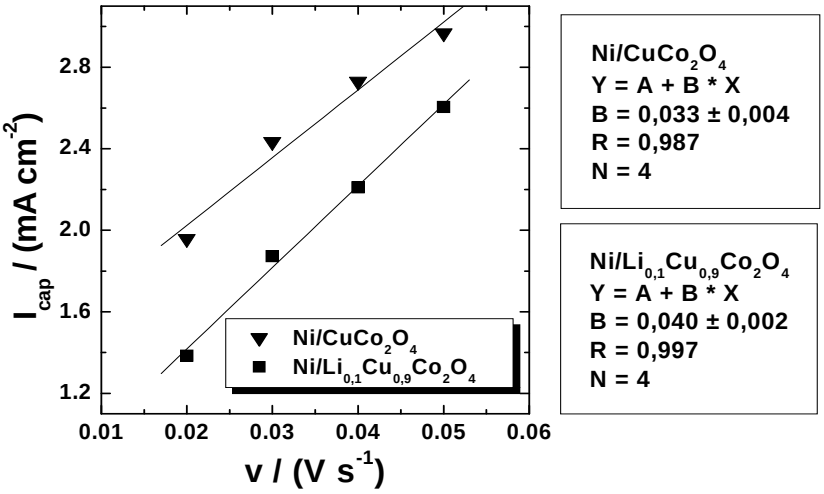

Fig. 4. Dependence of the capacitive current on the potential scan rate in the region corresponding to double-layer charging.

The R_F value for **$Ni/CuCo_2O_4$** was found to be 550, while for **$Ni/Li_{0.1}Cu_{0.9}Co_2O_4$** was of 666. The results are in agreement with those presented in the literature, showing that the R_F for Li containing oxides is higher than for the copper-cobalt oxides, and are in agreement with SEM measurements, too [18].

The values of the heterogeneous electron transfer rate constant (k_S) were estimated for **$Ni/CuCo_2O_4$** and for **$Ni/Li_{0.1}Cu_{0.9}Co_2O_4$** electrodes using Laviron's method for potential peak split $\Delta E_p < \frac{200}{n}(mV)$ where, n represents the number of electrons, and all other parameters have the common meaning, and considering $\alpha \approx 0.5$ [19]. Thus, using the calculated values [18] the dependence $n\Delta E_p$ vs. m^{-1} was plotted (Fig. 5), where n stands for the number of electrons and m is a parameter defined by the relation:

$$m = \frac{k_S}{nv} \cdot \frac{RT}{F} \quad (4)$$

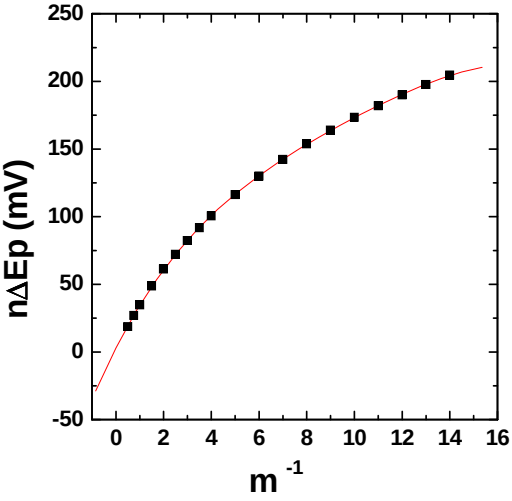

Fig. 5. Variation of $n\Delta E_p$ with m^{-1} [18].

Using the plot from Fig. 5 the m values corresponding to the experimental values of $n\Delta E_p$, measured for different potential scan rates for **$Ni/CuCo_2O_4$** and **$Ni/Li_{0.1}Cu_{0.9}Co_2O_4$** electrodes, were estimated. Then, from the relation (4) the k_s values at different potential scan rates were calculated (Table 1).

The k_s values point out that the Co(IV/III) transition is faster on **$Ni/Li_{0.1}Cu_{0.9}Co_2O_4$** electrode than on **$Ni/CuCo_2O_4$** electrode. In all cases, the values of the rate constants for the heterogeneous electron transfer indicate that the corresponding electrode processes can be considered as quasi-reversible ones.

Table 1.

Heterogeneous electron transfer rate constant (k_S) values corresponding to the Co(IV/III) transition for **$Ni/CuCo_2O_4$** and **$Ni/Li_{0.1}Cu_{0.9}Co_2O_4$** electrodes.

v ($mV\ s^{-1}$)	**ΔE_p (mV)**	**m**	**k_s (s^{-1})**
$Ni/CuCo_2O_4$			
5	43	0.78	0.15
10	75	0.37	0.15
25	144	0.14	0.14
			$\overline{k_S}$ = 0. 15
$Ni/Li_{0.1}Cu_{0.9}Co_2O_4$			
10	55	0.57	0.22
25	105	0.23	0.23
50	161	0.11	0.22
			$\overline{k_S}$ = 0. 22

CONCLUSIONS

The preparation, the morphological and structural characterization, as well as the investigation of the electrochemical behavior of Ni electrodes covered by spinel oxides (**$CuCo_2O_4$**, **$Li_{0.1}Cu_{0.9}Co_2O_4$**) conducted to the following conclusions:

- The SEM micrographs show that **Ni/$Li_{0.1}Cu_{0.9}Co_2O_4$** electrode is more porous than **Ni/$CuCo_2O_4$** electrode, which is in agreement with the observation made for the corresponding oxides powders.
- The analysis of **Ni/$CuCo_2O_4$** and **Ni/$Li_{0.1}Cu_{0.9}Co_2O_4$** electrodes by X-ray diffraction proved the existence of a cubic spinel structure.
- The roughness factor for **Ni/$Li_{0.1}Cu_{0.9}Co_2O_4$** is higher than for **Ni/$CuCo_2O_4$** which is in agreement with SEM measurements.
- For both investigated electrodes **Ni/$CuCo_2O_4$** and **Ni/$Li_{0.1}Cu_{0.9}Co_2O_4$** the voltametric response indicates the presence of redox cuasi-reversible transitions Co(IV/III) and Cu(II/I).

ACKNOWLEDGEMENTS

Authors acknowledge the assistance of Mr. M. Preda (Quebec University, Montreal (Canada)) (UQAM) for recording the X-ray diffraction patterns and Mr. R. Mineau (UQAM) for the SEM and EDAX analysis.

REFERENCES

[1] N. Fradette, B. Marsan, *J. Electrochem. Soc.*, **1998**, 145, 2320.

[2] A. Restovic, E. Rios, S. Barbato, J. Ortiz, J. L. Gautier, *J. Electroanal. Chem.*, **2002**, 522, 141.

[3] M. R. Tarasevich, B. N. Efremov, in *Electrodes of conductive metallic oxides*, Part A, S. Trasatti, Editor, Elsevier, Amsterdam, **1980**.

[4] A. C. Tavares, M. A. M. Cartaxo, M. I. da Silva Pereira, F. M. Costa, *J. Solid State Electrochem.*, **2001**, 5, 57.

[5] I. Nikolov, R. Darkaoui, E. Zhecheva, R. Stoyanova, N. Dimitrov, T. Vitanov, *J. Electroanal. Chem.*, **1997**, 429, 157.

[6] J. Haenen, W. Visscher, E. Barendrecht, *J. Electroanal. Chem.*, **1986**, 208, 273.

[7] F. Svegl, B. Orel, M. G. Hutchins, K. Kalcher, *J. Electrochem. Soc.*, **1996**, 143, 1532.

[8] P. Rasiyah, A. C. Tseung, *J. Electrochem. Soc.*, **1983**, 130, 2384.

[9] K. Fatih, B. Marsan, *Can. J. Chem.*, **1997**, 75, 1597.

[10] T. C. Wen, H. M. Kang, *Electrochim. Acta*, **1998**, 43, 1700.

[11] F. Svegl, B. Orel, I. Grabec-Svegl, V. Kaucic, *Electrochim. Acta*, **2000**, 45, 4359.

[12] O. Serdan, P. Ilea, I. C. Popescu, *Rev. Roum. Chim*., **2004**.

[13] O. Serdan, P. Ilea, B. Marsan, I. C. Popescu, *Studia, Chemia,* **2004**.

[14] JCPDS-International Centre of Diffraction Data, fiche#37-0878 **1995**.

[15] A. Ait Addi, J. Douch, M. Hamdani, *Ann. Chim. Sci. Mat.*, **1998**, 23, 589.

[16] O. Serdan, M. Rauliuc, B. Marsan, P. Ilea, L. Mureşan, I. C. Popescu, Journées d'électrochimie, Poster 4A-133, Poitiers, Franța, 3-6 juin **2003**.

[17] B. Marsan, N. Fradette, G. Beaudoin, *J. Electrochem. Soc.*, **1992**, 139, 1889.

[18] K. Fatih, PhD thesis, Universite de Sherbrooke, **2000**, Canada.

[19] A. J. Bard, Electroanal. Chem., vol. 12, Marcel Dekker Inc., New York, **1982**.

STUDIA UNIVERSITATIS BABEŞ-BOLYAI, CHEMIA, XLIX, 2, 2004

Dedicated to Professor Valer Fărcăşan at his 85th anniversary

ATOMIC FORCE MICROSCOPY STUDIES OF LANGMUIR-BLODGETT FILMS. I. STRUCTURES OF COLLAPSED STEARIC ACID MONOLAYERS

MARIA TOMOAIA-COTIŞEL[1], GHEORGHE TOMOAIA[2], AURORA MOCANU[1], VASILICA-DANIELA POP[1], NECULAI APETROAEI[3] and GHEORGHE POPA[3]

[1]"Babeş-Bolyai" University, Faculty of Chemistry and Chemical Engineering, Physical Chemistry Department,400028 Cluj-Napoca,Romania
[2]"Iuliu Haţieganu" University of Medicine, Orthopedic Surgery, 400015 Cluj-Napoca,Romania
[3]"A. I. Cuza" University, Plasma Physics Department, 700506 Iasi, Romania

ABSTRACT. Our previous theoretical studies on the collapse mechanism of stearic acid monolayers at the air/aqueous solution of pH 2 interface have suggested that the collapse mechanism can be described by a nucleation process subsequently followed by a growth of the nuclei. In the present work we will provide more evidence on the collapse mechanism and on collapsed structures of stearic acid monolayers by using atomic force microscopy (AFM) on Langmuir-Blodgett (LB) films of stearic acid transferred from monolayers, at the air/water interface, on hydrophilic substrates. Topographic and phase AFM images have shown several types of collapsed structures identified by us as straight bilayer ridges and buckling areas, three layered collapsed fragments, and multilayered colloidal particles. By using cross section profiles through the topographic images, the said collapsed structures were found in equilibrium with condensed stearic acid monolayer domains. These results are in substantial agreement with our earlier theory on collapse mechanism of Langmuir monolayers and with similar reported data in the literature. Finally, they confirm that AFM provides an accurate analysis on the packing of the molecules in monolayers and in collapsed structures and on the formation of LB film domains at the nanometer scale.

Key words: atomic force microscopy, Langmuir-Blodgett films, stearic acid, collapsed structures.

INTRODUCTION

Stearic acid (SA) is an example of an amphiphilic biocompound that is insoluble in water and self-assembles as a stable Langmuir monolayer at the air/aqueous solution of pH 2 interface. Due to its high surface stability, SA is considered as a model compound suitable for nanolayers research.

Traditionally valuable information on the molecular organization of SA in monolayers is obtained from compression isotherms [1-3], which are given in terms of surface lateral pressure as function of mean molecular area [1-7]. To study the surface properties and to visualize the surface structure of a biocompound nanolayer, a variety of experimental techniques and methods have been developed.

Thus, during the past several decade sophisticated methods have been developed such as fluorescent microscopy [8, 9], Brewster angle microscopy [10], and synchrotron X-ray diffraction [10-13], which provide a more detailed picture of the molecular organization in different biocompound monolayers. However, these methods show a limited lateral resolution of structures existing in the plane of the film.

By transfer of a monolayer to a solid substrate [10-13] a Langmuir-Blodgett (LB) film is obtained and further techniques are available for the LB film investigations. Therefore, absorption-reflection infrared spectroscopy and ellipsometry [2], Fourier transform infrared spectroscopy [13], electron scanning microscopy [14, 15] and surface plasmon resonance [16] have been used to investigate monolayer domains and molecular orientation of various biocompounds but none of these techniques can provide direct information on nano-meter scale structure of LB film surfaces.

Recently, the atomic force microscopy (AFM) was developed and it is used for visualization of various phases which can occur in nanolayers, for their surface structure investigations as well as for size analysis of supramolecular aggregates [17-29]. The AFM is a novel high-resolution surface imaging technique for nano-meter scale size structures with angstrom-scale lateral and normal resolution. AFM operates by measuring the forces acting between a probe (also called tip) attached to a cantilever and the LB film, which is called usually the LB sample.

Further, the AFM coupled with LB film technique offer the possibility of studying the evolution of film structures at collapse as the Langmuir monolayers evolve from two to three dimensions. The study of the mechanism of collapse and collapsed structures [14, 15, 30-38] is also useful to build-up model membranes for complicated biological membranes to investigate the structure, activity and function of biologically relevant biocompounds, under controlled conditions of lateral pressures. LB films formed by amphiphilic molecules, like stearic acid, occupy a unique place at the crossroads of materials science, nanoparticles technology, complex soft materials physics, interfacial physical chemistry of oriented supramolecular structures, colloidal and surface chemistry, physical biology, pharmacology, molecular biophysics and biomedicine.

The goal of our present work is to find more evidence about the collapse mechanism and to visualize the collapsed structures of SA films by using LB technique and AFM investigations.

EXPERIMENTAL SECTION. MATERIALS AND METHODS.

CHEMICALS AND LANGMUIR MONOLAYERS

Stearic acid was purchased from Sigma, n-hexane was purchased from Merck, and other chemicals were purchased from Reactivul Bucharest, all of high purity requested for Langmuir monolayer research.

Stearic acid (SA) was dissolved in n-hexane at a concentration of 1mg/ml and spread on acid aqueous solution of 0.01 M HCl of pH 2, in order to avoid ionization of SA molecules, in the teflon trough, at 20 ^{o}C. After a waiting time of

5 to 10 minutes to allow the solvent to be fully evaporated, the Langmuir monolayer of stearic acid was manually compressed at a speed of 10 cm^2/min and the compression isotherm was recorded as described by us in detail elsewhere [1].

The SA monolayer was compressed to its collapse and then transferred to the hydrophilic substrate by vertical dipping method or by horizontal transfer method, as we previously reported [2]. In detail, the transfer of LB films, at incipient collapse of SA monolayer (where its lateral surface pressure is 40.8 mN/m) or from an over compressed SA monolayer at 45 mN/m, was performed on glass by horizontal deposition method. For comparison, the transfer of LB films from over compressed SA monolayers at 45 mN/m was also performed on glass covered with thin aluminium mirror by vertical transfer method at low transfer speed of 0.5 cm/min. The over compressed SA monolayers have reached an advanced collapse state.

The aqueous subphase was prepared with water of 18 Mohm cm obtained by using an Elgastat system and it was adjusted at pH 2 with hydrochloric acid.

LANGMUIR-BLODGETT TECHNIQUE AND LB SAMPLE PREPARATION

The LB films of SA supported on 0.1 mm thick freshly cleaned glass or glass covered with aluminium mirror, were built up using Langmuir-Blodgett technique. Prior to SA film deposition, the glass was well cleaned with chromic acid and rinsed with two-distilled water. The hydrophilic glass support was lifted horizontally from water phase through the SA monolayer compressed at collapse (40.8 mN/m) or compressed over its lateral collapse pressure at 45 mN/m. To protect the LB films from dust, the plates with LB films were covered with 50 ml beakers. This procedure might make the evaporation of water slower as compared to that in an open air environment.

For comparison, the glass substrate covered with thin aluminium mirror was lifted vertically from water phase through the Langmuir nanolayer of SA over compressed at 45 mN/m, when the nanolayer exists in an advanced collapse state. Due to the experimental configuration of this transfer method, the support with LB film was held vertically in the ambient atmosphere at room temperature until the transferred SA film was dried (about 10 minutes).

This work demonstrates that, both models of LB samples, LB vertically and LB horizontally transferred, showed a good transfer quality of the LB films. At least three LB films were prepared for every independent LB sample, under controlled conditions.

Then, tens of AFM scans were made for each LB film, and the images from different LB films showed that the morphological reproducibility is good for one specific LB sample. Even more, LB samples of stearic acid on glass and on aluminium mirror were measured several days after the transfer and occasionally several months up to one year after the transfer of SA nanolayers. The reproducibility of AFM images demonstrated that the transferred SA films have a high stability.

ATOMIC FORCE MICROSCOPY IMAGING AND ANALYSIS

Investigation of the surface morphology and domain structure of the LB films of SA was conducted in tapping mode on a research AFM system described elsewhere [29]. The AFM was calibrated by using freshly cleaved highly oriented pyrolytic graphite (HOPG). Direct visualization of LB film structures was performed with AFM equipped with a 90 μm scanner (x-y), 1.5 μm (z) scanner, with scan control and commercial software.

Non-contact conical shaped tips of silicon nitride coated with aluminium were used for AFM tapping mode. The tip was on a cantilever with the length of 110 μm, width of 40 μm and thickness of 2 μm. The resonant frequency of the cantilever was in the range of 200 - 300 kHz with a spring constant of 17.5 N/m. The manufacturer specification for the terminal tip radius of curvature is less than 10 nm, the full tip cone angle less than 20 degrees and its height in the range of 15 – 20 μm.

The AFM images reported in the present work were two-dimensional (2D) topographies and the three-dimensional (3D) views of 2D-topographies, all performed in tapping mode. For comparison, occasionally, the phase image is also given. All images were processed using the standard procedures for AFM.

The AFM images cover a range of LB film areas from 10 x 10 μm^2 to 2 x 2 μm^2. AFM observations were repeated on different areas of the LB sample. The images were obtained from at least three macroscopically separated areas on each LB sample. Dimensions of the SA domains were measured directly from AFM topographic images and the thickness variations were estimated from cross section profile analysis.

An important property of AFM is its ability to measure the height of observed LB film domains. Therefore, the main criterion to distinguish among various structures, such as monolayer, bilayer, trilayer or other forms, is the height of the observed domains in LB films. The images of the domains have bell-shape forms, as observed in the cross section profiles. Because the lateral dimensions are broadened due to a tip-related effect [39], the size of a domain was determined as the width of its bell shaped form measured at its half height.

RESULTS AND DISCUSSION

COMPRESSION ISOTHERM OF LANGMUIR MONOLAYER OF STEARIC ACID

A Langmuir monolayer (also called nanolayer) is generally obtained by spreading a known number of SA molecules on the air/aqueous solution of pH 2 interface in a Langmuir teflon trough of a precise known area. Teflon barriers placed across the trough serve to vary the area of the SA nanolayer in compression – expansion cycles, and in consequence, the mean molecular area of the SA amphiphilic molecule is precisely determined, and simultaneously, the surface pressure is measured by using a surface tension sensor in the Langmuir technique [1, 2]. The surface pressure (π, expressed in mN/m) is

calculated as the difference between the surface tension of the pure subphase against air (σ_0, given in mN/m) and the surface tension (σ, in mN/m) of the air/water interface with Langmuir nanolayer.

By compression of stearic acid monolayer spread at the air/aqueous phase of pH 2 interface, the compression isotherm is obtained (Fig. 1) and it exhibits sharp modifications which illustrate phase transitions under controlled conditions. Previously, we have already demonstrated that SA film exhibits a variety of characteristic phases, like condensed liquid (CL, with characteristic limiting area of stearic acid molecule A'_0), solid (S, with limiting molecular area A_0) and collapsed phases under known experimental conditions [1-3]. The two dimensional (CL – S) phase transition from condensed liquid to solid is observed at a lateral surface pressure of about 26 mN/m.

The collapse surface pressure is the highest surface lateral pressure, marked by an arrow on the isotherm (Fig. 1), to which a Langmuir monolayer can be compressed at the air/water interface without the formation of a detectable collapsed bulk phase [3, 30] of the film forming SA molecules. This collapsed state corresponds to an incipient collapse of the SA monolayer (40.8 mN/m) at the air/water interface.

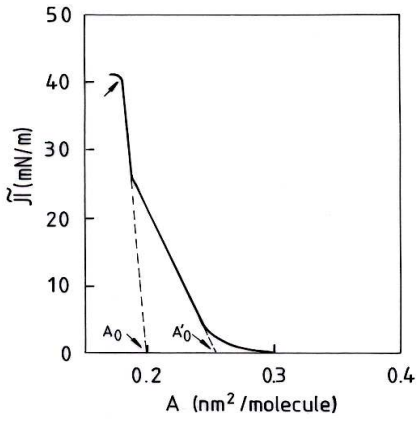

Fig. 1. Compression isotherm of stearic acid (SA) monolayer, surface pressure versus mean molecular area, at the air/aqueous solutions of pH 2 interface, at 20 ^{o}C. For symbols see the text. The arrow at high surface pressure indicates the incipient collapse.

To deeply understand the collapsed structures, SA monolayer was over compressed, above its incipient collapse state, to higher surface lateral pressures (45 mN/m). This new state corresponds at an advanced collapse state of SA films, which was further investigated by AFM on LB films of stearic acid transferred on solid substrates by both deposition methods described above under these new conditions.

STEARIC ACID MONOLAYER ORGANIZATION AT THE AIR/WATER INTERFACE

In our earlier studies, the characteristic phases in Langmuir monolayers of SA at the air/water interface have been evidenced by using compression isotherms, surface compressibility measurements and geometric molecular models [1]. At the monolayer incipient collapse (40.8mN/m), the rodlike SA molecules are vertically oriented in the most extended all-trans conformation of their saturated hydrocarbon chains. Some geometric considerations on the film organization may be useful for understanding the structural characteristics at collapse, or when over compressed above its collapse.

The study of molecular models showed that in the most extended conformation of SA molecule the polar COOH group can be readily accommodated beneath the hydrocarbon chain and the height of the entire molecule attains 26.2 Á [1]. This molecular height can be considered as an important parameter relevant to the monolayer's thickness and to the morphology of SA monomolecular film at its monolayer collapse. This height is in good agreement with the value of 2.5 nm determined for stearic acid monolayer by AFM investigations [27].

COLLAPSE MECHANISM OF LANGMUIR MONOLAYERS OF STEARIC ACID

From previous studies on the collapse mechanism of an insoluble Langmuir monolayer at the air/water interface theoretical models were developed [14, 15, 30-35]. The states of collapsing processes [14, 15, 33] for an over-compressed Langmuir monolayer are shown in Fig. 2.

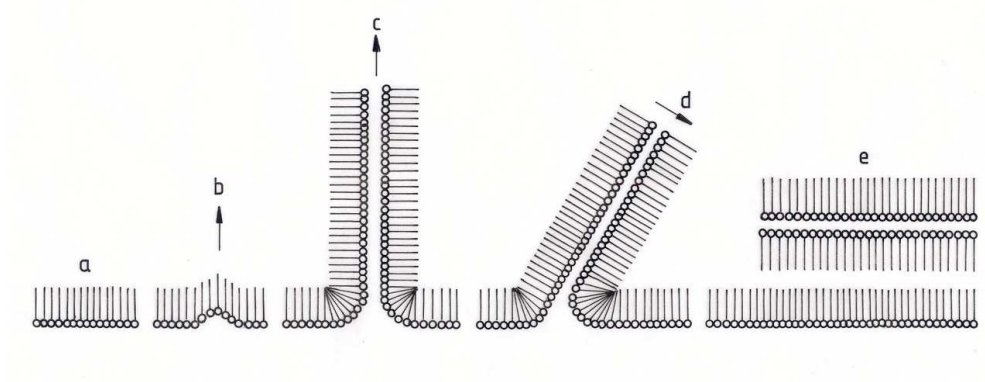

Fig. 2. States of collapsing processes and collapsed structures obtained during the over compression of condensed stearic acid monolayers. Arrows show the movement of molecules in different structures (see the text). The drawings are not at scale.

Experimentally, the incipient collapse is often observed at a very reproducible collapse pressure, corresponding to a metastable equilibrium between the nanolayer and the undetectable freshly collapsed bulk phase [30, 36].

The collapse pressure (π_c in mN/m) value and the corresponding molecular area (A_c) value for SA are easily determined from compression isotherm (see the arrow in Fig. 1). At high surface pressure of about 40.8 mN/m, the Langmuir monolayer is metastable and collapsing processes or relaxation phenomena occur, which may represent the formation of either two-dimensional micelles or islands of close packed surfactant molecules, both entailing formation of nuclei of the new phase and subsequent growth of these nuclei.

With heterogeneous kinetic processes, the Prout-Tompkins equation is frequently applied [37, 38], which was adapted [31] and refined by us [32-34] for the collapse mechanism (Fig. 2) of the insoluble Langmuir monolayers.

Theoretical studies of collapsing processes in SA monolayer [33] showed that by increasing the lateral surface pressure over the incipient collapse pressure of SA monolayer, at incipient collapse SA monolayer existing in a two-dimensional condensed phase (Fig. 2a), a buckling process might evolve in the plane of the monomolecular film (Fig. 2b) which entails film breaking and the formation of bilayers as vertical ridges (Fig. 2c) which can rise to the air phase. These ridges bend (Fig. 2d) and end up in breaking down over the remaining monomolecular film as a collapsed fragment and therefore, trilayers (Fig. 2e) may appear. Further, we will provide more detailed experimental evidence on collapsed structures obtained in SA monolayers by using LB technique and AFM investigations.

ATOMIC FORCE MICROSCOPY OF LB SAMPLES OF STEARIC ACID

We carried out studies at an incipient collapse of SA monolayers (for a collapse pressure of 40.8 mN/m) and at over compressed conditions beyond the monolayer collapse (called advanced collapse for a lateral surface pressure of 45 mN/m), in order to characterize their surface structure by AFM tapping mode and bring light on the collapse mechanism. The sensitivity of AFM measurements is very high and accurate information on the surface morphology at the molecular level is obtained.

For the beginning, the AFM observations have been carried out on LB samples horizontally transferred on glass, at incipient collapse, as shown in Fig. 3, namely 2D-topography (panel A), 3D-topography (B), and cross section profile (C) along the line shown in panel A. The three dimensional image (B) was obtained by image processing of the two-dimensional topography (A).The morphology of the SA film at incipient collapse is typically shown in Fig. 3 (panels A and B). The SA film structure consists of condensed monolayer domains aggregated in irregular and in circular forms with bridges among them. The highest thickness of the SA film remains almost unchanged at 28 ± 2Å as shown in cross section profile (Fig. 3C). This thickness corresponds to the height of SA molecules (25 Å [27]) in their all-trans conformation (26.2 Å [1]) vertically oriented on the LB surface. This value can be considered as an important parameter relevant for the thickness of a SA monolayer relatively well packed at incipient collapse in condensed domains. However, Fig. 3A and Fig. 3B show the presence of some pinholes particularly in the middle of the circular condensed domains and some other defects are visualized around the condensed domains.

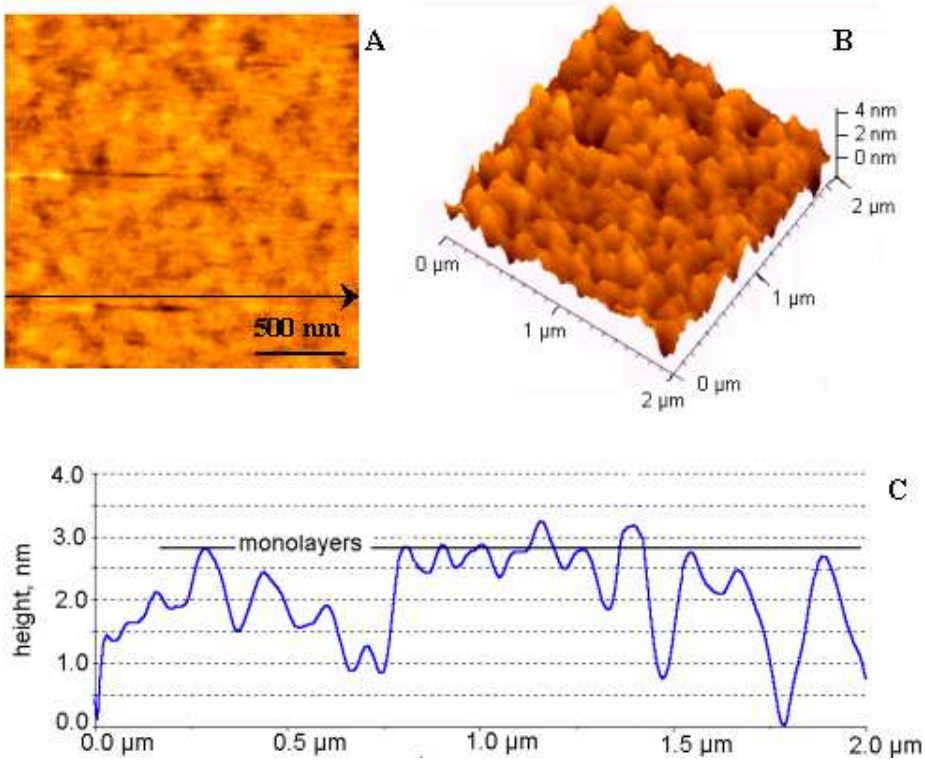

Fig. 3. AFM images, 2D topography (scanned area 2 x 2 µm^2, panel A), 3D topographic view (panel B) and cross section profile (panel C) along the line in panel A for stearic acid LB sample horizontally transferred on glass at incipient collapse (40.8 mN/m) from SA monolayers at the air/aqueous solution of pH 2 interface.

Further, the AFM images are given in Figs. 4 and 5 for an advanced collapse, when the SA monolayer was over compressed at 45 mN/m before the film transfer on glass substrate.

The morphology of the SA film is shown in Fig. 4, 2D-topography (A), 3D-topography (B), and section profile (C) along the line shown in panel A. Apparently, the surface of SA film contains two types of supramolecular aggregates with monolayer and trilayer structures as indicated in Fig. 4C. The trilayer domains are of irregular rounded forms (Fig. 4, panel A and B).

On Fig. 4C, the highest thickness of the SA film is about 77 Å and it represents the thickness of three layered highly ordered domains. The lower height value of 26 ± 2Å is almost constant and it represents monolayer domains as shown in cross section profile (Fig. 4C). The whole film surface is dominated by the three layered structures (see, the line in Fig. 4A) and monolayer domains (see, the marked square area in Fig. 4A) decorated with some large colloidal particles with a thickness of about 200Å (see arrows in Fig. 4B).

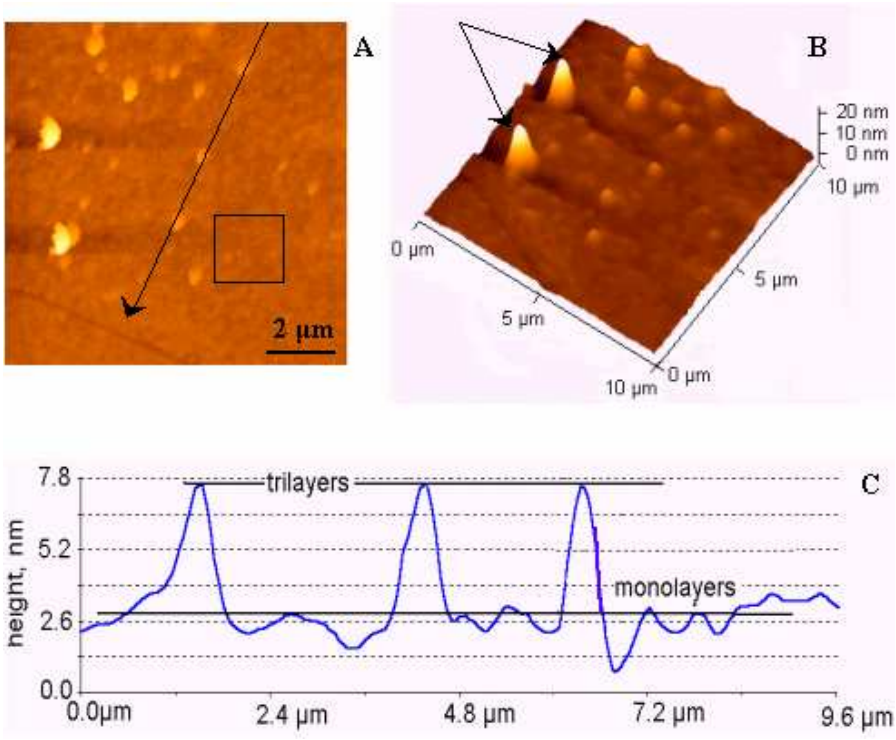

Fig. 4. AFM images, scanned area 10 x 10 µm^2, 2D topography (panel A) and 3D topographic view (B) of stearic acid LB sample horizontally transferred from over compressed monolayer at advanced collapse (45 mN/m) at the air/aqueous solution of pH 2 interface and cross section profile (C) along the oblique line in panel A (see the arrow); the marked area indicates monolayer domains.

Furthermore, to investigate deeply the morphology of monolayer domains at advanced collapse of SA films, enlarged AFM images were obtained by scanning the area marked in Fig. 4A and they are given in Fig.5 (panels A and B) together with the cross section profile (Fig. 5C) along the line shown in Fig. 5A. The section profile shows the height of SA film between 26 Å and 28 Å corresponding to monolayer domains of 240nm average size (Fig. 5C). On the other hand, the nano-structure of the SA monolayer at advanced collapse seems to be quite rough and several large holes (Figs. 5A and 5B) with a similar depth (Fig. 5C) were observed on the surface.

The marked area seen in large-scale AFM image (Fig.4A,10x10µm^2) showed a smooth, high quality surface of monolayer area. However, this smooth surface morphology at a high magnification (Fig. 5A, 2 x 2µm^2) presents larger monolayer domains at advanced collapse than those observed at incipient collapse of SA monolayers (for the same magnification, see Fig. 3A, 2 x 2µm^2). This observation can reflect some real modifications in the LB film morphology

due to the increased lateral surface pressure for advanced collapse state of SA monolayers. This might also be overlapped with an AFM artifact, which can be associated with a tip dilation of the lateral dimensions of nano-scale objects.

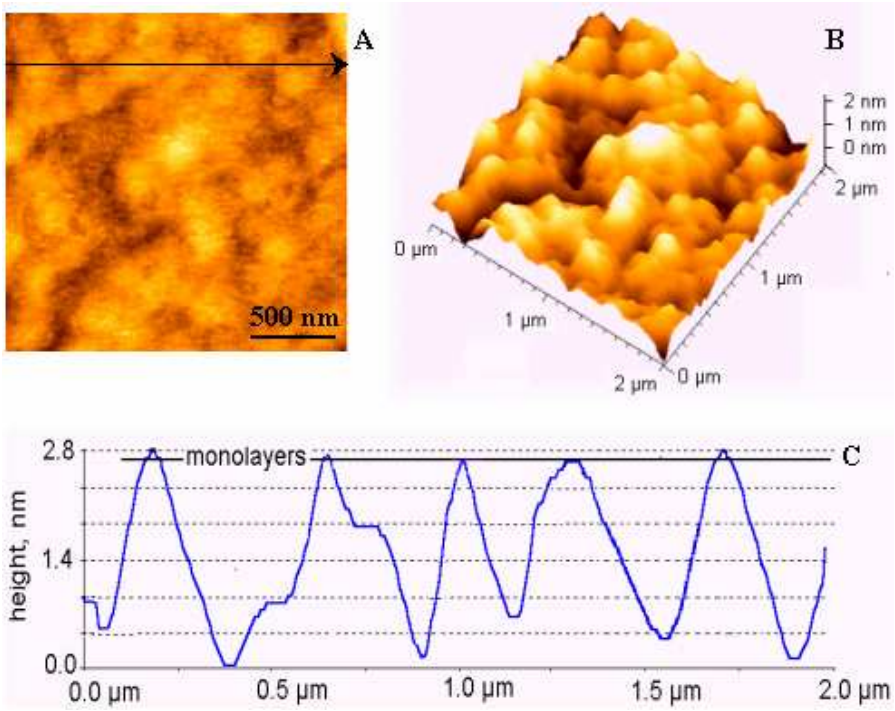

Fig. 5. AFM images of stearic acid LB sample obtained from the almost flat area (scan size 2 x 2 μm^2) which is marked as a square in Fig. 4A; 2D topography (A), 3D topographic view (B) and section profile (C) along the line in panel A.

It is to be mentioned that the AFM tapping mode allows simultaneous acquisition of both topographic data (topographic image) and material-properties data (phase image). The topographic image represents the sample surface structure which is obtained by monitoring the cantilever's oscillation amplitude changes in response to tip to sample spacing, as shown above. Simultaneously, the phase image is produced and can be used to map variations in surface properties such as elasticity, adhesion, and friction. The phase image is obtained by monitoring of the phase lag between the signal that drives the cantilever to oscillate and the cantilever oscillation output signal. Changes in the phase lag reflect changes in the mechanical properties of the sample surface.

To further check the morphology of the LB films of SA, the AFM observations have been carried out on LB films, vertically transferred on glass covered by aluminium mirror, at advanced collapse for a lateral pressure of 45 mN/m. These

AFM observations are given in Fig. 6, 2D-topography (A), phase image (B), section profile (C) along the line shown in panel A, and the 3D-topography (D) which was obtained by image processing of the two-dimensional topography (A).

The images of the LB film of SA (Figs. 6A and 6B) correspond to an advanced collapse state and they show a film structure with an irregular distribution of various domains mostly rounded in shape. The correlation between topographic (Fig. 6A) and phase (Fig. 6B) images suggests that these AFM imaging techniques are complementary and they permit to make observations both on the structural characteristics and on mechanical properties of LB film surfaces, respectively. It is to be noted that there are clear characteristic features in Fig. 6B, comparable with those in Fig. 6A, relevant for modifications of physical and chemical properties of various domains from the LB film surfaces.

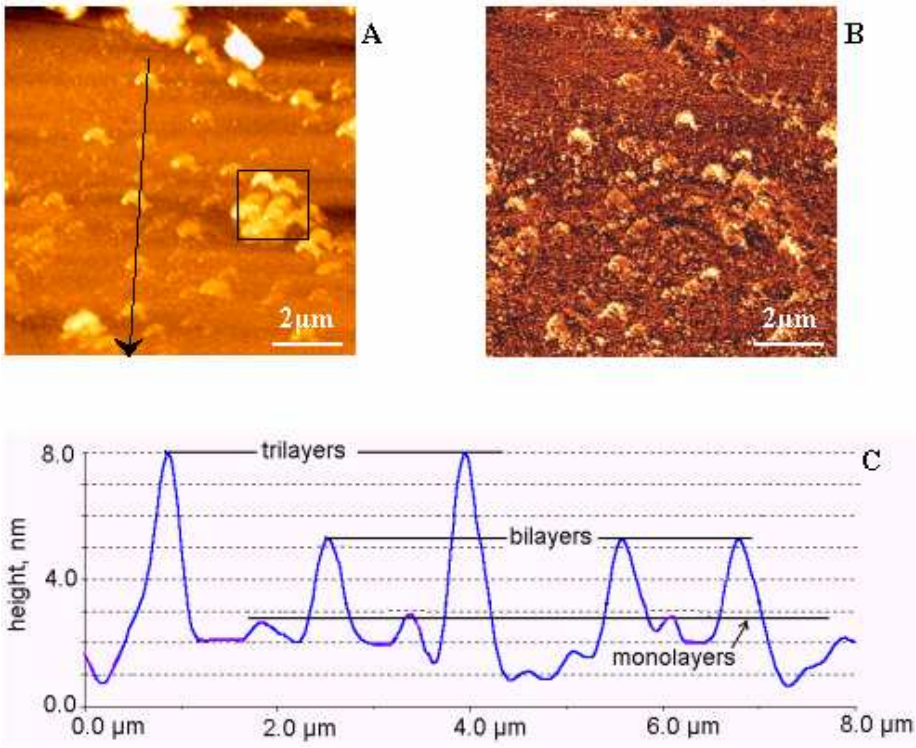

Fig.6. 2D topographic (A) and phase (B) AFM images (10 x 10 μm^2) of LB sample of stearic acid transferred from an over compressed monolayer at 45 mN/m, being in an advanced collapse state, on acid subphase of pH 2. LB sample was deposited by vertical transfer on glass covered by an aluminium thin film; panel C represents the cross section profile along the oblique line (see the arrow) shown in Fig. 6A; the marked area indicates trilayer domains.

The cross section profile (Fig. 6C) indicates the presence of “bilayer” domains with the height of about 53 Å, which is almost two times that of stearic acid monolayer, besides monolayers with the height of about 27 Å and trilayers with the height of 80 Å. These bilayer domains can designate the buckling areas (Fig. 2b) or bilayer ridges (Figs. 2c and 2d) which apparently grow up to a height corresponding to the thickness of a SA bilayer in substantial agreement with AFM observations on collapsed SA film transferred on hydrophobic HOPG [21]. The average size of SA domains is comprised in the range of 300 nm to 500 nm. The dimensions of these domains given in Fig. 6C are visualized also in Fig. 6D.

The marked area in Fig. 6A indicates trilayer domains (Fig. 2e) clustered as it is also evidenced in Fig. 6D. These trilayer domains are larger than in the rest of the scanned area. Fig. 6A shows also the presence of several large colloidal particles with the height in the range of 120 – 200 Å as determined from Fig. 6D (see arrows).

The image analysis of Figs. 3-6 indicates similar structural features of the LB films, formed at the collapse of stearic acid monolayers either horizontally transferred on glass (Figs. 3-5) or vertically transferred on an aluminium mirror (Fig. 6). This is attributed to the high stability of the hydrophobic groups, i.e., methyl groups on the surface of the outermost layer of the LB films in air. Previously, we have pointed out that odd numbered LB films of stearic acid can be deposited at more than 200 layers on hydrophilic glass [2]. The experimental LB film structures visualized by AFM two- and three dimensional topographical images, phase image and cross section profiles can be explained by collapse mechanism proposed previously [15, 32, 33].

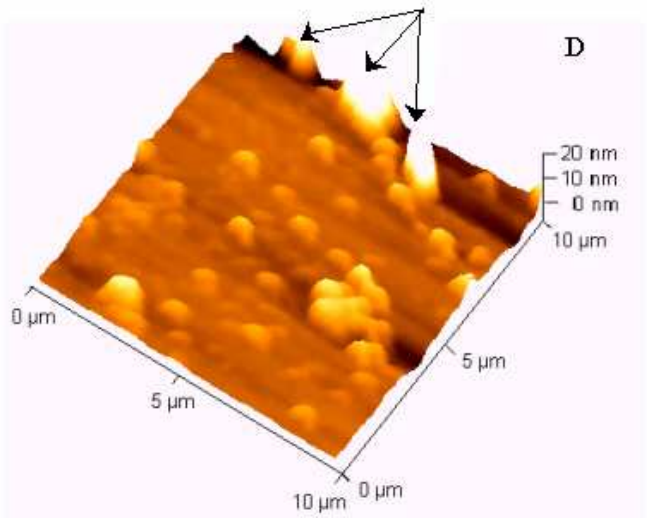

Fig.6D.The 3D view of the 2D topographic AFM image (Fig. 6A) for stearic acid LB sample. Arrows indicate colloidal particles.

It is to be emphasized that the height of a SA molecule in its extended all – trans conformation is about 26.2 Å as it was determined by us previously [1] from geometric models. This calculated length of a SA molecule is close to the value recently found of 25 Å /molecule of SA by AFM investigations [27] and it almost coincides with the height value of 26Å preponderantly found for monolayer domains in cross section profiles shown above.

In present studies, AFM technique has been found suitable to investigate the surface morphology, defects and domain structure of LB films of stearic acid horizontally and vertically transferred on solid substrates from Langmuir monolayers of stearic acid at the air/water interface for two lateral surface pressures characteristic for incipient and advanced collapse of SA monolayers. From AFM observations of the collapsed structures, trilayers and monolayer domains were found within the advanced collapsed SA film. In addition, straight ridges and buckling domains, which show a thickness of double molecular layers [21], and an accumulation of colloidal particles [22, 24, 27] were identified in total agreement with literature data.

CONCLUSIONS

The atomic force microscopy was used to study the surface structure of Langmuir-Blodgett films of stearic acid at the nanometer scale, the transition from monolayers to multilayered collapsed phase and the collapse mechanism. Analysis of topographic and phase images showed differences among various surface morphologies suggesting that there are also modifications of the surface properties of LB films in various supramolecular film arrangements.

LB films of stearic acid horizontally and vertically transferred from air/aqueous solution of pH 2 interface on glass and on glass covered with an aluminium mirror, respectively, showed a similar morphology at advanced collapse. From AFM observations of the collapsed structures and from section profile through topographic images, straight ridges or buckling areas, which show a thickness of double molecular layers, trilayers, colloidal particles and monolayer domains were identified in substantial agreement with our previously published theory on the collapse mechanism of Langmuir monolayers and with reported literature data. These results demonstrate that the surface structure of collapsed LB films of stearic acid is preserved in both vertical LB transfer and in horizontal LB transfer.

This approach might be very promising in the study of biologically relevant molecules since molecular processes like the orientation of molecules, their packing in the surface network, and the collapse of their self-assemblies can occur in biological membranes.

In this work, we were able to demonstrate that the SA films maintained their film stability for one year. This knowledge would be useful in determining the duration and the stability of these nanolayers with possible use in various medical micro-devices coated with fatty acids films and in drug delivery systems.

Further studies are in progress in our laboratories which will bring more detailed information regarding the stabilizing forces in the freshly collapsed and in advanced collapsed fragments within nanolayers.

REFERENCES

1. M. Tomoaia-Cotişel, J. Zsako, A. Mocanu, M. Lupea, E. Chifu, “Insoluble mixed monolayers. III. The ionization characteristics of some fatty acids at the air/water interface”, *J. Colloid Interface Sci.*, 1987,**117**, 464.
2. M. Tomoaia-Cotişel, E. Chifu, S. Jitian, I. Bratu, S. Bran, P.T. Frangopol, A. Mocanu,“The study of stearic acid films by ellipsometry and absorption-reflection IR spectroscopy”, *Studia Univ Babes-Bolyai Chem*., 1990, **35** (2), 17.
3. M. Tomoaia-Cotişel, “On the mechanism of procaine penetration into stearic acid monolayers spread at the air/water interface”, *Progr. Colloid Polym. Sci.,* 1990, **83**, 155.
4. G. Gabrielli, “Monolayers and planar or curved bilayers”, *Adv. Colloid Interface Sci.*,1991, **34**, 31.
5. M. Tomoaia-Cotişel, D. A. Cadenhead, “Interaction of procaine with stearic acid monolayers at the air/water interface”, *Langmuir,* 1991, **7**, 964.
6. M. Tomoaia-Cotişel, P.J. Quinn,“Biophysical properties of carotenoids”, Subcellular Biochemistry, Volume 30:Fat-Soluble Vitamins”, Chapter 10, Edited by P.J. Quinn and V.E. Kagan, Plenum Press, New York, pp. 219-242, 1998.
7. R. Maget-Dana, “The monolayer technique: a potent tool for studying the interfacial properties of antimicrobial and membrane-lytic peptides and their interactions with lipid membranes”, *Biochim. Biophys. Acta*, 1999, **1462**, 109.
8. H. Möhwald, “Phospholipid and phospholipids-protein monolayers at the air/water interface”, *Annu. Rev. Phys. Chem.,* 1990, **41**, 441.
9. B. Asgharian, D. A. Cadenhead, M. Tomoaia-Cotişel, “An epifluorescent microscopy study of the effects of procaine on model membrane systems”, *Langmuir,* 1993, **9**, 228.
10. “Langmuir-Blodgett films”, Edited by D. Möbius, Elsevier, New York, 1988.
11. “Langmuir-Blodgett films ”, Edited by K. Fukuda, M.Sugi, Elsevier, New York, 1989.
12. “Langmuir-Blodgett films”, Edited by G. Roberts, Plenum Press, New York, 1990.
13. A. Ulman, “An introduction to ultrathin organic films. From Langmuir-Blodgett to self-assembly”, Acad. Press, New York, 1991.
14. M. Tomoaia-Cotişel, A. Sen, P. J. Quinn, “Surface active properties of 1,2-distearoyl galactosylglycerols”, *J. Colloid Interface Sci.,* 1983, **94**, 390.
15. H. E. Ries, Jr., *Nature,* 1979, **281**, 287.
16. L. J. Noe, M. Tomoaia-Cotişel, M. Casstevens, P. N. Prasad, “Characterization of Langmuir-Blodgett films of 3,4-didecyloxy-2,5-di(4-nitrophenylazomethine) thiophene in a stearic acid matrix”, *Thin Solid Films*, 1992, **208**, 274.
17. J. A. DeRose, R. M. Leblanc, “Scanning tunneling and atomic force microscopy studies of Langmuir-Blodgett films”, *Surface Science Reports*, 1995, **22**, 73.
18. D. K. Schwartz, “Langmuir-Blodgett film structure”, *Surface Science Reports*, 1997, **27**, 241.
19. Y.F. Dufrêne, G.U. Lee,“Advances in the characterization of supported lipid films with the atomic force microscope”,*Biochim.Biophys. Acta,* 2000, **1509**, 14.
20. K. D. Jandt, “Atomic force microscopy of biomaterials surfaces and interfaces”, *Surface Science*, 2001, **491**, 303.
21. K. S. Birdi, D. T. Vu, “Structures of collapsed lipid monolayers investigated as Langmuir-Blodgett films by atomic force microscopy”, *Langmuir,* 1994, **10**, 623.

22. Z. Lu, B. Zhang, Z. Ai, J. Huang, H. Nakahara, “AFM studies on collapsing processes of a stearic acid monolayer. Part 1. Nucleation processes of a monolayer collapsing on the acidic subphase”, *Thin Solid Films*, 1996, **284-285**, 127.
23. H. Wang, W. Li, H. Ding, Y. Zhang, S. Xi, “A method to identify the collapse of monolayers at the air/water interface”, *Thin Solid Films*, 1996, **284-285**, 119.
24. K. Ekelund, E. Sparr, J. Engblom, H. Wennerstrom, S. Engstrom, “An AFM study of lipid monolayers. 1. Pressure-induced phase behavior of single and mixed fatty acids”, *Langmuir*, 1999, **15**, 6946.
25. E. Sparr, K. Ekelund, J. Engblom, S. Engstrom, H. Wennerstrom, “An AFM study of lipid monolayers. 2. Effect of cholesterol on fatty acids”, *Langmuir*, 1999, **15**, 6950.
26. E. Sparr, L. Eriksson, J. A. Bouwstra, K. Ekelund, “AFM study of lipid monolayers.III. Phase behavior of ceramides, cholesterol and fatty acids”, *Langmuir,* 2001, **17**, 164.
27. S. Ye, H. Noda, S. Morita, K. Uosaki, M. Osawa, “Surface molecular structures of Langmuir-Blodgett films of stearic acid on solid substrates studied by sum frequency generation spectroscopy”, *Langmuir,* 2003, **19**, 2238.
28. K. S. Birdi, “Scanning Probe Microscopes. Applications in Science and Technology”, CRC Press, New York, 2003.
29. N. Dumitraşcu, G. Borcia, N. Apetroaei, G. Popa, “Roughness modification of surfaces treated by a pulsed dielectric barrier discharge”, *Plasma Sources Sci. Technol*., 2002, **11**, 1.
30. G. L. Gaines, Jr., “Insoluble Monolayers at Liquid-Gas Interfaces”, Wiley Interscience, New York, 1966.
31. P. Baglioni,G. Gabrielli, G.G.T. Guarini, *J. Colloid Interface Sci.,* 1980, **78**, 347.
32. M. Tomoaia-Cotişel, J. Zsako, E. Chifu, D. A. Cadenhead, H. E. Ries, Jr., “Collapse mechanism of some carotenoid monomolecular films - membrane model”, *Progress in Photosynthesis Research,* Edited by J. Biggins, Martinus Nijhoff Publishers, Vol. **2**, Chapter 4, pp 333-337, 1987.
33. M. Tomoaia-Cotişel, J. Zsako, A. Mocanu, I. Albu, E. Chifu, “Relaxation phenomena in fatty acid monolayers”, *Studia Univ. Babes-Bolyai, Chem*., 1987, **32** (1), 58.
34. M. Tomoaia-Cotişel, J. Zsako, E. Chifu, D. A. Cadenhead, “Relaxation phenomena in apocarotenoid monolayers”, *Langmuir*, 1990, **6**, 191.
35. D. Vollhardt, U. Retter, *J. Phys. Chem*., 1991, **95**, 3723.
36. J. Zsako, M. Tomoaia-Cotişel, E. Chifu, “Insoluble mixed monolayers. I. Phase equilibria at the collapse of binary monolayers at gas/liquid interfaces”, *J. Colloid Interface Sci.,* 1984, **102**, 186.
37. E. G. Prout, F. C. Tompkins, *Trans. Faraday Soc.,* 1944, **40**, 488.
38. E. G. Prout, F. C. Tompkins, *Trans. Faraday Soc.,* 1946, **42**, 468.
39. O. I. Kiselyova, I. V. Yaminsky, Y. D. Ivanov, I. P. Kanaeva, V. Yu. Kuznetsov, A. I. Archakov, “AFM study of membrane proteins, cytochrome P450 2B4, and NADPH-cytochrome P450 reductase and their complex formation”, *Arch. Biochem.Biophys*., 1999, **371**, 1.

STUDIA UNIVERSITATIS BABEŞ-BOLYAI, CHEMIA, XLIX, 2, 2004

Dedicated to Professor Valer Fărcăşan
at his 85th anniversary

REACTIVITY OF A COAL IN GASIFICATION REACTIONS. A THERMODYNAMIC CASE STUDY

GAVRIL NIAC[a], OSSI HOROVITZ [b], ELENA MARIA PICĂ[a]

[a] Department of Chemistry, Technical University Cluj-Napoca, Romania
[b]Department of Physical Chemistry, "Babeş-Bolyai" University, Cluj-Napoca, Romania

ABSTRACT. Gibbs free energies, and equilibrium constants were calculated and zero-affinity plots were drawn based on average maceral phase composition, obtained by extrapolation of elemental content and higher heating value, to the ash content of the maceral phase, according to the two phase model of coals. Elements bound to the organic mass of coal (S, Al, Fe, Ca) were also considered. Their presence contributes to lowering the Gibbs free energy of gasification reactions. Zero-affinity plots show a much higher thermodynamic reactivity of the studied coal, as compared to graphite. Equilibrium constants (K_x) of gasification reactions for coal (Illinois No.6) approach the value 1 (ΔG_T^P=0) at temperatures 200-300℃ lower than the respective values for graphite.

Keywords: Gasification; Coal; Thermodynamic parameters; Illinois No.6 coal

INTRODUCTION

The concept of coal "reactivity" refers to a specific reactant and comprises two components: the *thermodynamic reactivity*, measured by the Gibbs free energy and the *kinetic reactivity*, expressed by rate constants or activation energies of the involved reactions. The classical way to calculate thermodynamic data (free energies, equilibrium constants) of coal gasification reactions with specific gasification agents, starts with the reactions of graphite and corrections are made for the other elements in coal. Calculations with the coal formula on a per carbon atom basis [1] is a better alternative [2, 3]. The problem is how to calculate the coefficients of such a formula, and how to express most conveniently the respective thermodynamic properties, especially the thermodynamic reactivity of the coal, as to allow comparison among coals differing in nature.

While minerals do not contribute to the thermodynamic properties of coal, ions bound ionically or covalently to organic matter, in the so called "maceral phase", participate to the reactions of gasification and should contribute to the Gibbs free energy of those reactions.

On the other hand, elemental composition (carbon content, hydrogen content, sulfur content) results from the organic as well as from the mineral part of the coal, therefore a per carbon atom formula can not be based upon elemental analysis data and averaging for several samples (having usually different ash contents), as practiced by several authors [2, 3]. Taking advantage of the *two*

phase model of coals [4-7], the composition of the maceral phase (the true carbonaceous matter) can be evaluated extrapolating the elemental composition (including some components of ash), for several samples from the same coal deposit, differing in ash content, to the ash content of the pure maceral phase. This is the average of the amount of ash produced by 100 g pure macerals. The maceral ash content may be found by extrapolation of SiO_2-content (considered to be a component of the mineral phase only) to the ash axis.

In order to get a synthetic view on thermodynamic properties of a reaction, *zero affinity curves* and *iso-conversion curves* were proposed, and a large number of reactions were studied [8-12]. Zero affinity curves are plots of *pressure, p* (more conveniently log *p*), vs. *temperature, T,* for $\Delta G_T^p = 0$, or $K_x = 1$ (K_x being the equilibrium constant written with mol fractions and ΔG_T^p the Gibbs free energy for the reaction at temperature *T* and pressure *p*). Such a curve divides the (log *p*) xT surface into two domains, on the one side $\Delta G < 0$ or $K_x > 1$, on the other $\Delta G > 0$ or $K_x < 1$. At pressures and temperatures lying within the first domain the reaction is thermodynamically favored, while the second domain is unfavorable to the reaction. Such a *zero affinity curve* has the advantage to be independent on how the reaction is written, *i.e.* amplifying the equation does not change the curve.

The goal of this paper is to:

- establish the per carbon atom formula of the maceral phase,
- calculate Gibbs free energies for reactions of the maceral phase, both considering and neglecting metal ions,
- draw log *p* vs. *T* plots for $\Delta G^p_T = 0$ or $K_x(p) = 1$ (zero affinity plots), characteristic for the thermodynamic reactivity of coal in gasification reactions,
- compare these plots with those of graphite.

As a specific example Illinois No.6 coal was chosen, for which the necessary data were published in the final technical report on the Project entitled *Illinois Basin Coal Sample Program*, supported by the State of Illinois [13].

Analytical Properties of Illinois No.6 Coal

The analytical data taken from Chaven [13] are summarized in Table 1 and 2. The composition of the maceral phase, calculated as described in an other paper is given in Table 3 [14]. Other elements were neglected, since their concentration in the macerals is practically zero.

Table 1.

Analytical properties of Illinois No. 6 coal

No.	A(mf) %	V(mf) %	Q, MJ/kg	C(mf) %	H(mf) %	S(mf) %	N(mf) %
1	10.4	41.10	29.33	69.4	5.1	4.4	1.2
2	38.3	28.50	19.85	46.9	3.4	4.1	0.9
3	18.7	37.00	26.88	63.8	4.5	4.5	1.2
4	11.5	40.10	28.44	68.1	4.8	3.8	1.2
5	8.3	35.10	31.01	75	4.9	1.2	1.7
6	10.9	35.90	30.36	72.8	5	2.8	1.6

A – ash content; V – volatile matter; Q – heating value; mf – moisture free;

Table 2.

Ash components in moisture free Illinois No. 6 coal

Ash, %	SiO_2	Al_2O_3	Fe_2O_3	CaO	MgO	K_2O	TiO_2	B_2O_3	ZnO	Na_2O	BaO	MnO
10.4	4.6	1.6	1.7	0.5	0.1	0.2	0.1	0.621	0.046	0.106	0.036	0.040
38.3	22.1	6.5	3.8	1.4	0.5	1	0.3	1.021	0.050	0.64	0.15	0.14
18.7	8.2	2.9	3.4	1.2	0.2	0.3	0.2	0.254	0.0093	0.151	0.082	0.092
11.5	6.1	2.3	1.4	0.6	0.1	0.3	0.1	0.328	0.0007	0.085	0.062	0.054
8.3	4	2	0.9	0.2	0.1	0.2	0.1	0.206	0.0006	0.085	0.039	0.019
10.9	5.5	2.2	1.7	0.4	0.1	0.3	0.1	0.129	0.028	0.108	0.05	0.044

Table 3.

Elemental composition of Illinois coal maceral phase

Element	C	H	S	N	Al	Fe	Ca	O (by diff.)
% in the maceral phase	78.33	5.38	2.79	1.58	0.38	0.62	0.14	10.78

Gibbs free energies of some gasification reactions of Illinois No.6 Coal

Based on analytical properties, the composition of Illinois coal maceral phase can be defined, on a per-carbon-atom basis [1] as follows:

$$CH_{0.824}O_{0.103}S_{0.013}N_{0.017}Al_{0,0021}Fe_{0.0017}Ca_{0.0005} \quad (1)$$

In the following calculations, both the complete above formula and a simplified formula, neglecting the metals content, were used.

In order to make thermodynamic calculations regarding the reactivity of coals, the following parameters were used for the reaction participants: standard enthalpies of formation, H_{298}^{o}, standard entropies, S_{298}^{o} and molar heat capacities under constant pressure C_p. For all the substances implied, other than coals, the values from usual thermodynamic tables, where available the CODATA Key Values [15], were used. The temperature dependence of molar heat capacities was calculated as: $C_p = a + bT + cT^2$ (for methane) and $C_p = a + bT + c'/T^2$ for all other compounds [10]. If necessary, the enthalpies of fusion and of vaporization were taken into consideration.

For the maceral part of coals, the *enthalpy of formation* corresponding to the formula was calculated from the higher heating value. As the standard enthalpy ΔH^{o}_{298} of the combustion reaction:

$$CH_{0.824}O_{0.103}S_{0.013}N_{0.017}Al_{0,0021}Fe_{0.0017}Ca_{0.0005} + 1.168\ O_2 =$$
$$= CO_2 + 0.412\ H_2O + 0.013\ SO_2 + 0.0085\ N_2 + 0.00105\ Al_2O_3 +$$
$$+\ 0.00085\ Fe_2O_3 + 0.0005\ CaO \quad (2)$$

refers to a mole, it is related to the higher heating value per kg of the maceral mass Q_s^c by the obvious relation:

$$\Delta H_{298}^{o} = -MQ_s^c/1000$$

where Q_s^c was obtained by extrapolation of the upper heating value of the anhydrous coal to 2.4% maceral ash content. *M* is the molecular mass of the formula (1). From the combustion reaction, the molar enthalpy of formation for the coal was calculated. The enthalpy of liquid water was used, since the upper heating value is concerned. The calculated value was -18.58 kJ/mol; while neglecting the metals in the formula, -21.42 kJ/mol was found. Since here the "molar mass" for coals has a purely conventional meaning, it should be more significant to compare the enthalpy values by referring to the unity mass of coal; these are -1226 kJ/kg (with the metals), and -1400 kJ/kg (without metals) respectively.

The *standard entropy* S_{298}^o for the coals, as well as the *molar heat capacity* C_p cannot be exactly calculated for complex solid substances such as the coals. Values for specific heats can be estimated from Neumann and Kopp-like formulas, such as the formula proposed by Szadeczky [16] for coals, with increments for solids [9, 17, 18]. For molar heat capacities the following formula was used:

$$C_p = 7.56 + 9.6\, n_H + 16.8\, n_O + 13.0\, n_N + 22.6\, n_S + 26.0\, n_M \ [\text{J.mol}^{-1}\text{K}^{-1}] \quad (3)$$

where n_i is the index of the element *i* in the formula (1); M - stands for the metals. The values 17.83 $\text{J.mol}^{-1}\text{K}^{-1}$ (with metals) and 17.72 $\text{J.mol}^{-1}\text{K}^{-1}$ (without metals) were found.

The standard entropy can be estimated for organic solids from the formula of I.I.Strelkov [19]: $S^o_{298} = 1.1\, C_p$. A somewhat higher value for the proportionality factor, viz. 1.2 [9, 19] resulted in 21.39 $\text{J.mol}^{-1}\text{K}^{-1}$ (1398 $\text{J.kg}^{-1}\text{K}^{-1}$) for the formula (1) and 21.26 $\text{J.mol}^{-1}\text{K}^{-1}$ (1405 $\text{J.kg}^{-1}\text{K}^{-1}$), without the metals. They are a reasonable good approximation of entropies, so much the more the reactions considered show large volume variations, and consequently important entropy variations.

For all substances, except the coals, enthalpies and entropies were calculated exactly with the formulae given above for the temperature dependence of C_p. For coal, the C_p value was assumed to be constant.

Molar Gibbs free energies at p = 1 atm: $\Delta G_T^o = \Delta H_T^o - T\Delta S_T^o$ of some gasification reactions at standard temperature, as well as at the temperatures of 100, 200 ... 1000^{o}C for the Illinois No.6 coal were calculated, with the consideration of metals in it an without them, as well as for graphite, for comparison.

Formulas of organic matter of coal per one carbon atom were used to calculate equilibrium gas composition for Wyoming coal gasification by Stephans [2] and Stephans and Miller [3], but the evaluation of indices for H and O was made in a conventional manner, and other elements were neglected.

* The Boudouard reaction (gasification with carbon dioxide):

$$C(s) + CO_2(g) = 2CO(g)\ (g) \quad (4)$$

is endothermic under standard conditions, with volume increase ($\Delta\nu = 1$).

For coal, there are two ways for this reaction, the one with H_2 formation:

$$CH_{0.824}O_{0.103}S_{0.013}N_{0.017}Al_{0,0021}Fe_{0.0017}Ca_{0.0005} + 0.929\ CO_2 = \\ = 1.929\ CO + 0.412H_2 + 0.013\ SO_2 + 0.0085\ N_2 + 0.00105\ Al_2O_3 + \\ + 0.00085\ Fe_2O_3 + 0.0005\ CaO \quad (4a)$$

with volume increase ($\Delta\nu = 1.4335$), and the other with H_2O formation:

$$CH_{0.824}O_{0.103}S_{0.013}N_{0.017}Al_{0,0021}Fe_{0.0017}Ca_{0.0005} + 1.341\ CO_2 = \\ = 2.341\ CO + 0.412\ H_2O + 0.013\ SO_2 + 0.0085\ N_2 + 0.00105\ Al_2O_3 + \\ + 0.00085\ Fe_2O_3 + 0.0005\ CaO. \quad (4b)$$

with the same volume increase ($\Delta\nu = 1.4335$). Both are endothermic at room temperature.

For these reactions, the Gibbs free energies are given in Table 4. For both, the values are always lower for coal as for graphite at the same temperature and reach the negative domain already between 400 and 500°C (as compared with over 700°C for graphite), thus coal exhibits a higher reactivity versus CO_2 than graphite. For the reaction with water formation (4b), the temperature dependence is greater than for hydrogen formation (4a); the ΔG values for the first reaction (4b) are higher than for the second (4a) at low temperature, but at higher temperatures the tendency for water formation (4b) prevails over that for H_2 formation.

Table 4

The Gibbs free energy ΔG^o_T (MJ/kg) of gasification with CO_2

T°C	Reaction (4)	Reaction (4a)		Reaction (4b)	
	Graphite	Coal	Coal*	Coal	Coal*
25	10.01	6.46	6.79	7.23	7.57
100	8.90	5.37	5.69	6.05	6.38
200	7.42	3.90	4.20	4.48	4.78
300	5.93	2.41	2.69	2.89	3.17
400	4.45	0.90	1.17	1.28	1.55
500	2.97	-0.60	-0.35	-0.32	-0.07
600	1.50	-2.12	-1.89	-1.93	-1.70
700	0.04	-3.65	-3.44	-3.55	-3.33
800	-1.42	-5.18	-4.99	-5.17	-4.97
900	-2.86	-6.72	-6.54	-6.79	-6.61
1000	-4.31	-8.27	-8.11	-8.42	-8.26

*neglecting the metal oxides

- The steam gasification of graphite has two possibilities, the one producing H_2 and CO:

$$C(s) + H_2O(g) = CO(g) + H_2(g), \quad (5)$$

the other, H_2 and CO_2:

$$C(s) + 2H_2O(g) = CO_2(g) + 2H_2(g) \quad (6)$$

Both are endothermic at standard temperature and occur with volume increase ($\Delta\nu = 1$). For the coal under consideration the reactions are written as follows:

$$CH_{0.824}O_{0.103}S_{0.013}N_{0.017}Al_{0,0021}Fe_{0.0017}Ca_{0.0005} + 0.929\ H_2O = \\ = CO + 1.341\ H_2 + 0.013\ SO_2 + 0{,}0085\ N_2 + 0.00105\ Al_2O_3 + \\ + 0.00085\ Fe_2O_3 + 0.0005\ CaO \qquad (5a)$$

and

$$CH_{0.824}O_{0.103}S_{0.013}N_{0.017}Al_{0,0021}Fe_{0.0017}Ca_{0.0005} + 1.929\ H_2O = \\ = CO_2 + 2.341\ H_2 + 0.013\ SO_2 + 0{,}0085\ N_2 + 0.00105\ Al_2O_3 + \\ + 0.00085\ Fe_2O_3 + 0.0005\ CaO \qquad (6a)$$

Both have the same volume increase ($\Delta\nu = 1.4335$ mols of gas per carbon atom).

The trends are much the same as for coal gasification with CO_2 (Table 5). The higher reactivity of coal as compared with graphite may also be clearly seen. The thermodynamic reactivity of coal versus steam is greater, at low temperature, as versus CO_2; from round 800^{o}C on, the trend is inverted. The steam gasification with formation of CO_2 (reaction (6a)) presents lower ΔG values than reaction (5a) for temperatures below 800^{o}C, i.e. the formation of CO_2 prevails over the formation of CO. The opposite occurs at higher temperatures.

Table 5.

The Gibbs free energy ΔG_T^o (MJ.kg^{-1}) for coal gasification with H_2O (5,6), carbon oxide conversion (7) and hydrogenation (8)

T(^{o}C)	Reaction (5)			Reaction (6)			Reaction (7)	Reaction (8)		
	C[1]	Coal	Coal*	C[1]	Coal	Coal*		C[1]	Coal	Coal*
25	7.62	4.72	5.04	5.24	2.85	3.15	-2.39	-4.23	-4.70	-4.55
100	6.78	3.82	4.14	4.65	2.16	2.46	-2.13	-3.71	-4.50	-4.35
200	5.63	2.59	2.89	3.83	1.18	1.46	-1.79	-2.95	-4.22	-4.07
300	4.46	1.33	1.61	2.99	0.18	0.44	-1.47	-2.14	-3.91	-3.75
400	3.28	0.06	0.32	2.12	-0.86	-0.61	-1.17	-1.29	-3.58	-3.42
500	2.10	-1.24	-0.99	1.23	-1.92	-1.69	-0.87	-0.42	-3.25	-3.09
600	0.92	-2.55	-2.32	0.33	-3.02	-2.79	-0.59	0.47	-2.92	-2.75
700	-0.27	-3.88	-3.67	-0.59	-4.13	-3.92	-0.32	1.38	-2.58	-2.41
800	-1.46	-5.22	-5.02	-1.52	-5.26	-5.06	-0.05	2.29	-2.25	-2.08
900	-2.66	-6.57	-6.39	-2.45	-6.41	-6.23	0.21	3.21	-1.93	-1.75
1000	-3.85	-7.94	-7.77	-3.39	-7.58	-7.41	0.46	4.13	-1.61	-1.43

[1] Graphite * neglecting the metal oxides

- The homogeneous reaction of carbon oxide conversion:

$$CO(g) + H_2O(g) = CO_2(g) + H_2(g) \qquad (7)$$

makes the difference between reactions (6) and (5). It is slightly exothermic and without volume variation. The values given in Table 5 for this reaction refer also to 1 kg of carbon.

- The coal hydrogenation reaction (possibly with hydrogen resulted from other reactions):

$$CH_{0.824}O_{0.103}S_{0.013}N_{0.017}Al_{0,0021}Fe_{0.0017}Ca_{0.0005} + 1.728\ H_2 = \\ = CH_4 + 0.1025\ H_2O + 0.013\ SH_2 + 0{,}017\ NH_3 + 0.0021\ Al + \\ + 0.0017\ Fe + 0.0005\ CaO \quad (8)$$

is exothermic, with volume decrease ($\Delta\nu = -1$ for graphite, and $\Delta\nu = -0.5965$ for coal). It presents rather important negative ΔG-values at standard temperature (Table 5). ΔG increases with temperature and becomes positive for graphite at round 550°C; for coals the values are much lower and still negative at 1000°C.

- Some reactions of incomplete combustion, with formation of carbon monoxide (and possibly water or hydrogen) were also considered for graphite (9) and for coal (9a, 10):

$$C(graphite) + 0.5\ O_2(g) = CO(g), \quad (9)$$

$$CH_{0.824}O_{0.103}S_{0.013}N_{0.017}Al_{0.0021}Fe_{0.0017}Ca_{0.0005} + 0.6705\ O_2 = \\ = CO + 0.412\ H_2O + 0.013\ SO_2 + 0.0085\ N_2 + 0.00105\ Al_2O_3 + \\ + 0.00085\ Fe_2O_3 + 0.0005\ CaO \quad (9a)$$

$$CH_{0.824}O_{0.103}S_{0.013}N_{0.017}Al_{0.0021}Fe_{0.0017}Ca_{0.0005} + 0.4645\ H_2O = \\ = CO + 0.412\ H_2O + 0.013\ SO_2 + 0.0085\ N_2 + 0.00105\ Al_2O_3 + \\ + 0.00085\ Fe_2O_3 + 0.0005\ CaO \quad (10)$$

All reactions occur with volume increase [$\Delta\nu = 0.5$ (9), $\Delta\nu = 0.763$ (9a), $\Delta\nu = 0.969$ (10)] and are exothermal. Their Gibbs free energies are compared in Table 6.

The partial oxidation of coal (9a) has more negative ΔG-values as that of graphite, while for the oxidation of coal with water (10) ΔG-values lie above those for partial oxidation of graphite and their temperature dependence is more pronounced, so that at 1000°C, the value for coal becomes equal to that of graphite.

It is of interest to calculate the Gibbs free energy for the formation of the maceral phase from elements:

$$C + 0.412\ H_2 + 0.0515\ O_2 + 0.013\ S + 0{,}0085\ N_2 + 0.0021\ Al + 0.0017\ Fe + \\ + 0.0005\ Ca = CH_{0.824}O_{0.103}S_{0.013}N_{0.017}Al_{0.0021}Fe_{0.0017}Ca_{0.0005} \quad (11)$$

as compared with the Gibbs free energy of graphite: $G_T^o(C) = H_T^o(C) - TS_T^o(C)$. This latter quantity is negative (Table 6), due to the prevailing influence of the entropy factor (the enthalpy being positive); there is a slight diminution of these values with increasing temperature. For coal, on the other hand, the reaction occurs with entropy diminution (gases are consumed), therefore ΔG increases with temperature. Since the standard enthalpy of formation is only slightly negative, the Gibbs free energy of formation becomes soon positive, at about 100°C.

Table 6.

The Gibbs free energy ΔG_T^o (MJ.kg^{-1}) for incomplete combustion (9,10) and for the formation of coal from elements (11)

T°C	Reaction (9)			Reaction (10)		Reaction (11)	
	Graphite	Coal	Coal*	Coal	Coal*	Coal	Coal*
25	-11.43	-15.32	-15.14	-9.17	-8.91	-0.23	-0.41
100	-11.99	-15.93	-15.75	-9.86	-9.61	0.03	-0.16
200	-12.74	-16.73	-16.57	-10.80	-10.57	0.38	0.20
300	-13.49	-17.55	-17.40	-11.75	-11.53	0.74	0.57
400	-14.24	-18.38	-18.24	-12.72	-12.52	1.12	0.96
500	-14.99	-19.21	-19.09	-13.69	-13.51	1.51	1.35
600	-15.72	-20.06	-19.95	-14.68	-14.51	1.93	1.78
700	-16.94	-20.91	-20.81	-15.67	-15.52	2.36	2.21
800	-17.19	-21.76	-21.68	-16.68	-16.54	2.80	2.66
900	-17.91	-22.62	-22.55	-17.69	-17.57	3.25	3.11
1000	-18.63	-23.49	-23.43	-18.71	-18.60	3.71	3.58

* neglecting the metal oxides

This latter quantity is negative (Table 6), due to the prevailing influence of the entropy factor (the enthalpy being positive); there is a slight diminution of these values with increasing temperature. For coal, on the other hand, the reaction occurs with entropy diminution (gases are consumed), therefore ΔG increases with temperature. Since the standard enthalpy of formation is only slightly negative, the Gibbs free energy of formation becomes soon positive, at about 100°C.

Equilibrium constants of gasification reactions

The equilibrium constant in partial pressures K_p is calculated from ΔG_T^o-values:

$$K_p = \exp\left(\frac{-\Delta G_T^o}{RT}\right)$$

and the constant in mole fractions K_x is obtained by:

$$K_x = K_p \cdot p^{-\Delta\nu}$$

($\Delta\nu$ - the variation in the number of gas moles).

For reactions with strongly negative ΔG-values (for instance the combustion reaction) the value of the equilibrium constant is enormous and its calculation is of no interest; the reactions are virtually complete. So is also the hydrogenation reaction of coal (inasmuch the temperatures are not too high), except the graphite hydrogenation, where over 550°C the equilibrium constant becomes less than 1. It is worth calculating the equilibrium constants for ΔG values near to zero, when the conversion (obtained from these constants) is neither close to 1 (as for $\Delta G << 0$), nor close to 0 (as for $\Delta G >> 0$).

Table 7.

The equilibrium constants K_p for some reactions of graphite and coal

T(°C)	Reaction 4	Reaction 4a		Reaction 4b	
	Graphite	Coal	Coal*	Coal	Coal*
25	$9.17.10^{-22}$	$4.89.10^{-18}$	$1.02.10^{-18}$	$4.19.10^{-20}$	$8.71.10^{-21}$
100	$1.12.10^{-15}$	$3.17.10^{-12}$	$9.04.10^{-13}$	$1.08.10^{-13}$	$3.09.10^{-14}$
200	$1.49.10^{-10}$	$2.61.10^{-7}$	$9.72.10^{-8}$	$2.74.10^{-8}$	$1.02.10^{-8}$
300	$3.25.10^{-7}$	$4.37.10^{-4}$	$1.94.10^{-4}$	$9.47.10^{-5}$	$4.20.10^{-5}$
400	$7.25.10^{-5}$	$8.44.10^{-2}$	$4.22.10^{-2}$	$3.01.10^{-2}$	$1.51.10^{-2}$
500	$3.88.10^{-3}$	4.20	2.30	2.14	1.17
600	$8.34.10^{-2}$	87.9	51.6	58.8	34.5
700	0.941	993	616	817	507
800	6.73	$7.27.10^{3}$	$4.71.10^{3}$	$7.07.10^{3}$	$4.58.10^{3}$
900	33.9	$3.81.10^{4}$	$2.56.10^{4}$	$4.22.10^{4}$	$2.84.10^{4}$
1000	132	$1.55.10^{5}$	$1.08.10^{5}$	$1.93.10^{5}$	$1.34.10^{5}$

T(°C)	Reaction 5			Reaction 7
	Graphite	Coal	Coal*	
25	$9.26.10^{-17}$	$2.24.10^{-13}$	$4.35.10^{-14}$	$1.04.10^{5}$
100	$4.09.10^{-12}$	$6.39.10^{-9}$	$1.74.10^{-9}$	$3.74.10^{3}$
200	$3.50.10^{-8}$	$4.20.10^{-5}$	$1.51.10^{-5}$	237.6
300	$1.32.10^{-5}$	$1.37.10^{-2}$	$5.96.10^{-3}$	40.94
400	$8.72.10^{-4}$	0.86	0.424	12.24
500	$1.97.10^{-2}$	19.1	10.4	5.11
600	0.220	218	127	2.66
700	1.50	$1.54.10^{3}$	951	1.60
800	7.17	$7.73.10^{3}$	$5.01.10^{3}$	1.07
900	26.3	$3.01.10^{4}$	$2.03.10^{4}$	0.77
1000	78.4	$9.59.10^{4}$	$6.68.10^{4}$	0.59

*neglecting the metal oxides

For the homogeneous equilibrium (7), the equilibrium constants are given in Table 7. They decrease rapidly with increasing temperature. The K_p values for the gasification with CO_2 and hydrogen formation (4a)

$$K_p = \frac{p_{CO}^{1.929} \cdot p_{H_2}^{0.412} \cdot p_{SO_2}^{0.013} \cdot p_{N_2}^{0.0085}}{p_{CO_2}^{0.929}}$$

or with neglect of the metals

$$K_p = \frac{p_{CO}^{1.923} \cdot p_{H_2}^{0.412} \cdot p_{SO_2}^{0.013} \cdot p_{N_2}^{0.0085}}{p_{CO_2}^{0.923}}$$

and for the reaction (4b) are given also in Table 7. They highlight the same regularities concerning the reactivity of coals in the two reactions as the ΔG values.

The equilibrium constants for the reactions of coals with steam (5) are presented in Table 7 too. For the other reaction with steam (6) the equilibrium constants are simply the product of the K_p-values for reaction (5) with those for reaction (7).

Zero-affinity plots for gasification reactions

A means to characterize the reactivity as a function of both *temperature* and *pressure*, is the *iso-conversion-* and *zero-affinity plots,* proposed by Voiculescu and Niac [8-12]. These curves are plotted in lg p vs. T coordinates, and represent the place of the points of zero Gibbs free energy of reaction $\Delta G_T^p = 0$, i.e., where the equilibrium constant $K_x = 1$ for iso-conversion plots. These plots divide the space into two areas: one for $\Delta G_T^p > 0$ ($K_x < 1$), the other for $\Delta G_T^p < 0$ and $K_x > 1$; the latter is the domain where reactions go with good conversion.

The pressure for zero affinity depends upon temperature according to the equation:

$$\ln p = \frac{-\Delta G_T^o}{\Delta \nu RT}$$

In the case of reactions with $\Delta\nu = 0$, only the temperature affects the equilibrium, and there is a constant temperature for zero-affinity*:* $T_z = \Delta H_T^o / \Delta S_T^o$. So is reaction (7), with T_z (as mentioned above) about 800°C; the domain $\Delta G < 0$ is the area on the left of the vertical $T = T_z$ for any pressure.

The gasification reactions of coals with carbon dioxide (4a, 4b), steam (5a, 6a) and oxygen (9a, 10) proceed all with an increase of the number of gas moles ($\Delta\nu > 0$). For the steam gasification reactions (4a), (4b), (5), (5a), (6) and (6a), the pressures for $K_x = 1$ were calculated and the zero-affinity curves were plotted in Figures 1 and 2 within the pressure domain 1 to 10^3 bar. The area $\Delta G < 0$ is situated at the right and bellow the plots. This domain is shifted to the left (lower temperatures) for coal as against graphite. At lower temperatures, the plots for reactions (4a) and (4b) lie very near to one another, while the plots for the steam gasification reactions (5a), (6a) are shifted leftwards (higher reactivity). At 800°C, all the curves cross together: the thermodynamic coal reactivity becomes the same for all these reactions. The water gas reaction (Fig. 2) gives the vertical straight, since $\Delta\nu = 0$ and the reaction does not depend on pressure.

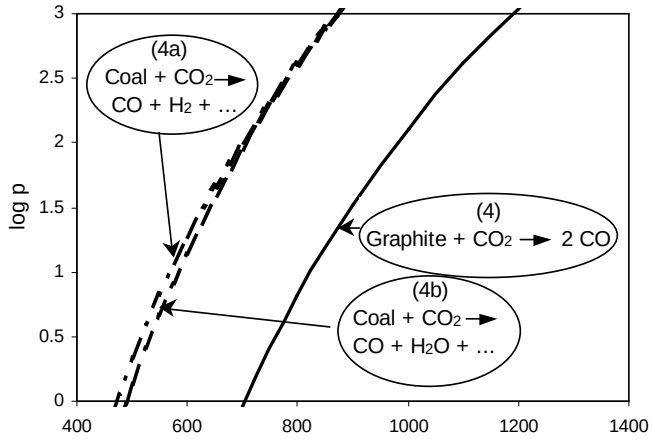

Fig. 1. Zero-affinity plots for the Boudouard reactions of graphite (4) and coal (4a, 4b)

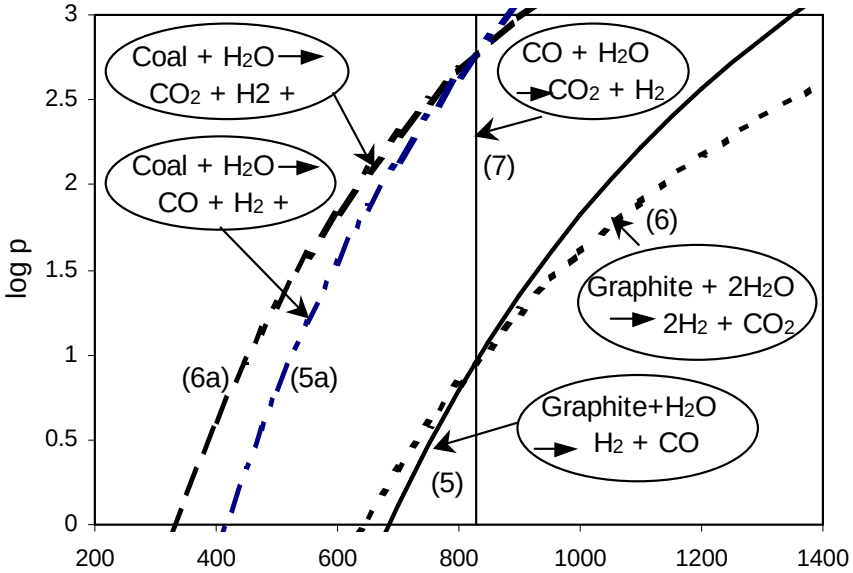

Fig. 2. Zero-affinity plots for reaction of graphite (5), (6), coal (5a), (6a) and carbon monoxide (7) with water vapor

CONCLUSIONS

During the first stage of coals gasification in ordinary technical conditions, thermal decomposition takes place, with loss of volatile components and production of semi-coke. The proper gasification reactions are then reactions of this coke; especially for lignites, this means an important loss of reactivity. One should take advantage of the high thermodynamic reactivity of lignites, by designing gasogens for low temperature gasification, with the use of the own moisture of the coal [20-22]. On the other hand, small quantities of inorganic impurities and/or additives can act as catalysts and enhance the reaction rate. For high-rank coals however, this would be of less help, since their equilibrium temperatures are much higher.

REFERENCES

1. D. van Krevelen, *Fuel*, **1950**, 29, 269.
2. D. R. Stephans, *Thermodynamic equilibria for Wyoming Coal*, Lawrence Livermore Laboratory, **1976**, UCID 17044.
3. D. R. Stephans and D. G. Miller, *Thermodynamic equilibria for Wyoming Coal: New calculations*, Lawrence Livermore Laboratory, **1976**, UCID 17044.
4.G. Niac, *Erdöl, Erdgas, Kohle*, **1995**, 111, 275-280.

5. H. Naşcu, G. Niac and D. I. Comşulea, *Fuel*, **1995**, 74, 119-123.
6. G. Niac and I. Mureşan, *Energy & Fuels,* **2000**, 14, 364-372.
7. G. Niac and C. Sârbu, *ACH Models in Chemistry*, **2000**, 136 (5-6), 561-570.
8. V. Voiculescu and G. Niac, *Rev.Chim. (Rom.)*, **1978**, 29 (11), 1026-1030.
9. G. Niac*, Metalurgia* (Rom), **1979**, 31, 551-554.
10. G. Niac, V. Voiculescu, I. Bâldea and M. Preda, *Formule, Tabele, Probleme de Chimie-Fizică*, Editura Dacia, Cluj-Napoca, **1984**, 176-180.
11. V. Voiculescu, *Rev.Chim. (Rom.)*, **1985**, 36 (2) 136-140.
12. V. Voiculescu, G. Niac and L. Simoiu, *J.Chem.Educ.* **1998**, 75, 203-206.
13. Ch. Chaven, J. M. Lytle, K. M. Henry and Ch. C. Rohl,"*Illinois Basin Coal Sample Program*", ICCI Project Number 95-1/7.1A-1, 2-4.
14. G. Niac, To be published.
15. * * * *CODATA Key Values for Thermodynamics*, Hemisphere Publ.Corp., New York, **1989**.
16. E. Szadeczky-Kardoss, *A szén petrográfiája,* Akademiai Könyvkiado, Budapest, **1956** p.53.
17 S. Sternberg and F. Daneş, *Termodinamică chimică aplicată*, Editura Academiei, Bucureşti, **1978**, p.134.
18. G. Niac and I. Focşa, *Mine, Petrol şi Gaze (Rom.)*, **1981**, 435-437.
19. M. H. Karapetyants, *Termodinamica chimică*, Editura Tehnică, Bucureşti, **1953**, p.411.
20. F. H. Franke, K. I. Klöcher, W. Koch and H. Kreusing, *Brennstoff Wärme-Kraft*, **1979**, 31 (3), 85-89.
21. F. R. Block, *Chem.-Ing.-Techn*., **1979**, 51 (10), 969-971.
22. G. Niac and I. Pop, *Rev. Chim. (Rom.)*, **1988**, 39, 38-44.

STUDIA UNIVERSITATIS BABEŞ-BOLYAI, CHEMIA, XLIX, 2, 2004

Dedicated to Professor Valer Fărcăşan at his 85th anniversary

STUDIES ON THE NATRIUM SULPHATE SALTING-OUT CRYSTALLIZATION. I. EQUILIBRIUM OF THE CRYSTALLIZATION

ALEXANDRU POP, ADINA GHIRISAN, SIMION DRĂGAN and VASILE MICLAUŞ

Faculty of Chemistry and Chemical Engineering, "Babeş-Bolyai" University, 400028 Cluj-Napoca, Romania

ABSTRACT. The separation of anhydrous natrium sulphate through salting-out crystallization with methanol and ethanol has been analysed and discussed. The equilibrium data for the systems natrium sulphate – water – methanol and natrium sulphate – water – ethanol at different temperatures have been reported. On the basis of selective solubility and mass balance the optimal mixing ratio inorganic phase/organic solvent and maximum potential for the best degree separation have been established.

INTRODUCTION

Crystallization is the process where solid particles are formed from a homogeneous phase. In crystallization the solution is concentrated and usually cooled until the solute concentration becomes, at that temperature, higher than its solubility. Thus, the solute comes out of the solution under the form of crystals of relatively high purity.

The salting-out crystallization is the method by means of which, in contrast to the crystallization induced by evaporation, the desired salt can be selectively precipitated in organic solvents – water mixtures [1].

The method of crystallization of inorganic salts with organic solvents is often used for the recovery of inorganic salts from fibre spinning baths, metallurgical wastes and other effluents. A special case of salting-out crystallization is the dehydration of salt hydrates, when anhydrous salt can be obtained from a single component solution.

The first industrial application of the crystallization with organic solvents is the manufacturing of KNO_3 (1970) from KCl and HNO_3 using isobutanol [2]. The success of this first process has stimulated the studies of the equilibrium and kinetics of other inorganic compound(s) crystallization with organic solvents, the most important being natrium sulphate [3-6].

Natrium sulphate has many industrial applications among which the manufacture of glass, cellulose and paper, natrium sulphide, detergents and sometimes the storage up of the heat. The production is related to its processing from natural deposits, from intermediate or by-products from industrial processes such as: a) chlorination of pyrite ashes b) manufacture of natrium bicromate, potassium chloride c) treatment of wastewaters from cellulose.

An important source of natrium sulphate is the wastewater from fibre spinning baths of the viscose plants. A possibility to improve the recovery of natrium sulphate from this source is the selective method of salting-out crystallization with organic solvents, particularly methanol and ethanol. Another advantage of this kind of crystallization is that it proceeds without heat in the crystallizer.

The literature data refer to the following systems: natrium sulphate – ammonia; natrium sulphate – water – ammonia; natrium sulphate – ethanol; natrium sulphate – methanol; natrium sulphate – water – methanol; natrium sulphate – isopropanol; natrium sulphate – water – glycol at normal temperature [7–10]. These data allow only a comparison between different separation efficiency in normal conditions of temperature. New studies are required to establish the phase equilibrium for the natrium sulphate – water – organic solvent systems.

The present research aims at obtaining the equilibrium data for the systems natrium sulphate – water – methanol and natrium sulphate – water – ethanol at different temperatures and establishing the optimum mixing ratio for inorganic phase/organic solvent with the best degree of separation by means of the process of salting-out crystallization.

EXPERIMENTAL

The most suitable solvents for the salting-out crystallization of natrium sulphate are methanol, ethanol, acetone, propanol as well as their mixtures with one another and also with water [11]. The precipitating solvents used in this research are methanol and ethanol. The experiments were carried out in a batch isothermal stirred vessel of 0.5 l. Stirring was achieved mechanically by using a blade stirrer. The temperature was regulated by a thermostated batch and measured by a thermometer.

The solubility of natrium sulphate in mother liquor was determined gravimetrically with barium chloride. The solid phase was analysed by drying the waste at 200 ^{0}C.

RESULTS AND DISCUSSION

In almost all cases, the solubility of the salt decreases considerably if the solvent contains an organic component. During crystallization, temperature is another important factor in the nucleation and growth of crystals. It is known that the equilibrium and kinetics of the crystallization are very sensitive to the variation of the temperature. The relationship between solubility and temperature is exponential. [12]

The main results of our study include the effect of both the temperature and the concentration of the organic solvent on the solubility of the natrium sulphate. Table 1 lists the solubility of natrium sulphate in ethanol solutions versus temperature.

The values of the solubility in brackets are registered for the decahydrate ($Na_2SO_4 \cdot 10H_2O$) known as Glauber's salt. This hydrate appears at low temperature (25 – 30 ^{0}C) and low concentration of ethanol (< 50%). In all other cases, the solid phase was separated as anhydrous natrium sulphate.

Table 1

The natrium sulphate solubility

Temp. (^{0}C)	Ethanol concentration (mass %)						
	3	10	20	30	50	60	80
25	[18.5]	[11.83]	[5.98]	[2.60]	[0.52]	0.18	0.002
30	[26.8]	[19.0]	10.42	[4.45]	0.60	0.19	0.004
35	29.0	20.5	11.38	4.80	0.64	0.204	0.006
40	28.5	20.2	11.32	5.01	0.69	0.215	0.009
45	28.31	20.0	11.34	5.22	0.73	0.228	0.01
50	27.82	19.65	11.31	5.37	0.76	0.243	0.014
60	27.25	19.46	11.33	5.67	0.84	0.268	0.018
70	26.84	19.3	11.32	5.71	0.89	0.289	0.02

At low ethanol concentration it is difficult to obtain a general correlation between solubility and temperature. The values from the first two columns in Table 1 show that the solubility has a maximum at 35 ^{0}C and 3 % (mass concentration of ethanol) and at 35 ^{0}C and 10 % ethanol.

At higher concentration of ethanol, more than 20 %, the variation of the solubility of natrium sulphate increases continuously and rapidly with the temperature. Simultaneously the presence of the organic alcohol decreases the solubility of the salt, with the increase of ethanol concentration.

These observations show that in order to achieve the best degree of separation, the process must take place at a temperature lower than 25 ^{0}C and at a higher concentration of alcohol in solution. For the experiments developed in the conditions represented in Table 1, the maximum degree of separation for the equilibrium condition was attained at 25 ^{0}C and 80 %, when the mother liquor has only 0.002 % natrium sulphate.

Table 2 lists the temperatures of the system during the transition of decahydrate Na_2SO_4 .10 H_2O to anhydrous natrium sulphate with ethanol concentration. These data were obtained by means of the analysis of the equilibrium diagram for the system natrium sulphate – water – ethanol at different temperatures.

Table 2.

The variation of temperature for the transition of Na_2SO_4 .10 H_2O to Na_2SO_4 (with ethanol concentration).

Concentration of ethanol (%)	Temperature of transition (^{0}C)	Solubility of Na_2SO_4 (%)
0.00	32.4	33.27
3.09	31.6	29.38
11.33	31.0	20.14
25.34	30.65	7.247
33.17	30.0	3.356
45.85	27.5	0.943
52.25	25.2	0.409
56.56	20.0	0.194

The presence of ethanol changes the temperature of the transition to lower values. In the binary system Na_2SO_4 – water the transition point is at 32.4 ^{0}C. In this way, in a saturated solution of Na_2SO_4, the decahydrate $Na_2SO_4.10\ H_2O$ will crystallize in normal conditions.

These data show that at 56.6 % ethanol the anhydrous salt Na_2SO_4 could be separated even at 20 ^{0}C. By extrapolation it can be concluded that at higher ethanol concentrations, the temperature of crystallization can be further decreased. This conclusion is an important industrial advantage in the salting-out crystallization. The precipitation with organic alcohol represents the direct way to obtain the anhydrous inorganic salt at normal temperature. Dehydration of decahydrate $Na_2SO_4.10\ H_2O$ can be performed without heating.

The results of the salting-out crystallization with methanol at 25 ^{0}C are listed in Table 3.

The listed values in Table 3 show a gradual increase in the efficiency of separation with methanol concentration. Simultaneously, the concentration of methanol influences the composition of the solid phase. At 25 ^{0}C and methanol concentration lower than 10 % the separated solid phase obtained is decahydrate $Na_2SO_4.10\ H_2O$. At the concentration of 17.27 % methanol, the solid phase is registered as heptahydrate $Na_2SO_4.7H_2O$ whereas at the concentration of 21.2 % a mixture of heptahydrate $Na_2SO_4.7H_2O$ and anhydrous Na_2SO_4 is determined. In the range of 22 % and 57.67 % methanol concentrations, the separated solid phase was determined as anhydrous natrium sulphate.

Table 3.

Experimental results of the natrium sulphate salting-out crystallization with methanol at 25^{0}C

Exp. Nr.	Na_2SO_4 (%)	Methanol (%)	Water (%)	Efficiency of separation (%)	The separated solid phase
1	25.30	4.66	70.03	19.32	$Na_2SO_4.10\ H_2O$
2	22.18	9.52	68.30	29.20	$Na_2SO_4.10H_2O$
3	15.80	17.26	66.84	51.21	$Na_2SO_4.7H_2O$
4	12.96	21.18	65.83	59.60	$Na_2SO_4.7H_2O + Na_2SO_4$
5	3.75	25.79	70.61	88.04	Na_2SO_4
6	3.07	30.37	66.51	90.20	Na_2SO_4
7	1.68	39.90	58.42	94.64	Na_2SO_4
8	0.84	47.40	51.76	97.32	Na_2SO_4
9	0.673	53.22	46.19	97.86	Na_2SO_4
10	0.38	57.78	42.04	98.78	Na_2SO_4

From the results obtained so far, the experimental conditions for the direct obtaining of the anhydrous natrium sulphate can be settled. The solubility of Na_2SO_4 in methanol/water mixture decreases considerably with the increase of methanol fraction. On the basis of this diagram the optimal mixing ratio m_A/m_B (A – inorganic phase; B – methanol or organic alcohol) could be established. The solubility of natrium sulphate in the system natrium sulphate – water – methanol at 40 ^{0}C is shown in Figure 1.

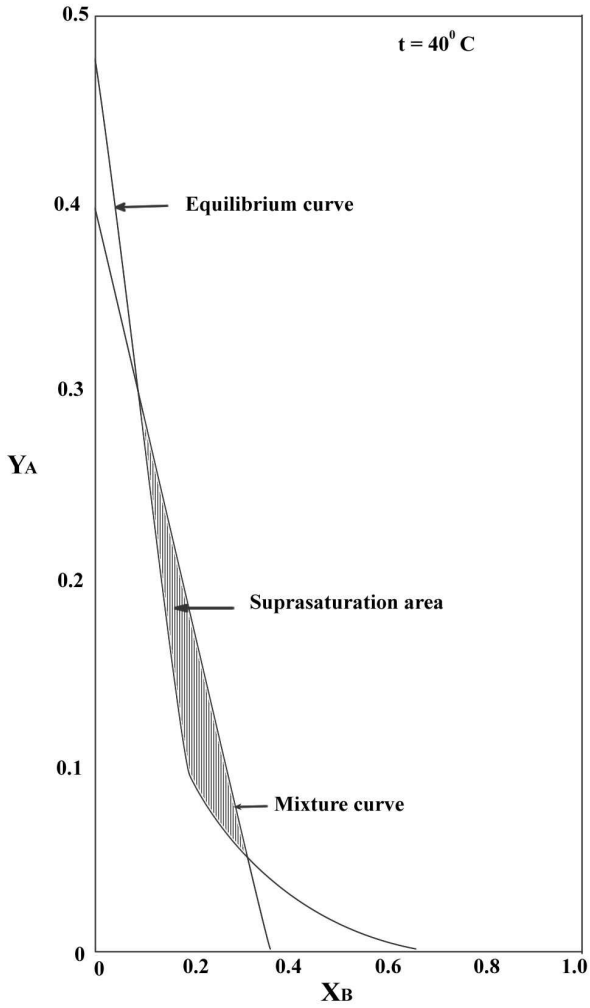

Fig. 1. Solubility of natrium sulphate in the system– water – methanol at 40 ^{0}C (Y_A = kg Na_2SO_4/kg water; X_B = kg CH_3OH/kg water).

Figure 1 offers the possibility of getting acquainted with the field of crystallization in strict dependence on the natrium sulphate and methanol concentration.

To illustrate the used method, the operation curve (mixture curve) for the mixture with Y_A = 0.4 kg Na_2SO_4/kg water and B_E = 0.35 kg methanol/kg water is drawn on the diagram. The solution (mother liquor) and the solid crystals are in contact for a long time, long enough to reach an equilibrium. The crystallization equilibrium is attained when the solution of mother liquor is saturated and the natrium sulphate concentration reaches constant values. The

concentration of the salt can be described as a point in the field of supersaturated solution or unsaturated solution, depending on the mixing ratio $m_{a/}mb_o$.

In conclusion, at an optimal mixing ratio the supersaturated solution yields the maximum amount of crystals. This ratio can be obtained from the mass balance. The optimisation of the salting-out crystallization can be carried out in two stages: a) at maximum solid concentration in suspension; b) at maximum amount of crystals.

The optimisation of the salting-out crystallization dependent on mass fraction of methanol in mixture m_B/m_T is shown in Figure 2. It can be observed that the maximum of solid concentration C_S is obtained at the same fraction of methanol in mixture m_B/m_T at which the potential ΔY is maximum. This potential ensures a high speed of crystallization. Besides, the relative suprasaturation $\Delta Y/Y^*$ becomes lower. In this way the secondary nucleation can be avoided and the quantity of methanol can be reduced in comparison with the other variant (b).

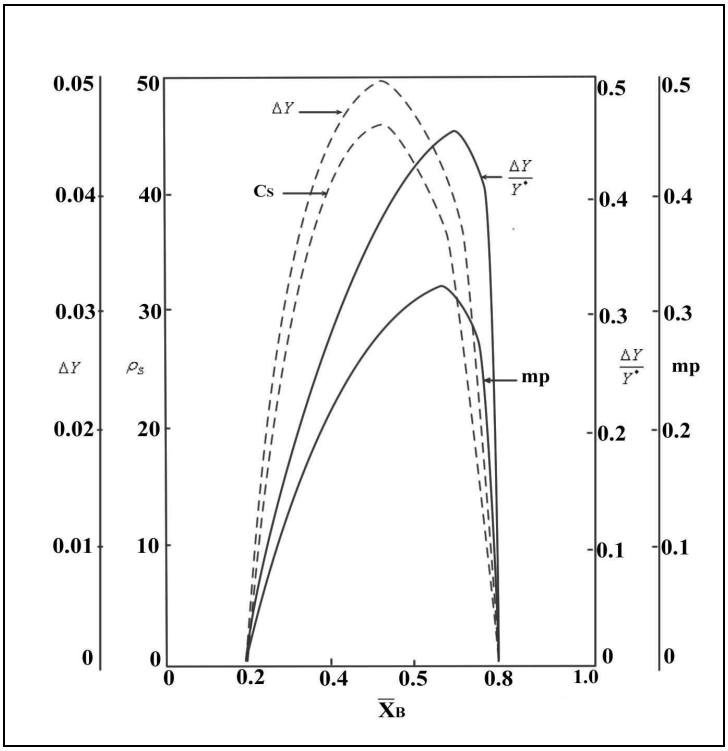

Fig. 2. The optimization of the mixing ratio: ΔY - potential difference (kg/kg); C_S (ρ_S) – solid concentration in suspension (kg solid/m^3 suspension); ΔY/Y* - relative suprasaturation (kg/kg); Y* - kg salt/kg methanol; m_p – sepatated salt (kg recovered salt/kg existing salt); $\overline{X}_B$ - methanol fraction in the mixture (kg methanol/kg mixture).

On the basis of mass balance it was estabished that at m_B/m_T =0.5, as Figure 2 shows, the entirely mixing ratio, inorganic phase/methanol is m_A/m_B = 1.35. This mixing ratio corresponds to the maximum value of the solid concentration in suspension and also to the maximum potential.

CONCLUSIONS

The analysis of the results obtained points out to the main advantages of the salting-out crystallization with ethanol and methanol. These advantages can be summarized as follows:

1) the salting-out crystallization allows the direct precipitation of the anhydrous sodium sulphate from solutions by using organic alcohols even at room temperature;
2) the process requires a lower amount of alcohol by increasing the salt concentration in the starting solution although the efficiency remains constant
3) the cost of salting-out crystallization can decrease up to 75 % for a separation degree higher than 95 % in contrast to the conventional process.

REFERENCES

1. V. Hopp, *Grundlagen der Chemischen Technologie*, Wiley –VCH 2001, p. 631
2. C. Calistru and C. Leonte, *Tehnologia substanțelor anorganice*, Ed. Didactică şi Pedagogică, Bucureşti, 1972
3. L. Filipescu and E. Pincovski, *Echilibrul solid-lichid. Aplicații în tehnologia sărurilor minerale*, Ed. Tehnică, Bucureşti, 1980
4. K. Winnacker, L. Kuchler, *Chemische Technologie,* 4. Aufl., Carl Hanser Verlag, Munchen, Wien, 1984
5. G. Liebermann and H.H. Emous, *Wiss. Z.T.H.*, Ed. Leuna, Merserburg, 1975, **17**, 553
6. H.D. Kohn, I.Yaron and J.D. Wolf, *J.Appl.Chem*., London, 1963, 13, 259
7. W.R. Rousseau and R.C. Zumastein, *World Congres III of Chemical Engineering*, Tokyo, 1986, Vol. II
8. O.H. Picht, J. Hung, *J. Ind. Chem.*, 1989, **17(2)**, 179
9. S.J. Jancic and E.J. Jong, *Industrial Crystallization*, Ed. Elsevier, 1984, 1184
10. A. Mersmann, *J. Crystal Growth*, 1990, **30**, 241
11. H. Hoppe, *Chem. Process Eng.*, 1969, 61
12. M. Fedtke, W. Pritzkow, G. Zimmerman,*Technischen Chemie, 6.Aufl.,* Deutscher Verlag fur Grundstoffindustrie, p.92, Stuttgart 1996

STUDIA UNIVERSITATIS BABEŞ-BOLYAI, CHEMIA, XLIX, 2, 2004

Dedicated to Professor Valer Fărcăşan
at his 85th anniversary

MATHEMATICAL MODEL FOR THE DISCONTINOUS SOLID - LIQUID EXTRACTION OF CAROTENOIDS (part I)

B.R.H. MIŞCA, I. OPREAN, D.I. MANCIULA

ABSTRACT. The carotenoids form an important non-nitrogenated group of natural pigments giving the yellow, red or blue colour to the tissues in which they are found. The biochemical role of these pigments exerts a particular influence in the processes of photosynthesis, respiration and germination, in the protection against photodestruction and in oxygen transport to the tissues. Many carotenoids extracts are being used as additive agents in the staining of food and pharmaceutical products. The recovery of these products from the plant material is mainly achieved using solid-liquid extraction technique. In this paper the basic consideration take for development of the mathematical model for solid – liquid extraction are presented: the general design of the technological process, the mass transport equation of the solute, the overall behaviour of the solid layer in the presence of the wetting fluid. It is evaluated the mass balance for the process and the driving forces evolution, the non dimensional similitude groups for non steady-state extraction. The calculus of static retention for the wetting liquid are presented too.

INTRODUCTION

Carotenoids are non nitrogenated pigments giving the yellow, red or blue colour to the tissues in which they are found. Carotenoids are found in all organs of the plants, both chlorophyllic and nonchlorophyllic. In the superior plants they are found in the leaves, fruits, stalks, roots, seeds, petals and pollen. They are water insoluble substances, but are soluble in organic solvents, the carotenoid pigments presenting specific absorption spectra in visible and ultraviolet light, which are used for their identification and quantitative determination. They are sensitive to heat, light, acids and oxygen. The biochemical role of the carotenoid pigments, although incompletely known, exerts a particular influence in animal life in the process of sight, growth, reproduction but also in plant life in the processes of photosynthesis, respiration, germination, in the protection against photodestruction, in oxygen transport to the tissues.

The carotenoids form an important group of natural pigments. Many carotenoid extracts are being used as additive agents in the food products due to the lack of toxicity, their chemical structure, their role as active biological precursors and to the possibility of transformation into other active biologic products [1]. The recovery of these substances from the plant material is mainly achieved using solid-liquid extraction technique [2].

THE MATHEMATICAL MODEL

The modelling of solid-liquid extraction should take into account the elementary processes interpenetrating and conditioning each other. These processes are important in the definition of the overall transfer and transport rate of the solute from the solid to the liquid mass, but also for more efficient separation process. The following fundamental aspects should be considered:

1. The general design of the technological process;
2. The mass transport equation of the solute;
3. The overall behaviour of the solid bed in presence of the wetting fluid.

The first of these fundamental aspects takes into account the nature of the design of technological process: discontinuous, semicontinuous or continuous. This aspect is found in the form and structure of the total or partial balance of the materials. In the case of the discontinuous extraction, the correlation relations can also be described in the forms presented below:

The overall property balance in the two phases can be written:

$$- dP_1 = dP_2$$

and explaining in relation with the value of the potential in each phase :

$$- d(M_1u_1) = d(M_2 u_2) \qquad (1).$$

Because in the case of the discontinuous process the amounts of materials involved in the contact do not changed:

$$- M_1du_1 = M_2du_2 \text{ , respectively } - M_1/M_2 = du_2/du_1 ; \qquad (2),$$

this relation also offers the slope of the operation straight line.

Identifying the value of each differential equation with the corresponding expression, the following relations are obtained:

$$du_1 = - dP/M_1; \quad du_2 = dP/M_2 , \qquad (3).$$

and then making a subtraction of the two relations member by member:

$$d(u_1-u_2) = - (1/M_1 + 1/M_2)dP, \qquad (4).$$

Accepting the hypothesis that the quantity of materials is not changed during the transfer process, the magnitude $- (1/M_1 + 1/M_2)$ is constant for a given situation and therefore, the letter C can designate it.

The general kinetic equation of the property transfer $dP = k\ A\ \Delta U\ d\tau$ becomes under these conditions:

$$\frac{d\ (u_1-u_2)}{u_1-u_2} = -k\ C\ A\ d\ \tau \qquad (5).$$

In the hypothesis of the constant values for k, A, M_1, M_2 in time, the relation can be integrated by the separation of the variables

$$\int_{u_{1i-2i}}^{u_{1f-2f}} \frac{d\ (u_1-u_2)}{u_1-u_2} = k\ C\ A \int_0^{\tau} d\ \tau \qquad (6).$$

Designating the differences of the driving force in the initial and final moments by Δu_i and $\Delta u_{f,}$ respectively $\Delta u_i = u_{1i} - u_{2i}$ and $\Delta u_f = u_{1f} - u_{2f}$; the integration of the relation generates the expression :

$$\ln \frac{\Delta u_f}{\Delta u_i} = -k\ C\ A\ \tau \quad \text{or} \quad \Delta u_f = \Delta u_i e^{-kCA\tau} \qquad (7).$$

The equation of the property balance $dP = - C^{-1} du$ in the above mentioned conditions can be integrated between the limits of the driving force differences for the limit of the process time :

$$P = -\frac{1}{C}\int_{\Delta u_i}^{\Delta u_f} d\ u \quad \text{or} \quad P = \frac{1}{C}\left(\Delta u_i - \Delta u_f\right) \qquad (8),$$

and the elimination of C between the relations (7) and (8) leads to the expression:

$$P = k\ A \frac{\left(\Delta u_i - \Delta u_f\right)}{\ln \frac{\Delta u_i}{\Delta u_f}} \tau \qquad (9).$$

In the above relations M1 and M2 are the property carrying entities, in this case concentration, [M] = [kg], [3].

The main steps of the mass transfer between the solid particles and the dissolving fluid which should be considered in the drawing up of the mathematical model of the solid-fluid extraction are :

- liquid diffusion in the solid porous granule;
- penetration of the cell membranes;
- solute dissolution in the intracellular solvent
- diffusion of the solute towards the solvent block surrounding the solid particle.

The so called extraction of the solute described by means of the above presented steps and influenced by usual parameters for the control of the transfer and transport processes: temperature, concentration, stirring degree, nature of the materials, is also technologically dependent on other practical aspects: size of the solid granules, the design of the raw material layer, physical properties of the solvent, the texture of the solid.

In the case of the solid-liquid extraction a normal phenomenon of drawning of the solid bed by the wetting fluid occurs. For an a complete recovery of the solute and for the economy of the process surges the need to remove the fluid remaining in the spaces between the particles. The fluid is retained between the granules of the solid material by the adhesion forces, by inclusion or absorption. When the fluid is drained from the solid packed by gravitational flow, the draining rate is the highest at the beginning of the process, (the maximum level difference between the upper level of the fluid and the level of the draining orifice), then it decreases in time, until the draining of the fluid ceases. In the solid packed remains a quantity of fluid adhering to the solid, this quantity being called residual saturation or static retention.

The variation of the saturation with the height of the solid packed was determined experimentally [4]. The draining height h_d is defined as the portion of the solid bed in which the sudden variation of the residual saturation from the saturation limit to drowning ($\varepsilon_r = 1$) takes place. In the lower part of the solid bed the saturation is always close to drowning because of the combined effects of wetting and gravity.

The values of the magnitudes intervening in the calculation of the quantity of fluid retained can be determined with the equations [5]:

- medium residual saturation:

$$\varepsilon_m = \frac{(H - h_d)}{H}\varepsilon_{r0} + \frac{h_d}{H} \tag{10}.$$

- drainage height:

$$h_d = \frac{0.275/g}{\left(K/g\right)^{0,5}\left(\rho_l/\sigma\right)} \tag{11}.$$

Permeability K for the layer can be calculated with Kozeny's relation:

$$K = \frac{1}{150}\frac{d_p^2\varepsilon^2 g}{(1-\varepsilon)^2} \tag{12}.$$

The final residual saturation is:

$$\varepsilon_{r0} = 0,075 \quad \text{for} \quad \frac{K\ \rho_l}{\sigma} \le 0,02 \tag{13}.$$

$$\varepsilon_{ro} = \frac{0,0018}{\left(K\ \rho_l/\sigma\right)} \quad \text{for} \quad \frac{K\ \rho_l}{\sigma} \ge 0,02 \tag{14}.$$

Besides the fluid retention, the arrangement of the granules in a fixed bad leads to the modification of the specific magnitudes on which the transport and/or transfer is dependent.

An important aspect of solid-fluid contact is the diffusion within the porous granular material, another less studied aspect is the dependence on the operation parameters of the diffusion coefficient [6,7].

The variation of the quantity of property representing the amount of solute extracted in time is given by the mathematical equation:

$$\frac{P - P_f}{P_0 - P_f} = e^{-\frac{kA\ \tau}{M}}$$ which can be written in the criteria form:

$$\frac{P - P_f}{P_0 - P_f} = e^{-B_i F_0 G} \quad (15).$$

The quantity of property accumulated or extracted in time ΔP is calculated by the integration of the equation:

$$\Delta P = \int_0^\tau P dP = \int_0^\tau k(P_f - P_0) e^{-B_i F_0 G} = \frac{k(P_f - P_0)}{B_i F_0 G}\left[1 - e^{-B_i F_0 G}\right] \quad (16).$$

The analytical expression of the non steady-state diffusion becomes of the order II Fick's law diffusion equation. Depending on the mathematical method chosen for solving this equation, the final solution will have different forms and numerical coefficients, the differences between the solutions representing the accuracy of the calculus which, of course, is in direct relation with the chosen solving method. The solution of the non steady-state diffusion has great importance in the experimental determination of the diffusion coefficient, the most important physical parameter both as value and as physical significance for the mass transfer processes.

It should be pointed out that the experimental determination of the diffusion coefficients is a delicate operation involving specific equipment, long working times and a large amount of calculus [7].

CONCLUSIONS

The multitude of the mathematical models shows the phenomenon's complexity on a micro- and macro-scale; the calculus relations cannot detect this aspect in totality. Usually, the nature of the raw material is a decisive factor in the option selection of one or another model. This is due to the behaviour of the system: solvent-solute-solid matrix, i.e., the technological parameter called effective diffusion coefficient. The determination of effective diffusion coefficient is compulsory for a correct description of the extraction process. Being a material constant and dependent on the operational conditions, its determination is made by experimental measurements or by calculation, starting from data also obtained experimentally, too. The advantage of the determination by calculation is the accessible direct measurement of certain process parameters: concentrations, time or quantities.

Although apparently simple, the solid-liquid extraction operation is difficult enough to be caught in exact calculation relations, the accuracy of the estimations depending on the accuracy of the determination of the effective diffusion coefficient.

Notations

P = quantities of transported properties;
u = potential of properties, for mass transfer concentration, kg/kg;
k = overall transfer coefficient, kg/(m^2kg/kg);

A = transfer area, m^2;
$Bi_d = \beta * l / D_{ef} * \rho$; Biot number for diffusion;
$Fo_d = D_{ef} * \tau / l^2$; Fourier number for diffusion;
G = geometrical simplex of similitude;
H = height of the granular raw material, m;
g = gravitational acceleration, m/s^2;
d_p = particle diameter, m;
l = characteristic length, m;
β = partial mass coefficient, kg/m^2s;
ρ = density of fluid, kg/m^3;
σ = interfacial strength, N/m;
τ = time, s;
ε = free space into solid, m^3/m^3;
D_{ef} = effective coefficient of diffusion, s/m^2;
M = quantities of raw material, respectively solvent, kg;
1,2 = index for raw material, respectively solvent.

REFERENCES

1. Tamas V., Neamtu G.; *Pigmenti carotenoidici si metaboliti*; Ed. Ceres, Bucuresti, 1986.
2. Misca B.R.H., Literat L; *Hippophae fructus Oil Separation*, Selected Topics on Chemical Reaction Engeniering, 2-9 oct. 1994, Harmonia, Slovakia, p. 89 – 90.
3. Misca B-R.H.; *Teza de doctorat*; Cluj – Napoca, 1998.
4. Preiss J., Bord W.L.; *Liquid Retention in Packing Column*; Ind. Eng. Chem., 46, (1954), p. 1164 – 1171.
5. Dobre T., Floarea O.;.*Separarea compusilor chimici din produsele naturale*; Editura Matrix Rom, Bucuresti, 1997.
6. Misca B.R.H., Literat L,Ozunu A.; *Stabilirea etapei determinante de viteza la extractia din medii poroase prin analiza dimensionala generala*, Sesiunea jubiliara “50 de ani de la infiintarea Facultatii de Chimie Industriala si Ingineria Mediului din Timisoara”, 29 - 30, oct,1988.
7. Misca B.R.H.,Ozunu A,Dragan S.; *Determinarea coeficientului de difuziune in medii poroase*, Comunicare Simpozion “75 de ani de invatamint chimic romanesc la Alma Mater Napocensis” 20 - 21 mai, 1994, Cluj-Napoca.

STUDIA UNIVERSITATIS BABEŞ-BOLYAI, CHEMIA, XLIX, 2, 2004

Dedicated to Professor Valer Fărcăşan at his 85th anniversary

A NOVEL DISILOXANEDIOLATO - DERIVATIVE OF TIN(IV)

PETRONELA. M. PETRAR, GABRIELA CRETIU NEMES, IOAN SILAGHI-DUMITRESCU

Faculty of Chemistry and Chemical Engineering, Babes-Bolyai University, 400028 Cluj, Romania, isi@chem.ubbcluj.ro

ABSTRACT. Bis[μ^2-(bis(tetrahydrofuran)-lithium(tetraphenyl-disiloxane-1,5-diolato)]-dimethyltin (IV) (**1**) has been obtained from the reaction of diphenylsilanediol with butylithium and dimethyltin dichloride.

The crystal of (**1**) is monoclinic, space group P2(1)/n with the unit cell dimensions: a = 10.4609(9) Å, b = 19.9896(16) Å, c = 17.9295(15) Å, $\alpha = 90.00^o$, $\beta = 105.791(2)^\circ$, $\gamma = 90.00^\circ$. The tin atom has a slightly distorted *octahedral* environment. The silandiol ligands coordinate also two lithium atoms forming thus two planar LiO_2Sn chelate rings.

INTRODUCTION

Metallasiloxanes have known a continuously increasing interest in the last decades because of their practical applications. For instance, stannasiloxanes are precursors of inorganic polymers leading to ceramic materials or molecular sieves [1, 2], and they have found some uses in heterogeneous catalysis [3] or as single source mixed metallic oxides precursors [4]; their potential as homogeneous catalysts has also been studied [3].

RESULTS AND DISCUSSION

In an attempt to synthesize the four-member ring $Ph_2SiO_2SnMe_2$ which might easily undergo ring-opening polymerization**,** a novel stannadiphenylsiloxane was obtained using diphenylsilanediol, butylithium and dimethyltin dichloride as starting materials (Scheme 1).

Lithiation of the diphenylsilanediol was carried out at room temperature, followed by dropwise addition of dimethyltin dichloride to the reaction mixture wherefrom compound **1** has been isolated:

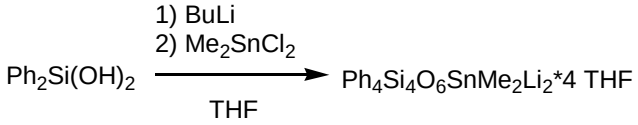

Scheme 1

The reaction mechanism resulting in the expansion of the silanediolate unit to a disiloxanediolate ligand is unknown. Similar reaction outcomes have been reported in the literature [1], but no satisfactory explanation was found for the chain expansion.

The simplest rationalization of this result consists of a condensation of silanediol (**2**) when disiloxane (**3**) is formed.

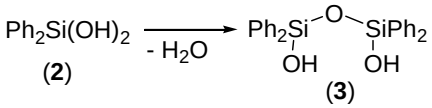

(**2**) (**3**)

Subsequent lithiation of (**3**) followed by addition of Me_2SnCl_2 leads to bis[μ^2-(bis(tetrahydrofuran)-lithium(tetraphenyldisiloxane-1,5-diolato)]-dimethyltin (IV) (**1**)

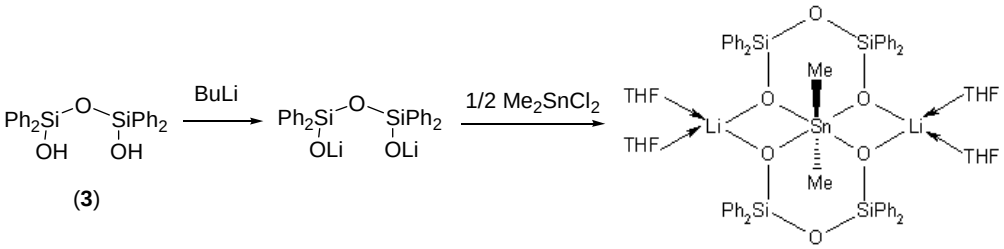

An analogous product was reported in the case of reaction of the dilithium salt of tetraphenyldisiloxane-1, 5-diol with MCl_4 [2], (M = Sn, Zr, Hf) but an expansion of the siloxane unit to eight-membered rings occurs in the case of titanium tetrachloride [3] (Scheme 2).

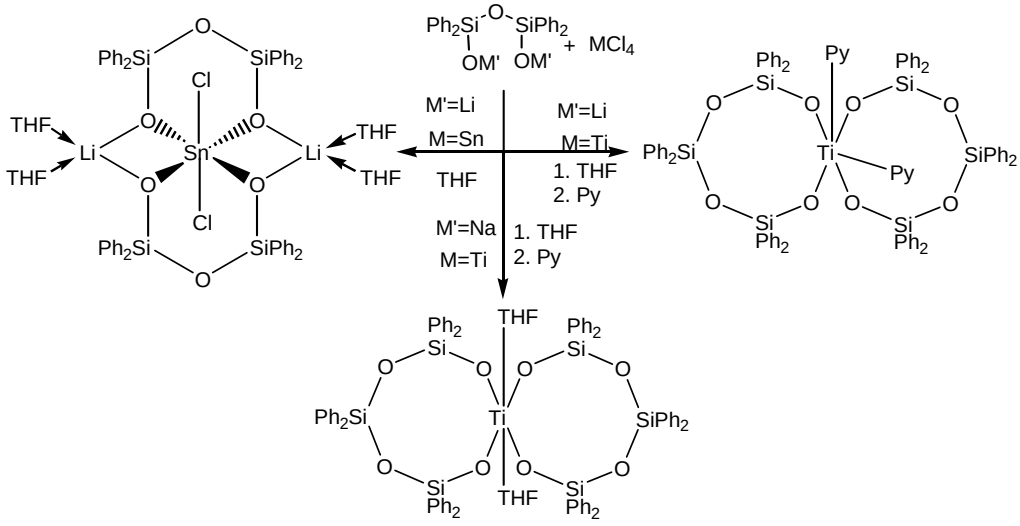

Scheme 2

It can be said that the target metal to which the siloxanediolate ligand is transferred plays an important role in the outcome of the reaction.

Thus, the chain expansion does not necessarily occur during the lithiation step since tin has been known to favor the cleavage of Si-O bonds and rearrangement of the disiloxane ligand into a trisiloxanediolate unit [4].

It is yet difficult to say whether the nature of the alkali metal or that of the target metal is the determining factor in the chain expansion in the case of siloxane or silandiolate units transfer.

CRYSTAL AND MOLECULAR STRUCTURE OF 1

Transparent, acicular crystals of **1** were crystallized from THF and characterized through single-crystal X-ray diffraction.

The unit cell of **1** is shown in Figure 1, and, the data collection, crystal data and refinement data are summarized in Table 1.

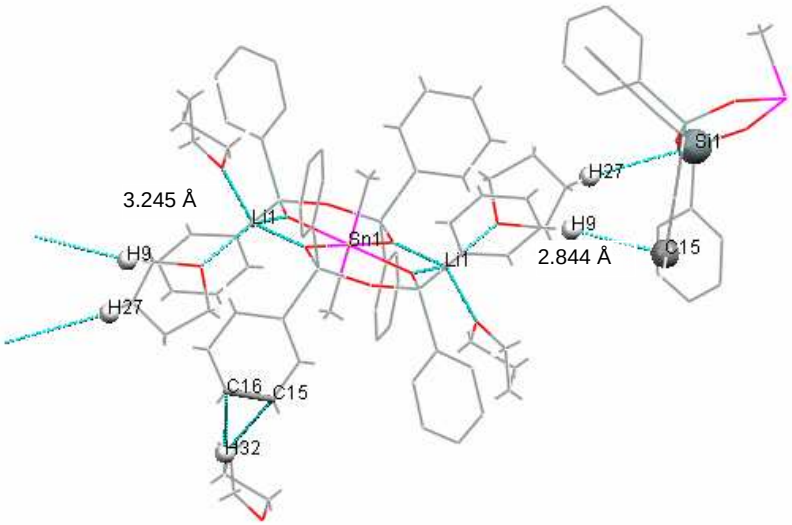

Figure 1. View along the *a* axis of a unit cell of **1**

The unit cell of the stannadisiloxane contains six molecules of **1**, four of them having the tin atom positioned in the center of the *a* axis, while the other two lie in the middle of the *bc* plan and are oriented in opposite direction. Thus, infinite, parallel sheets are formed through H(phenyl)···C(phenyl) (2.844 *Å*) and H(THF)···Si (3.245 *Å*) interactions.

The molecular structure of **1** is shown in Figure 2 and some selected bond lengths and angles are given in Table 2.

Table 1.

Crystal data and refinement data for **1**

Empirical formula	C66 H78 Li2 O10 Si4 Sn
Formula weight	1276.21
Temperature	297(2) K
Wavelength	0.71073
Crystal system	Monoclinic
Unit cell dimension	a=10.4609(9)Å, α =90.00° b =19.9896(16)Å, β =105.791(2)° c =17.9295(15)Å, γ =90.00° Volume 3607.7(5) $Å^3$
Space group	P2(1)/n
Z	2
Density (calculated)	1.175Mg/m^3
Absorption coefficient	0.471mm^{-1}
F(000)	1332
Crystal size	0.39 mm block-colorless
θ range for data collection	1.56 to 26.37°
Reflections collected	7366
Independent reflections	6230 (R_{int} = 0.0000)
Absorption correction	None
Refinement method	Full-matrix least-squares on F^2
Data / restraints / parameters	11/378
Goodness-of-fit on F^2	1.222
Final R indices	[I>2σ(I)] R1 =0.0630, wR2 = 0.1971
R indices (all data)	R1 =0.0743, wR2 =0.2047

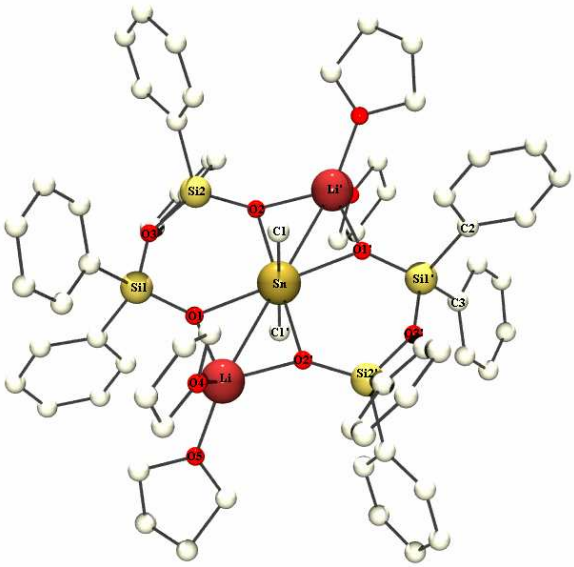

Figure 2. Molecular structure of **1**

Table 2.

Selected geometrical data for **1**

Bond	Length (Å)	Angle	Value (°)
Sn-C1	2.116(4)	C1-Sn-C1'	180.000(1)
Sn-O1	2.181(3)	O1'-Sn-O1	180.000(1)
Sn-O2	2.191(3)	O1-Sn-O2	80.47(10)
Si1-O1	1.597(3)	Sn-O1-Si1	126.34(16)
Si1-O3	1.597(3)	Sn-O2-Si2	126.01(17)
Si2-O2	1.597(3)	O3-Si1-O1	110.88(16)
Si2-O3	1.597(3)	Si1-O3-Si2	146.0(2)
Si1-C2	1.883(5)	O3-Si2-O2	110.91(16)
Si1-C3	1.866(5)	C3-Si1-C1	109.4(2)
O1-Li	1.934(8)	C1-Si1-O3	106.7(2)
O2-Li	1.946(8)	C3-Si1-O1	112.1(2)
		O1-Li-O2	93.4(3)
		Li-O2-Sn	93.36(3)
Dihedral	**Value (°)**	**Atoms**	**Distance (Å)**
O1-Si1-O3-Si2	-7.5(4)	Li-Sn	2.999(7)
O1'-Si1'-O3'-Si2'	7.5(4)	Li-O4	1.982(9)
O2-Si2-O3-Si1	3.1(5)	Li-O5	1.965(9)
Sn-O1-Si1-O3	4.5(3)	Li-O1	1.934(8)
Sn-O2-Si2-O3	3.7(3)	Li-O2	1.934(8)
O1-Li-O2-Sn	-1.9(3)		

Compound **1** is a bicyclic stannasiloxane with hexacoordinated tin atom. The slight distortion from octahedral geometry around the tin is due to the strain in the lithiostannoxane rings. The stannadisiloxane rings are almost planar, coplanar with each other and additionally two four-member rings containing lithium are formed. The methyl groups are in *trans* orientation, with a C-Sn-C angle of 180°. The Sn-O, Si-O and Si-C bond lengths are in the range of values observed for other cyclic stannasiloxanes [5, 6, 7]. A feature of this specific type of cyclostannasiloxanes seems to be a large Si-O-Si angle. Thus, for the dichloro-substituted tin analogue this angle is 141.3(8)°, with about 10° larger than the values obtained for related lithium-bridged cyclometallasiloxanes [5]. In **1,** this angle is even larger (around 146°). The Si-O-Si angle value is often regarded as a measure of the strain in siloxanic rings [7].

^{1}H-NMR CHARACTERISTICS

The ^{1}H-NMR spectrum of (**1**) (recorded in $CDCl_3$) shows that the six hydrogen atoms coming from the two methyl groups give a singlet at 0.5 ppm, which proves their equivalency (at least at the temperature of measurement). This in turn, suggests that the octahedral environment of Sn is retained in solution.

Lockhart and Manders established an empirical relation (eq. 1) between $^2J_{Sn\text{-}H}$ and the C-Sn-C angle and applied it successfully to several compounds [8]:

$$\theta = 0.0161\left|^2J\right|^2 - 1.32\left|^2J\right| + 133.4 \qquad \text{eq. 1}$$

In the case of hexacoordinated dimethyltin derivatives, with the methyl groups in a *trans* orientation the values of $^2J_{Sn\text{-}H}$ are greater than 83 Hz, which correlates with an C-Sn-C angles larger than 135°.

A coupling constant smaller than 80 Hz indicates a *cis* geometry, which is however rare for this kind of compounds. Nevertheless, the relation has been applied with good results to some *cis* isomers of hexacoordinated tin derivatives as well [8]. In our case, $^2J_{Sn\text{-}H}$ from the spectrum of **1** is 70.6 Hz leading to a θ angle of 120.45°, in accordance with a very deformed *cis* geometry.

THEORETICAL CHARACTERIZATION OF (1) THROUGH SEMIEMPIRICAL CALCULATIONS

Calculations at the PM3 semiempirical level [9] were performed using the Spartan'02 program [10] in order to estimate the relative stability of *cis* and *trans* isomers of **1**. Their optimized molecular structures and heats of formation are given in Figure 3**.**

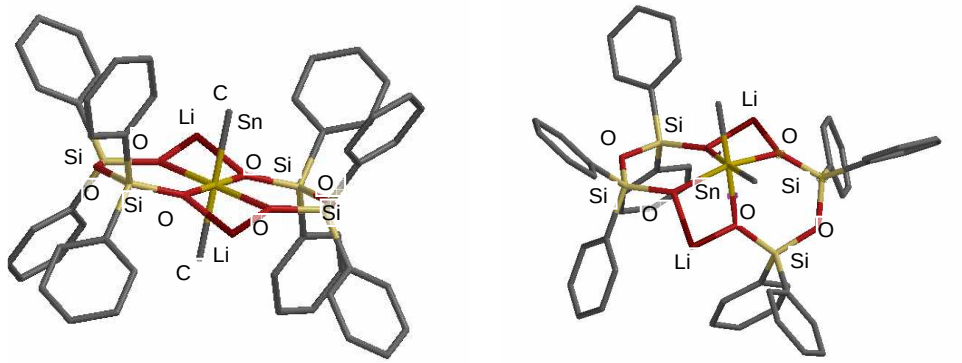

a, ΔH_f^o= -384.11 kcal/mol **b,** ΔH_f^o = -384.22 kcal/mol

Figure 3. Calculated structures and heats of formation of simplified models (THF ommited) of the *trans* (**a**) and *cis* (**b**) isomers of stannasiloxane **1** (hydrogen atoms have been omitted for clarity)

The difference between the heats of formation of the two isomers is insignificant, so we can assume that the formation of the *trans* isomer in the solid state is kinetically controlled, rather than being thermodynamically dictated.

The geometrical data for the *trans* isomer agree fairly well with experimental data obtained through single-crystal X-ray diffraction. A deviation from planarity in the case of the four rings (for instance the dihedral O1-Si1-O3-Si2 has a calculated value of 12.5º) could be explained by the lack of the packing forces, which appear in crystalline state.

There are no significant differences between the two isomers at the PM3 level, as far as bond lengths are concerned. The geometry around the silicon atoms is in both cases a distorted tetrahedron and that around the tin- a distorted octahedron. The distortion is as expected greater for the *cis* isomer and it is correlated with an increased ring-strain in the stannasiloxanic cycles. A measure of this tension is the Si1-O3-Si2 angle, which takes a value of around 132° for six-member siloxanic rings and of about 165° in the strain-free polydiphenylsilanediolate chain. Based on these grounds, the tension within the stannasiloxanic cycles is greater in the case of the *cis* isomer for which the calculated value of the Si1-O3-Si2 angle is around 127° for both rings. The *trans* isomer exhibits less ring-strain, but the calculated angle is still far from the experimental-determined value of 145.95°, which is indicative of a very low-tensioned ring.

CONCLUSIONS

The X-ray diffraction analysis indicates the formation of the isomer with the *trans* geometry of bis[μ2-(bis(tetrahydrofuran)litihium (tetraphenyldisiloxane-1,5-diolato)]dimetil-tin(IV) **1**. This structure does not seem to be retained in solution: the C(methyl$_1$)-Sn- C(methyl$_2$) has a value of 120.45, calculated from ^{1}H-NMR $^2J_{Sn-H}$, which could imply a rearrangement of the stannasiloxane. This comes as no surprise, given the kinetic labilety of the Sn-O bond in organometallic derivatives. A computational study at the PM3 level of the theory indicates that the two geometric isomers have very similar heats of formation in gaseous phase. The formation of the *trans* isomer seems thus to be kinetically controlled.

EXPERIMENTAL DETAILS

All the reactions were carried out in a standard vacuum line (Schlenck Line) under inert atmosphere at room temperature. The solvent used in the synthesis was freshly distilled.

The NMR spectrum was recorded on a Varian Gemini 300 MHz apparatus in $CDCl_3$ and using TMS as internal standard. The melting point was determined on a Leitz microscope heating stage 250.

The crystal data were collected at room temperature (293 K) on a Brucker AHX diffractometer and Graphite monochromated MoK α radiation (λ=0.71073 Å).

Refinement was carried out using the SHELXL-97 program [11] and the structure as solved by direct method and refined by the full matrix least square method. Probably that some disorder in the crystal prevent a better wR2 (0.1971) value.

Molecular orbital calculation were performed with the Spartan 02 package [10].

Preparation of bis[μ^2-(bis(tetrahydrofuran)lithium(tetraphenyldisiloxane-1,5-diolato)] dimethyltin (IV).

2 g of diphenylsilanediol were dissolved in 10 ml THF and 11.69 ml BuLi 1.6 M were added dropwise, while continuously stirring. The mixture was stirred for another half an hour and then one equivalent of Me_2SnCl_2 was added dropwise to the reaction mixture. The white precipitate was filtrated of, and on cooling the THF solution below 0°C, acicular, transparent crystals of **1** were obtained (mp: 132°C).

^{1}H RMN (CDCl3) δ(ppm): 0.5 (s, Me)**,** 1.8 (t, THF), 3.7 (t, THF), 6.7 - 7.0 (m, Ph).

ACKNOWLEDGEMENTS

The financial support from Romanian National University Research Council (CNCSIS Grant A 195/2003) is gratefully acknowledged. We thank dr. Varga Richard for the technical assistance in determining the X-ray structure.

REFERENCES

[1] I. Abrahams, M. Motevalli, S.A.A. Shah, A.C. Sullivan, *Organomet. Chem.*, **1995***, 492*, 99.

[2] M. Lazell, M. Motevalli, S.A.A. Shah, C.K.S. Simon, A.C. Sullivan, *J. Chem. Soc., Dalton Trans.*, **1996**, *7*, 1449.

[3] M.A. Hossain, M.B. Hursthouse, M.A. Mazid, A.C. Sullivan, *Chem. Commun.*, **1988**, *19*, 1305.

[4] J. Beckmann, K. Jurkschat, U. Kaltenbrunner, N. Pieper, M. Schurmann, *Organometallics*, **1999**, *18*, 1586.

[5] R. Murugavel, A. Voigt, M.G. Walawalkar, H.W. Roesky, *Chem. Rev*., **1996**, *96*, 2205.

[6] L. King, A.C. Sullivan, *Coord. Chem. Rev.*, **1999**, *156*, 19.

[7] J. Beckmann, K. Jurkschat, M. Schurmann, D. Muller, S. Rabe, *Organometallics,* **1999**, *18*, 2326.

[8] T.P. Lockhart, W.F. Manders, *Inorg. Chem.,* **1986**, *25,* 893.

[9] J.J.P. Stewart, *J. Comp. Chem.,* **1989**, *10*, 221.

[10] Spartan02, Wavefunction Inc., 18401, Von Karman Avenue, Suite 370, Irvine, CA 92612 USA.

[11] Sheldrick, G. SHELXL-97 Program for Crystal Structure Refinement, 1997, Institüt für Anorganische Chemie der Universität, Tammanstrasse 4, D-3400 Gottingen, Germany.

STUDIA UNIVERSITATIS BABEŞ-BOLYAI, CHEMIA, XLIX, 2, 2004

Dedicated to Professor Valer Fărcăşan at his 85th anniversary

ELECTRONIC PROPERTIES OF THE ZIGZAG CARBON-NITRIDE NANOTUBES

SIMONA RADA[1], IOAN SILAGHI DUMITRESCU[1]

[1]Departament of Chemistry, "Babeş-Bolyai" University, Cluj-Napoca, 400084, Romania

ABSTRACT. The influence of possible defects of atoms due to deviations from the 1:1 stoechiometry inside of zigzag carbon-nitride nanotubes has been considered in this paper. PM3 calculations demonstrate that small quantities of nitrogen incorporated into carbon nanotube lead to thermodynamic instability relative to the pure carbon nanotubes.

This doping of the carbon nitrogen nanotubes does not significantly modify the bands in the vicinity of the Fermi level and these tubes are semiconductors.

Keywords: *carbon-nitrogen nanotubes, semiempirical calculations, electronic properties and oscillator strengths.*

INTRODUCTION

Since their discovery [**1**], carbon nanotubes and related materials have attracted much interest due to their many exceptional properties. Recently, nitrogen doping of carbon nanotubes has gained increasing attention [**2, 3**]. Up to date, only small quantities of nitrogen (<10%) have been incorporated experimentally into carbon nanotubes and filaments [**4-10**].

In this study we determined the structural, energetic and electronic properties of the (10,0)CN nanotubes with deviations from the 1:1 stoechiometry. Plots of density of states have carried out the electronic properties analysis.

METHOD OF CALCULATIONS

Carbon-nitrogen nanotubes with zigzag geometry have been considered theoretically by performing *PM3-RHF* [**11**] type semiempirical molecular orbital calculations by using Spartan '02 package [**12**].

The densities of states (*DOS*) have been calculated by the extended Hückel tight-binding method using BICON-CEDIT package [**13**]. Calculations of the oscillator strength were carried out using ICON-EDIT package [**14**].

RESULTS AND DISCUSSION

Enthalpy of formation

The structure of the basic *(10,0)C* nanotubes was taken from reference [**15**]. This tube has been virtually doped with 0, 1, 2, 3, 4, 5, 10, 20, 30, 40 or 50 nitrogen atoms. After geometry optimization we found that the carbon-nitrogen distances vary between 1,39 and 1,41Å, the C-N-C angles ranging from 117-120^0 and the N-C-N angles between 119 and 123^0. These values are in agreement with the experimental results, [**16**].

Figure 1 shows the dependence of the enthalpies of formation of the carbon nitrogen nanotubes with the nitrogen content (*x*). It comes out that the carbon nitride nanotubes are thermodynamically unstable with the increasing of *x*. This might explain the synthesis of carbon-nitride nanotubes containing no more than 13%N [**17**].

Density of states

The density of states obtained for *(10,0)C* nanotubes are shown in **Figure 2a**. From the partial *DOS(E)* plot it can be seen that the lowest bands (valence bands) are composed of *C(2s)* derived states and the conduction bands are consisted of *C(2p)* derived states.

When the band gap is not very large, usually ranging from 0,5 to 3,0eV, the material is a semiconductor, while an insulator has an E_g>3eV [**18, 19**].

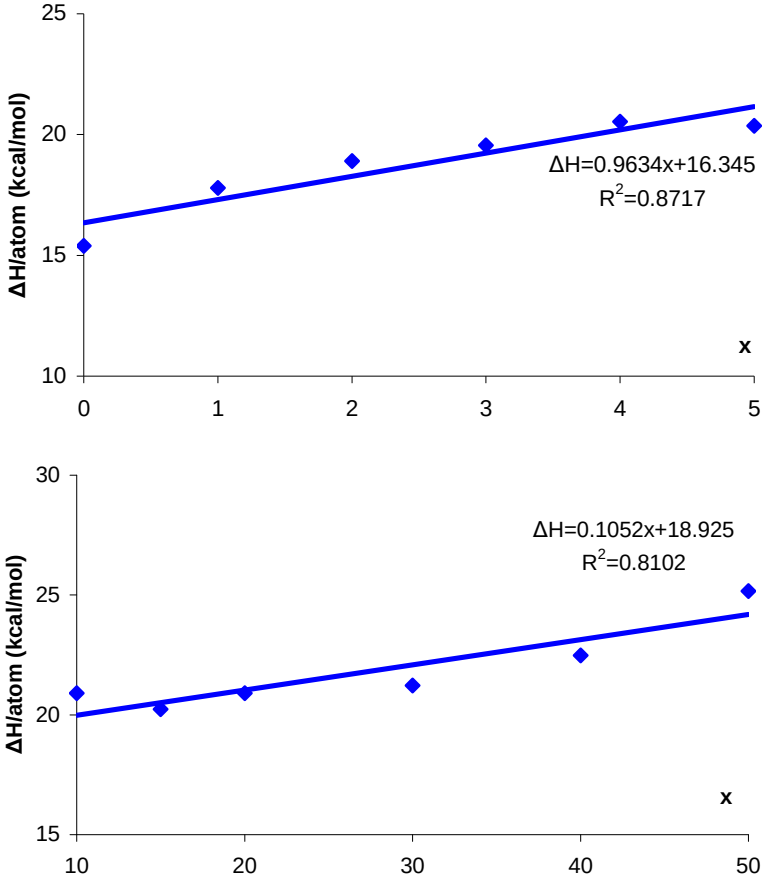

Fig. 1. Enthalpy of formation (per atom) as a function of nitrogen content (x) for (10,0)$C_{100-x}N_x$ tube.

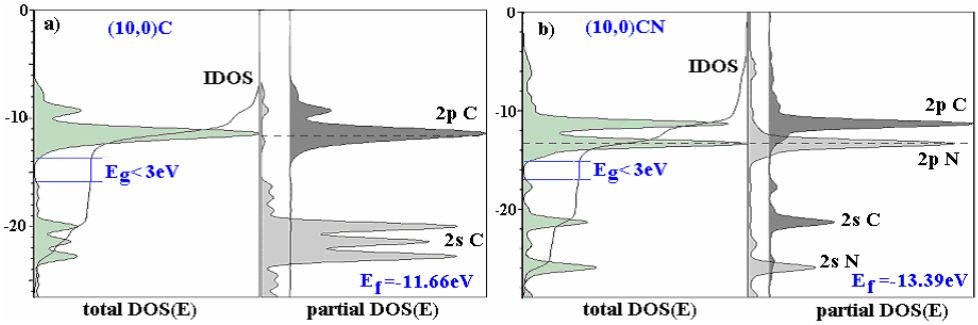

Fig. 2. The total, partial *DOS* and *IDOS* diagrams for (10,0)C and (10,0)CN tube.

The total DOS(E) and integrated DOS (*IDOS*) diagram confirm that (10,0)C nanotube is a semiconductor, which is in agreement with the experimental results published by Dresselhaus [**20**].

The total DOS and the N(2s, 2p), C(2s, 2p) contributions for (10,0)CN tube (with the 1:1 stoechiometry) are given in **Figure2b**. The partial DOS(E) plot shows that the lowest band is derived N(2s), C(2s) orbitals and conduction bands are composed of 2p orbitals of the nitrogen and carbon, respectively. Because the band gap energy is 2eV the nanotube is a semiconductor.

Clearly, in all cases displayed in **Figure 3**, the doping with nitrogen maintains the semiconductor character of the tube. Doping of the tube leads to a lowering of the Fermi level to the valence bands of the undoped tube. In the lowest unoccupied bands of the undoped tube new bands are formed. These bands correspond to the formation of an acceptor level in semiconductors with very low dopant concentration. The Fermi level is not located in the middle of Van Hove singularities which is an indication that the overlap is not very strong [**21**].

These date suggest that carbon nanotubes with small quantities of nitrogen give the same response as a tube with a closer to 1:1 stoechiometry and such tubes could be used as nanodevices.

Electronic transition

One spectral quantity that can be obtained is the oscillator strength of the electronic transitions, *f*, [**22**]. Oscillator strengths of approximate 1 signify intense transitions, while oscillator strengths of rough 0.001 denote weak transitions, [**23, 24**]. The highest values of oscillator strengths for the (10,0)&1,2,3,4N tubes lie between 0.80 (4553.8 cm^{-1}) and 0,95 (4027.9 cm^{-1}) shown intense transitions, **Table 1**.

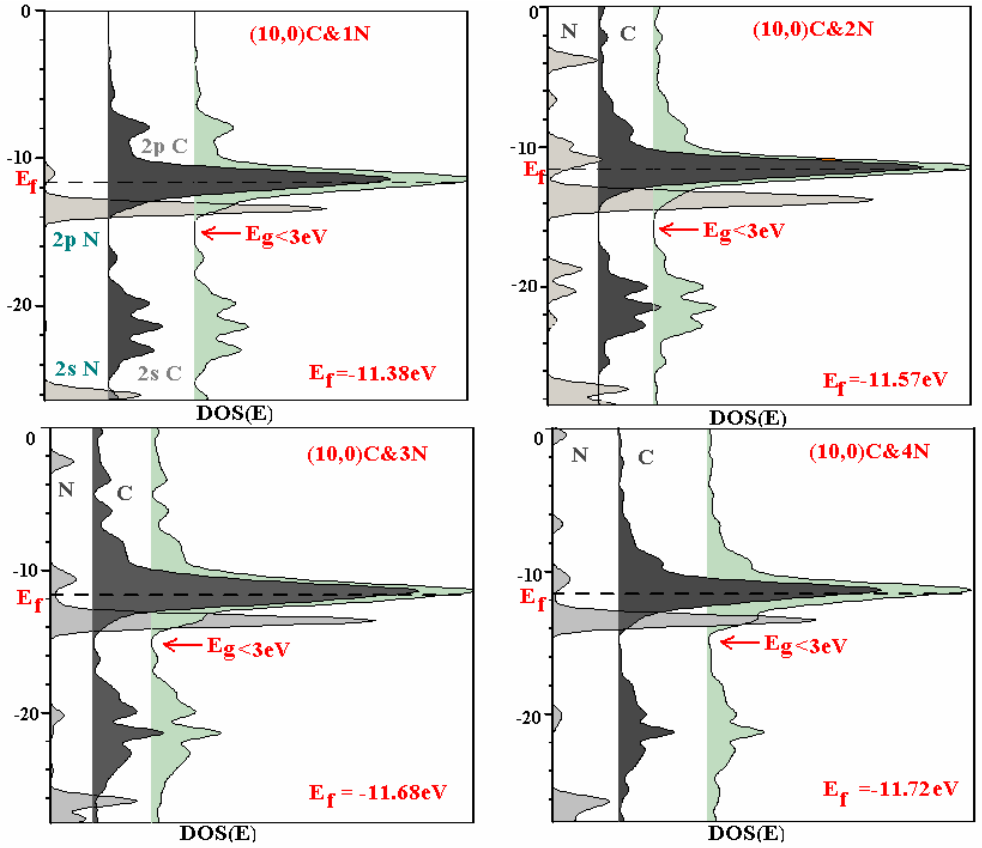

Fig. 3. The total and partial *DOS* diagrams for (10,0)C&xN tube where x =1, 2, 3, 4.

Table 1.

Calculations of oscillator strengths, *f*, wave numbers, *ú* and gap energy, E_g, for *(10,0)* nanotubes (values of *f* >0.1).

tub	ú (cm^{-1})	E_g (eV)	f	Electronic transition bring from filled to unfilled levels
(10,0)C	4764.0	0.6	0.14	homo-5→lumo+5
(10,0)C&1N	4105.6; 4755.7; 2221.9	0.5	**0.94** 0.34 0.23	homo-1→lumo+4 homo-3→lumo+4 homo-2→lumo+1
(10,0)C&2N	3950.7 2359.8 4914.2	0.5	**0.91** 0.26 0.25	homo-1→lumo+5 homo-2→lumo+2 homo-3→lumo+5
(10,0)C&3N	9743.7 10521.3 3909.2 11799.8 11022.2	0.6	**0.80** 0.57 0.38 0.23 0.22	homo-2→lumo homo-4→lumo homo→lumo+1 homo-4→lumo+1 homo-2→lumo+1

tub	ú (cm^{-1})	E_g (eV)	f	Electronic transition bring from filled to unfilled levels
(10,0)C&4N	4027.9 4127.0	0.5	**0.95** 0.25	homo→lumo+5 homo-1→lumo+5
(10,0)C&5N	4638.6	0.6	0.17	homo-1→lumo+5
(10,0)C&10N	2850.5	0.5	0.16	homo-3→lumo+1
(10,0)C&20N	7018.3	0.9	0.23	homo-3→lumo+4
(10,0)C&30N	8856.6 5192.3 12850.0 6879.1	1.1	0.40 0.27 0.23 0.20	homo-1→lumo+5 homo-2→lumo+2 homo-4→lumo+5 homo-4→lumo+2
(10,0)CN	6945.2 2281.6	0.9	0.43 0.21	homo-4→lumo+5 homo-2→lumo

The results are in agreement with the electronic density states plots shown in **Figure 3**, which denote the splitting of the Van Hove singularities corresponding to C orbital derived states.

CONCLUSION

All carbon nitride nanotubes are thermodynamically unstable relative to their carbon analogues and their stability decreases with the increasing of the nitrogen content. The $C_{100-x}N_x$ tubes have semiconductor properties for all x = 0-50.

ACKNOWLEDGEMENTS

We thank Prof. G. Calzafferi for the access to the ICON-EDIT and BICON-CEDIT packages of programs.

REFERENCES

1. S. Iijima, *Nature,* **1991***, 354*, 56.
2. D. M. Teter, R. J. Hemley, *Science,* **1996***, 271*, 53.
3. Y. Miyamoto, M. L. Cohen, S. G. Louie, *Solid State Commun.,* **1997***, 102*, 605.
4. W. Q. Han, P. K. Redlich, T. Seeger, F. Ernst, M. Ruhle, N. Grobert, W. K. Hsu, B. H. Chang, Z. Q. Zhu, H. W. Kroto, D. R. M. Walton, M. Terrones, H. Terrones, *Appl.Phys. Lett.,* **2000***, 77(12),* 1807.
5. S. Trasobares, O. Stephan, C. Colliex, W. K. Hsu, D. R. M. Walton, H. W. Kroto, *J. Chem. Phys.,* **2002***, 116*, 8966.
6. S. Trasobares, O. Stephan, C. Colliex, G. Hug, W. K. Hsu, H. W. Kroto, D. R. M. Walton, *European Phys. J.,* **2001***, 22 B*, 117.
7. M. Xucun, X Guichang, W. Enge, *Science in China (Series E),* **2000***, 43*, 71.
8. H. Yan, Q. W. Li, Y. Cheng, J. Zhang, Z. F. Liu, *J. Chem. Mater.,* **2002***, 12*, 1179.
9. R. Czerw, M. Terrones, J. C. Charlier, X. Blasé, B. Foley, R. Kamalakaran, N. Grobert, H. Terrones, D. Tekleab, P. M. Ajayan, W. Blau, M. Ruhle, D. L. Carroll, *Nano Lett.,* **2001***, 1*, 457.

10. C. C. Kaun, B. Larade, H. Mehrez, J. Taylor, H. Guo, *Phys. Rev.,* **2002***, 65B*, 205416.
11. J. J. P. Stewart, *J. Comput. Chem,* **1989***, 10*,209.
12. Spartan '02, Wavefunction, Inc., Irvine, C. A.
13. M. Brandle, R. Rytz, G. Calzaferri, *BICON-CEDIT – manual*, University of Bern, **1997**.
14. G. Calzaferri, S. Glaus, D. Bruhwiler, *ICON-EDIT – manual*, University of Bern, **1997**.
15. S.Weber, http://www.jcystal.com/steffenweber/JAVA/jnano/jnano.html, 2000.
16. H. Yan, Q. W. Li, Y. Cheng, J. Zhang, Z. F. Liu, *J. Chem. Mater.,* **2002***, 12*, 1179.
17. S. Trasobares, O. Stephan, C. Colliex, W. K. Hsu, D.R. M. Walton, H. W. Kroto, *Eur. Phys. J.*, **2001**, *22B*, 117.
18. N. C. Greenham, R. H. Friend, *Solid State Physics, Advances in Research and Application*, edited by H. Ehrenreich and F. Spaepen, **1995**, *49*, 1, Academic Press, New York.
19. C. Dekker, *Physics Today*, **1999**, *may*, 22.
20. M. S. Dresselhaus, edited by L. P. Biro, C. A. Bernando, G. G. Tibbetts, Ph. Lambin, *Carbon Filaments and Nanotubes: Commom Origins, Differing Applications?*, Kluwer Academic Publishers, **2001**, p.11.
21. E. Cappelluti, L. Pietronero, *Europhys. Chem.,* **1996***, 36*, 619.
22. G. Calzaferri, R. Rytz, *J. Phys. Chem***., 1995***, 99*, 12141.
23. R. Rytz, G. Calzaferri, *J. Phys. Chem.,* **1997***, 101 B*, 5664.
24. M. M. Hjort, S. Stafstrom, *Phys. Rev.,* **2000***, 61 B*, 14089.

STUDIA UNIVERSITATIS BABEŞ-BOLYAI, CHEMIA, XLIX, 2, 2004

Dedicated to Professor Valer Fărcăşan
at his 85th anniversary

EXTRACTION EFFICIENCY OF FLAVONOIDS FROM V*ACCINIUM MYRTILLUS* L LEAVES USING DIFFERENT EXTRACTION TECHNIQUES AND SPECTORPHOTOMETRIC QUANTIFICATION

C. COBZAC(1), M. MOLDOVAN(1), N.K. OLAH(2), L. BOBOŞ(1), S. GOCAN(1)

(1) "Babes-Bolyai" University, Faculty of Chemistry and Chemical Engineering, 11 Arany Janos, 400028 Cluj-Napoca, Romania
(2) S.C. PLANTEXTRAKT SRL Radaia, Cluj-Napoca, Romania

ABSTRACT. This paper studies the extraction efficiency of some flavonoids from Vaccinium Myrtillus leaves using different methods: Soxhlet extraction, microwave extraction and sonication.

Each extraction technique was optimized according to characteristic parameters (extraction time, extraction solvent volume and composition of extraction system).

The total flavonoid content was measured spectrophotometrically, as indicated in Romanian Pharmacopoeia (RF X). The obtained results were compared.

Key words: *Vaccinium myrtillus L. Leaves, Soxhlet extraction, Microwave extraction, Sonication, Flavonoids.*

I. INTRODUCTION

Vaccinium Myrtillus L. (blueberry) belongs to the genus *Vaccinium*, widely spread over all the world, with over 200 species of evergreen and deciduous woody plants varying from dwarf shrubs to trees. The genus *Vaccinium* includes many economically importantfarmed small fruit species, like blueberries and cranberries. It grows in Europe and Asia, especially in Scandinavia, Eastern Europe and at high altitides in Southern Europe.

Blueberries, rich in anthocyanins, have been found to be beneficial for health [1, 2, 3]. The flavonoids contained in leaves have diuretic and antibacterial actions [4, 5]. Fruits and leaves were used in traditional medicine in Europe as early as the Middle Ages [6].

Phytotherapy is often using finaly ground medicinal and aromatic plants, where all the compounds occuring in the plant are present, and also raw extracts containing only substances soluble in the extraction solvent used [7]. Different methods can be employed to identify and quantify the bioactive compound or to obtain the raw extract: traditional methods (Soxhlet extraction, solvent reflux) and modern methods (sonication, microwave assisted extraction, superfluid extraction, presurized fluid extraction) [8, 9].

The total content of compound belonging to a specific class, in this case flavonoides can be determined using spectrophotometric methods [10].

II.EXPERIMENTAL

Plant material

Vaccinium Mirtyllus follium from Fares Bio Vital (Bucharest) was finaly ground and then Soxhlet extracted with chloroform to remove chlorophyll and other lipophilic compounds.

Extraction procedure

Flavonoids from 1g samples were extracted using different techniques: reflux extraction, Soxhlet extraction, ultrasound solvent extraction (sonication) and microwave extraction.

A) Reflux extraction was done using 50ml methanol for 30min. After filtration the methanolic extract was evaporated at 75^0C and then dissolved in 10ml methanol. The obtained extract was named S_1. The extract named S_2 was obtained in similar conditions but using a mixture of methanol-water (70:30, v/v) as extraction agent, instead of methanol.

B) Soxhlet extraction was done for 5h using 100ml methanol. The methanolic extract was concentrated at 75^0C and the dry residuum was dissolved in 10ml methanol. The obtained extract is S_3.

C) The ultrasound extraction was performed in a ultrasonic bath (35kHz) and optimized for:
   - extraction time,
   - solvent volume,
   - solvent composition.

The extraction conditions are shown in table 1.

Table 1.

The experimental conditions for ultrasound extraction.

Sample	Time (min.)	Volume (ml)	Solvent composition
S_4	15	30	MeOH
S_5	30		
S_6	45		
S_7	60		
S_8	30	10	MeOH
S_9		20	
S_5		30	
S_{10}		40	
S_{11}		50	
S_{12}	30	50	MeOH - H_2O (90:10, v/v)
S_{13}			MeOH - H_2O (70:30, v/v)
S_{14}			MeOH - H_2O (50:50, v/v)

D) Microwave assisted solvent extraction was perform at 2,45 GHz under different conditions as shown in table 2.

Table 2.

Microwave assisted solvent extraction conditions.

Sample	Volume (ml)	Time (min.)	Power (W)	Solvent composition
The influence of extraction time				
S_{15}	30	1	72	MeOH
S_{16}		2		
S_{17}		3		
S_{18}		3 (each minute 1 min cooling)		
S_{19}		2 (each minute 1 min cooling)		
The influence of microwave power				
S_{20}	30	1,25	96	MeOH
S_{16}		2	72	
S_{21}		1,25	108	
S_{22}		2	81	
The influence of extraction volume				
S_{23}	10	2	72	MeOH
S_{16}	20			
S_{24}	30			
S_{25}	40			
S_{26}	50			
The influence of solvent composition				
S_{26}	50	2	72	MeOH
S_{27}				MeOH - H_2O (90:10, v/v)
S_{28}				MeOH - H_2O (80:20, v/v)
S_{39}				MeOH - H_2O (70:30, v/v)
S_{30}				MeOH - H_2O (60:40, v/v)
S_{31}				MeOH - H_2O (50:50, v/v)
S_{32}				MeOH - H_2O (40:60, v/v)
S_{33}				MeOH - H_2O (30:70, v/v)
S_{34}				MeOH - H_2O (20:80, v/v)

After extraction the samples were filtrated, evaporated to dryness at 75^0C, and then dissolved in 10ml methanol.

Quantitative determination

The total content of flavonoids was determined following the official spectrophotometric method from Romanian Pharmacopoeia (RF X)[10], using $AlCl_3$ as colorimetric reagent. 3ml aluminum chloride (25g/L) was added to 2ml methanolic extract obtained as described above, 5ml sodium acetate (100g/L) and all was brought up to 25ml in a volumetric flask with distilled water. The absorbance was measured after 15min in a 1cm cell, at 430nm. The reference sample was obtained as described above but without adding aluminum chloride. The calibration curve was plotted for rutin (metanolic solution - 0.1mg/ml) as reference compound.

III. RESULTS AND DISCUSSION

The calibration curve and the equation are presented in figure 1. The absorbance for extracts S_1 - S_{34} and the flavonoids concentrationin V*accinium Myrtillus* L. leaves depending upon the extraction condition, are presented in the table 3.

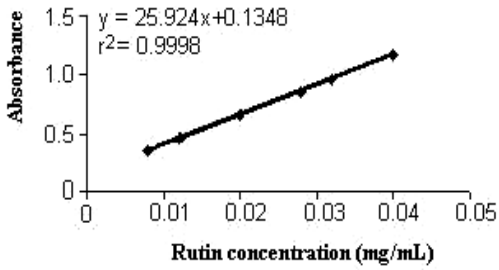

Figure 1. The calibration curve for rutin.

Table 3.

The total concentration of flavonoids compound determined by different extracting techniques.

Sample	Absorbance	Concentration (mg/ml)	Concenration (µg /g*)
Reflux extraction			
S_1	0,5617	4.39 x10^{-3}	164.7
S_2	0,8330	0.0267	267
Soxhlet extraction			
S_3	0,6090	0.0171	171
Sonication (influence of extraction time)			
S_4	0,3548	8.486 x10^{-3}	84.9
S_5	0,3575	8.59 x10^{-3}	85.9
S_6	0,3495	8.282 x10^{-3}	82.8
S_7	0,3512	8.347 x10^{-3}	83.5
Sonication (influence of solvent volume)			
S_8	0,3130	6.874 x10^{-3}	68.7
S_9	0,3500	8.3 x10^{-3}	83
S_{10}	0,4830	0.0134	134
S_{11}	0,5520	0.0161	161
Sonication (influence of solvent composition)			
S_{12}	0,5314	0.0153	153
S_{13}	0,5918	0.0176	176
S_{14}	0,6131	0.0185	185
MASE (influence of extraction time)			
S_{15}	0,2286	3.618 x10^{-3}	36.2
S_{16}	0,2723	5,304 x10^{-3}	53.0
S_{17}	0,2885	5.929 x10^{-3}	59.3
S_{18}	0,3078	9.381 x10^{-3}	93.8
S_{19}	0,3184	7.082 x10^{-3}	70.8

Sample	Absorbance	Concentration (mg/ml)	Concenration (µg /g*)
MASE (influence of power)			
S_{20}	0,2908	6.018 x10^{-3}	60.2
S_{21}	0,3212	7.19 x10^{-3}	71.9
S_{22}	0,3990	0.0102	102
MASE (influence of solvent volume)			
S_{23}	0,2492	4.4128 x10^{-3}	44.13
S_{24}	0,3303	7.541 x10^{-3}	75.4
S_{25}	0,4020	0.0103	103
S_{26}	0,3210	7.183 x10^{-3}	71.8
MASE (influence of solvent composition)			
S_{27}	0,3738	9.22 x10^{-3}	92.2
S_{28}	0,3870	9.728 x10^{-3}	97.3
S_{29}	0,4950	0.0139	139
S_{30}	0,5234	0.015	150
S_{31}	0,6730	0.02	200
S_{32}	0,7650	0.0243	243
S_{33}	0,7637	0.02425	245.5
S_{34}	0,7061	0.022	220

* raw mathreial

IV. CONCLUSIONS

Reflux and Soxhlet extraction with methanol as the extraction solvent show good efficiency (S_1 and S_3). When water is added the extraction process improves (S_2).

When sonication is used the total flavonoid concentration decreases. In this case the parameter that has a greater influence is the solvent composition (S_{14}).

Microwave extraction is a modern and efficient technique that shows very good extraction efficiency. The solvent composition has a great influence on the extraction process (S_{32}, S_{33}). The rest of the parameters (volume, time and power) have to be optimized in respect to the solvent composition.

The methods providing the best extraction efficiency are:

- Reflux extraction with a solvent composition: MeOH-H_2O (70:30, v/v)
- Microwave extraction using a solvent composition: MeOH-H_2O (30:70, v/v).

REFERENCES

[1] N. Katsube, K. Iwashita, T. Tsushida, K. Yamaki, M. Kobori, *J. Agric. Food Chem*., **2003**, *50,* 519-525.

[2] R.A. Moyer, K.E. Hummer, C.E. Finn, R.E. Wrolstad, *J. Agric. Food Chem*., **2002**, *50,* 519-525.

[3] R.L. Prior, G. Cao, A. Martin, E. Sofic, J. McEwen, C. O´Brien, N. Lischner, M. Ehlenfeldt, W. Kalt, G. Krewer, M. Mainland, *J. Agric. Food Chem*., **1998**, *46*, 2686-2693.

[4] M. Kähkönen, A. Hopia, M. Heinonen, *J., Agric. Food Chem.*, **2001**, *49*, 4076-4082.

[5] K. Robards, M. Antolovich, *Analyst,* **1997**, *122*, 11R-34R.

[6] A. Cignarella, M. Nastasi, E. Cavalli, L. Puglisi, *PubMed*., 1996, *84*, 311-322.

[7] Sz. Nyiredy, K. Glowniak, Planar Chromatography, A retrospective view for the third millenium, Springer Verlag, Ed.Sz.Nyiredy, Budapesta, **2001**, 550

[8] R.E. Majors, *LC-GC*, **1999**, *17*, 8-14

[9] J. Namiesnik, T. Goreki, *J.P.C-Mod.chromatography*, **2000**, *13*, 404-413

[10] xxx Romanian Pharmacopoeia, X Editions, Ed. Medicala, Bucuresti, **1999**, 862.

STUDIA UNIVERSITATIS BABEŞ-BOLYAI, CHEMIA, XLIX, 2, 2004

Dedicated to Professor Valer Fărcăşan at his 85th anniversary

ANTHOCYAN EXTRACTION FROM *VACCINIUM MYRTILLUS* FRUITS USING DIFFERENT EXTRACTION TECHNIQUES AND SPECTROPHOTOMETRIC AND TLC QUANTIFICATION

C. COBZAC[(1)], N.K. OLAH[(2)], C. BATIU[(1)], M. MOLDOVAN[(1)], S. GOCAN[(1)]

(1) "Babes-Bolyai" University, Faculty of Chemistry and Chemical Engineering, 11 Arany Janos, 400028 Cluj-Napoca, Romania
(2) S.C. PLANTEXTRAKT SRL Radaia, Cluj-Napoca, Romania

ABSTRACT. The paper presents a study of anthocyan extraction from blubbery fruits - *Vaccinium mirtyllus fructus.* The used extraction methods were: Soxhlet, centrifugation, reflux, microwave and sonication. The total anthocyan content was determined spectrophotometrically and the delphinidine content was determined by TLC. The best results were obtained when the centrifugation was performed at room temperature. Also typical chromatograms for the extract are similar for all extraction techniques.

Key words: *Vaccinium myrtillus L. fructus, Soxhlet, extraction, Microwave extraction, Sonication, reflux, anthocyan.*

I. INTRODUCTION

The anthocyanidins (aglycones) are polyhydroxy and polymethoxy derivates of the 2-phenylbenzopyrylium cation. They are largely responsible for the scarlet through purple to blue colours of flowers, fruits, roots and leaves of higher plants, fruit juices, red wines, etc. They accumulate in the vacuoles of epidermal or subepidermal cells, but they may also be confined to the leaf mesophyll [1,2].

The bluberry (Vaccinium myrtillus) is a bushy shrub of the cowberry family, 15 to 40 cm high. Bluberries grow on flat terrain in shadowy pine and fir woods. A popular herb widely used in holistic medicine, the bluberry can be consumed fresh or dried, with or without sugar [3-5].

The bluberry is particularly rich in vitamin C, but also contains tanning agents, pectin's, organic acids, sugar, anthocyan dyes, carotenoids, and vitamin D. The leaves contain arbutin, a phenol glycoside. Fresh berries are a potent cure for gastric catarrh, while dried bluberries help relieve intestinal inflammation and diarrhea. When consumed in large quantities, fresh bluberries are a potent cure for gout, rheumatism and metabolic disorders [6,7].

The bioactive compound can be extracted using different techniques, like classical methods - maceration, reflux, Soxhlet [8-10] and modern methods - superfluid extraction (SFE), microwave assisted solvent extraction (MASE) and sonication [11-14].

The total anthocyan content, expressed in delphinidine, was spectrophotometrically measured at 536 nm, where delphinidine showed a maximum of absorbance (Merck Index). The TLC analysis was performed as described in [15] and quantity of extracted delphinidine was determined using calibration curve method.

II. EXPERIMENTAL

Different techniques were used to extract the bioactive compounds from *Vaccinium myrtillus* fruits. A sample of 1 g dried blubbery fruits was mixed with 2 g purified sand.

Extraction procedure

Soxhlet extraction was perform using 100 ml methanolic solution of HCl (5%) until a colourless extract was obtained. After solvent evaporation the residuum was solved with 10 ml methanol. The obtained sample was called A.

The room temperature extract was obtained by sample centrifugation (15 min. at 5000 rpm) with 10 ml methanolic solution of HCl. The extraction procedure was repeated two more times. The combined methanolic extracts were dried and dissolved in 10 ml methanol obtaining the sample B.

Reflux extraction was performed for 30 min. using 30 ml methanolic solution of HCl. The extract was dried and dissolved in 10 ml methanol. This was sample C.

Sonication was performed in a sonication bath (35 kHz) for 15 min. with 10 ml methanolic solution of HCl. The extraction was repeated two more time. The methanolic solutions were unified, dried and then dissolved in 10 ml methanol in order to obtain sample D.

Microwave extraction was performed with a home made apparatus ITIM Cluj-Napoca (microwave power systems 200-1200W, frequency 2.45GHz). The extraction procedure was applied for 2 min. with 30 ml methanolic solution of HCl, at an imput coefficient of 60%. After filtration the plant material was extracted under the same experimental conditions two more times. The combined methanolic extracts were dried up and then dissolved in 10 ml methanol obtaining the E extract.

TLC Analysis

Thin layer chromatography was performed on silica gel G F254 plates (Merck). The samples (extracts A-E) were applied on the plate using a Hamilton microsiringe as bands (20 µl). For quantitative delphinidine analysis, the applied volume was 10 µl/spot from methanolic solution with different concentrations: 1.2, 2.1, 2.7, 3.0, 3.9, 4.7, 5.5 and 6.1 mg/ml.

The plate was developed in a normal development chamber with n-butanol – acetic acid – water, 40:10:20 (v/v), as mobile phase. Densitometric evaluation of the chromatographic plate was performed in reflection mode at 536 nm using a Desaga CD 60 apparatus.

Spectrophotometric analysis

An aliquot of 0.05 ml methanolic extracts was diluted with methanol in a 10 ml volumetric flask and measured at 536 nm using methanol as reference solution. The calibration curve was performed using methanolic solutions with different compound concentration (0.005, 0.010, 0.015, 0.020 and 0.025 mg/ml).

III. RESULTS AND DISCUSSIONS

Chromatographic analysis

In figure 1 is presented the chromatogram of delphinidine (1) and of each plant extract.

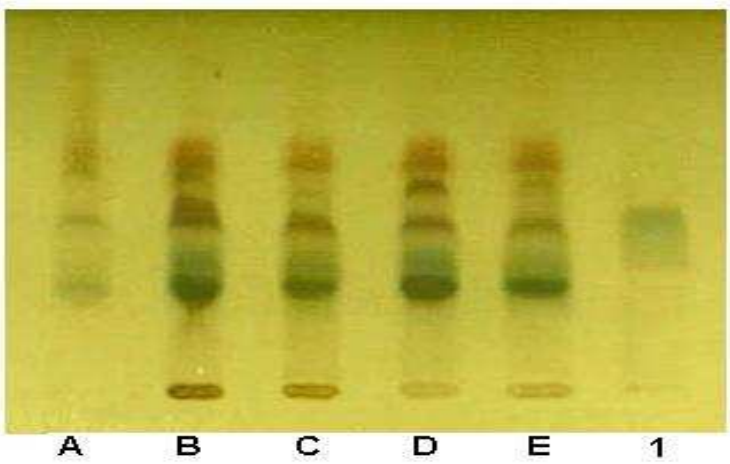

Figure 1. The typical chromatogram of delphinidine (1) and different blubbery fruit extracts (**A**, **B**, **C**, **D**, **E**)

The delphinidine spot was identified at R_f = 0.40. It can be observed that in every extract delphinidine is present in different quantities. Based on chromatograms presented in figure 1 we can observe that the fingerprints of the extracts are similar. These mean that there were no changes in the composition of extracts, no degradation processes of biocompound were occur. We can say that the extract composition does not depend up on the extraction techniques used.

The calibration curve and the coresponding parameters are presented in Figure 2.

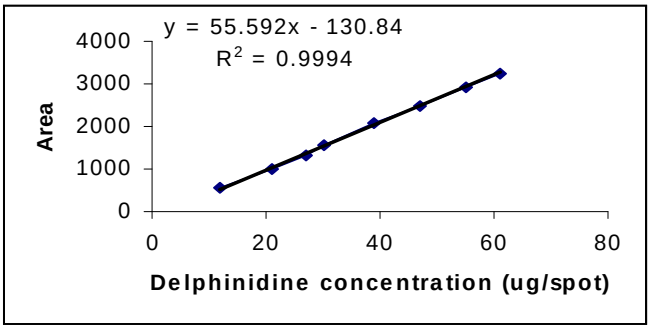

Figure 2. Calibration curve for delphinidine

In the Table 1 are presented the experimental data and the TLC determined delphinidine content.

Table 1.

Experimental data for determination of delphinidine content in the methanolic extracts.

Extract	Area	Delphinidine concentration (µg/spot)	Delphinidine content (mg/g)
A	1382	27.21	13.605
B	2878	54.12	27.06
C	2405	45.62	22.81
D	2420	45.89	22.945
E	2101	40.15	20.075

Spectrophotometric determination

The calibration curve and the parameters are presented in figure 3.

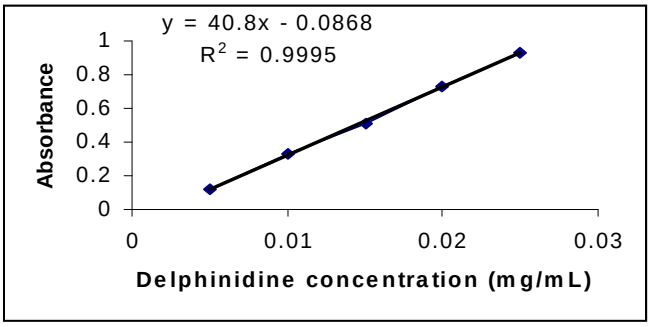

Figure 3. Calibration curve and its parameters.

The total anthocyan content in blubbery fruits was determined based on the extracts absorbance and calibration curve (Table 2).

Table 2.

Experimental data used for determination of total anthocyan content.

Extract	Absorbance	Concentration (mg/ml)	Total anthocyan content (mg/g)
A	0.350	0.0107	21.4
B	0.740	0.0202	40.4
C	0.684	0.0189	37.8
D	0.687	0.019	38.0
E	0.643	0.0179	35.8

From quantitative data presented in tables 1 and 2 we can say that the content of anthocyan and delphinidine is correlated with the extraction techniques used. The biocompound extracted quantities using reflux, sonication and microwave as extraction techniques are comparable. The prolonged heating and thermolability of the anthocyan can explain the lower extraction efficiency of the Soxhlet techniques. Centrifugation at room temperature provides the better extraction efficiency than other tested techniques.

IV. CONCLUSIONS

From this experiment we can conclude that the extraction composition does not depend upon the extraction techniques used. The extracted biocompound quantities are depending upon the extraction techniques involved. The best extraction technique is centrifugation at room temperature.

REFERENCES

1. Istudor, V., Farmacognozie, Fitochimie, Fitoterapie vol.II, Ed. Medicală, Bucureşti, **2001**.
2. Neamțu, G., Cîmpeanu, G. and Socaciu, C., Biochimie vegetală, Ed. Didactică şi Pedagogică, Bucureşti, **1993**.
3. Cignarella, A., Nastasi, M., Cavalli, E. and Puglisi, L., *PubMed*., **1996**, *84*, 311.
4. Katsube, N., Iwashita, K., Tsushida, T., Yamaki, K. and Kobori, M., *J. Agric. Food Chem.*, **2003**, *50*, 519.
5. Kähkönen, M., Hopia, A. and Heinonen, M., *J. Agric. Food Chem*., **2001**, *49*, 4076.
6. Moyer, R. A., Hummer, K. E., Finn, C. E. and Wrolstad, R. E. *, J. Agric. Food Chem*., **2002**, *50,* 519.
7. Prior, R. L., Cao, G., Martin, A., Sofic, E., McEwen, J., O´Brien, C., Lischner, N., Ehlenfeldt, M., Kalt, W., Krewer, G. and Mainland, M., *J. Agric. Food Chem.*, **1998**, *46*, 2686.
8. M.Schuhmacher, J.L.Domingo, A.Xifro, S.Granero, J.L.Llobet, *J.Environ.Sci.Health,* **1998**, *33*, 195.
9. A.M.Kipopoulou, E.Manoli, C.Samara, *Environ.Pollut.,* **1999**, *106*, 369
10. fitochimie
11. L. E. Garcia- Ayuso, M. Sanchez, F. de Alba şi M. D. Luque de Castro, *Anal Chem*., **1998**, *70*, 2426.
12. V. Camel, *Trends Anal. Chem*., **2000**, *19*, 229.
13. C. S. Eskilsson, E. Björklund*, J. Chromatogr. A.*, **2000**, *902*, 227.
14. J.Namiesnik, T.Gorecki, *J.P.C.-Mod.TLC,* **2000**, *13*, 404.
15. H.Wagner, S.Bladt, E.M.Zgainski, Drogenanalyse, Dunnschichtchromatographische Analyse von Arzneidrogen, Springer Verlag, Berlin, Heidelberg, New York, **1983**, 272

STUDIA UNIVERSITATIS BABEŞ-BOLYAI, CHEMIA, XLIX, 2, 2004

Dedicated to Professor Valer Fărcăşan
at his 85th anniversary

BONDING IN FERRIC-OXO COMPLEXES

RADU SILAGHI-DUMITRESCU

Department of Chemistry, "Babeş-Bolyai" University, 11 Arany Ianos Str. Cluj-Napoca RO-400028, Romania and *Department of Chemistry and Center for Metalloenzyme Studies, University of Georgia, Athens, Georgia 30602, U.S.A.,*

ABSTRACT. Iron (IV) oxo complexes have been implicated in key biological oxidations with heme and non-heme enzymatic systems. Related to these, a non-heme iron (III) oxo complex has recently been described. Intriguingly, the Fe(III)-oxo interaction was proposed to consist of one σ bond, while the absence of π bonding would be compensated by three hydrogen bonds between the oxo atom and the ligand scaffold surrounding the iron. Here, we report density functional calculations unambiguously indicating that hydrogen bonding *weakens the* Fe-O bond, and Fe-O π bonding *does in fact exist* in the above-mentioned Fe(III)-oxo adduct.

INTRODUCTION

Iron (IV) oxo complexes have been implicated in key biological oxidations with heme and non-heme enzymatic systems[1-10]. Related to these, the S=5/2 iron (III) oxo complex **1** (Figure 1) has recently been described[11,12]. **1** featured a 1.81-Å Fe-O bond, which was shorter by ~0.1 Å than the Fe-OH bond in the homologous Fe(III)-OH complex[11,12]. Intriguingly, the Fe(III)-oxo interaction in **1** was proposed to consist of one σ bond, while the absence of π bonding would be compensated by three hydrogen bonds between the oxo atom and the ligand scaffold surrounding the iron[12]. Here, we report density functional calculations unambiguously indicating that, contrary to previous reports, hydrogen bonding *weakens* Fe(III)-O bonding. Additionally, we demonstrate that Fe(III)-O π bonding *does in fact exist* in the above-mentioned Fe(III)-oxo adduct.

RESULTS AND DISCUSSION

Table 1 shows key geometrical parameters for **1**, obtained from X-ray diffraction[11,12] and DFT (UBP86/6-31G**)[13-15] unconstrained geometry optimization. Also shown is data for the model **1-H**, formally obtained via protonation of the oxo atom in **1** to yield a ferric-hydroxo adduct. Additionally, since NH---O hydrogen bonding has been proposed to play a key role in iron-oxo bonding within **1**[12], we also report geometry optimization of **1-t** (cf. Figure 1), which is formally obtained from **1** by removing the three hydrogen bond-donating termini of the urea ligands. For **1** and **1-H**, the calculated Fe-O bond lengths are in good agreement with experiment and with previously reported B3LYP results[12]. In this respect, our data further supports the idea that the experimentally-observed **1** is an oxo, not a hydroxo, compound[11,12].

Table 1

Key geometrical parameters for S=5/2 **1**, **1-H** and **1-t**

	Fe-O	Fe-N_{ax}[a]	Fe-N_{eq}[b]	H···O[c]
1 (exptl)	1.81	2.27	2.06	1.91
1 (DFT)	1.82	2.14	2.09	1.69
1-H (extpl)	1.92	2.19	2.02	2.13
1-H (DFT)	1.95	2.07	2.30	2.14
1-t (DFT)	1.75	2.62	2.12	2.72

[a] nitrogen atom trans to (hydr)oxo. [b] urea nitrogens, average of three values.[c] NH---O hydrogen bonds, average of three values (cf. Figure 1). The X-ray crystal structures of **1** and **1-H** each feature two short (~ 1.75 Å) such hydrogen bonds and a longer one (elongation of the latter is due to steric clash between the hydroxo and NH protons in **1-H**). DFT-optimized **1** features three identical hydrogen bonds at ~1.7 Å; this latter result would seem to indicate the presence of a hydroxo, not oxo, ligand in the crystal structure of **1**.

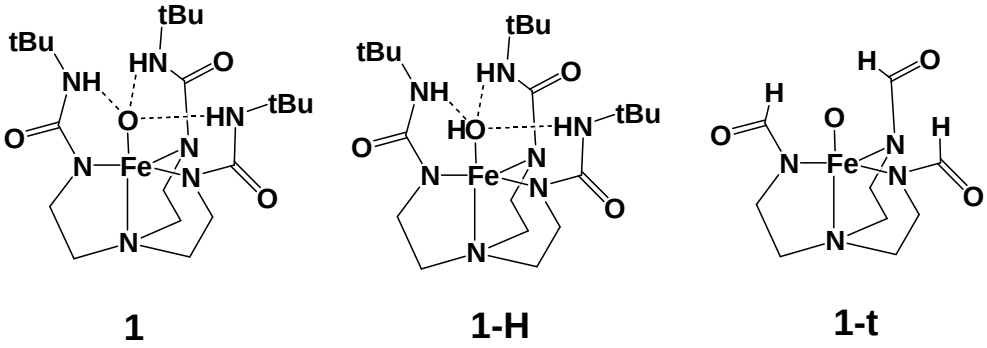

Fig. 1. Models employed in the present study.

Figure 2 shows molecular orbitals illustrating Fe(III)-oxo bonding (orbitals shown for **1-t** rather than for **1**, for simplicity). For the σ, π_{xz} and π_{yz} interactions, the bonding orbitals are all doubly-occupied, while the antibonding orbitals are all singly-occupied. This then amounts to a formal bond order of 1.5, arising from 1/2 σ bond and two 1/2 π bonds. Similarly, for **1-H** the bond order is 1, with 1/2 σ bond and 1/2 π bond. Others have by contrast reported that the Fe-O bond order in **1** was in fact ~1, and that this arose from one single σ bond and no net π bonding[12,16]. To compensate for the absence of π bonding, a key role for NH----O hydrogen bonding in stabilizing the Fe(III)-oxo bond was proposed[12]. Table 1 instead shows that when the three hydrogen bonds are removed (i.e., in model **1-H**), the Fe-O bond shortens by 0.06 Å. This is consistent with the hydrogen bonds competing with the iron for the oxo p orbitals. Thus, the formal iron-oxo bond order in **1** is 1.5, and NH---O hydrogen bonding contributes to weakening, rather than strengthening of the iron-oxo interaction.

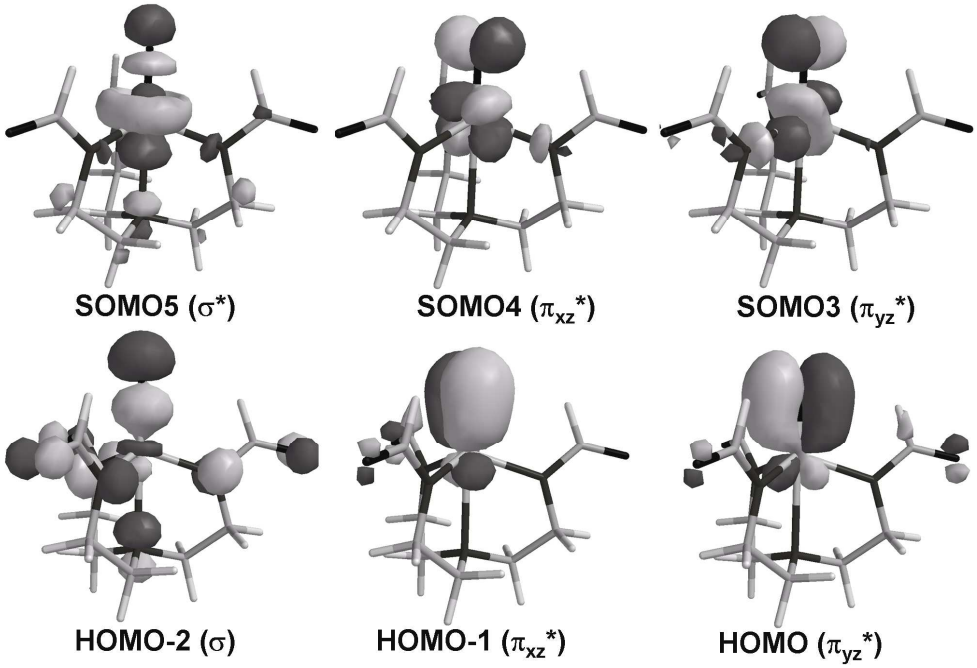

Fig. 2. Molecular orbitals illustrating the Fe(III)-oxo interaction (isocontour 0.045). We use convention of labeling the five singly-occupied orbitals on iron as SOMO1 through SOMO5.

1 was proposed[11,12] to have relevance for the Fe(IV)-oxo complexes widely invoked in biological processes[1-8]. Scheme 1 shows a comparison of the molecular orbital diagrams for experimentally observed S=1 Fe(IV)-oxo[8,9] and S=5/2 Fe(III)-oxo complexes. Notably, S=5/2 Fe(III)-oxo contains one additional electron in a σ* orbital, compared to S=1 Fe(IV)-oxo. Thus, while the latter features one σ bond and two 1/2 π bonds (a formal bond order of 2.0), the former features 1/2 σ and two 1/2 π bonds (amounting to a formal bond order of 1.5). Consistent with this, the iron-oxygen distance in **1** is longer by ~0.1 Å than typical Fe(IV)-oxo bonds[17-19].

Notable in Fe(IV)-oxo complexes is the high covalence of the iron-oxo π interaction. Thus, within the singly-occupied π_{xz}* and π_{yz}* orbitals, 50% of each electron formally resides on the oxo atoms[17-19]. The Fe(III)-oxo interaction in **1** is less covalent, with only ~30% of the σ*, π_{xz}* and π_{yz}* electrons delocalized onto the oxygen. Fortuitously, in both Fe(IV)-oxo and Fe(III)-oxo, a total of ~one spin unit is localized on the oxygen.

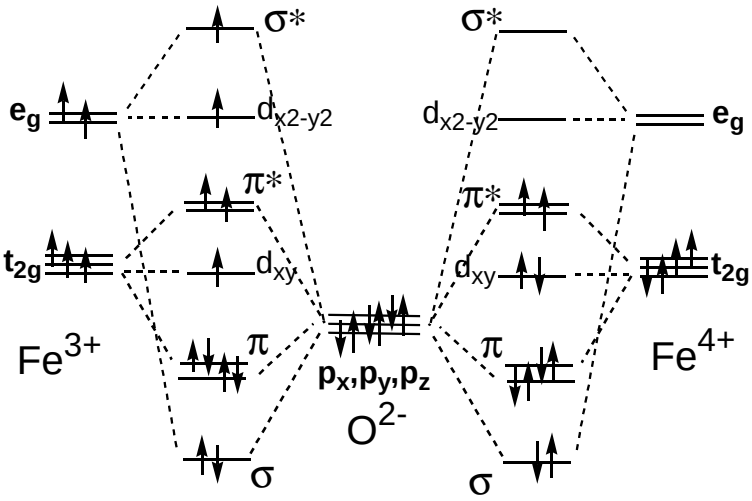

Scheme 1

Thus, **1** features an iron-oxo bond even weaker than Fe(IV)-oxo bonds invoked in substrate oxygenation by highly reactive species such as cytochrome P450 Compound I (which undergoes the reaction shown in Scheme 2)[20]. **1** also features as much spin density on the oxo atom as P450 Compound I[20]. Why doesn't **1** exhibit P450 – like reactivity? It has been proposed[12] that the protecting hydrogen-bonding scaffold around the oxo atom stabilizes the oxo ligand electronically and protects it sterically. Alternatively, the more ionic character of Fe(III)-oxo bond compared to Fe(IV)-oxo, outlined above, may disfavor P450-type chemistry (which, as shown in Scheme 2 and as largely ignored in current literature[9], consists of *oxygen atom* and not an O^{2-} ion transfer).

$$\mathbf{[FeO]^{2+} + R\text{-}H \rightarrow R\text{-}OH + Fe^{2+}}$$

Scheme 2

EXPERIMENTAL

Geometries were optimized with the BP86 functional, which uses the gradient-corrected exchange functional proposed by Becke (1988)[14], the correlation functional by Perdew (1986)[15], and the DN** numerical basis set (comparable in size to 6-31G**), as implemented in Spartan[13]. For the SCF calculations, a fine grid was used, and the convergence criteria were set to 10^{-6} (for the root-mean square of electron density) and 10^{-8} (energy), respectively. For geometry optimization, convergence criteria were set to 0.001 au (maximum

gradient criterion) and 0.0003 (maximum displacement criterion). Charges and spin densities were derived from Mulliken population analyses after DFT geometry optimization.

ACKNOWLEDGMENT

Dr. I. Silaghi-Dumitrescu (UBB) is thanked for helpful discussions.

REFERENCES

1. D. L. Harris, *Curr. Opin. Chem. Biol*., **2001**, *5*, 724-735.
2. A. N. P. Hiner, E. L. Raven, R. N. F. Thorneley, G. Garcia-Canovas, J. N. Rodriguez-Lopez, *J. Inorg. Biochem*., **2002**, *91*, 27-34.
3. I. S. Isaac, J. H. Dawson, *Essays Biochem*., **1999,** *34*, 51-69.

[4] I. Schlichting, J. Berendzen, K. Chu, R. M. Sweet, D. Ringe, G. A. Petsko, S. G.Sligar, *Science,* **2000**, *287*, 1615-1622.

5. M. Sono, M. P. Roach, E. D. Coulter, J. H. Dawson, **Chem. Rev**., **1996**, *96*, 2841-2887.
6. E. I. Solomon, PNAS 2003, **100**, 3589-3594.
7. E. I. Solomon, T. C. Brunold, M. I. Davis, J. N. Kemsley, S.-K. Lee, N. Lehnert, F. Neese, A. J. Skulan, Y.-S. Yang, J. Zhou, *Chem. Rev*., **2000**, *100*, 235-350.
8. M. Costas, M. P. Mehn, M. P. Jensen, L. J. Que**, 2004**, DOI: 10.1021/cr020628n.
9. S. Shaik, S. Cohen, S. P. de Visser, P. K. Sharma, D. Kumar, S. Kozuch, F. Ogliaro, D.Danovich, *Eur. J. Inorg. Chem*., **2004**, 207-226.
10. J. R. Price, E. W. Barr, T. E. Glass, C. Krens, J. M. Bollinger, Jr, *J. Am. Chem. Soc*., **2003**, *125*, 13008-13009.
11. C. E. MacBeth, A. P. Golombek, V. G. Young, Jr, C. Yang, K. Kuczera, M. P. Hendrich, A. S. Borovik, *Science*, **2000**, *289*, 938-941.
12. C. E. MacBeth, R. Gupta, K. R. Mitchell-Koch, V. G. Young, Jr, G. H. Lushington, W. H. Thompson, M. P. Hendrich, A. S. Borovik*, J. Am. Chem. Soc*., **2004**, *126*, 2556-2567.
13. Spartan 5.0, Wavefunction, Inc., 18401 Von Karman Avenue Suite 18370, Irvine, CA 92612 U.S.A.
14. A. D. Becke, *Phys. Rev*., **1988**, 3098-3100.
15. J. P. Perdew*, Phys. Rev*., **1986**, B33, 8822-8824.
16. One possible source of confusion when applying automatic analyses such as NBO (used by MacBeth et al) is, in this case, the presence of two apparently non-bonding molecular orbitals with iron d_{xy} and d_{x2-y2} character, mixed with small amounts of oxygen p_x/p_y character. Taken together, and presumably due to their slight deviation from ideal symmetry, these two orbitals are likely to account for the formal cancellation of ~0.5 of the Fe-oxo bond order seen from the NBO analysis of MacBeth et al. We maintain that this cancellation cannot justify an assignement of

a formal bond order of 1. The iron-oxo s, p_{xz}* and p_{yz}* molecular orbitals still feature one unpaired electron each, and not two unpaired electrons each. To obtain a formal bond order of 1 with one s bond and no p bond, one would need to (1) have an empty iron d_{z2} orbital, and (2), have two doubly-occupied iron-oxo p* orbitals (or four singly-occupied p*), which is physically impossible.

17. H. Kuramochi, L. Noodleman, D. A. Case, *J. Am. Chem. Soc*., **1997**, *119*, 11442-11451.
18. S. Yamamoto, J. Teraoka, H. Kashiwagi, *J. Chem. Phys*., **1988**, *88*, 303-312.
19. R. Silaghi-Dumitrescu, unpublished results.
20. R. Silaghi-Dumitrescu, *J. Biol. Inorg. Chem*., **2004,** *9*, 471-476.